SIMULATION AND EXPERIMENTAL ANALYSIS OF LATERAL AND TORSIONAL VIBRATION OF A CRACKED OVERHANGING ROTOR SHAFT

ABDUALHAKIM AHMED TLAISI

SIMULATION AND EXPERIMENTAL ANALYSIS OF LATERAL AND TORSIONAL VIBRATION OF A CRACKED OVERHANGING ROTOR SHAFT

By

© Abdualhakim Ahmed Tlaisi

A Thesis Submitted to the

School of Graduate Studies

in partial fulfillment of the requirements for the degree of

Doctor of Philosophy

Faculty of Engineering and Applied Science

Memorial University of Newfoundland

January 2013

St. John's Newfoundland Canada

In the Name of ALLAH, the Beneficent, the Merciful

To **Prophet Mohammed** (Peace *and Blessings be upon him); t*o my mother, Norya; to my father, Ahmed; to my brother, Mohammed; to my wife, Enas; to my sons, Suehail, Seraj-eddin, Sajeda, and AbduALLAH

Abstract

Crack detection in cylindrical rotor shafts is an important area for research. Crack detection in cylindrical rotor shaft is a difficult task because the changes observed in the vibration characteristics of the shafts, even in the presence of large-sized cracks are very small. Early identification of the presence of cracks becomes essential to prevent sudden failures of rotating shafts. The problem of detecting cracks in shafts cannot be solved analytically without making many assumptions. Therefore, extensive experimental and numerical analysis is required, using modal testing and appropriate numerical techniques such as the Finite Element Method (FEM), for the identification of cracking in rotor shafts.

In this study experimental and numerical investigations were carried out to identify the presence of a crack in a cylindrical overhanging rotor shaft with a propeller attached to the free end of the rotor. The rotor shaft was supported on a test frame using two supports. The rotor shaft had a cantilevered portion carrying the propeller. The rotor shaft was supported using ball bearings that were attached to the two test frame supports.

In the experimental study, cracks of different depths were created on the shaft at the position of the maximum bending moment. The shaft's vibration responses for lateral and

torsional vibrations were measured using an accelerometer, and shear strain gages fixed at three different locations, respectively. The response parameters of the shaft were then obtained using the modal analysis software, LMS Test Lab™. These experimental results were used to validate the numerical results obtained from a finite element analysis (ANSYS) using the beam element, BEAM4, and the three-dimensional iso-parametric elements (element types 186 and 187).

A finite element model for the shaft and its supports was created using the beam element "BEAM4" available in the ANSYS software package to simulate the dynamic response of un-cracked and cracked shafts. In this study, a linear "three-to six- spring" model was used to represent the elastic deformation effects of each of the two ball bearings, supporting the shaft, over the frame supports. The number, nature and stiffness values of these spring constants were determined to obtain the best agreement between the experimental and numerical results for the uncracked shaft. The stress intensity effects caused by the existence of cracks were simulated using a short beam element.

Subsequently a numerical study was performed using finite element models for the un-cracked and the cracked shafts (with varying crack depths) which were created using 3-D iso-parametric elements (element types 186 and 187), available in the ANSYS FEM program. The open crack was embedded in the shaft and the mesh generation was suitably modified to incorporate the stress intensity effects present at the crack tip. The impedance and mobility frequency response functions were used to identify the crack depth in the shaft system. Impedance and mobility were measured and simulated

numerically in the vertical direction for the resonant frequencies and anti-resonant frequencies. The results indicated that the use of the rate of change of frequencies, modal amplitudes (of displacements, velocities and accelerations) as a function of crack depth ratio can successfully predict the presence of cracks in the shaft for cracks having depth to diameter ratio greater than 0.2. The results also showed that the rate of change of the frequency of torsional vibration can be used successfully to predict the presence of cracks of smaller depth ratio.

Using the terminology existing in the literature, the approach developed in this study will provide a sound and robust procedure for a third level of damage assessment (wherein the crack depth is determined) by using vibration techniques.

Acknowledgements

First of all, I would like to thank my Lord. Thank you, thank you God for Your countless blessings, I thank You for helping me complete this work; may His name be praised and glorified.

I would like to express sincere appreciation to my supervisor Dr. M. R. Haddara for his support, assistance, and guidance during my program at Memorial University. I thank you Dr. Haddara once again because helped me join Memorial. I also thank him for helping me to develop a plan to complete the various stages of the academic program from the beginning.

I would also like to thank my co-supervisor Dr. Ayhan, who provided continuous help to overcome all the obstacles that I faced during the course of my study, without his support I may have not been able to complete my task.

I am most grateful to my real guide during my thesis program at Memorial University, Dr. A. S. J. Swamidas, for his encouragement and constant support. I also thank him for the advice and guidance he gave me, using his experience in the field of research. He gave me a lot of his time and effort to direct my thesis investigations, I thank him for that.

The author would like to express his sincere gratitude to the Staff of the Structural Lab of the faculty of Engineering and Applied Science at the Memorial University.

I also for would like to thank the financial support provided by the Government of Libya and funding agency (National Research Council of Canada) for funding the costs.

Finally, I would like to thank my wife for her constant encouragement and support of all my undertakings and for her care for our children.

Table of Contents

Abstract....iv

Acknowledgements....vii

List of Tables....xiii

List of Figures....xv

List of Appendices....xxxii

Chapter 1 Introduction....1

1.1 General....1

1.2 Objective and Scope of Study....3

1.3 Outline of the thesis....6

Chapter 2 Literature Review....8

2.1 Introduction....8

2.2 Experimental Approach....9

2.2.1 Introduction....9

2.2.2 Crack Detection and Modal Testing....9

2.2.2.1 Beam....11

2.2.2.2 Rotor shaft....15

2.3 Analytical and Numerical Approaches....23

2.3.1 The Finite Element (FE) Approach....24

2.3.2 Nonlinear Dynamics of a Cracked Rotor....30

2.3.3 Detection and Monitoring of Cracks Using Mechanical Impedance....32

2.3.4 Crack Detection Methods using Other Techniques....38

2.4 Summary....40

Chapter 3 Fabrication of Experimental Model and Test Setup....42

3.1 Introduction....42

3.2 Fabrication of Test Frame....43

3.3 Shaft-Propeller Test Rig and Experimental Setup....43

3.3.1 Test Rig Description....46

3.3.2 Test Instrumentation System and Methodology....51

3.3.3 Calibrations for Torque Measurement....55

3.4 Test Procedure and Measurements....55

3.4.1 Off-line Experimental Transverse Vibration Modal Analysis....56

3.4.2 Modal Testing and Analysis of Cracked Shaft....59

3.5 Experimental Results....65

3.5.1 Measured Natural Frequencies and Mode Shapes for Lateral Vibration....66

3.5.2 Rate of Change of Bending Frequencies with Respect to Crack Depth Ratio73

3.5.3 Measured Natural Frequencies for Torsional Vibration....75

3.6 Summary....77

Chapter 4 Modeling of the Rotor Shaft System for Crack Detection Using Transverse Vibrations and Beam Elements....79

4.1 Introduction....79

4.2 Theory and Modeling of the Bearing Support....80

4.3 Description of the Numerical Model in ANSYS using Beam4 Element....82

4.4 Results from ANSYS - Beam4 and Discussions....87

4.5 Summary....100

Chapter 5 Crack Detection in Rotor Shafts Using Vibration Measurements and Numerical Analyses using Three-Dimentional Isoparemetric Elements....102

5.1 Introduction....102

5.2 Modeling of Rotor Shaft-Bearing-Propeller System with ANSYS Workbench.103

5.2.1 Elements Used in Analysis....104

5.2.2 Mesh Convergence Study and Geometry....105

5.2.3 Contact Behaviour....106

5.2.4 Materials....108

5.3 Presentation of the Results and Discussion....110

5.4 Summary....135

Chapter 6 Crack Detection in Shafts Using Mechanical Impedance from Experimental Measurements and Numerical Computations..... 137

6.1 Introduction..... 137

6.2 Definition of Mechanical Impedance..... 138

6.3 Mechanical Impedance and Multi-Degree-of-Freedom Systems..... 138

6.4 Relationship Between Input and Output in the Dynamic Response of a Rotating Shaft..... 140

6.5 Presentation of Results and Discussion..... 142

6.6 Summary..... 155

Chapter 7 Conclusions and Recommendations..... 157

7.1 Conclusions..... 157

7.2 Recommendations..... 164

Bibliography..... 167

Appendices..... 177

List of Tables

Table 3-1 The Measured Diametral Values for the Three Rotor Shafts.....47

Table 3-2 (a) Experimental Values of the Natural Frequencies for Various Crack Depth-Ratios, (Shaft #1).....67

Table 3-2 (b) Experimental Values of the Natural Frequencies for Various Crack Depth-Ratios, (Shaft # 2).....68

Table 3-2 (c) Experimental Values of the Natural Frequencies for Various Crack Depth-Ratios, Horizontal (Shaft # 3).....68

Table 3-3 Theoretical and Experimental Values of the Mass Moment of Inertia and the Torsional Natural Frequencies..... 76

Table 4-1 Experimental and Numerical Values of the Natural Frequencies for Various Crack Depth-Ratios..... 90

Table 4-2 Differences between Numerically and Experimentally Obtained Frequencies, for Various Crack Depth-Ratios for the Equivalent Shaft Length Modeling.....95

Table 5-1 Numerical Values of the Natural Frequencies for Various Crack Depth-Ratio.....106

Table 5-2 Material Properties Used in the Numerical Modal.....108

Table 5-3 Experimental and Numerical Values of the Natural Frequencies for Various Crack Dept-Ratios.....111

Table 5-4 Mathematical Equations Obtained for the Frequency Ratio Curve and its Slope as a Function of Crack Depth-Ratio.....128

Table A.1.1 (a) Experimental Values (Shaft # 1) of Natural Frequencies for Various Crack Depth-Ratios.....177

Table A.1.1 (b) Experimental Values of the Natural Frequencies for Various Crack Depth-Ratios for Shaft # 1 178

Table A.1.1 (c) Experimental Values of the Natural Frequencies for Various Crack Depth-Ratios for Shaft # 1 179

Table A.1.2 (a) Experimental Values of the Natural Frequencies for Various Crack Depth-Ratios for Shaft # 2 180

Table A.1.2. (b) Experimental Values of the Natural Frequencies for Various Crack Depth-Ratios for Shaft # 2 181

Table A.1.2 (c) Experimental Values of the Natural Frequencies for Various Crack Depth-Ratios for Shaft # 2 182

Table A.1.3 (a) Experimental Values of the Natural Frequencies for Various Crack Depth-Ratios for Shaft # 3 182

Table A.1.3 (b) Experimental Values of the Natural Frequencies for Various Crack Depth-Ratios for Shaft # 3 183

Table A.1.3 (c) Experimental Values of the Natural Frequencies for Various Crack Depth-Ratios for Shaft # 3 184

Table D.2.1 Experimental and numerical values of the natural frequencies for various crack depth-ratios 199

List of Figures

Figure 1.1 Boat Propeller Shaft..... ..5

Figure 1.2 Hybrid Shaft Generator (HSG).....5

Figure 1.3 Components in Turbines and Generators for Nuclear and Thermal Power Plants..... ..5

Figure 2.1 A Sketch of Rotor System RK 4.....27

Figure 2.2 Rotor System and Crack Model Cross-Section.....31

Figure 2.3 Marine Propulsion-Shafting Systems; a) Modeling 1 and b) Modeling 2.....34

Figure 3.1 Schematic Diagram of the Shaft-Bearing-Propeller System Model.....44

Figure 3.2 Fabrication Diagram of the Rotor Shaft-Supporting-Bottom Steel Plate with a Fixed Aluminum Plate.....44

Figure 3.3 Figure of the Propeller Giving (a) Actual Experimental Propeller Used in the Study; and (b) Numerical Modal Used in Analysis.....45

Figure 3.4 Fabrication Diagrams of the Upper and Lower Parts of Torque Applying Arm.....46

Figure 3.5 The Shaft-Propeller System Bearing Test Rig Setup.....48

Figure 3.6 Jaw Coupling..... 49

Figure 3.7 Schematic of Un-Cracked Shaft During on-Line Monitoring Studies (the Jaw Coupling at the Backside of Bearing 1 is Disconnected During Modal Tests).....49

Figure 3.8 (a) Details of Bearing Support; and (b) Dimensions of the Mounted Bearing.....50

Figure 3.9 The Saw-Cut Crack at the Right of the Bearing Number 2.....51

Figure 3.10 The Test Instrumentation Equipment: (a) LMS Test Lab with Rotor Shaft; (b) Impact Hammer and Tips; (c) Accelerometer; (d) Strain Gage; (e) Data Acquisition; and (f) Aluminum Arm for Impact Loading on Shaft.....54

Figure 3.11 Impact Hammer and Accelerometer Locations.....57

Figure 3.12 Experimental Procedures for Impact Testing of the Rotor Shaft.....58

Figure 3.13 Photo of the Attached Accelerometer.....59

Figure 3.14 (a) LMS Test Lab with the Shaft During Modal Tests; (b) the Clamped End of the Cylindrical Shaft at Bearing 1; and (c) The Saw-Cut Crack with 70% Crack Depth Ratio.....60

Figure 3.15 Schematic of the Torsional Vibration Measurement Instrumentation; (a) Strain Gage; (b) Torsional Load Application System (c) Strain Gauges Used During Modal Tests; (d) Schematic of the Torsional Strain Gauges; and (e) Shear Strain Gage Used.....63

Figure 3.16 Photo of the Platform Suspension Setup; (a) Platform; and (b) Platform with Propeller.....64

Figure 3.17 First Mode Shapes of Un-Cracked and Cracked Rotor Shaft from Experimental Work (a) Vertical (b) Horizontal.....69

Figure 3.18 Second Mode Shapes of Un-Cracked and Cracked Rotor Shaft from Experimental Work (a) Vertical (b) Horizontal.....70

Figure 3.19 Third Mode Shapes of Un-Cracked and Cracked Rotor Shaft from Experimental Work (a) Vertical (b) Horizontal.....71

Figure 3.20 Fourth Mode Shapes of Un-Cracked and Cracked Rotor Shaft from Experimental Work (a) Vertical (b) Horizontal.....72

Figure 3.21 Depth of Crack Vs. Percent Decrease in Natural Frequencies for Experimental Results: (a) Vertical (b) Horizontal.....74

Figure 3.22 Rate of Change of Frequency (with Respect to Crack Depth Ratio) Vs. Crack Depth Ratio of the First Four Frequencies; (a) Mode One; (b) Mode Two; (c) Mode Three; (d) Mode Four.....75

Figure 3.23 Depth of Crack and Percent Decrease in Torsional Natural Frequencies for Experimental Results; and (b) Rate of Change of the curve in part a vs. Crack Depth Ratio..... .77

Figure 4.1 Finite Element Model for Cylindrical Shaft and Bearings: (a1) and (a2) Six Translational Springs Modeling; (b1) and (b2) Four Translational and Two Rotational Springs Modeling ;(c1) and (c2) Eight Translational Springs Modeling; (d1) and (d2)

Eight Translational Springs and Two Rotational Springs Modelling; and (e1) and (e2) Twelve Translational Springs Modelling.....82

Figure 4.2 Bending Moment Diagram Along the Rotor Shaft.....85

Figure 4.3 A Rotor Shaft Modeled and Discretized Using Beam Elements.....85

Figure 4.4 Degrees of Freedom Numbering for a Three-Dimensional Shaft Element.....86

Figure 4.5 Sketch of the Moment of Inertia of: (a) Circle; (b) Circular Segment; and (c) Semi-Circle.....86

Figure 4.6 Schematic Diagram of; (a) One Element Representing Crack Effect; and (b) a Wider Element Representing the Crack Effect.....89

Figure 4.7 Experimental and Numerical Values of Non-Dimensionalized Vertical Natural Frequencies Vs Crack Depth Ratios (a) First Natural Frequency (b) Second Natural Frequency; and (c) Third Natural Frequency.....93

Figure 4.8 Rate of Change of Frequency (with Respect to Crack Depth Ratio) Vs. Crack Depth Ratio of the First Four Frequencies; (a) Mode One; (b) Mode Two; (c) Mode Three; (d) Mode Four.....94

Figure 4.9 Mode Shapes Comparison for First Four Vertical Frequencies a) Experimental and b) Numerical.....98

Figure 4.10 Mode Shapes Comparison for First Four Horizontal Natural Frequencies a) Experimental and b) Numerical.....99

Figure 5.1 a) Details of Bearing Support; b) Schematic Diagram of Shaft-Propeller-Bearing; and c) Inner and Outer Bearing.....104

Figure 5.2 Geometries of the Elements.....105

Figure 5.3 Finite Element Mesh Used for the Various Components of the Rotating Shaft System; and b) Mesh Around the Crack Region.....109

Figure 5.4 Bending Mode Shapes for: a) Coupled Vertical Bending of Rotor Shaft and Support # 1; and b) Bending of Support # 2.....112

Figure 5.5 Mode Shapes Comparison for First Four Vertical Frequencies a) Experimental and b) Numerical.....115

Figure 5.6 Mode Shapes Comparison for First Four Horizontal Natural Frequencies a) Experimental and b) Numerical.....116

Figure 5.7 Depth of Crack vs. Percent Decrease in Bending and Torsion Natural Frequencies for Experimental Results a) Vertical; b) Horizontal.....117

Figure 5.8 Comparison of Rate of Change of Frequency (with Respect to Crack Depth Ratio) vs. Crack Depth Ratio of the First Four Frequencies; (a) Mode One; (b) Mode Two; (c) Mode Three; (d) Mode Four.....120

Figure 5.9 Experimental and Numerical Vertical Bending Frequency Response Functions of: a) Accelerations (ARFs); b) Velocities (VRFs) and (c) Displacements (DRFs) for Shaft # 2.....121

Figure 5.10 Schematic Of Vertical Bending Frequency Response Functions For Different Depth of Crack of Experimental and Numerical Computations. Shaft # 2..... 124

Figure 5.11 Comparison Of Experimental Results For Resonant Frequency Vertical Amplitudes: a) Acceleration Amplitude versus Crack Depth Ratio; b) Slope Of Modal Acceleration Amplitude versus Crack Depth Ratio; c) Velocity Amplitude versus Crack Depth Ratio; d) Slope Of Modal Velocity Amplitude versus Crack Depth Ratio; e) Displacement Amplitude versus Crack Depth Ratio; And f) Slope Of Modal Displacement Amplitude versus Crack Depth-Ratio.....129

Figure 5.12 Comparison of Experimental Results for Anti-Resonant Frequency Amplitude Response: a) Acceleration Amplitude versus Crack Depth-Ratio; b) Slope of Modal Acceleration Amplitude versus Crack Depth Ratio; c) Velocity Amplitude versus Crack Depth Ratio; d) Slope of Modal Velocity Amplitude versus Crack Depth-Ratio; e) Displacement Amplitude versus Crack Depth Ratio; and f) Slope of Modal Displacement Amplitude versus Crack Depth-Ratio.....130

Figure 5.13 Comparison of Experimental and Numerical Results for Resonant Frequency of Shaft # 2 for (First and Second Modes): a) Acceleration Amplitude versus Crack Depth-Ratio; b) Velocity Amplitude versus Crack Depth-Ratio; and c) Displacement Amplitude versus Crack Depth-Ratio.....131

Figure 5.14 Comparison of Experimental and Numerical Results for Slopes of Resonant Frequency Amplitudes of Shaft # 2 for (First and Second Modes): a) Slope of the Modal Acceleration Amplitude vs. Crack Depth-Ratio; b) Slope of the Modal Velocity

Amplitude vs. Crack Depth-Ratio; and c) Slope of the Modal Displacement Amplitude vs. Crack Depth-Ratio.....132

Figure 5.15 Comparison of Experimental and Numerical Results of Shaft # 2 for (at Four Resonant Modes): a) Experimental and Numerical Frequency Ratio versus Crack Depth-Ratio; b) Relationship between Numerical and Experimental Results of Frequency Ratio; and c) Experimental and Numerical Slope of the Frequency Ratio versus Crack Depth-Ratio Curves.....133

Figure 5.16 Comparison of Experimental and Numerical Results for (First and Third Modal Frequencies): a) Experimental and Numerical Ant-Resonant Frequency Ratio versus Crack Depth Ratio; b) the Relationship between Numerical and Experimental Results of Anti-Resonant Frequency Ratio and c) Experimental and Numerical Slope of the Frequency Ratio versus Crack Depth Ratio.....134

Figure 6.1 Block Diagram for Input-Output Relationship in Frequency Domain..... 142

Figure 6.2 Block Diagram for the Inverse Input-Output Relationship in Frequency Domain.....142

Figure 6.3 Responses of the System for; a) Experimental; and b) Numerical Computations of Velocity Response Functions (VRFs) for Shaft #2..... 144

Figure 6.4 Comparison of Velocity Responses Functions (VRF) in Experimental and Numerical Computations a) Intact VRFs; b) Cracked 10% VRFs; c) Cracked 20% VRFs;

d) Cracked 30% VRFs; e) Cracked 40% VRFs; f) Cracked 50% VRFs; g) Cracked 60% VRFs; and h) Cracked 70% VRFs; for Shaft # 2.....145

Figure 6.5 Change of the Impedances with Crack Depth for both Experimental and Numerical Results for Shaft # 2.....148

Figure 6.6 Variation of Experimental and Numerical Impedance for Different Crack Depths for Shaft # 2..... 149

Figure 6.7 (a) Changes in the Mobility between Intact and 70% Crack Depth-Ratio for Experimental and Numerical Results for Shaft # 2.....150

Figure 6.7 (b) Changes in the Impedance between Intact and 70% Crack Depth-Ratio for Experimental and Numerical Results for Shaft # 2.....151

Figure 6.8 Comparison of Experimental and Numerical Results for: a) Experimental and Numerical Torsional Frequency Ratio Versus Crack Depth-Ratio; and b) Experimental and Numerical Torsional Slope of the Frequency ratio for First Mode.....153

Figure 6.9 Comparison of Experimental and Numerical Results for: a) Amplitude Ratio Versus Crack Depth Ratio; and b) Slope of Impedance Amplitude Versus Crack Depth-Ratio.....154

Figure B.1.1 First Mode Shapes of Un-Cracked and Cracked Rotor Shaft from Experimental Work (a) Vertical (b) Horizontal.....186

Figure B.1.2 Second Mode Shapes of Un-Cracked and Cracked Rotor Shaft from Experimental Work (a) Vertical (b) Horizontal 186

Figure B.1.3 Third Mode Shapes of Un-Cracked and Cracked Rotor Shaft from Experimental Work (a) Vertical (b) Horizontal 187

Figure B.1.4 Fourth Mode Shapes of Un-Cracked and Cracked Rotor Shaft from Experimental Work (a) Vertical (b) Horizontal 187

Figure B.2.1 First Mode Shapes of Un-Cracked and Cracked Rotor Shaft from Experimental Work (a) Vertical (b) Horizontal 188

Figure B.2.2 Second Mode Shapes of Un-Cracked and Cracked Rotor Shaft from Experimental Work (a) Vertical (b) Horizontal 188

Figure B.2.3 Third Mode Shapes of Un-Cracked and Cracked Rotor Shaft from Experimental Work (a) Vertical (b) Horizontal 189

Figure B.2.4 Fourth Mode Shapes of Un-Cracked and Cracked Rotor Shaft from Experimental Work (a) Vertical (b) Horizontal 189

Figure C.1.1 Rate of Change of Frequency (with Respect to Crack Depth Ratio) vs. Crack Depth-Ratio of the First Four Frequencies; (a) Mode One; (b) Mode Two; (c) Mode Three; (d) Mode Four 190

Figure C.2.1 Rate of Change of Frequency (with Respect to Crack Depth-Ratio) vs. Crack Depth-Ratio of the First Four Frequencies; (a) Mode One; (b) Mode Two; (c) Mode Three; (d) Mode Four..... 191

Figure C.3.1 Rate of Change of Frequency (with Respect to Crack Depth-Ratio) vs. Crack Depth-Ratio of the First Four Frequencies; (a) Mode One; (b) Mode Two; (c) Mode Three; (d) Mode Four..... 192

Figure C.3.2 Rate of Change of Frequency (with Respect to Crack Depth-Ratio) vs. Crack Depth-Ratio of the First Four Frequencies; (a) Mode One; (b) Mode Two; (c) Mode Three; (d) Mode Four..... 193

Figure C.4.1 Rate of Change of Frequency (with Respect to Crack Depth-Ratio) vs. Crack Depth-Ratio of the First Four Frequencies; (a) Mode One; (b) Mode Two; (c) Mode Three; (d) Mode Four.....194

Figure C.4.2 Rate of Change of Frequency (with Respect to Crack Depth-Ratio) vs. Crack Depth-Ratio of the First Four Frequencies; (a) Mode One; (b) Mode Two; (c) Mode Three; (d) Mode Four.....195

Figure E.1.1 Mode Shapes Comparison for First Four Vertical Frequencies (10%) a) Experimental and b) Numerical..... 200

Figure E.1.2 Mode Shapes Comparison for First Four Horizontal Frequencies (10%) a) Experimental and b) Numerical.....201

Figure E.2.1 Mode Shapes Comparison for First Four Vertical Frequencies (20%) a) Experimental and b) Numerical....202

Figure E.2.2 Mode Shapes Comparison for First Four Horizontal Frequencies (20%) a) Experimental and b) Numerical....203

Figure E.3.1 Mode Shapes Comparison for First Four Vertical Frequencies (30%) a) Experimental and b) Numerical....204

Figure E.3.2 Mode Shapes Comparison for First Four Horizontal Frequencies (30%) a) Experimental and b) Numerical....205

Figure F.1 Bending Mode Shapes for First: a) Vertical; and b) Horizontal....206

Figure F.2 Bending Mode Shapes for Second: a) Vertical; and b) Horizontal Modes....206

Figure F.3 Bending Mode Shapes for Third: a) Vertical; and b) Horizontal....207

Figure F.4 Bending Mode Shapes For Bending Of: A) Rotor Shaft-Propeller; And B) Rotor Shaft-Support #1....207

Figure F.5 Bending Mode Shapes for Fourth: a) Vertical; and b) Horizontal Modes....208

Figure F.6 Bending Mode Shapes for: a) Coupled Horizontal Bending of Rotor Shaft and Torque Bar; and b) Bending of Support # 2....208

Figure F.7 Coupled of Vertical and Horizontal Bending of the Rotor Shaft with: a) Propeller and Torque Bar; and b) Torque Bar....209

Figure G.1.1 Schematic of Experimental and Numerical Frequency Response Functions of: a) Accelerations (ARFs); b) Velocities (VRFs) and (c) Displacements (DRFs) for Shaft # 1.....210

Figure G.1.2 Schematic of Experimental and Numerical Frequency Response Functions of: a) Accelerations (ARFs); b) Velocities (VRFs) and (c) Displacements (DRFs) for Shaft # 3.....211

Figure H.1.1 Schematic of Frequency Response Functions for Different Depth of Crack of Experimental and Numerical Computations: Shaft # 1.....212

Figure H.1.2 Schematic of Frequency Response Functions for Different Depth of Crack of Experimental and Numerical Computations: Shaft # 3.....213

Figure I.1.1 Comparison of Experimental Results for Resonant Frequency Amplitudes: a) Acceleration Amplitude Versus Crack Depth-Ratio; b) Slope of Modal Acceleration Amplitude Versus Crack Depth-Ratio; c) Velocity Amplitude Versus Crack Depth Ratio; d) Slope of Modal Velocity Amplitude Versus Crack Depth-Ratio; e) Displacement Amplitude Versus Crack Depth Ratio; and f) Slope of Modal Displacement Amplitude Versus Crack Depth-Ratio; shaft # 1.....214

Figure I.1.2 Comparison of Experimental Results for Resonant Frequency Amplitudes: a) Acceleration Amplitude Versus Crack Depth-Ratio; b) Slope of Modal Acceleration Amplitude Versus Crack Depth-Ratio; c) Velocity Amplitude Versus Crack Depth-Ratio; d) Slope of Modal Velocity Amplitude Versus Crack Depth-Ratio; e) Displacement

Amplitude Versus Crack Depth-Ratio; and f) Slope of Modal Displacement Amplitude Versus Crack Depth Ratio; Shaft # 3.....215

Figure I.1.3 Comparison of Experimental Results for Anti-Resonant Frequency Amplitude Response: a) Acceleration Amplitude Versus Crack Depth Ratio; b) Slope of Modal Acceleration Amplitude Versus Crack Depth Ratio; c) Velocity Amplitude Versus Crack Depth Ratio; d) Slope of Modal Velocity Amplitude Versus Crack Depth-Ratio; e) Displacement Amplitude Versus Crack Depth Ratio; and f) Slope of Modal Displacement Amplitude Versus Crack Depth Ratio; Shaft # 1.....216

Figure I.1.4 Comparison of Experimental Results for Anti-Resonant Frequency Amplitude Response: a) Acceleration Amplitude Versus Crack Depth-Ratio; b) Slope of Modal Acceleration Amplitude Versus Crack Depth-Ratio; c) Velocity Amplitude Versus Crack Depth Ratio; d) Slope of Modal Velocity Amplitude Versus Crack Depth-Ratio; e) Displacement Amplitude Versus Crack Depth-Ratio; and f) Slope of Modal Displacement Amplitude Versus Crack Depth-Ratio; Shaft # 3.....217

Figure I.1.5 Comparison of Experimental and Numerical Results for Resonant Frequency of Shaft # 1 for (First and Second Modes): a) Acceleration Amplitude Versus Crack Depth Ratio; b) Velocity Amplitude Versus Crack Depth Ratio; and c) Displacement Amplitude Versus Crack Depth Ratio.....218

Figure I.1.6 Comparison of Experimental and Numerical Results for Resonant Frequency of Shaft # 3 for (First and Second Modes): a) Acceleration Amplitude Versus Crack

Depth-Ratio; b) Velocity Amplitude Versus Crack Depth-Ratio; and c) Displacement Amplitude Versus Crack Depth Ratio.....219

Figure I.1.7 1Comparison of Experimental and Numerical Results for Slopes of Resonant Frequency Amplitudes of Shaft # 1 for (First and Second Modes): a) Slope of the Modal Acceleration Amplitude vs. Crack Depth-Ratio; b) Slope of the Modal Velocity Amplitude vs. Crack Depth-Ratio; and c) Slope of the Modal Displacement Amplitude vs. Crack Depth-Ratio.....220

Figure I.1.8 Comparison of Experimental and Numerical Results for Slopes of Resonant Frequency Amplitudes of Shaft # 3 for (First and Second Modes): a) Slope of the Modal Acceleration Amplitude vs. Crack Depth-Ratio; b) Slope of the Modal Velocity Amplitude vs. Crack Depth-Ratio; and c) Slope of the Modal Displacement Amplitude vs. Crack Depth-Ratio.....221

Figure J.1.1 Comparison of Experimental and Numerical Results of Shaft # 1 for (at Four Resonant Modes): a) Experimental and Numerical Frequency Ratio Versus Crack Depth-Ratio; b) Relationship Between Numerical and Experimental Results of Frequency Ratio; and c) Experimental and Numerical Slope of the Frequency Ratio vs. Crack Depth-Ratio Curves.....222

Figure J.1.2 Comparison of Experimental and Numerical Results of Shaft # 3 for (at Four Resonant Modes): a) Experimental and Numerical Frequency Ratio Versus Crack Depth-Ratio; b) Relationship Between Numerical and Experimental Results of Frequency Ratio;

and c) Experimental and Numerical Slope of the Frequency Ratio vs. Crack Depth-Ratio Curves.....223

Figure J.1.3 Comparison of Experimental and Numerical Results for (First and Third Modal Frequencies): a) Experimental and Numerical Ant-Resonant Frequency Ratio Versus Crack Depth-Ratio; b) The Relationship Between Numerical and Experimental Results of Anti-Resonant Frequency Ratio and c) Experimental and Numerical Slope of the Frequency Ratio vs. Crack Depth-Ratio.....224

Figure J.1.4 Comparison of Experimental and Numerical Results for (First and Third Modal Frequencies): a) Experimental and Numerical Ant-Resonant Frequency Ratio Versus Crack Depth-Ratio; b) The Relationship Between Numerical and Experimental Results of Anti-Resonant Frequency Ratio and c) Experimental and Numerical Slope of the Frequency Ratio vs. Crack Depth-Ratio.....225

Figure K.1.1 Responses of the System for; a) Experimental; and b) Numerical Computations of Velocity Response Functions (VRFs) for Shaft # 1.....226

Figure K.1.2 Comparison of Velocity Responses Functions (VRF) in Experimental and Numerical Computations: Intact VRFs, Cracked 10% VRFs, Cracked 20% VRFs, Cracked 30% VRFs, Cracked 40% VRFs, Cracked 50% VRFs, Cracked 60% VRFs, and Cracked 70% VRFs; for Shaft # 1.....227

Figure K.1.3 Responses of the System for; a) Experimental; and b) Numerical Computations of Velocity Response Functions (VRFs) for Shaft # 3.....228

Figure K.1.4 Comparison of Velocity Responses Functions (VRF) in Experimental and Numerical Computations: Intact VRFs, Cracked 10% VRFs, Cracked 20% VRFs, Cracked 30% VRFs, Cracked 40% VRFs, Cracked 50% VRFs, Cracked 60% VRFs, and Cracked 70% VRFs; for Shaft # 3.....229

Figure L.1.1 Change of the Impedances with Crack Depth for both Experimental and Numerical Results for Shaft # 1.....230

Figure L.1.2.1 Variation of Experimental and Numerical Impedance for Different Crack Depths for Shaft # 1.....231

Figure L.1.2.2 Variation Of Experimental And Numerical Impedance For Different Crack Depths for Shaft # 3.....232

Figure L.1.3.1.1 Changes in the Mobility between Intact and 70% Crack Depth Ratio for Experimental and Numerical Results for Shaft # 1.....233

Figure L.1.3.1.2 Changes in the Mobility between Intact and 70% Crack Depth Ratio for Experimental and Numerical Results for Shaft # 3.....234

Figure L.1.3.2.1 Changes in the Impedance between Intact and 70% Crack Depth-Ratio for Experimental and Numerical Results for Shaft # 1.....235

Figure L.1.3.2.2 Changes in the Impedance Between Intact and 70% Crack Depth-Ratio for Experimental and Numerical Results for Shaft # 3.....236

Figure L.1.4.1 Comparison of Experimental and Numerical Results for: a) Amplitude Ratio Versus Crack Depth Ratio; and b) Slope of Impedance Amplitude Versus Crack Depth Ratio Shaft # 1.....237

Figure L.1.4.2 Comparison of Experimental and Numerical Results for: a) Amplitude Ratio Versus Crack Depth-Ratio; and b) Slope of Impedance Amplitude Versus Crack Depth-Ratio Shaft #3.....238

Appendices

Appendix A - Measured Natural Frequencies for Lateral Vibration.....177

Appendix B - The Experimental Mode Shapes for the Various Crack Depth Ratios.....186

Appendix C - Rate of Change of Frequencies for Experimental Results for All the Rotor Shaft.....190

Appendix D - Shows the ANSYS Codes that were Used to Find the Values of Natural Frequencies.....196

Appendix E - The Mode Shapes Comparison for First Eight Natural Frequencies of (Four Vertical and Four Horizontal) Experimental and Numerical Analyses for Cracked Shaft.....200

Appendix F - Mode Shapes for Local and Coupled Vertical and Horizontal Numerical Computations for Uncracked Rotor Shaft-Propeller-Supports-Torque Bar.....206

Appendix G - Frequency Responses of the Rotor Shaft System.....210

Appendix H - Comparison Frequency Response Function for Experimental and Numerical Computations.....212

Appendix I - Comparison of Experimental Results of Resonant and Anti-Resonant Frequency Amplitudes.....214

Appendix J - Comparison of Experimental and Numerical Results of Resonant Frequency Shaft.....222

Appendix K - Velocity Frequency Response of the Rotor Shaft System.....226

Appendix L - Mechanical Impedances of Rotor Shaft-Propeller-Bearing System Obtained for Vertical Vibrations.....230

Chapter 1

Introduction

1.1 General

Vibration and noise in industrial machines or in the environment around them occur when dynamic forces excite these machines. This industrial noise has direct and indirect effects on the health and safety of those industrial systems as well as those operating them. These effects usually manifest themselves in the form of reduced performance, wear and tear, faulty operation, or even irreversible damage in the form of cracks. The industrial noise also has an effect on the nearby buildings, machinery, equipment, vehicles, etc.

Many factors can contribute to vibrations in physical systems, such as variations in distributed mass, eccentrically placed masses/loads, misalignment in shafts, bearing fatigue, foundation motion, mechanically loose connections, intense acoustic environmental noise, highly varying thermal gradients and cracked shafts or rotors to name a few. Cracks in shafts will be the major concern of this research.

The appearance of a transverse crack in a rotor shaft brings with it a greater risk of collapse. Even though the presence of a crack may not lead to sudden failure, it will affect considerably its dynamic behaviour. Cracking of cylindrical shafts is an important area for research, since the changes observed in their vibration characteristics even during large-sized cracking are much smaller than those observed for rectangular beams. Unless

the crack depth is more than 50% of the shaft diameter, it is very difficult to detect the presence of any crack in a rotating shaft with the use of methodologies used for crack detection in beam-type of structures. Hence early identification of crack existence becomes essential to prevent sudden failures in rotating shafts.

According to Wauer (1990) and Dimarogonas (1996), the vibrational behaviour of cracked shafts has received considerable attention during the last four decades. The diagnosis of these cracked shafts remains problematic. Sometimes, it is difficult to find differences between successive states of vibration, even if the crack is medium sized. Thus, it is of the utmost importance to discover the identifiable specific characteristics of the cracked shaft at the earlier possible instance.

There are two stages in crack development: crack initiation, and crack propagation. The former is caused by mechanical stress raisers, such as sharp keyways, abrupt cross-sectional changes, heavy shrink fits, dents and grooves, and/or metallurgical factors, such as flaws, fretting and forging. The latter stage, namely, crack propagation, can accelerate the growth rate under different conditions such as operating faults generated during sustained surging in compressors, negative sequence current or grounding faults in generators and coupled turbines, the presence of residual stresses in the rotor material, thermal stresses, and environmental conditions such as the presence of a corrosive medium. Also, from the physical morphology of a cracked rotor, cracks can be classified based on their geometries and orientation as follows: cracks perpendicular to the shaft axis are known as transverse cracks; cracks parallel to the shaft axis are known as

longitudinal cracks; cracks at an angle to the shaft axis are known as slant cracks; cracks that open and close, when the affected part of the material is subjected to alternating stresses, are known as breathing cracks; cracks that primarily remain open are known as gaping cracks or notches; cracks that appear open on the surface are known as surface cracks; and cracks which are not visible on the surface are known as subsurface cracks [Sabnavis et al. (2004)].

Usually, rotor shafts are subjected to one or more types of vibration, such as longitudinal, lateral, and/or torsional vibration. Longitudinal vibrations, or axial vibrations, are excited by fluctuating propeller thrusts in marine transmission systems, internal combustion gas engines, and mass forces. Lateral vibrations occur at various points along a shaft's axis of rotation, which is in a direction perpendicular to the shaft centerline, when dynamic forces act perpendicular to the shaft axis. Torsional vibrations occur in a rotor shaft when changes occur in dynamic rotational inertias due to propeller force or other fluctuations.

1.2 Objective and Scope of Study

The objective of this research is to develop an identification algorithm to predict the presence, location and size of a crack in its early stages of development on a rotor shaft performing, torsional and lateral vibrations, using a combination of analytical and numerical techniques. The results of the experimental investigations are to be used to validate and verify the results obtained from analytical and numerical computations.

A rotor shaft is a rotating element which usually has a varying or constant circular cross section. It is used to transmit power or motion from the generating location to output

elements such as gears, pulleys, flywheels, cranks, and sprockets. Most rotor shafts are made for transmitting the torque to output elements. Keys, splines, setscrews, pins, press or shrink fits, and tapered fits are common torque-transfer elements. Usually rotor shafts are manufactured from cold-drawn or hot-rolled, and low carbon steels. The manufacturing process depends on the use of the rotor shaft used. Low carbon steel may be used to manufacture low strength shafts, while high strength shafts are made using heat treated medium or high carbon steel.

Rotor shafts have many engineering applications. Marine drive shaft as shown in Figures 1.1 and 1.2 (Nautic, 2012; Rolls-Royce plc, 2012), and power plant shafts as shown in Figure 1.3 (Doosan, 2012)) are some of these applications. These shafts operate in harsh conditions and are subjected to high stresses. As a result of these stresses, defects develop and may cause deterioration in performance of the equipment leading ultimately to full system damage. The early prediction may help in preventing of major damage to humans and structures.

In the present study, the aim is to model a typical rotor shaft. Experimental and analytical approaches are used to detect the presence of cracks. The scope of the present study can be summarized as follows: (i) To carry out an experimental investigation to identify the presence of transverse cracks on a shaft, having a cantilever overhang; (ii) To correlate the above experimental results through numerical analysis using ANSYS finite element software; and (iii) To define parameters for the detection of the crack occurrence in the shaft-propeller-bearing system.

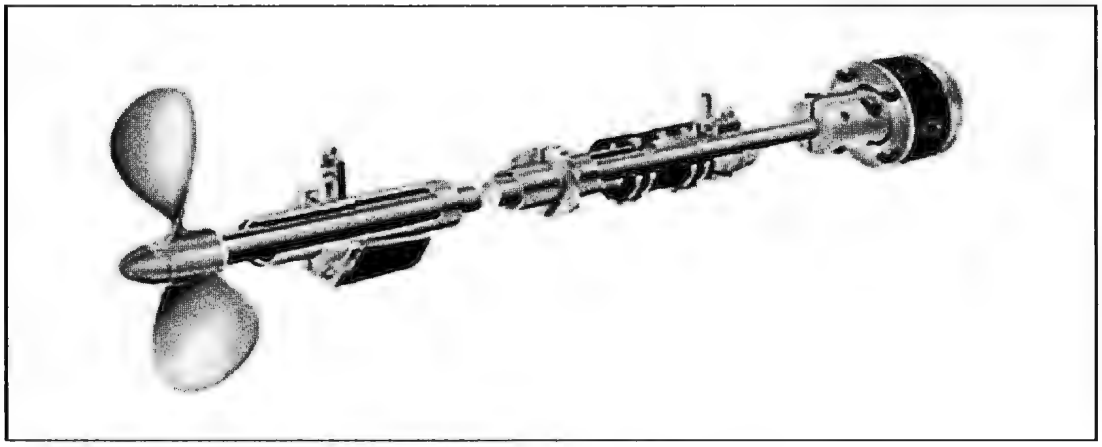

Figure 1.1 Boat Propeller Shaft

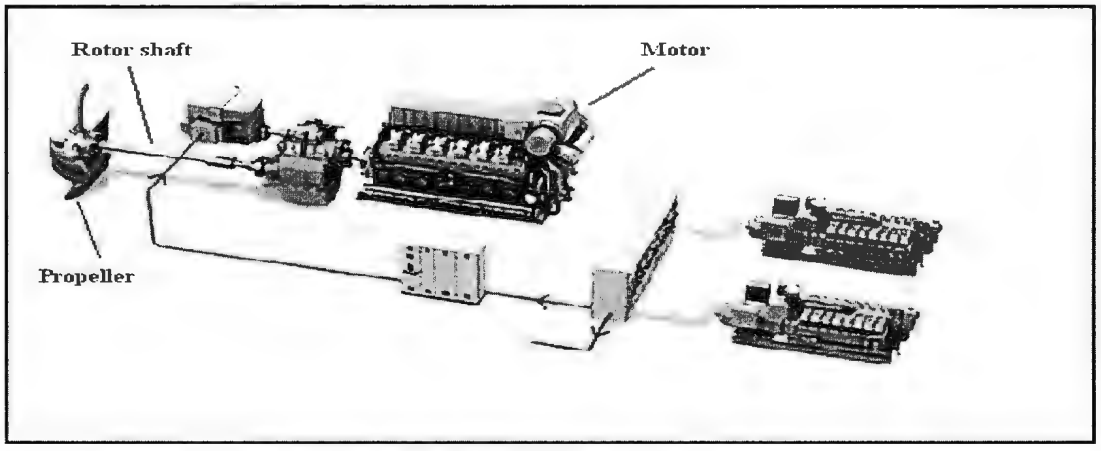

Figure 1.2 Hybrid Shaft Generator (HSG)

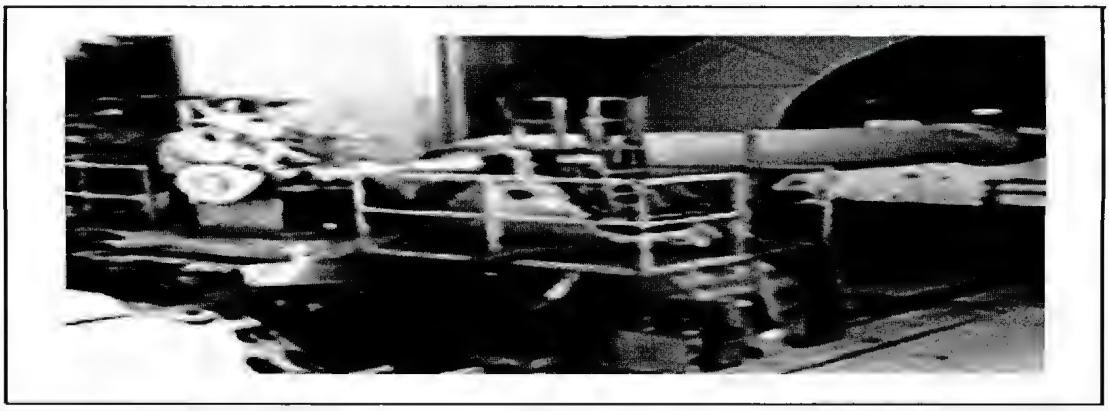

Figure 1.3 Components In Turbines And Generators For Nuclear And Thermal Power Plants

1.3 Outline of the thesis

The thesis contains two major components:

(i) An experimental study of the vibration of rotor shafts. Modal analysis software, LMS Test Lab™; has been used to analyze the results.

(ii) A numerical analysis for the vibrations of both un-cracked and cracked shafts modeled using a finite element procedure (ANSYS).

The thesis is organized as follows:

Chapter 1 provides a brief introduction of vibrational concepts, the vibrational behaviour of cracked shafts, types of cracks, types of vibrations, the scope of work, and the objectives of this study as well as the outline of the thesis.

Chapter 2 presents a review of experimental and numerical studies available in the literature dealing with the effects of different types of cracks on the lateral and torsional vibrations of rotor shafts.

Chapter 3 describes the details for fabricating a shaft-propeller-bearing test rig, the experimental setup, test equipment, their calibration, basic testing procedures and experimental results obtained.

Details of numerical modeling of the uncracked and cracked rotor shaft system with bearings, propellers and frame supports for lateral and torsional vibrations using beam elements are given in Chapter 4. The numerical and experimental results are compared and discussed in this chapter.

Crack detection in shafts using lateral and torsional vibration measurements and numerical analyses are described in Chapter 5. Modeling of shaft-bearing-support system is carried out using ANSYS Workbench and three-dimensional solid elements. Mesh convergence study, modelling of contact behaviour, materials used, analyses and comparison of numerical/experimental results are also given in this chapter.

Chapter 6 presents the crack detection procedure in shafts using mechanical impedance measurements. This chapter includes the following sections:

(i) The relationship between input and output of the dynamic response of a rotating shaft,

(ii) Computing the mechanical impedance for multi-degree-of-freedom systems;

(iii)Presentation and discussion of the results and reporting of salient findings.

Finally, Chapter 7 contains conclusions and recommendations for future study. It summarizes the findings from the experimental and numerical investigations carried out in this study. It also highlights the salient findings from this research investigation.

Chapter 2

Literature Review

2.1 Introduction

The appearance of transverse cracks in overhanging shafts having propellers carries with it a greater risk of sudden collapse. Even though the presence of a crack may not lead to sudden failure, it will affect considerably its dynamic behaviour. In the last four decades, many numerical and experimental studies have been carried out to identify the effects of different type of cracks, such as transverse, longitudinal, slant, breathing cracks and notches. In these studies the researchers have used various methods to identify crack presence in structures, viz., (i) Traditional vibration-based methods using modal testing and numerical analysis and others using conventional neural networks wavelet and fuzzy logic procedures; and (ii) Non-traditional methods based on ultrasonic guided waves, structural intensity, magnetic induction, radio frequency identification tag, acoustic intensity and acoustic Laser-Doppler Vibrometer (Sabnavis et al. 2004). However, these non-traditional methods are only applicable to specific situations where the crack location is known in an approximate manner. Therefore, researchers have sought better and more efficient procedures for crack detection and identification through vibration analysis, whether using Fast Fourier Transform (FFT) methods, time domain responses or other nonlinear estimation of dynamic response.

The reviewed literature is classified into two categories; viz., (i) Experimental approach; and (ii) Analytical approach. The experimental approach is classified into two

subsections, viz., modal testing and non-destructive test methods. The analytical approaches are used to simulate the behaviour of the structural model with the damage present and to correlate the experimentally observed vibration signature. This approach has been classified into four subsections: detection and monitoring of cracks using mechanical impedance, investigation through the finite element approach, analysis through nonlinear dynamics of cracked rotors, and crack detection methods through several other techniques.

2.2 Experimental Approach

2.2.1 Introduction

It has been observed that experimental studies have been preferred more than numerical ones while carrying out crack detection and identifications. Several variables and system characteristics such as natural frequencies, mode shapes, and damping ratios are changed under the presence of a crack. These dynamic characteristics are often measured through experimental modal analysis and are the focus of vibration based crack assessment.

2.2.2 Crack Detection and Modal Testing

Many researchers have used modal testing in different applications to detect material defects and to extract the frequencies, damping and mode shapes of the tested system. Over the past six decades the experimental modal analyses have focused on two approaches, viz., (i) Those methods based on frequency and damping estimation using (FFT) methods; and (ii) Those based on time-domain complex exponential methods

utilizing polynomial functions (Allemang, 1990). In both the approaches, the procedures start with the consideration of the basic matrix vibration equation given by

$$[M]\{\ddot{x}\}+[C]\{\dot{x}\}+[K]\{x\}=\{f(t)\} \tag{2.1}$$

where [M], [C] and [K] are the system mass, damping and stiffness matrices, $\ddot{x}$, $\dot{x}$ and {x} are the system response parameters (viz., accelerations, velocities and displacements), and {*f*} the forcing functions causing the system motion.

Frequency response function procedures use the solution approach given by

$$\{X(\omega)\} = [H(\omega)]\{F(\omega)\} \tag{2.2}$$

where {X (ω)} is the output, {F(ω)} is the input and [H(ω)] is the matrix of frequency response functions.

The time-domain complex exponential approaches use Laplace transform approaches using impulse response functions and can be expressed as

$$[A][X(s)] = [B]\{F(s)\} \tag{2.3}$$

where [A] represents the system matrices in the Laplace domain, X(s) represents the system response in the Laplace domain, [B] represents the forcing function matrices in the Laplace domain and {F(s)} is the forcing function in the Laplace domain. Most of the other procedures developed for vibration analysis can be traced to these two approaches, based on frequency domain (FFT) procedures, or time domain impulse response function using Laplace transform procedures.

In the following sections some of the modal testing experimental studies carried out on cracked beams and rotor shafts are reviewed to highlight the different approaches used for the purpose.

2.2.2.1 Beam

Rytter (1993) studied vibration based inspection to measure dynamic characteristics of the beam and identify the location and the size of the damage that can occur in the structure. He has carried out an extensive survey of the studies carried out on crack detection and identification. He used short beam elements in his study and he mentioned that this model has been used before [Kirsmer, (1944), Thomson, (1949) and Petroski, (1981)] but either gives a general solution to the problem. He implemented and tested these and other models using simulation as well as experimental results.

Doebling, et al. (1996) reviewed literature on the damage identification and health monitoring of structural and mechanical systems from changes in their vibration characteristics. He was mainly concerned with the structural damage and the procedures used to measure structural vibration response. Additionally, he reviewed the majority of the experimental studies carried out earlier and was considering only the problem of linear damage detection. Also he succinctly reviewed the historical development of the damage-identification methods and applications. In this report, the author mentioned that the modal frequencies, mode shapes and measured flexibility coefficients were used in the analysis technique in many of the articles. Some articles also used property matrices in detection of nonlinear response and damage detection. He summarized the types of

civil engineering structures that have received considerable attention in the literature such as beams, trusses, plates, shells, bridges, offshore platforms, aerospace structures and composite structures. In general, the scope of this report could be summarized as follows: (i) Methods that used the change in modal properties to identify the changes that occur in the mechanical properties; (ii) Some application techniques that could help to solve some intricate engineering problems; and (iii) Presentation of some recommendations for future studies.

Schwarz and Richardson (1999) reviewed some of the important articles related to modal testing during the past 30 years. They covered three aspects in this paper, viz., frequency response function measurement techniques, sources of excitation, and methods to extract modal parameters directly from a set of FRF measurements (frequency, damping, and mode shape). Frequencies, damping and mode shapes were estimated. Also they stated that the mode shapes were obtained from peak values of the imaginary part of the FRF when they used displacement and acceleration FRFs; also mode shape components were obtained from peak values of the real part of the FRF when they used velocity FRF.

Owolabi (2001, 2003) carried out an experimental study to investigate the presence of a crack on two types of aluminum beams, viz., those with fixed-fixed and simply supported boundary conditions. He developed methodologies to detect crack location and size. He used modal testing technique (STAR structural analysis) and applied a sinusoidal force at a particular point (sine sweep method) on the structure (close to the center of the model) to measure the first three natural frequencies and the changes in slopes of the mode

shapes as well as the acceleration frequency responses at seven different location on each beam with different crack depth ratios, which are the ratios of the depths of the crack to the diameter of the shaft, (varied from 10% to 70%). He compared these results with the previous theoretical work carried out by Yang, et al. (2000) and found a good agreement. He mentioned that this technique could be used as a diagnostic tool to identify cracks in beams.

Downer (2010) used the modal testing and design of experiments approach to extract the frequencies, mode shapes and damping ratio. He also determined the effect of various structural factors on a measured response and related the modal frequencies to these structural parameters (defect size and location). He used two types of beams, viz., a cantilever beam (clamped-free) and a real prototype beam (Electric transmission tower wooden poles). He used two types of non-destructive test methods to detect hidden internal defects and the strength of the poles. Additionally from the experimental work he created regression models of multiple modal frequencies of the beam by using the theory of the design of experiments. The author mentioned that once the regression models were acquired it can be easily used to detect defects in the poles. Finite element analysis also was carried out to validate his experimental work. One of the best results in this research is the capability to predict the maximum stress of specimens by using regression models instead of commercial ultrasonic NDT equipment.

Elshafey et al. (2011) used modal test technique and presented their damage model on the basis of detailed experimental investigations. They used a steel beam fixed at one end and

hinged at the other to identify the occurrence and location of structural damage by using the change in the mode shapes. The vibration frequencies and mode shapes as well as FRF (Frequency Response Function) function were used. They reported that better results for identifying the structural damage were obtained when they used the results of second mode.

Fayyadh and Abdul Razak (2011) applied a mode shape weighting function method to detect cracks on a steel beam based on the change of natural frequencies, mode shape, and stiffness. Weighting function method could be estimated based on the area under the curve of the mode shapes which represented the change in the bending stiffness *EI*. They used modal testing technique to obtain modal parameters for un-cracked and cracked steel beam. At the mid-span of steel beam (75mm width and 180mm depth) different depths of cuts were made (2, 5, 10, and 20 mm with a constant width of 2 mm). Twelve accelerometers with a sensitivity of 100 mV/g and a force transducer at a fixed point were used to pick up the responses and excitation of the beam, respectively. Additionally, they obtained modal frequencies, damping, frequency response functions for the first four mode shapes and predicted the presence of a crack. They concluded that the mode shapes one and three were more sensitive than mode shapes two and four to detect crack on the beam. He also observed that the weighting function method does not have the sensitivity of the crack detection algorithms for identifying natural frequencies or mode shapes.

2.2.2.2 Rotor shaft

Wauer (1990) reviewed literature on the dynamics of cracked rotors. He covered papers related the dynamics of cracked rotors published since 1944. In this review he also covered studies used for modeling of the cracked part of the structure as well as diagnostic techniques procedures that were available to detect crack on the structures.

Thompson (1991) used smooth and notched shafts of aluminum 2024-T351 for his experimental work. The main objective of his work was to study the growth of a surface crack by using experimental and analytical studies (3D-FEA). In both cases, he used smooth shafts and fillet notched shafts. These shafts were subjected to constant amplitude tensile and torsional loads. He focused on the small crack growth rate, and evaluated the effect of this crack on the fatigue life by applying the linear elastic fracture mechanics (LEFM) prediction technique and accounted for small crack deviations from LEFM behaviour. Also, he studied the effect of shear lip growth on the surface crack under the effect of a fillet notch and a torsional load. He mentioned that most crack shapes considered in circular shafts were straight, semi-elliptical fronted cracks. From this experimental study, he determined that if the surface crack's length was greater than 0.02 inches, the fatigue life predictions were perfect for all cases. But when larger cracks were used in the notched-torsional case, the prediction results from finite element models were not reliable. Also, he determined that the LEFM is acceptable to predict surface crack growth rates in torsion if it is used at low loads with long growing cracks.

Hamidi et al. (1992) developed two mathematical models (using three-dimensional stress intensity factors at the crack region) to determine the bending natural frequencies of a rotor. They used natural frequencies, mode shapes and frequency response functions to identify the presence of a crack. The analytical methods were compared with the results of experimental measurements. The following conclusions were made: (i) When crack depth was more than 30% of the shaft radius, the rate of change of natural frequencies was very high; and (ii) The speed of rotating shaft did not affect the values of natural frequencies; this was probably due to the fact that the stiffness of the shafts were not reduced significantly by the rotating speed effects on the shaft.

Wang et al (1992) stated that the natural frequencies of systems with many complicated coupling mechanisms were difficult to predict. Therefore, it was necessary to perform a certain number of tests on these mechanical subsystems to determine the probable vibration problems in design. Moreover a study of both torsional and translational motions of a rotating drive shaft was important in understanding the problems associated with dynamic behaviour. However, it is not easy to measure the vibration when the shaft was rotating (on-line). The authors mentioned several conventional methods for measuring torsional vibration by using slip rings, accelerometers, and strain gauges on the rotating shaft. In addition, they also mentioned an up-and-coming popular method by using non-contact transducers. In their work, the authors used a special measurement system which included: (1) Sensors, probes and light sources (optical module). Also, the optical module contained a source of light, lens, and branches of fibre cable; (2) A data acquisition/transmission module; and (3) A data analysis software package. In the paper,

the torsional measurement system was designed simultaneously to measure both torsional and translational motions at certain points along the rotating shaft.

Munoz et al. (1997) applied a modal testing procedure to detect a crack on an off-line rotor. The changes in rotor shaft frequencies gave a good indication of the presence of cracks. They stated that the method can be used to detect cracks of areas greater than 2.5% of the rotor cross-sectional area; but this claim seems to be rather exaggerated from other studies published on the same subject.

Dorfman and Trubelja (1999) used a simplified model of the Turbine Generator system to examine the influence of cracks in the shaft. This model showed the relationship between the shaft excitation forces which represented input to the model and the shaft torsional vibration response which represented the output. This ratio (output to the input) is known as the transfer function. The transfer function is basically dependent on the mass, stiffness, and damping of the shaft. They found that a properly designed data acquisition monitoring system, such as Structural Integrity Associate's Transient Torsional Vibration Monitor System (SI-TTVMS), would give a good signal and detect rotor faults before failure.

Adewusi (2000) conducted an experimental study on a rotor shaft with a transverse surface crack. In his study, he investigated the influences of a propagating and non-propagating crack with and without transverse load on the dynamic response of rotor shafts. That investigation gave some relevant information that can be used to detect the crack in a rotating shaft. In the experimental setup, he used simply supported and

overhanging shafts. He divided the results of this study into two categories, viz., conventional analysis and wavelet analysis results. These two parts were further categorized under: start-up data (Bode plots and frequency cascades) and steady state data (Frequency waterfalls and orbits). Surface notch and surface slot of pre-defined depth were the two types of transverse crack shapes that were considered. The depths of cracks used varied between 1mm and 4mm (10% and 40% of the shaft diameter). The dynamic response of the rotating shaft had very little change when the depth of crack was less than 3mm. Therefore, the author focused his attention only on two crack depths of sizes, 30% and 40% of the shaft diameter. From experimental studies, he concluded that there was a difference in the critical speed of the un-cracked shaft between horizontal and vertical directions. For a simply supported shaft, he found that by increasing resonance bandwidth and decreasing shaft stiffness the critical/resonance speed will be decreased. The percentage of increase in this case was greater than that due to the crack alone. For a shaft with an overhang and from start-up results he found that the critical speed of the cracked shaft (3mm notch) increased when compared with an un-cracked shaft. The critical speed of the cracked shaft (4mm notch) decreased with and without crack propagation. Also, the resonance bandwidth increased in the vertical direction due to a side load.

Zakhezin and Malysheva (2001) used a numerical Finite Element based crack detection technique and modal tests on a single span shaft. They included system damping in their model and calculated the system's eigen-values and eigen-vectors up to a frequency of 1,100 Hz. These values were calculated for a rotor with and without cracks at varying

locations and depths. The method was tested and results verified to indicate the good quality of results obtained.

Adewusi and Al-bedoor (2002) applied neural networks techniques to detect the inception of cracks on rotors. They carried out experimental studies on a rotor (overhung arrangement and simply supported arrangement) with and without a propagating crack. In this study, a two neuron network was used to detect the propagating crack and a three neuron network to detect the propagating and non-propagating cracks.

Gounaris and Papadopoulos (2002) performed experiments to identify the crack location and size using a cracked circular rotor shaft. This shaft was modeled as a Timoshenko beam and the gyroscopic effect and the axial vibration were considered. Also they considered the case where a transverse crack that remained always opens during the rotation of the shaft. The shaft was excited at one end and the response was measured at the other end. The main idea was to measure the changes that occur in coupling of vibration (bending and axial) due to the effect of transverse surface crack when the shaft was rotating.

Bieryla et al (2005) carried out a survey of problems due to shaft-cracking since 1974. This work was purely experimental, and the aim of his work was to detect the capability of torsional vibration signature analysis which could be used as a diagnostic tool for shaft crack monitoring in rotating drive shafts. By using ultrasonic measurement and a continuous cyclic fatigue load a small crack (notch) on the shaft was measured. Also during the investigation, the shaft was subjected to the effect of fatigue cycling and the

signature of the torsional vibration was measured. For the torsional vibration test, they used a cracked shaft mounted on bearings and rotated by a motor. The authors fabricated a laboratory test rig containing the shaft with four fatigue crack depths (0%, 37%, 52%, and 64% of shaft diameter). They concluded that the change of natural frequency was a good indicator to show that something was impairing the shaft's condition. The experiments showed that the torsional rigidity decreased with crack growth. The first torsional natural frequency decreased nonlinearly due to crack depth. These values of natural frequencies changed within the range of 0.1 to 0.2 Hz. Therefore, this method can be used to monitor and diagnose the shaft online to prevent failure due to crack growth. Also, they mentioned that there was a sensitive relationship between the torsional frequency as a function of crack growth and location of the crack.

Garrett et al (2005) presented an experimental study on rotor shafts. The first part of the study was implemented on a real shaft to investigate the effect of torsional vibrations and to explore the range of fatigue crack growth in a rotating shaft while carrying out a laboratory test. The experimental work explained some changes in the value of torsional natural frequency. These changes could be denoted by the extent of the fatigue crack on the shaft. The second part of the study was carried out for two locations of the crack, one in the middle and the other at the end of the shaft. From this study, the authors concluded the following: (i) The torsional natural frequencies were not always apparent and it could have an effect on crack sensitivity in modes; (ii) The torsional finite element modeling was simpler and more straightforward than the lateral modeling; (iii) The natural frequencies were not the same at all locations along the shaft due to the growth of a

crack; (iv) The torsional modes were more sensitive to small crack growth than the other modes; and (v) For the crack at the center of the shaft, the changes occurred in modes one and four: mode one showed the natural frequency drop of 10 Hz and mode four decreased by 60 Hz. The other modes did not change with crack depth. For the crack at the end, modes eight and thirteen were the best indicators to monitor.

Cho et al. (2006) measured the torsional wave in a rotating shaft by using a noncontact method (magnetostrictive patches and a solenoid). In this work, two problems were noticed during the vibration experiment, viz., (i) How to produce sufficient power to generate torsional waves; and (ii) How to guarantee that there was no interference from the shaft rotational motion. Magnetostrictive patches were fastened to the shaft axis for measuring the torsional motion. Furthermore, the configuration of an arrayed patch was employed for frequency localization and sufficient power generation. In their paper, they assumed that the effect of the lateral vibrations was negligible because it was very small compared to the torsional motion measured by the magnetostrictive strips. In addition, the authors used the transduction method to detect a perimeter crack in a rotating shaft as well as to estimate the damage location (with small error) and compare them with the exact crack size and location.

Pennachi and Vania (2008) presented the results of an experimental study concerning the diagnosis of a crack during the load coupling of a gas turbine; they compared the experimental and analytical results of the shaft vibration using the model of the rotating shaft of a 100MW power plant. The authors stated that the load coupling affected the

propagation of cracks. Also the propagation of the crack increased due to the presence of differences between the hot dynamic alignment and the cold static alignment.

Ganeriwala et al. (2011) presented experimental results obtained for a wind turbine under the influence of different cracks. A modal testing technique was used. Two single wind turbine blades (4 feet long and made from fibreglass) were used, one was an un-cracked blade and the second was a cracked blade. On the cracked blade there were two cracks, one located along an edge of the blade (5in, 10in, and 20 in deep edge crack) and the other on the surface of the blade (1.3in, 2.6in, and 3.9in deep surface crack). Thirteen accelerometers and an impact hammer were used to obtain modal frequencies, damping, frequency response functions and mode shapes, for both cases; these results were used to predict the presence of the crack. From modal testing they found some modes of the blade to be significantly affected by the presence of a crack. The modal parameters were significantly affected by the longer depth of crack. In this study, the following conclusions were made: (i) The modal parameters of modes 3 to 8 showed significant changes due to the presence of edge cracks (ii) Significant changes in the modal parameters of modes 1 and 2 were observed under the influence of edge or surface cracks; (iii) Lower frequency modes did not indicate the presence of localized blade cracks than higher frequency modes; and (iv) Mode shapes showed significant changes due to the presence of edge crack rather than surface crack.

Saravanan and Sekhar (2012) used experimental and analytical procedures for monitoring the rotor-bearing system to examine the presence of a transverse breathing crack; they

used the concept of operational deflection shape and used kurtosis of vibration to detect time history. Also the shape and amplitude of kurtosis curve based on the experimental results were used to detect cracks on the shaft. In the experiments, a single crack and two cracks were used. The length and the diameter of the shaft were 800mm and 16mm respectively. The shaft was supported on two ball bearings and the disc (disc mass = 0.656 kg) was mounted at the center of this shaft. The breathing crack was located in the middle of the shaft and the shaft was divided into 20 elements to measure the shape of the operational deflection. They used rotational laser vibrometer to measure the vibration response at different locations on the rotating shaft. The authors found that the changes that occur in the kurtosis were significant when the crack was located close to the bearings while it was small when the crack location was closer to the middle. They reported that the use of kurtosis results were useful for identifying cracks during detection and monitoring purposes.

2.3 Analytical and Numerical Approaches

Many researchers have used analytical and numerical techniques to detect the presence of fissures and cracks in the rotor shafts. The focus of these methods is to detect the changes that occur in the vibration characteristics of the system due to the presence of cracks. The following system characteristics are considered in these approaches, viz., frequencies, mode shapes and damping ratios. These parameters were commensurate with the physical properties of the system such as mass, damping and stiffness. Any changes in these properties due to damage in turn affected these parameters. These approaches could be classified into two categories: non-model and model-based approaches. Non-model

methods detect cracks in a direct manner, by determining the value of natural frequencies, mode shapes, damping ratios, stiffness, and flexibility matrices or the variables derived from these quantities. The model-based approaches defined the second category in which the selections of parameters were known to define the model of the structure under the given assumptions. As a result of the changes that occurred in the values of these parameters, the damages that occurred in the structure could be determined and identified. Commonly, finite element models were used in this case (Liu, 2004).

In this review, the analytical and numerical approaches are classified into four subsections: investigation through the finite element approach, analysis through nonlinear dynamics of cracked rotors, detection and monitoring of cracks using mechanical impedance, and crack detection methods through several other techniques.

2.3.1 The Finite Element (FE) Approach

Sekhar and Srinivas (2003) used shell elements with 4 nodes using the CQUAD4 elements available in commercial finite element analysis software NASTRAN and FEMAP to model hollow cracked composite shafts, fabricated using stacking sequences of boron-epoxy, carbon-epoxy and graphite-epoxy materials. The finite element formulation was based on first order shear deformation theory. They created a crack on the shaft by using Boolean operations. Spring elements were used to represent the effects of the bearings. They have stated that the stacking sequences such as 90/0/90/0 and 90//90/0/0 produced a higher frequency than other sequences of stacking. They also

found that for all the three materials used in their study, the eigen-frequencies decreased with increases in crack depth.

Kisa and Gurel (2006) used the combination of finite element method and synthesis method (substructure technique) to analyze beams which had a circular cross-sectional area and non-propagating open cracks. Natural frequencies and mode shapes of a beam with more than one crack could be easily determined by using this method. The substructure technique was used to reduce the non-linear behaviour of the overall structures to a number of linearly displaced segments; thus, the analytical or numerical results could be easily found. This method was applied here for the first time with more than one crack on a beam that had a circular cross-sectional shape. Three types of applications were given in the paper to calculate the natural frequencies and mode shapes of a beam having varying depth of cracks and crack locations. The first example was that of a cantilever beam with a single crack. The natural frequency of the cracked beam was found to be lower than that of un-cracked beam and this frequency decreased with an increase in crack depth. Also, they reported that when the crack was closer to the fixed end it had a larger effect on the basic natural frequency than the case where a crack was closer to the free end. The second example was that of a cantilever beam with three cracks. They assumed that the cracks were of the same depth. From the results, it was shown that the reduction of the first frequency was higher when the cracks were closer to the fixed end while the second and third natural frequencies were higher when the cracks were closer to the midpoint. The first natural frequency remained constant when the cracks were closer to the free end. The second and third natural frequencies, when the

cracks were closer to the fixed end, were less affected. They also mentioned that the natural frequencies, in some cases, provided information about the location of a crack more accurately than the mode shapes. When the cracks were closer to the fixed end, the changes in the first natural frequency were a better indication and more useful than the changes in the first mode shape. The third example was a simply supported beam with three cracks. They assumed that the cracks had the same depth. The results showed if the cracks were closer to both supports, the reduction in the second and the third natural frequencies would be large. Also, the reduction in the first natural frequency would be large when the cracks were closer to the middle of the beam. The authors concluded that the magnitude of natural frequencies and form of mode shapes of a beam were related to the location and depth of cracks.

Ferfecki and Ondrouch (2007) used three methods to simulate, calculate, and measure the stiffness of a shaft, its vibration responses, and the trajectories of the center of the shaft. The Finite Element method was used to determine the stiffness of the center of the shaft for various loads in different directions. These results have been compared with the results obtained by MATLAB software. From finite element analysis results for a depth of crack of 3mm and a transverse width of 0.4mm, it was found that the surfaces of the notch never came in contact during bending vibration. The main reason for this behaviour was the change in the stiffness was so small. The Floquet Theorem was used in the numerical calculations, and the results from this theorem were practically identical to the experimental work. It was assumed that the model had the following properties: the configuration of the rotor shaft was represented by a cylindrical beam; the discs and

stationary parts were rigid and discs were axisymmetric; the effects of inertia and the gyroscopic motion of the rotating parts were also considered; all material damping was assumed to be linear; the dynamic forces were either constant or changing with respect to time. This work was implemented on the rotor system RK 4 containing depths of cracks as follows: 0%, 10%, 30%, and 50% of the rotor diameter.

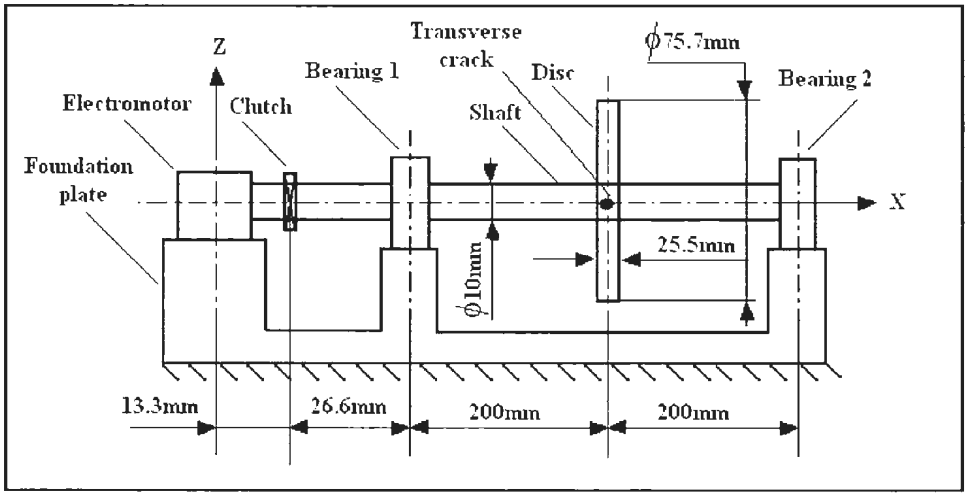

Figure 2.1A Sketch of Rotor System RK 4

From numerical results, they concluded that the crack in the shaft directly affected the lateral vibration of the shaft when the shaft rotational speed was close to the secondary resonance. From experimental measurements, the stiffness of the shaft, its vibrational responses, and the trajectories of the centre of the shaft were measured. They found from the analytical results, that the crack in the shaft directly affected the lateral vibration of the shaft when the rotational speed was near the secondary resonance.

Lissenden et al. (2007) implemented experimental and analytical methods to model crack propagation and to determine the natural frequencies and mode shapes for a line shaft

system. The shaft was modeled for both straight and semi-elliptical surface cracks under the effects of quasi-static and dynamic bending loads. Also they predicted the effect of a crack on stiffness by using 3-D finite element model. This model was created and analyzed by using the ANSYS software. It treated the un-cracked and cracked cases by keeping sets of nodes joined together to represent un-cracked case and decoupled to create the crack. From the three approaches they used, they found, no significant decrease in torsional stiffness for quasi-static loading, while a gradual decrease in torsional stiffness and natural frequency for dynamic tests. Additionally, from the results of 3-D FEM, the model indicated that the first torsional natural frequency was directly proportional to the crack depth propagation.

Li et al. (2008) used FE-based simulation (through ANSYS) to model the dynamic characteristics of a faulty multi-span rotor system. This system was connected together by axial membrane coupling, considering each span to be elastic and supporting a rigid rotor at the free end. They examined in detail the bending-torsion coupling vibration of a single-span rotor and the whole rotor system; they analyzed four cases for the occurrence of cracks and rubbing faults (crack location was in the middle of the span and the crack depths were 0.0, 0.2D, 0.4D, and 0.6D, where D is the diameter of the rotor). They examined viz., (i) The nonlinear dynamic characteristics, (ii) Responses of the rotor system, (iii) The influences of membrane coupling, and (iv) Effect of gearing on the rotor system. They concluded that detailed examination of both coupling and gear response would help one to properly diagnose the cracks occurring in the rotor-system.

Ramesh and Sekhar (2008) investigated the detection of two cracks using different configurations of a rotor-bearing system. Finite Element model of a simple rotor-bearing system was used in this study. The authors used continuous wavelet transformation (CWT) to detect a crack, but they found no qualitative difference between a single-crack and a two-crack system. So, the identification of multiple cracks became difficult using CWT of the transient response. This problem was then solved using the concept of the Operational Deflection Shape (ODS). The ODS indicated the displacement of the rotor along its length at a particular speed (generally operating speed). But this technique of ODS used for the cracked and un-cracked systems, was not be sufficient to detect the cracks when the crack depths are very small. Therefore, a new approach, called the Slope Deviation Curve (SDC) or the Amplitude Deviation Curve (ADC), was introduced; this curve was generated from the ODS by a simple transformation. Thus, online detection of crack parameters by this method was reported to be an effective tool, even in the detection of small cracks at around 10% from the depth of crack to shaft diameter.

Sudhakar and Sekhar (2010) presented a modified model-based analysis technique and used modified least squares minimization algorithm to reduce the errors in the identified fault parameters. The idea of this method was to model the fault as an equivalent load that will be generated on the cracked rotor-bearing system; the equivalent loads were calculated using measured vibration responses at all degrees of freedom of the system. The difference between this equivalent load and the theoretical model fault load was minimized by least squares algorithm. Also they used finite element method to validate theoretical results. They reported that their method was effective in identifying a crack

even when the vibrations were measured with 4 degree-of-freedom (DOF) (or, 8, 16, 20, or 24 DOF) systems. They found the method to be very sensitive to the mode shapes and location of the crack.

2.3.2 Nonlinear Dynamics of a Cracked Rotor

Yang and Suh (2005) mentioned the reasons that cause the non-linearity in rotating machines: Surface cracks, fluid-film bearings, squeeze-film dampers, nonlinear springs, and clearances in rolling element bearings. In their paper, an enhanced focus on investigating the crack and fluid film pressure induced non-linear responses by using the fundamental concept of instantaneous frequency was made. The instantaneous frequency was defined as the temporal gradient of phase. Two plain journal bearings, a four-disc, system modeled with 15 nodes, and a 60-degree-of-freedom were used for their model. Their conclusions were as follows: (i) At low rotating speeds the transverse surface cracks had a strong effect, and at high speeds the bearing film force effect was dominant; (ii) The breathing crack depended on the rotation and vibration amplitude as well as the direction of the shaft deflection; (iii) At high speeds, the crack breathing had a significant effect on the rotor dynamic responses, basically supporting the non-linear behaviour of shaft; (iv) They found the rotational speed and relative crack depth to be the main reasons for variation in bearing clearance on dynamic responses of the rotor model system; (v) The vibration amplitude decreased when the bearing clearance was decreased, but when the surface area of the crack increased, the vibration amplitude increased; and (vi) The authors stated that the system became more complicated if many sources of non-linearity were considered.

Sinou and Lees (2007) analyzed the non-linear dynamic response of an on-line rotating shaft, shown in Figure 2.2, to predict the influence of a breathing transverse crack. Also they investigated the development of the orbit of the cracked rotor at half and one-third of the first critical speed. They used Harmonic Balance Method to obtain shaft response parameters by considering the effects of different crack depths and locations.

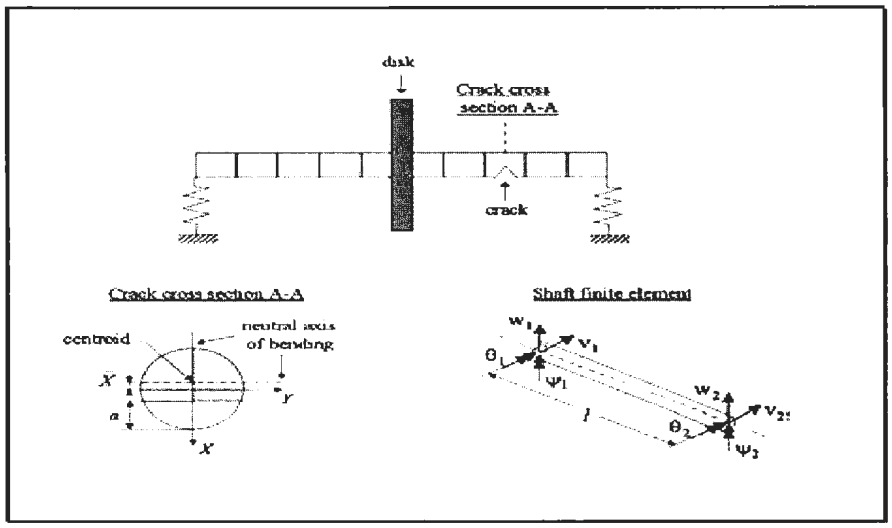

Figure 2.2 Rotor System And Crack Model Cross-Section.

Jian-bin et al. (2012) investigated the presence of fatigue fracture, in diesel engine crankshafts using dynamic monitoring and detection procedures. They used the metal magnetic memory detection methodology and monitored on-line the changes in engine crankshaft characteristics. They tested a diesel engine generating an acceleration of 295G and a multi-function electromagnetic detector to detect the presence of stress concentration areas. They used two detecting points of the crack on the crankshaft and used magnetic memory tester to examine the effects of the following parameters: (i)

Various stress concentration areas; (ii) Different engine speeds and their effects on changes in magnetic memory signals; and (iii) Measured changes that occurred in between the two detection points due to change in the temperature of crankcase. The authors found no effect in the magnetic memory signal values due to the change of engine speed and temperature, when the temperature was below 500^0C; whereas the change of the inertial loads had clear effects on the vibration response.

2.3.3 Detection and Monitoring of Cracks Using Mechanical Impedance

Manley (1941) mentioned that the concept of mechanical impedance had been used since 1939 for monitoring vibration of shafts. It was used for the analysis of vibrational problems in engine systems. In his paper, the resonant frequencies were determined by developing damped linear systems. The theory behind this states that the resonant frequencies of vibrating systems (axial vibration) were not affected if the damping forces were small. The author stated that the method of impedance could be applied to the case of torsional vibration of shafts.

Kane and McGoldrick (1949) discussed the longitudinal vibrations of marine propulsion-shafting systems. Their purpose was to: (i) Estimate the longitudinal critical speeds, and (ii) Calculate with more precision which elements were critically affecting the longitudinal vibration. This study was mainly concerned with the types of vibrations that occur in the electric-drive propulsion system of a marine vessel. It was concluded that the longitudinal vibrations were less affected than the torsional vibrations. The vibratory system was limited to the rotating elements in the torsional vibrations. The longitudinal

vibrations, however, were affected by the machinery masses and their foundations. The authors used three methods to estimate the natural frequency: the fixed end approximation method, the two body approximation method, and the mechanical impedance method. The natural frequency for the fixed end approximation method was estimated by using this formula

$$f = \frac{F_R}{2\pi}\sqrt{\frac{\bar{K}}{m_p + \frac{\bar{m}}{3}}} \tag{2.5}$$

$$\bar{K} = \frac{EA}{l} \tag{2.6}$$

where f was frequency in cycles per second, A the cross section area in m^2, l the equivalent length of shaft, m_p the total mass of propeller and virtual mass of surrounding water, m mass of shaft, F_R flexibility factor depending on thrust bearing foundation stiffness, and $\bar{k}$ the shaft stiffness.

The natural frequency for the two body approximation method was estimated by solving the positive roots of ω in the equation

$$\omega^4 - \omega^2\left(\frac{k_1}{m_1} + \frac{k_1 + k_e}{m_2}\right) + \frac{k_1 k_e}{m_1 m_2} = 0 \tag{2.7}$$

where ω was the circular frequency in rad/sec, k_1 the static spring constant of the shaft, k_e the effective stiffness spring constant of the combined gear, thrust bearing, and turbine

foundations, m_1 the total mass of propeller and virtual mass of surrounding water, m_2 the total mass of turbines, wet condenser, gears, one fourth the mass of machinery foundations, and one half the mass of the shaft.

The natural frequency for the third method was estimated by using the mechanical impedance method. The two models that were applied in this method consisted of the mass of the propeller and the virtual mass of the surrounding water m_p, the fixed machinery masses m_c, and the gear masses m_g. Figure 2.3 shows these models.

The authors concluded that the paper provided guidance for deciding whether the thrust bearing, mounting, machinery foundations, and propeller clearances need to be included in the rotor modelling procedure. Also, they found an agreement between the computed values of natural frequencies for all the models, as well as for the experimental results.

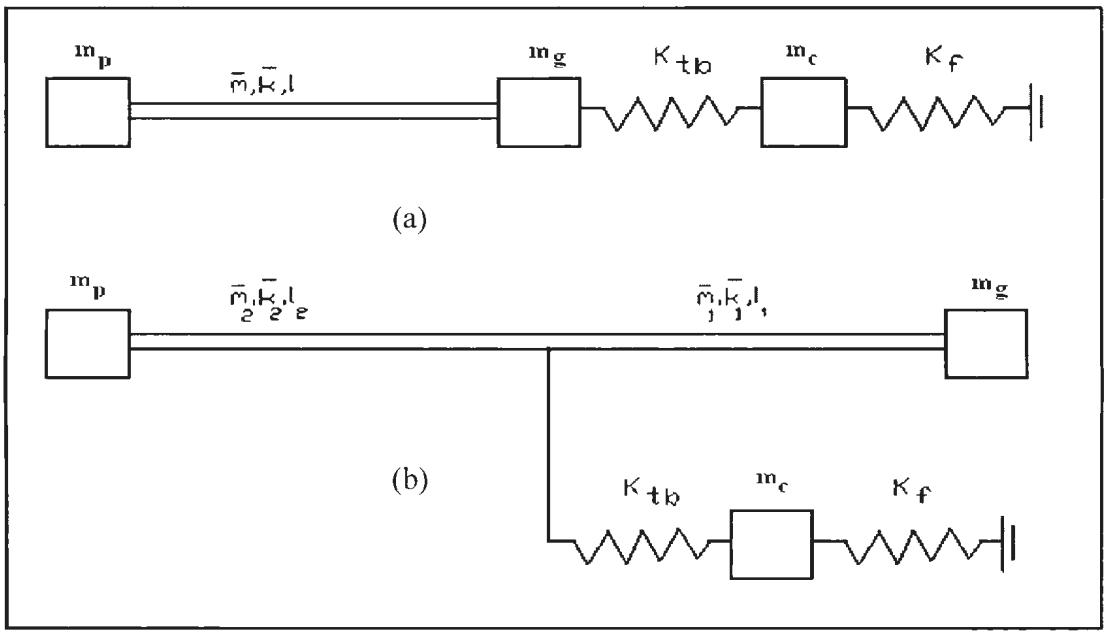

Figure 2.3 Marine Propulsion-Shafting Systems; a) Modeling 1 and b) Modeling 2

Chenea (1952) used the concept of impedance to analyze an elastic bar, a tapered and stepped shaft, and a string in longitudinal, torsional and lateral oscillations, respectively. He applied the models as continuous systems, and considered both the free and forced vibration. He assumed that the cross-sectional area of an elastic bar changed gradually and that there was internal and external damping in the system. The model consisted of a spring connected with damping in a series and then connected to another damping in parallel. By the same technique, he used this model for torsional oscillation. In both cases, he found the natural frequencies of the systems.

On (1967) used experimental and analytical procedures for determining mechanical impedance and to find its effects on the dynamic response. He developed the concept of mechanical impedance in terms of point and transfer impedance parameters. He developed two DOF (degree-of-freedom) and three DOF lumped mass models, for theoretically representing, complex aerospace structures, as large inter-connected matrix systems. He compared his theoretical results with experimental results on such aerospace structures and found them to be reasonably good. He mentioned that this approach could be extended to many systems subjected to steady state, transient and random excitations.

Bamnios and Trochidis (1995) investigated the influence of a transverse open crack on the mechanical impedance experimentally and analytically. Cantilever beams were used to obtain the change of the mechanical impedance at different locations and sizes of the crack under the effect of longitudinal and bending vibrations. From vibration results they

found that the changes of mechanical impedance were more in the lateral directions than in the longitudinal direction.

Prabhakar et al. (2001) investigated the influence of a transverse surface crack for open and breathing cases (depending on the rotor deflection) and shaft carrying a disk at the center. They used FEM analysis to show this influence on the mechanical impedance of the rotor-bearing system. They attempted to use the concept of mobility to detect the crack by using different crack parameters and force locations. They found that the mechanical impedance changed and was sensitive to the presence of the crack; it decreased (for an open crack) as the crack depth increased, and the decreases were greater when the location of the crack moved toward the disk. In breathing crack the mechanical impedance increased as the crack depth increased. The mechanical impedance sensitivity was more apparent in the breathing crack. Additionally, when the rotating frequency of the shaft for the breathing crack was doubled the sudden change in mechanical impedance was easily observed. For a breathing crack, the mechanical impedance was sensitive to low or high crack depths, even if the crack depth ratio was less than 0.1 (ratio between crack depth and shaft diameter). Finally, the authors recommended that the measurements of mechanical impedance could be used as a good indicator for the detection of the presence of cracks.

Bamnios et al. (2002) carried out analytical and experimental studies on cracked beams to investigate the effect of a transverse open crack on the mechanical impedance under various boundary conditions. They used a spring connecting the two segments of the

cantilever beam as a model of the crack. The beam had a uniform rectangular cross-section and the crack was assumed open and to be of uniform depth. Additionally, bending vibrations were considered and the bending spring constant K_T was given by:

$$K_T = 1/c \quad \& \quad c = (5.346w/EI)*J(a/w) \tag{2.8}$$

where, w was the depth of the beam, E the modulus of elasticity of the beam, I the area moment of inertia for the beam cross-section and J (a/w) is the dimensionless local compliance function. It can be expressed as

$$J(a/w)=1.8624(a/w)^2-3.95(a/w)^3+16.37(a/w)^4-37.226(a/w)^5+76.81(a/w)^6-$$
$$126.9(a/w)^7+172(a/w)^8-43.97(a/w)^9+66.56(a/w)^{10} \tag{2.9}$$

They found that the impedance and natural frequencies were affected by the presence of a crack, as well as by its size and location. Also, the natural frequencies of the cracked beam reduced when compared with the un-cracked beam. As seen from the reported numerical results, the crack had a strong effect on the mechanical impedance and this effect depended on the crack's location. The changes of the mechanical impedance and the natural frequencies could be used as indicators for the presence of a crack. There was agreement between analytical and experimental studies in all cases.

Prabhakar et al. (2002) investigated experimentally the influence of a transverse surface crack on the mechanical impedance of a rotor bearing system. This system consisted of rigid disks, distributed parameter finite shaft elements, and discrete bearings. The experimental work was done to validate their previous numerical analysis results. They

tried to use the concept of mobility for detecting and monitoring the crack using different crack parameters and force locations. The authors did this experiment for an un-cracked and a cracked shaft. They used different depths (20% and 40% of diameter) to represent the crack depth) at the location. Also, they measured the mobility in two directions, horizontal and vertical, at the bearing locations. This measurement was taken at different rotor speeds. They found that the mobility was directly proportional to the depth of the crack, as well as to the rate of change of mobility at the rotating frequency. Moreover, since the crack depth was assumed to grow vertically, the rate of change of mobility in the vertical direction was greater than that in the horizontal direction. There was considerable agreement between experimental results and numerical simulations. Therefore, the authors suggested using this method to detect the crack, and monitoring in a rotor-bearing system.

2.3.4 Crack Detection Methods using Other Techniques

Crack initiation and fatigue failure are the consequence of large cycles of high amplitude stresses. Torsional vibrations of rotors represented one of the main reasons for fatigue failure in shaft. The types of failures, the singular data acquisition requirements, and monitoring torsional vibration were discussed by Larry et al. (1999). The turbine generator had components such as retaining rings, shaft cracks, and blade root cracks which could cause sudden fail in generator. In this paper, the authors used a simplified model of the turbine generator system to detect, analyze and safely shutdown the turbine generator. This model showed the relationship between the shaft excitation forces, which represented input to the model, and the shaft torsional vibration response, which

represented the output. This ratio (output to the input) is known as the transfer function. The transfer function was basically dependent on the mass, stiffness, and damping of the shaft. The authors addressed the issues concerning data acquisition, measurements, and data analysis. A high-speed personal computer was used to measure and calculate the torsional frequency. Measurements were used for recording and analyzing instantaneous time history. Lab View was the commonly used software for analysis of data. Their conclusion from metallurgical test data and fracture mechanics analysis showed that the turbine would fail due to crack initiation and crack growth in about 6 months due to the sporadic nature of the forcing excitation. Also the availability of a data acquisition monitoring system, such as Structural Integrity Associate's Transient Torsional Vibration Monitor System (SI-TTVMS) would provide a good signal and detection system before rotor failure occurred.

Zhinong et al. (2006) presented bi-spectrum analysis to the fault diagnosis of the rotor crack based on blind identification. They used this approach to investigate the bi-spectrum characteristics of experimental rotor with cracks of different depths and locations. They considered four cases, one for a non-cracked rotor and the other for cracked rotors with different crack depths and locations. Additionally, two sensors were used, one mounted near the bearing block and the other mounted near the mass rotor plate. All the data collected from different rotors were measured at the same point and at the same speed. They concluded that this method was a powerful one for the diagnosis of rotor cracks, and that the experimental work provided quite useful and sufficient data on this topic. Also, it was concluded that the highest vibration amplitude of the 2x

(parametric bispectrum) occurred when the crack was closer to the span center. This method would present a suitable method for field application.

2.4 Summary

A comprehensive review of the existing literature on the dynamic behaviour of un-cracked and cracked shafts has been presented. Many crack detection techniques have been developed and used in the past few decades. In general these techniques could be classifieds: (i) Based on frequency changes [Rutter (1993), Sabnavis et al. (2004) and Kumar and Rastogi (2009)]; (ii) Based on mode shape changes [Wauer, (1990) and Sabnavis et al., (2004)]; (iii) Based on mechanical impedance changes [Kane and McGoldrick, (1949)]; (iv) Based on stress fluctuations [Kumar and Rastogi, (2009)]; (v) Closeness of the rotational speed to the secondary resonance [Ferfecki and Ondrouch, (2007)]; (vi) Peaks in vibration amplitudes and unstable vibrations [Wauer, (1990)]; (vii) Changes of stiffness due to a crack [Wauer, (1990)]; (viii) Histogram signature analysis technique [Wauer, (1990)]; (ix) Neural networks [Sabnavis et al., (2004)]; (x) Non-contacting transducers [Wang et al., (1992)]; and (xii) Least squares identification method in the frequency domain [Kumar and Rastogi, (2009)]. Most of the above studies have focused on large size cracks. Generally rotor shafts fail due to high-cycle fatigue. Therefore early detection of cracks is more important than detecting cracks of larger depths at later stages. Few studies have focused on small sized cracks which will be needed to prevent sudden failures in rotor shafts. In the present study attention is focused on determining parameters that will lead to procedures to the small crack size in rotor shafts.

The changes in mechanical impedance have been used since 1939 for determining problems in engine systems. Only a few studies have been reported on the use of mechanical impedances to identify cracks in shafts: moreover all of these studies have been on single span determinate shafts. Hence in the present study an indeterminate overhanging shaft has been used. In this study cracking in a shaft will be investigated experimentally and numerically and analyzed when subjected to the effect of torsional and lateral vibrations. Also the mechanical impedance techniques will be extended to identify the natural frequencies of indeterminate marine propulsion-shafting systems bearing a propeller and subjected to lateral vibrations; as well the procedure will be used to detect the changes that occur due to the presence of cracks in rotor shafts.

Chapter 3

Fabrication of Experimental Model and Test Setup

3.1 Introduction

Experimental fabrication and testing of the cracked and un-cracked rotor shaft models were made to identify the transverse crack existence in the structural laboratory of Memorial University. In order to investigate the behaviour of un-cracked and cracked shafts, three separate models were fabricated and tested for different crack depths (from 0% to 70% of diameter). LMS data acquisition system, accelerometers, impact hammer and strain gages experimental setup were used for measuring the cracked and un-cracked shaft response parameters under lateral and torsional vibrations. In the experimental study, cracks of different depths were located at the (un-cracked) maximum bending moment position. Shaft response parameters for lateral (using an accelerometer) and torsional (using shear strain gages fixed at three different locations) vibrations were obtained using the modal analysis software, LMS Test Lab^{TM}. The experimental results were used to validate the numerical results (given in the subsequent chapters) obtained using Finite element formulation. The open crack was made in the rotor shaft using a steel saw blade which made the saw cut to be slat ended rather than sharp edged.

This chapter is organized as follows, viz., (i) Details of the experimental setup in the laboratory with associated instrumentation; (ii) Test procedures, calibration and measurements; (iii) Off-line experimental modal testing and analysis of cracked structures; and (iv) experimental results, discussion and summary.

3.2 Fabrication of Test Frame

The rotor shaft test frame shown in Figures 3.1 and 3.2 was made of steel and supported on two bearings. The length of this shaft was 1.22 m and of diameter of 0.015875 m; the propeller with blades (as shown in Figure 3.3) was made from bronze and had a weight of 1.5687 kg, and was fixed to the overhanging end of the supported span (see Figure 3.1). An aluminum arm, which had a weight of 0.356 kg and length of 30 cm, as shown in Figure 3.4, was used to apply various magnitudes of impact torque at various locations of shaft. During modal tests the rotor shaft, with the overhang, was locked (or fixed) to the bearing support # 1, using a fixed Aluminum plate as shown in Figures 3.1 and 3.2. All these parts were joined together by welding the test frame supports to the huge bottom steel plate support.

3.3 Shaft-Propeller Test Rig and Experimental Setup

The assembled rotor shaft-bearing-propeller system test rig is shown in Figure 3.5. It was designed and developed to investigate the vibration on characteristics of the uncracked and cracked shaft using modal testing. The main objective of this experimental study was to study the effect of cracks on the lateral and torsional vibrations of a shaft.

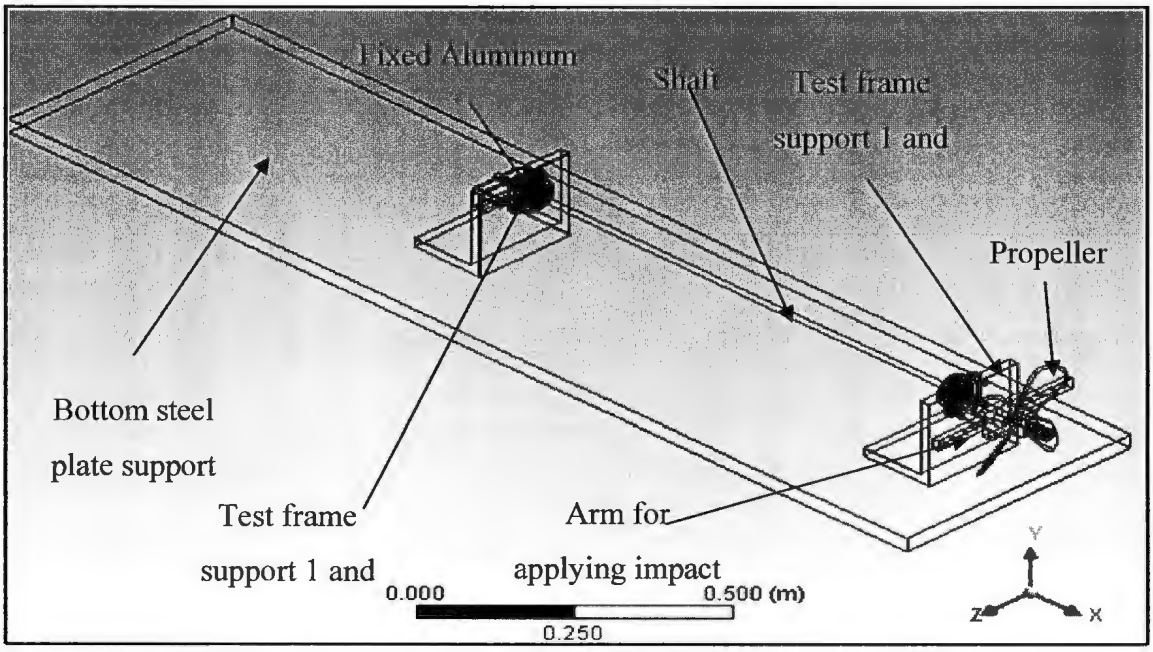

Figure 3.1 Schematic Diagram of the Shaft-Bearing-Propeller System Model

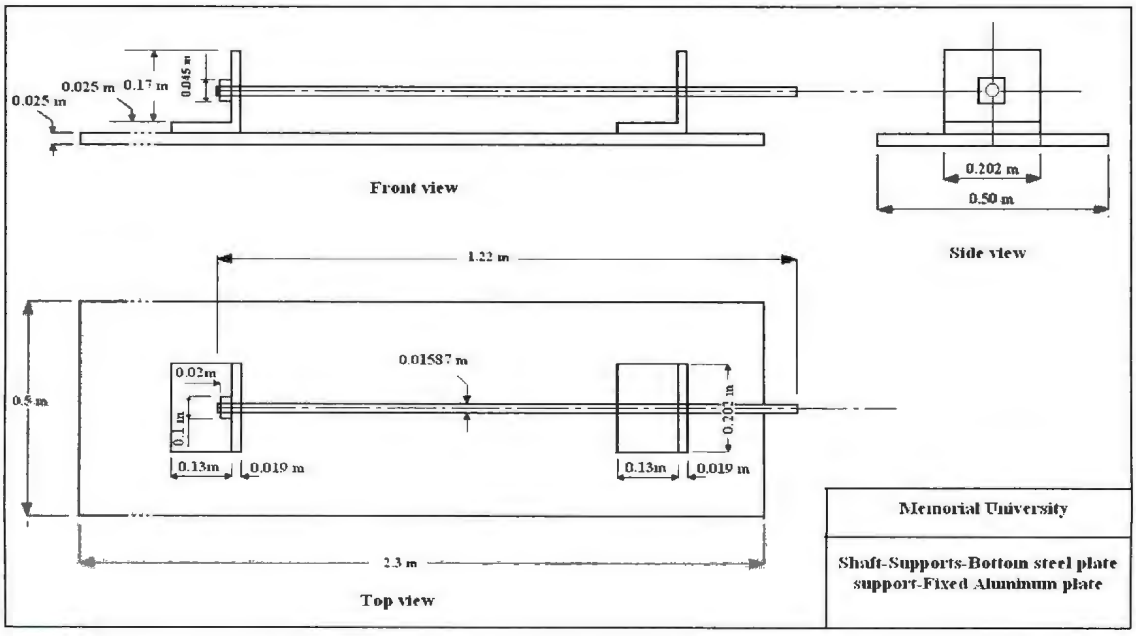

Figure 3.2 Fabrication Diagram of the Rotor Shaft-Supporting-Bottom Steel Plate with A Fixed Aluminum Plate.

(a)

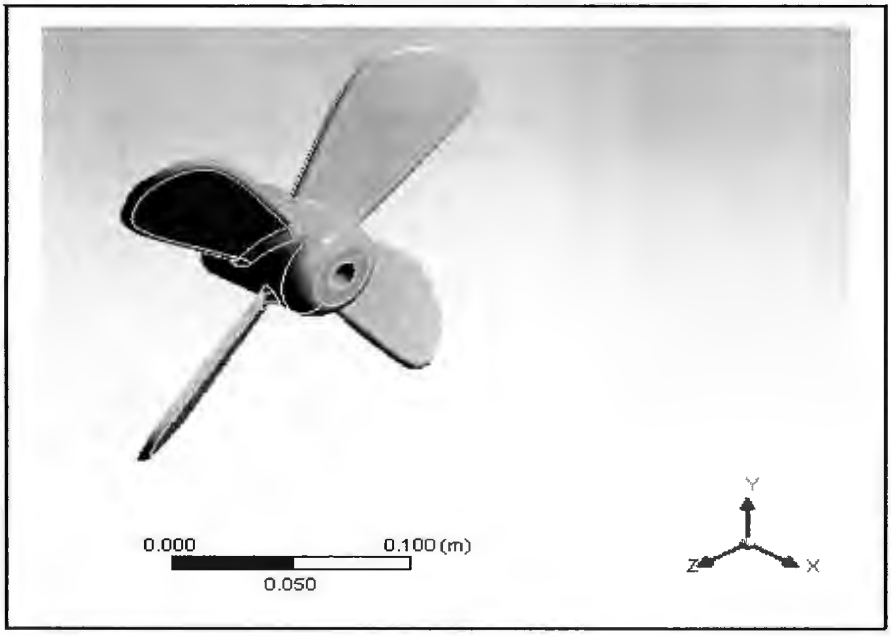

(b)

Figure 3.3 Figure of the Propeller Giving (a) Actual Experimental Propeller Used in the Study; and (b) Numerical Model Used in Analysis.

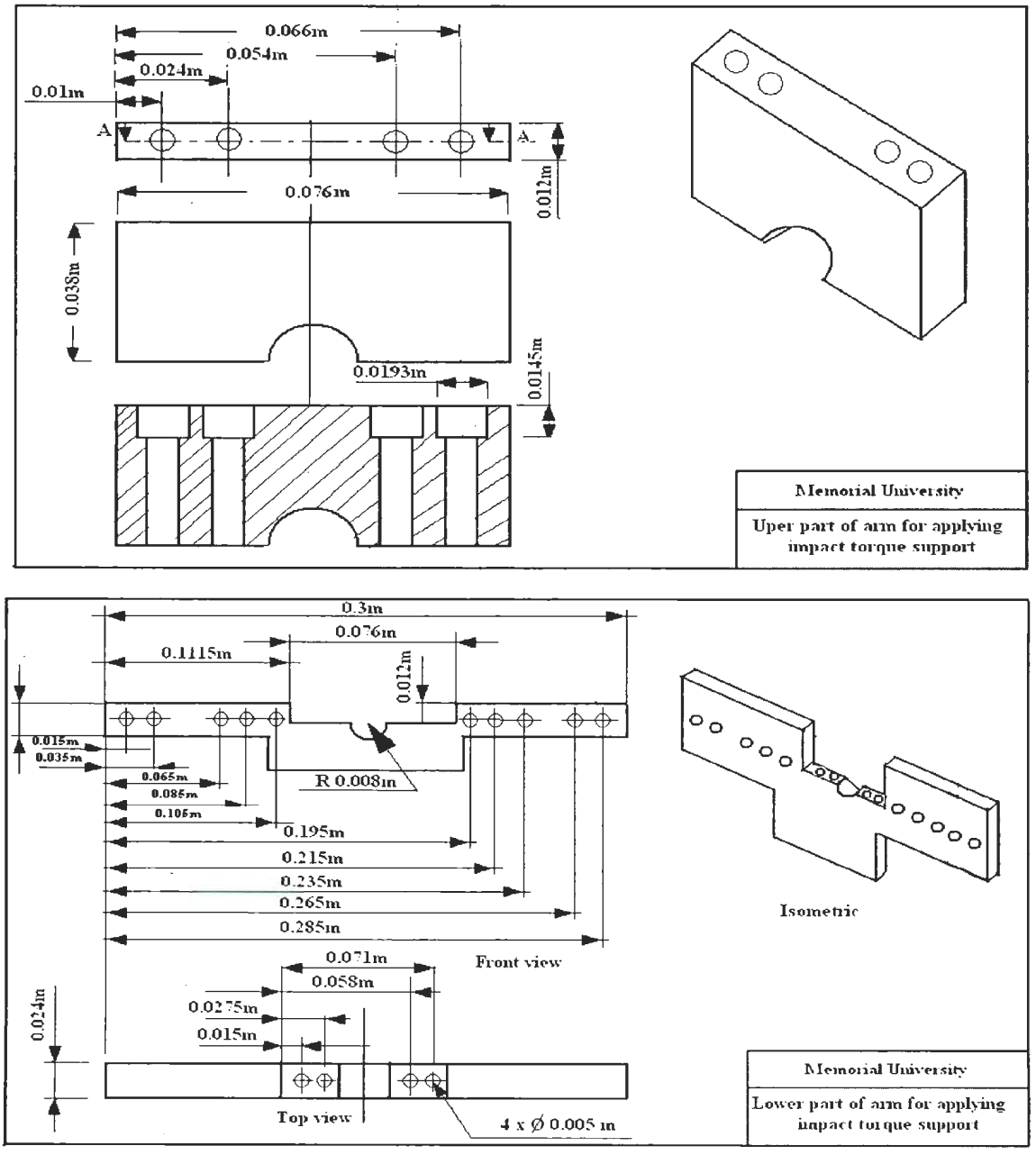

Figure 3.4 Fabrication Diagrams of the Upper and Lower Parts of Torque Applying Arm

3.3.1 Test rig description

The rotor shaft model used in the experiments consists of a motor driven rotor-propeller system (initially, the test was fabricated to carry out on-line vibration measurements while the shaft was rotating). The motor was connected to the rotor shaft through a jaw

coupling shown in Figure 3.6. The rotor shaft was made of steel and had a supported span length of 0.97 m and diameter (average) of 0.015875 m; the propeller was overhanging at one end of the supported span (see Figure 3.7). The measured diameter values at different points for the three rotor shafts are given in Table 3.1. Young's modulus of elasticity was taken as E = 200 GPa and material density was taken as 7870 kg/m^3. The shaft was supported on two bearings as shown in Figures 3.7. These bearings of type 5967k81 (McMaster-Carr Ball bearing, 2011) consisted of two mounted bearings having greased fittings and deep-grooved ball-bearing inserts and two set screws used to fix the shaft to the bearings, as shown in Figure 3.8. Experimental program were carried out to identify the shaft characteristics (natural frequencies, damping and mode shapes) with and without the presence of the crack. Manually-made saw cuts (0.65 mm wide) of different depths ratios (from 0% to 70% ratio) were made at a distance of 0.02 m to the right of bearing support 2, as shown in Figure 3.9.

Table 3-1 The Measured Diametral Values for the Three Rotor Shafts

Shaft	Rotor shaft diameter at various locations, m					
	D_1*	D_2*	D_3*	D_4*	D_5*	$D_{average}$
Shaft # 1	0.01589	0.01589	0.01588	0.01588	0.01589	0.015886
Shaft # 2	0.01586	0.01587	0.01587	0.01586	0.01586	0.015864
Shaft # 3	0.01587	0.01594	0.01591	0.01588	0.01589	0.015898

* 1, 2, 3, 4 and 5 are locations along the length of the rotor shaft.

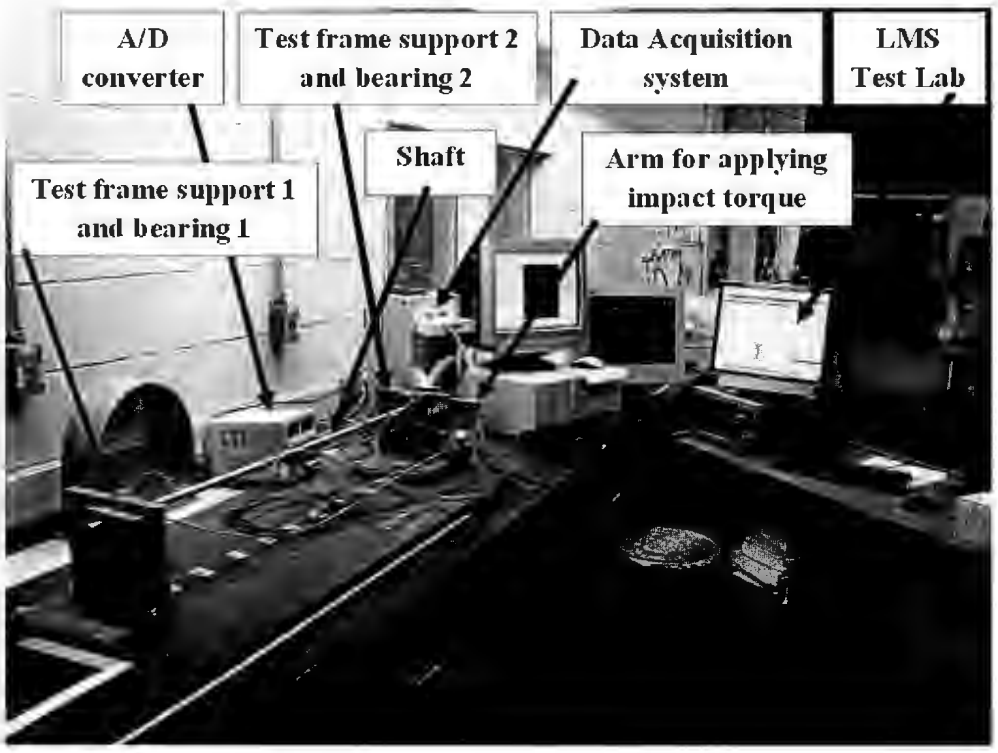

Figure 3.5 The Shaft-Propeller System Bearing Test Rig Setup

Figure 3.6 Jaw Coupling

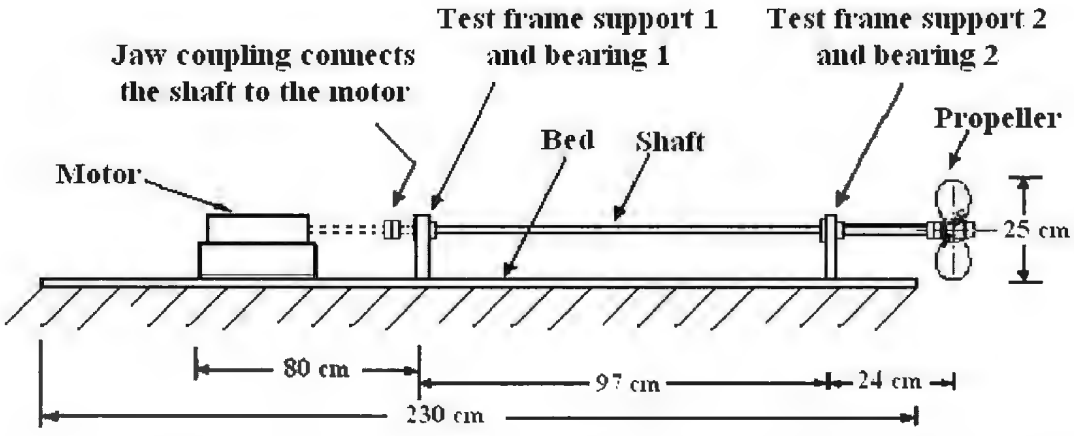

Figure 3.7 Schematic of Un-Cracked Shaft during on-Line Monitoring Studies (the Jaw Coupling at the Backside of Bearing 1 is Disconnected During Modal Tests)

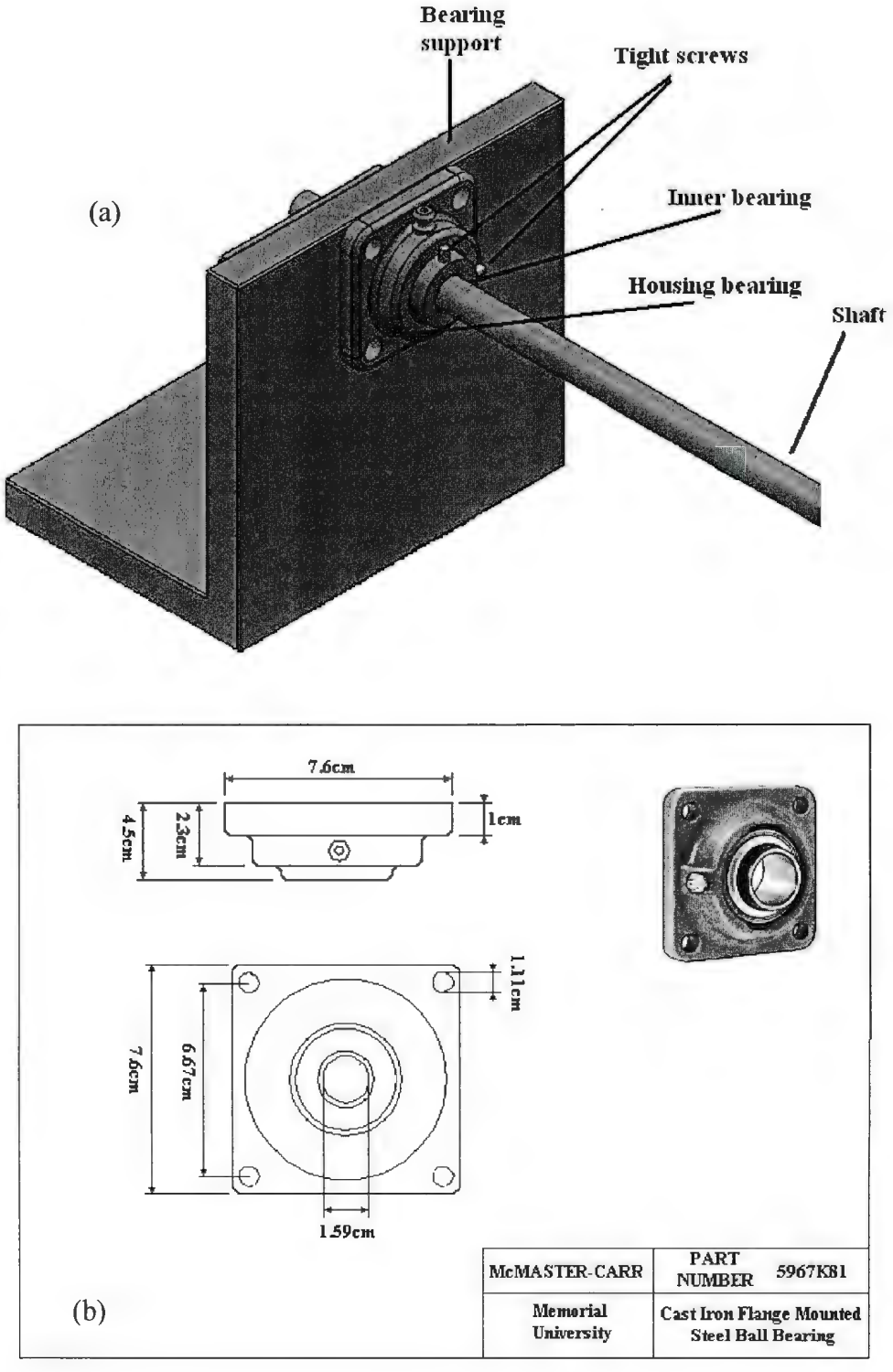

Figure 3.8 (a) Details of Bearing Support; and (b) Dimensions of the Mounted Bearing

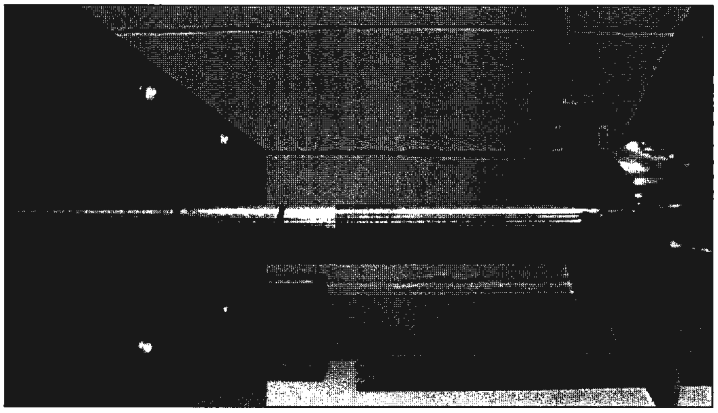

Figure 3.9 The Saw-Cut Crack at the Right of the Bearing Number 2

3.3.2 Test Instrumentation System and Methodology

The test instrumentation system used to measure the two types of vibrations, viz., lateral and torsional modes of a rotor shaft system, is shown in Figure 3.5. For the experimental portion of the study, the Engineering Innovation [LMS Test Lab ™ as shown in Figure 3.10 (a)] software package with two measurement channels was used. The first input channel recorded the time history output from the modal hammer used in the study, shown in Figure 3.10 (b). The number designation of the impact hammer type is 8206-002 and the maximum force (non-destructive) that it can deliver is 4448N. Three tips can be used with the impact hammer, viz., Aluminum tip, Plastic tip and rubber tip. The maximum forces that can be delivered by each tip are given respectively as 350, 275 and 25 N, for Aluminum, plastic and rubber tips [calibration Chart for impact hammer, (2009)]. In this study, plastic tip (DB-3991-002) material was used for bending modal tests. The second channel recorded the time history output from the accelerometer device shown in Figure 3.10(c). Figure 3.10 (d) and (e) show the experimental setup used to

measure the torsional vibration of the rotor shaft. In the torsional vibration measurement system three strain gages were fixed at three locations, one placed near the bearing support 1, the second placed at the middle of the supported span, and the last one placed near propeller as shown in the Figure 3.10 (d). An aluminum arm, shown in Figure 3.10 (f) was used to apply impact torque at certain location of shaft. Five data acquisition channels shown in [Figure 3.10 (e)] were used to acquire the data (in a multi-blexel manner), viz., three for torsional strain measuring gages, one for accelerometer channel, and the fifth for impact load with a maximum mass of 22kg. Also data acquisition system signals received from the strain gauges were transmitted to a PCI6024E data acquisition card. The excitation voltage used in the setup was 10 Volts. The corresponding range for the torque was ±2 N.m as measurable by the strain gauges. There was no filter applied to the signal during the data collection. The Lab view^{TM} software was used to record the data during the experiments. The gain factor applied to the signals coming from the data acquisition card was 200.

The following instrumentation was used for recording and measuring:

a) Impact hammer for use in delivering impulse forces to the test shaft structures. One impact hammer moved to many points (14 points).
b) One accelerometer for measuring the rotor shaft accelerations for model analysis.
c) LMS Test-Lab setup and software for recording and determining the natural frequencies, damping, and mode shapes of the shaft using modal analysis based on frequency response function (FRF).

d) Strain gauges for measuring the associated torsional shear strains of the shaft system.

e) An aluminum arm was used to apply various magnitudes of impact torque at various locations of shaft.

f) Data acquisition channels were used, viz., three for torsional strain measuring gages. Two personal computers are used to estimate and collect data.

(a)

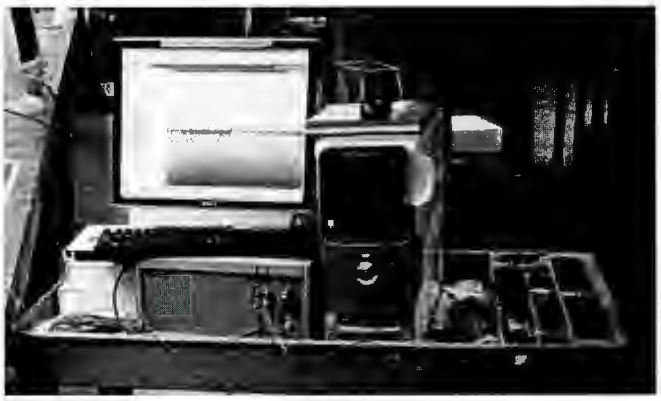

(b)

Figure 3.10 part 1of 2

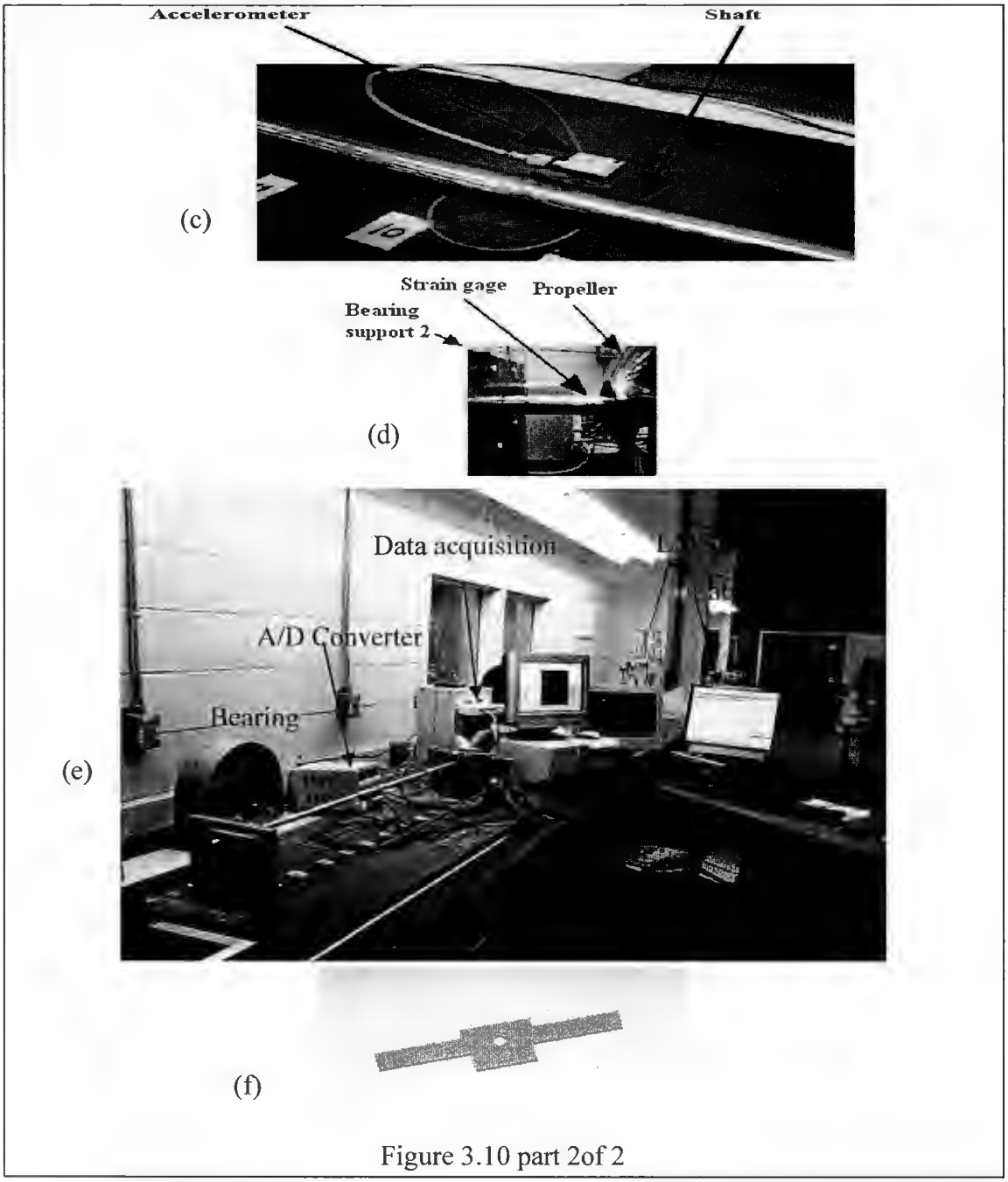

Figure 3.10 part 2of 2

Figure 3.10 The Test Instrumentation Equipment: (a) LMS Test Lab with Rotor Shaft; (b) Impact Hammer and Tips; (c) Accelerometer Device; (d) Strain Gage; (e) Data Acquisition; and (f) Aluminum Arm for Impact Loading on Shaft.

3.3.3 Calibrations for Torque Measurement

The calibration of the test setup was produced before the start of experiments. In this investigation, calibrations were preformed only during the experimental study when measurements were made for torsional motion using five (multiplexed) data acquisition channels, viz., three for torque gages, one accelerometer ($\pm$ 4g's) channel, and the fifth for impact load using the weights hung from aluminum arm used for torsional loading. The summarized steps for torsional calibrations are given below, viz.,

(i) Use Lab view software;

(ii) Read voltage readout from software for the strain gauges;

(iii) Apply load to shaft by using impact hammer, and compute the torque applied for different increments of load;

(iv) Plot load vs. strain (converted using the sensitivity of the strain gauges)

(v) Using Microsoft Excel to get linear a equation $y = mx + b$

(vi) Input formula into software and Check software by loading shaft.

3.4 Test Procedure and Measurements

The experimental work carried out in this study was an off-line experimental modal analysis since on-line modal testing could not be properly done. The test procedure, measurements and analysis made in the experimental study can be separated into two parts: (i) off-line, experimental modal analysis using LMS Test Lab ^{TM} to find vertical and horizontal transverse vibrations using an accelerometer; and (ii) off-line, experimental modal analysis using strain gage to determine the torsional frequency. In

both cases, dynamic signals containing inherent natural frequencies, damping factor, and mode shapes were recorded and analyzed to correlate with the results obtained from numerical methods.

3.4.1 Off-line Experimental Transverse Vibration Modal Analysis

Modal analysis deals with the measurement and consequent analysis of the dynamic response of the rotor shaft structure. It was used in this study off-line to predict and identify dynamic characteristics of the rotor shaft structure before carrying out the second part of experimental (on-line) study, in a subsequent study. Since it was very difficult to obtain take vibration measurements when a shaft was rotating unless one had equipment for remote transmission and acquisition of data from the rotating and vibrating shaft, only off-line dynamic measurements were made.

In this part, an impact hammer was used at several locations (14 points) as shown in the Figure 3.11 (a) and (b) to excite the structure. At each location the impact force was applied (through the modal impact hammer) five times in the transverse directions. Each time the modal analysis was carried out and the dynamic response parameters from each set of five measurements were added and averaged to give the response parameters at that point. The accelerometer was located at a fixed place (point 9) and the direction of arrow given in the accelerometer would indicate the direction of vibration, whether vertical or horizontal. The accelerometer and impact hammer responses were transmitted to the personal computer which contained the LMS modal analysis software to analyze these

responses and give the results as, frequencies, damping factor, and mode shapes as shown in Figure 3.12.

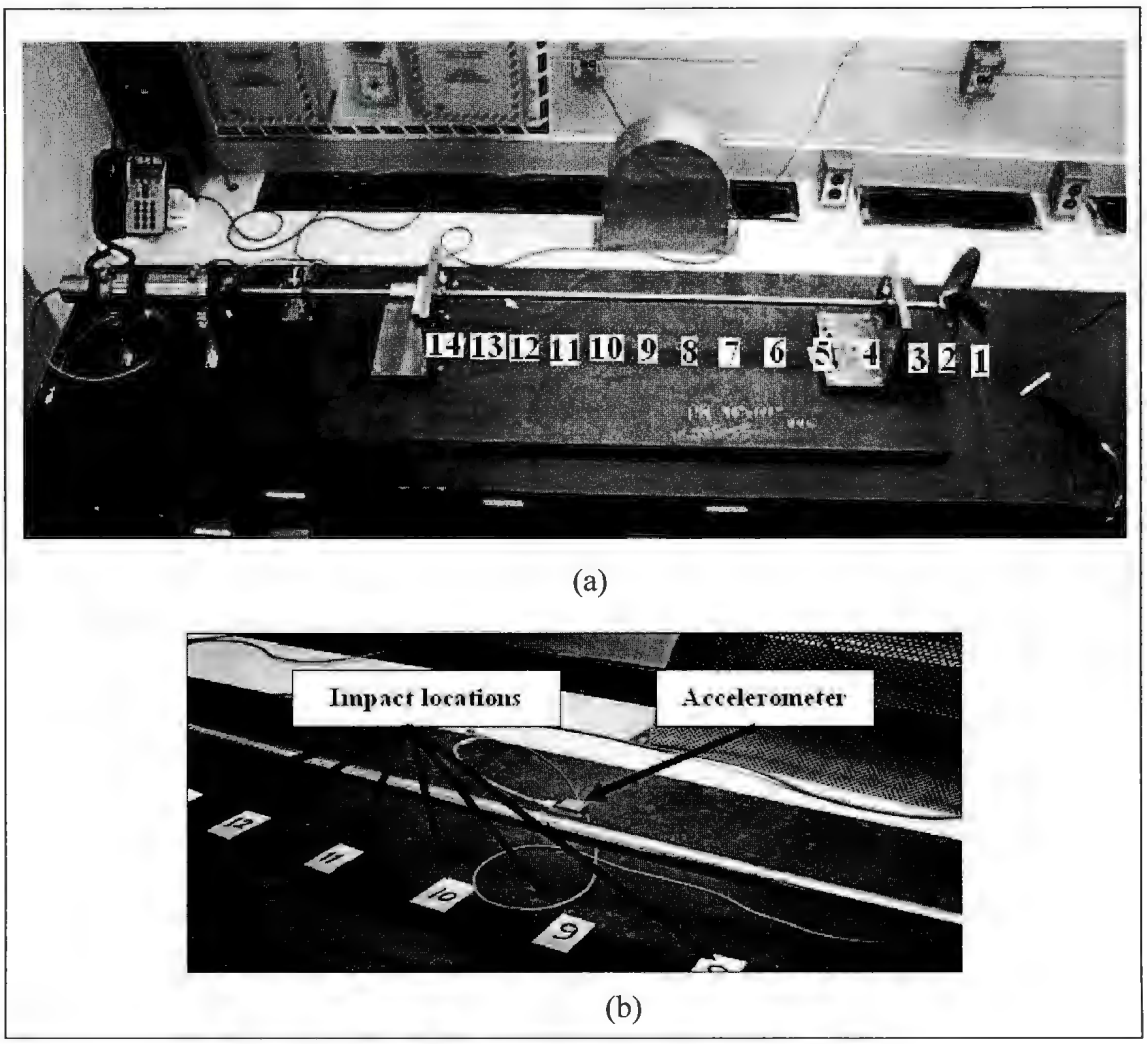

Figure 3.11 Impact Hammer and Accelerometer Locations

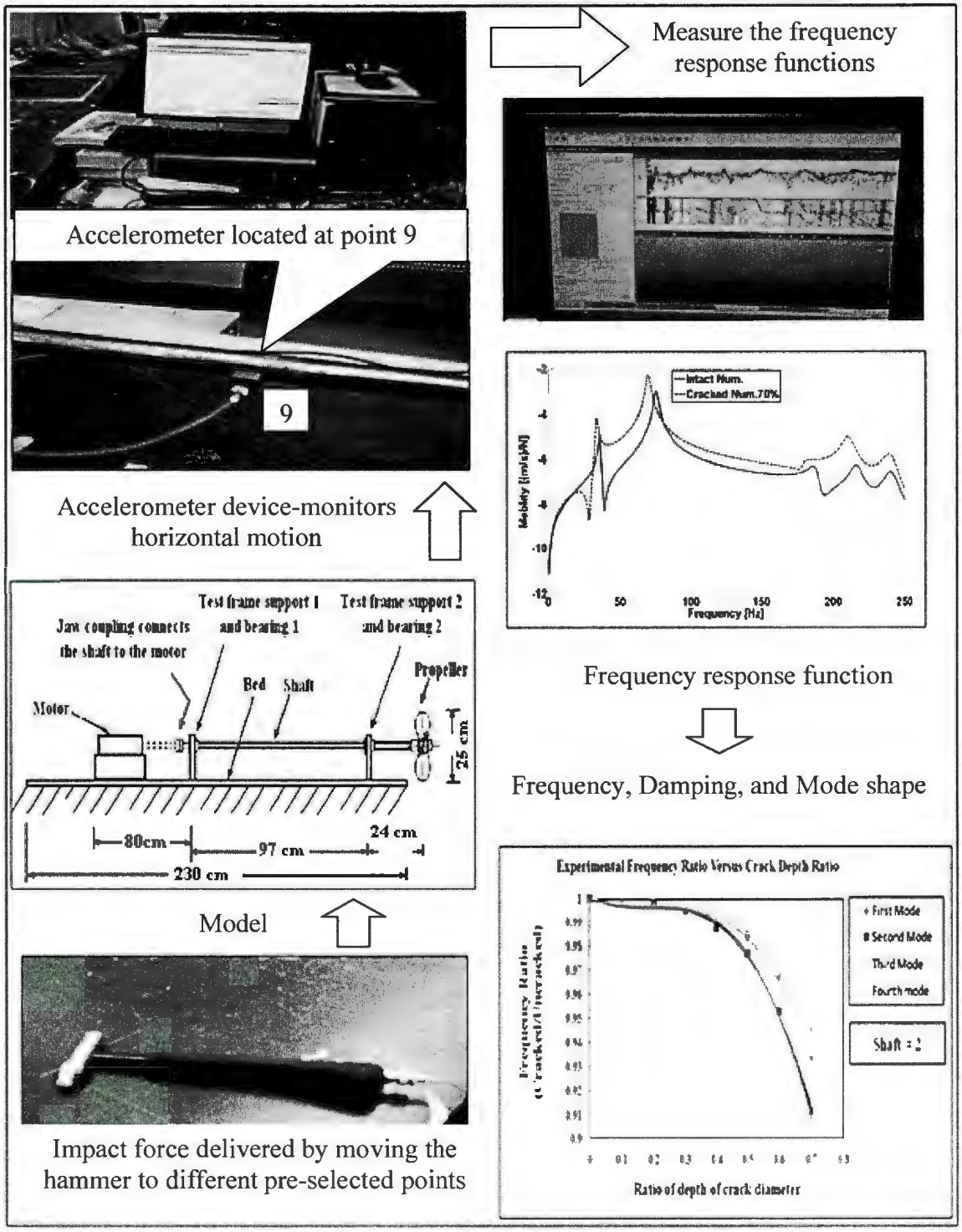

Figure 3.12 Experimental Procedures for Impact Testing of the Rotor Shaft

3.4.2 Modal Testing and Analysis of Cracked Shaft

Manually-made saw cuts (0.65 mm wide) were used as cracks of different depths. The experimental results were used to validate the most appropriate numerical model. The equipment system used to measure the two types of vibrations, viz., lateral and torsional modes of a cylindrical shaft system, is shown in Figure 3.5. For the experimental portion of the study, the Engineering Innovation (LMS Test Lab ^{TM}) software package with two measurement channels was used. The first input channel recorded the time history output from the modal hammer used in the study, shown in Figure 3.13(a). The second channel recorded the time history output from the accelerometer device (type Miniature DeltaTron 4507) shown in Figure 3.13; alternately a set of shear strain gages can also be used instead of an accelerometer, to record torsional data.

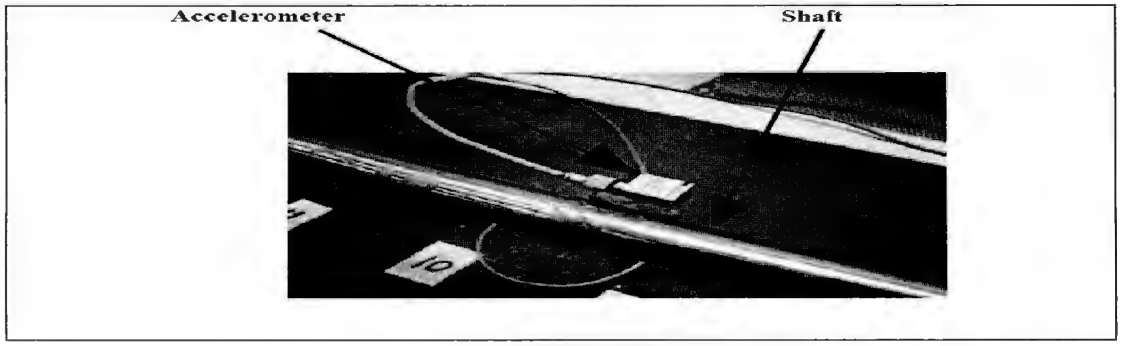

Figure 3.13 Photo the Attached Accelerometer

As shown in Figure 3.14 (a), in subsequent on-line monitoring studies, the backside end of the continuous rotor shaft with the cantilever overhang (in the forward end) would be connected to an electric motor and driven at a maximum speed of 4000 rpm; but in the present experimental modal testing, the backside connection to the electric motor was disconnected and modal testing was done in a "static" configuration of the cylindrical

shaft, with the propeller attached to the overhanging end. During modal tests, the rotor shaft with the overhang was locked (or fixed) to the bearing support (bearing support 1) as shown in Figure 3.14 (b). The fixed rotor shaft of 15.87 mm diameter and 1220 mm length was supported on two bearings with greased fittings, and deep-grooved ball-bearing inserts. Two set screws, separated by 90°, were used to fix the bearings to the rotor shaft at each of the bearings 1 and 2. These experimental tests were repeated for three different shaft-bearing systems, viz., rotor shaft No. 1, No.2 and No. 3. The three rotor shafts were of almost of the same diameter (measured average values were 0.01588 m, 0.01586 m, 0.01589 m respectively, as shown in Table 3.1). For each crack depth three separate tests (with five averaging tests, as described earlier) were carried out and the results processed through the LMS Test Lab system. Then the results were added and averaged to get the final results reported herein.

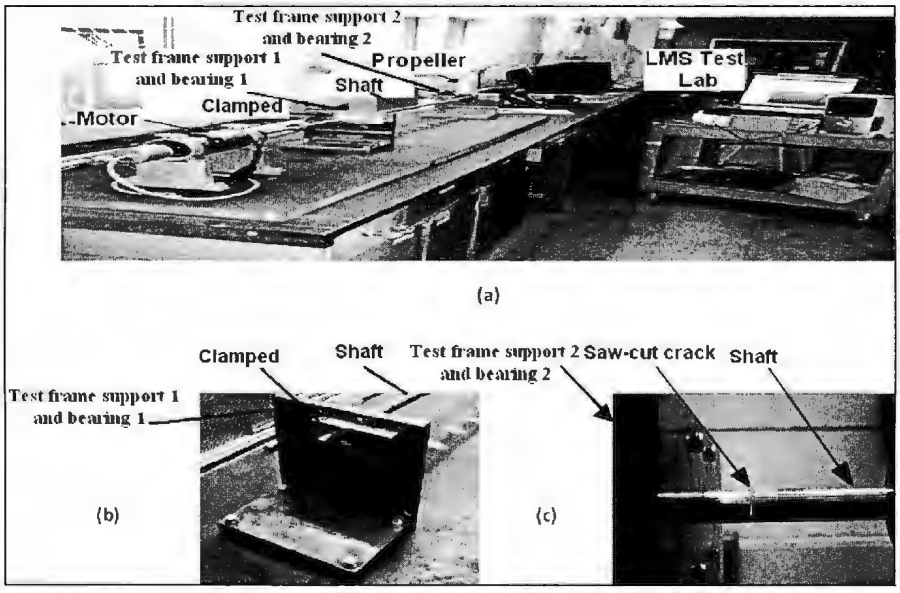

Figure 3.14 (a) LMS Test Lab with the Shaft during Modal Tests; (b) The Clamped End of the Cylindrical Shaft at Bearing 1; and (c) The Saw-Cut Crack With 70% Crack Depth Ratio.

Figure 3.15 shows the experimental setup used to measure torsional vibration of the cylindrical shaft. In the torsional vibration measurement system three strain gages were fixed at three locations, one placed near the bearing support 1, the second placed at the middle of the supported span, and the last one placed near the propeller (in the overhanging end) as shown in the Figure 3.15 (a). Two sets of Suzette type (K-XY3X) model strain gauges with connection cables (4-wire circuit), fixed at three locations, were used. They were assembled in half bridge configurations. These sets of strain gauges were mounted 180^0 apart on the circumference of the shaft (along the neutral axis of the un-cracked beam) at a given longitudinal location. The manner in which they were oriented enabled the measurement of torsional strains while any incidental strains due to beam bending would cancel each other. Figures 3.15 (c) and (d) show the sets of strain gauges used during modal tests and locations along the shaft. An aluminum arm was used to apply various magnitudes of impact torque at various locations of shaft. Five (multiplexed) data acquisition channels were used, viz., three for torque gages, one accelerometer ($\pm$ 4g's) channel (which were multi-plexed), and the fifth one for impact load with the modal hammer.

In the earlier tests and numerical analyses, neither ANSYS software package (2010), used in analysis, nor the LMS Test Lab ^{TM} system was able to indicate the presence of the first torsional frequency in the shaft-propeller system. The probable reasons for this were determined as follows: (i) The elastic spring support provided at frame support locations 1 and 2, did not permit the torsional rotations at these support locations; (ii) The BEAM4 type of beam element did not give the first torsional mode due to the improper lumped

mass values used for torsional motions (in ANSYS 2010, Section 3.12.7); probably higher order beam elements (such as BEAM188 or BEAM189, having warping as an additional degree of freedom) could have given the first torsional frequency (this was not attempted since the use of warping as another variable, along with the available six degree-of-freedoms at a point, looked superfluous for the shaft vibration); and (iii) The LMS Test Lab™ did not give the torsional mode since the accelerometer used (for getting the modal amplitudes) measured only the bending motions, and as well the LMS software used in the study did not attempt to extract the torsional vibration features from the monitored vibration signals. Hence a different procedure had to be devised to determine the torsional frequency(s) of the shaft-propeller system. For the analytical portion of the investigation to calculate the natural frequency of torsional vibration, the rotational stiffness of the shaft and mass moment of inertia of a propeller (in addition to the aluminum plate used for generating sudden impact torsional moments in the shaft) about the axis of rotation had to be determined. Figure 3.16 shows a standard trifilar suspension arrangement that was used to determine the platform and propeller properties. This trifilar suspension structure was a circular, stiff, plywood platform attached and hooked to a hanger via very stiff ropes. The three ropes were attached on the top to keep platform suspension as flat as possible. Also in this experiment, a stop watch was used to record the period of torsional oscillations.

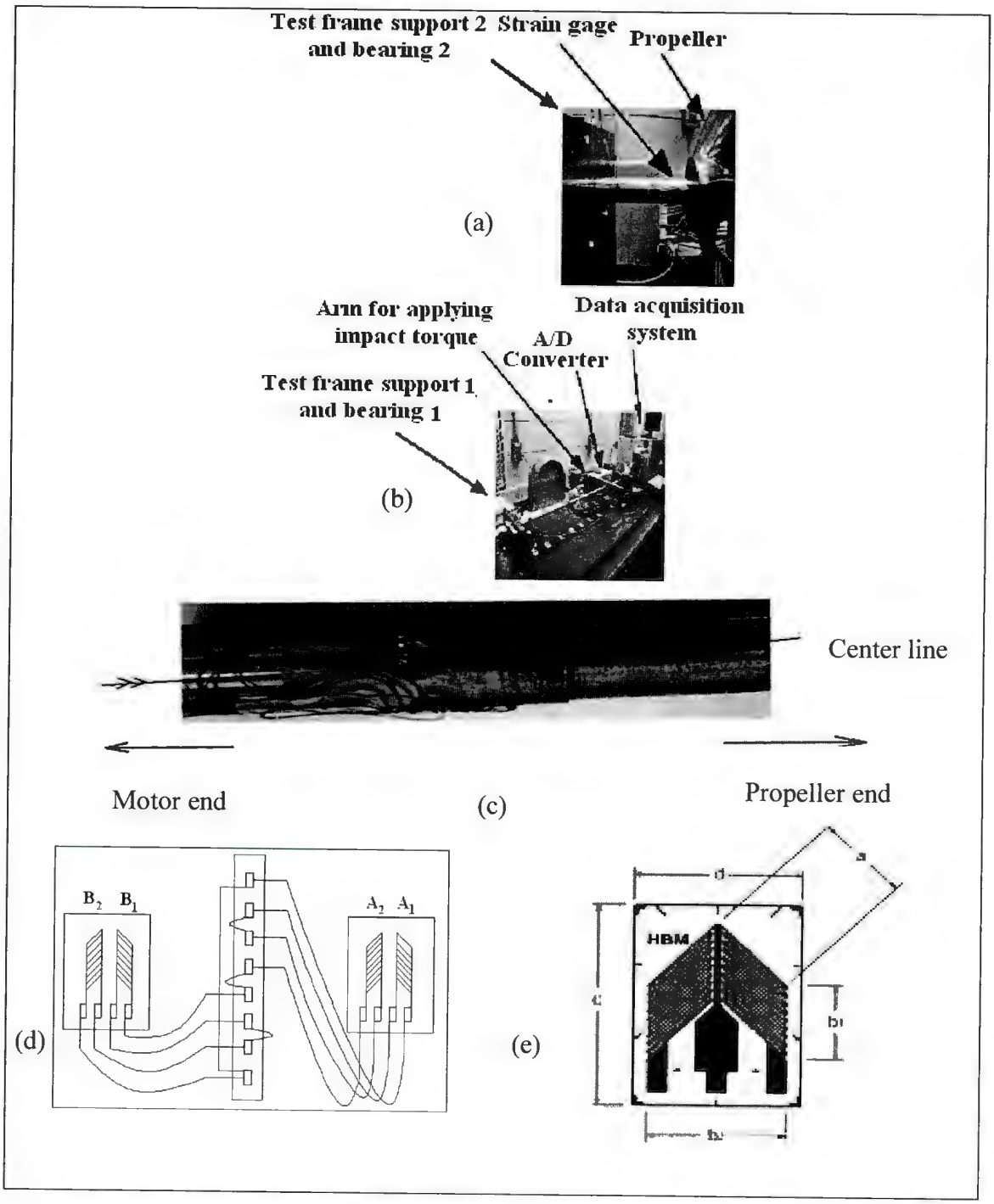

Figure 3.15 Schematic of the Torsional Vibration Measurement Instrumentation; (a) Strain Gage; (b) Torsional Load Application System (c) Strain Gauges Used during Modal Tests; (d) Schematic of the Torsional Strain Gauges; and (e) Shear Strain Gage Used.

The device shown in Figure 3.16 was used to determine the frequency of oscillation of the objects placed on the platform. By using two equations given below to calculate mass moment of inertia and by subtracting the mass moment of inertia of the platform from the mass moment of inertia of the combined object (propeller) and platform, the mass moment of inertia of the propeller was determined (Laboratory Handout 2007).

$$J_{cm} = (mgr^2) / (L\omega_{nd}^2) \tag{3.1}$$

$$J_{disk} = (0.5)\, mr^2 \tag{3.2}$$

where J_{cm} is the mass moment of inertia for platform and object, J_{disk} is the theoretical value of mass moment of inertia of the platform disk, ω_{nd} is the torsional frequency of motion of the above device, for platform, and L is the length of the rope.

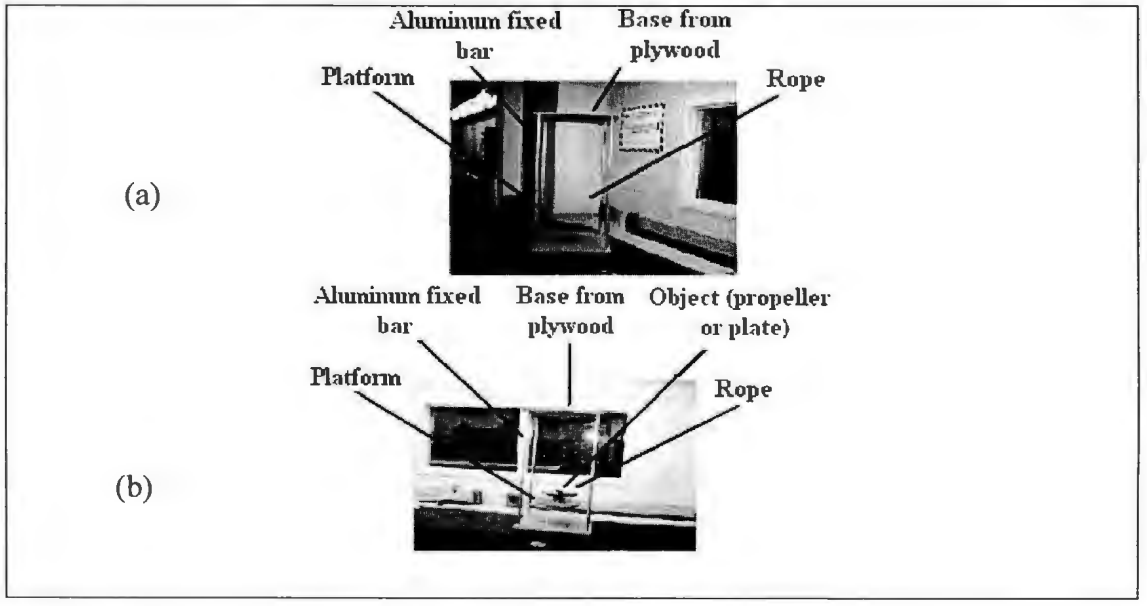

Figure 3.16 Photo of the Platform Suspension Setup; (a) Platform; and (b) Platform with Propeller

Now, the torsional natural frequency ω_n of the cylindrical shaft (with the propeller and the torsion impact device) was calculated by using the formula:

$$\omega_n = (K_s/J_T)^{0.5} \tag{3.3}$$

$$K_s = I_p G/L_s \tag{3.4}$$

$$I_p = \pi d^4/32 \tag{3.5}$$

$$G = E / (2(1+\upsilon)) \tag{3.6}$$

$$J_{shaft} = (0.5)\, Mr^2 \tag{3.7}$$

$$J_T = J_{shaft} + J_{propeller} + J_{plate} \tag{3.8}$$

where K_s was the torsional stiffness of the shaft, J_T total polar mass moment of inertia for shaft, propeller and plate, I_p the polar area moment of inertia of the shaft, L_s the length of shaft, G the shear modulus of the shaft, E modulus of elasticity, υ the Poisson ratio of shaft material, J_{shaft} polar mass moment of inertia for shaft, M mass of shaft, r the shaft radius, $J_{propeller}$ polar mass moment of inertia for propeller, and J_{plate} polar mass moment of inertia for the plate used for torsional impact.

3.5 Experimental Results

In this part, modal parameters such as natural frequencies, modal damping, and mode shapes for lateral vibration were extracted for the cracked and un-cracked rotor shafts. These results are presented in the following subsection.

3.5.1 Measured Natural Frequencies and Mode Shapes for Lateral Vibration

As mentioned above LMS Test Lab™ was used to measure the lateral vibration (vertical and horizontal) and to extract the mode shapes, in the experimental studies. Each part of the experiment was repeated three times (along with the five averages needed by the software) and the only the average results are reported in this work. The rest of the results obtained are reviewed in detail in Appendix A. Tables 3.2 (a), (b) and (c) summarize the results obtained for the first four transverse frequencies measured (for the three shafts) from the experiments on un-cracked and cracked rotor shafts. These experimental were done for the three different rotor shaft-bearing systems, viz., designated as shaft # 1, shaft # 2 and shaft # 3. The three shafts were of almost of the same diameter (measured average values were 0.01588 m, 0.01586 m, 0.01589 m respectively).

Figures 3.17 to 3.20 give the averaged experimental data of the four vertical and horizontal mode shapes, for various crack depth ratios for shaft # 2 (results for the other two shafts, viz., shaft # 1 and shaft # 3, are presented in appendix B). Since only vertical frequencies were of concern, we considered only Figures 3.17(a), 3.18(a) and 3.19(a). It is seen from these three figures that the identifier of the mode shape change due to crack during its early stages of growth is shown better by the third mode shape than the other two mode shapes; hence the crack presence can be best detected by monitoring the third vertical bending mode of the rotor shaft. It should also be noticed that the changes in mode shapes shown in Figure 3.19 (a) (for the third mode) are higher than the frequency changes shown in Figure 3.17 (a). This can be appreciated if it can be noticed that this

case (third mode) is similar to the case of a fixed-simply supported case (or a cantilever case), where the crack occurs around the fixed edge (bearing 2).

Table 3-2 (a) Experimental Values of the Natural Frequencies for Various Crack Depth-Ratios, V - Vertical and H – Horizontal. (Shaft #1)

Frequency	Crack depth ratios							
	0.0%		10%		20%		30%	
	V	H	V	H	V	H	V	H
First	34.768	41.344	34.417	41.544	34.119	41.182	34.325	41.196
Second	76.78167	78.279	76.413	78.57567	76.05867	78.31	75.205	78.02033
Third	190.634	199.089	190.757	197.944	189.998	197.769	189.865	197.829
Fourth	365.8	335.241	364.3547	335.2313	362.3233	335.7223	365.426	336.0583
First natural frequency for torsion	43.716		43.213		42.826		42.628	
Frequency	Crack depth ratios							
	40%		50%		60%		70%	
	V	H	V	H	V	H	V	H
First	33.80933	41.09267	33.79633	40.815	32.64033	40.52267	30.60033	39.84867
Second	75.48633	77.35933	74.19133	76.54333	72.79567	76.23	67.299	74.95233
Third	189.449	197.708	188.0927	197.1897	186.1117	196.4363	178.986	195.956
Fourth	358.8217	335.4333	355.349	333.2633	345.0703	331.14	327.8163	321.8417
First natural frequency for torsion	42.292		41.864		41.723		41.497	

Table 3-2 (b) Experimental Values of the Natural Frequencies for Various Crack Depth-Ratios, V- Vertical and H – Horizontal (Shaft # 2).

Frequency	Crack depth ratios							
	0.0%		10%		20%		30%	
	V	H	V	H	V	H	V	H
First	36.395	42.980	36.315	42.959	36.262	42.904	36.212	42.91
Second	75.975	80.034	76.056	79.985	75.852	79.903	75.617	79.309
Third	196.119	199.544	195.849	199.462	195.667	199.503	195.398	199.424
Fourth	367.423	369.148	366.861	368.992	366.391	368.896	365.457	368.605
Frequency	Crack depth ratios							
	40%		50%		60%		70%	
	V	H	V	H	V	H	V	H
First	36.02723	42.77933	35.791	42.70067	35.21133	42.23533	33.98633	41.728
Second	74.99833	79.09533	74.20733	79.09067	72.38067	79.03467	69.24733	77.91233
Third	194.5687	199.3333	193.421	199.0703	190.7537	198.4617	185.5763	197.3003
Fourth	362.876	367.6683	359.1237	366.059	349.9673	362.3057	333.337	354.9043

Table 3-2 (c) Experimental Values of the Natural Frequencies for Various Crack Depth-Ratios, V - Vertical and H – Horizontal (Shaft # 3).

Frequency	Crack depth ratios							
	0.0%		10%		20%		30%	
	V	H	V	H	V	H	V	H
First	33.855	40.629	33.774	40.656	33.751	40.615	33.736	40.550
Second	74.614	79.914	74.593	79.809	74.487	79.844	74.215	79.826
Third	192.190	197.813	191.962	197.817	191.742	197.771	191.298	197.652
Fourth	352.959	355.931	353.392	355.628	352.642	355.315	349.39	353.132
Frequency	Crack depth ratios							
	40%		50%		60%		70%	
	V	H	V	H	V	H	V	H
First	33.54967	40.47867	33.335	40.339	32.80367	40.03433	31.67467	39.535
Second	73.44333	79.603	72.554	79.372	70.73833	78.92633	67.54433	77.9527
Third	190.0337	197.4143	188.644	197.0687	185.412	196.3743	180.0857	195.0663
Fourth	344.4017	350.252	339.052	347.5507	328.8137	343.1973	315.164	336.204

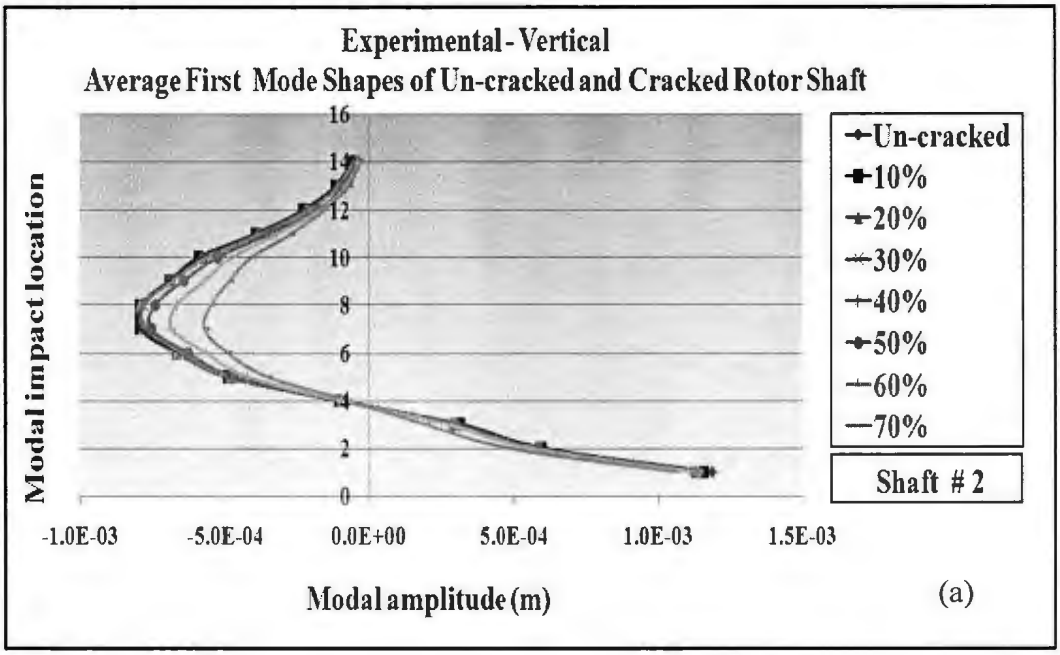

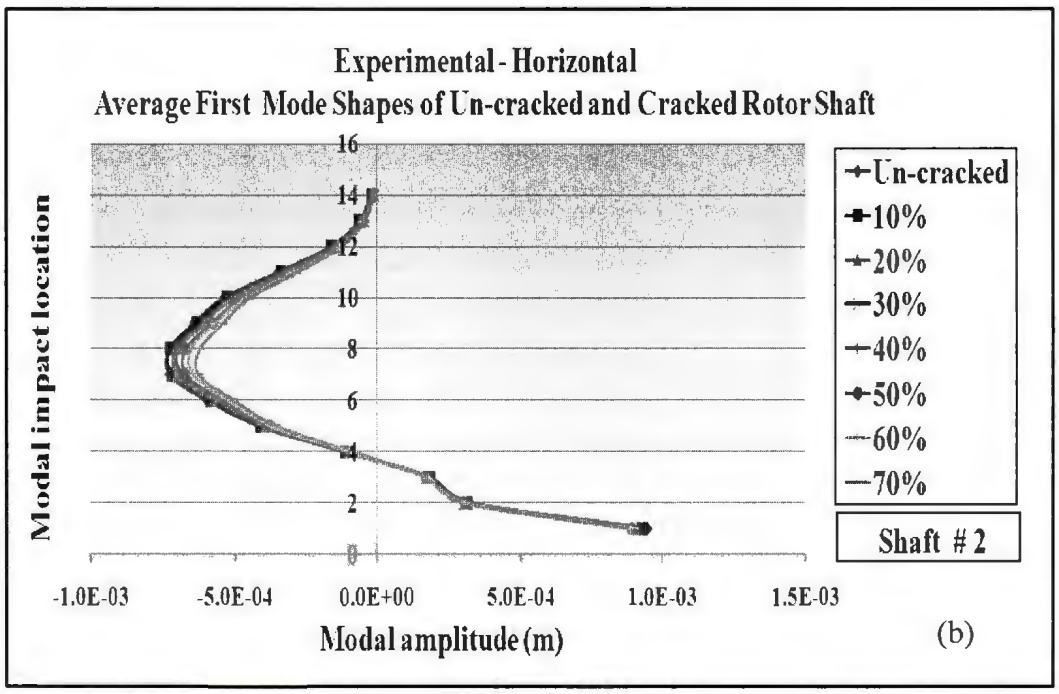

Figure 3.17 First Mode Shapes of Un-Cracked and Cracked Rotor Shaft from Experimental Work (a) Vertical (b) Horizontal

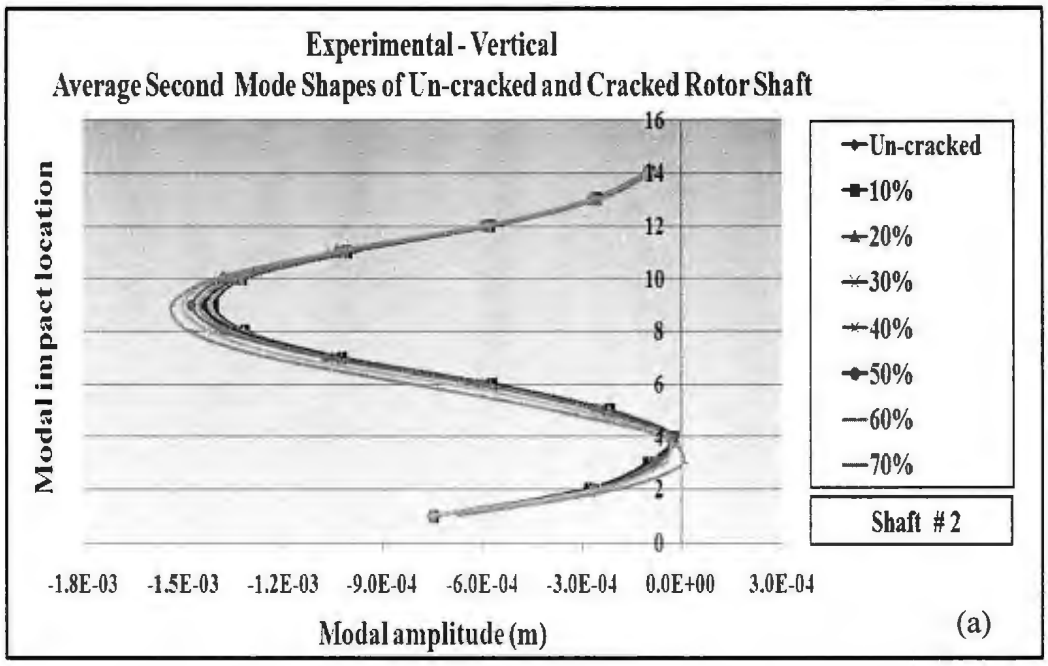

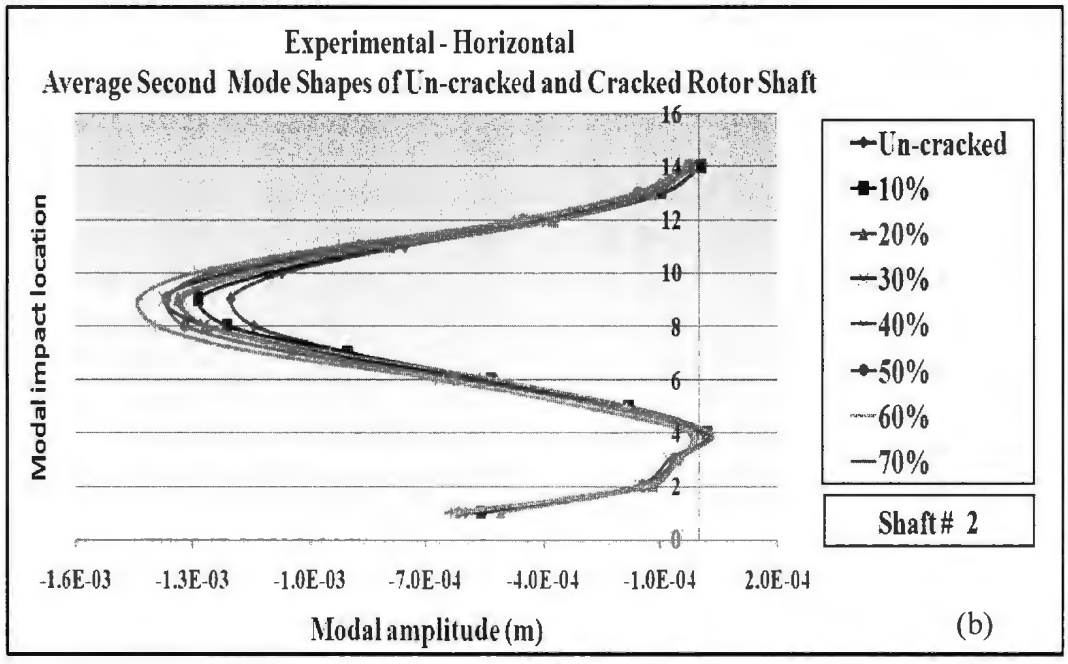

Figure 3.18 Second Mode Shapes of Un-Cracked and Cracked Rotor Shaft from Experimental Work (a) Vertical (b) Horizontal.

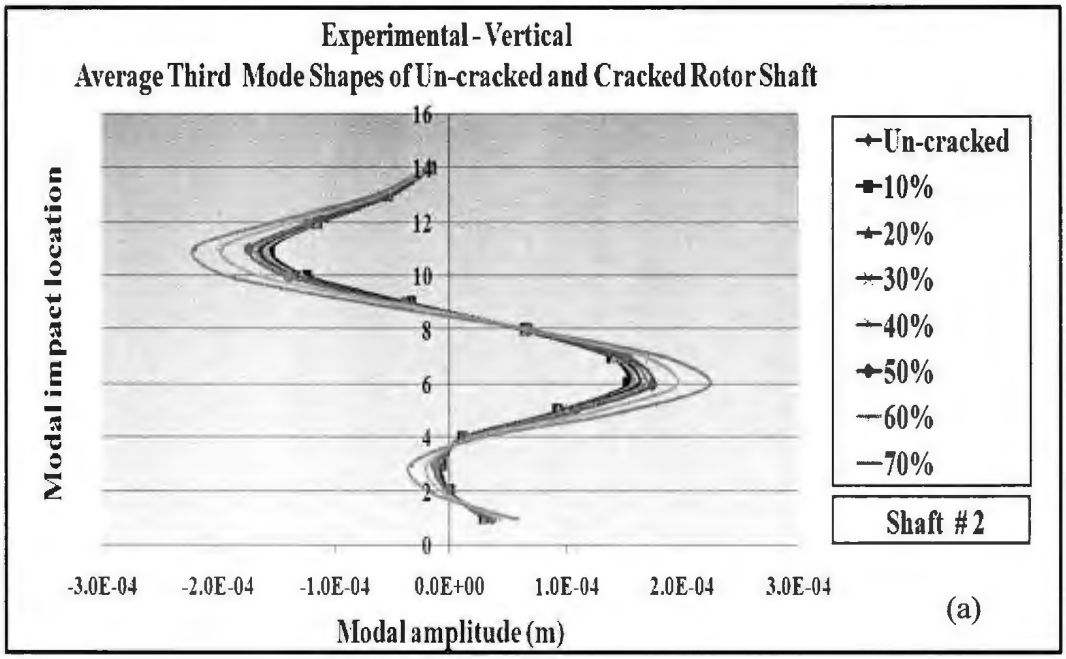

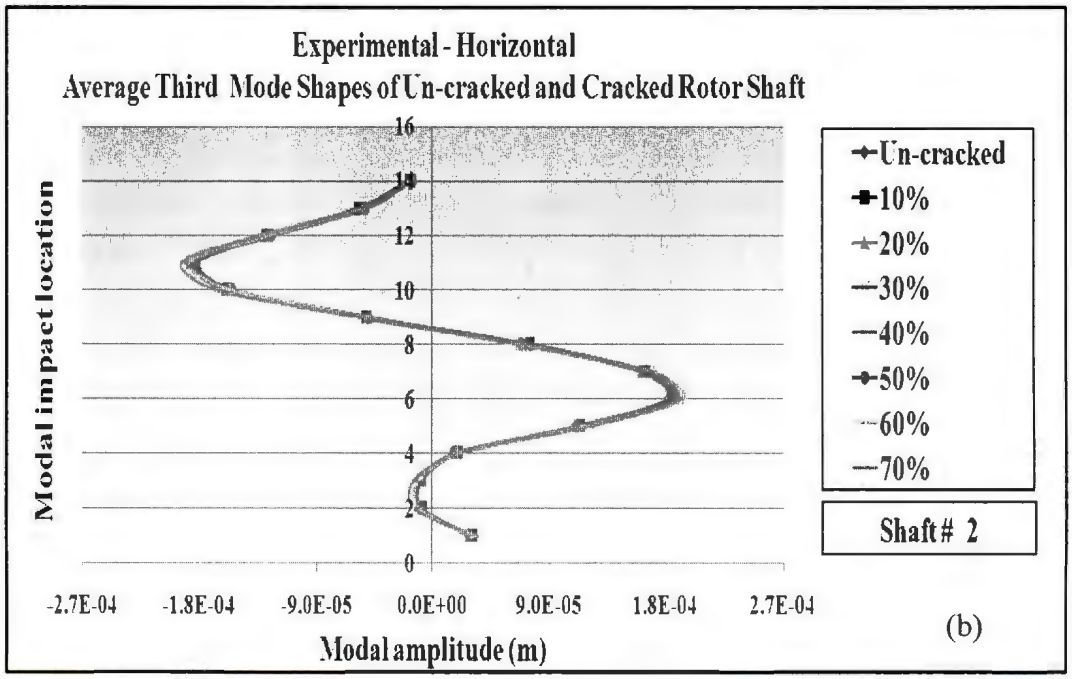

Figure 3.19 Third Mode Shapes of Un-Cracked and Cracked Rotor Shaft from Experimental Work (a) Vertical (b) Horizontal.

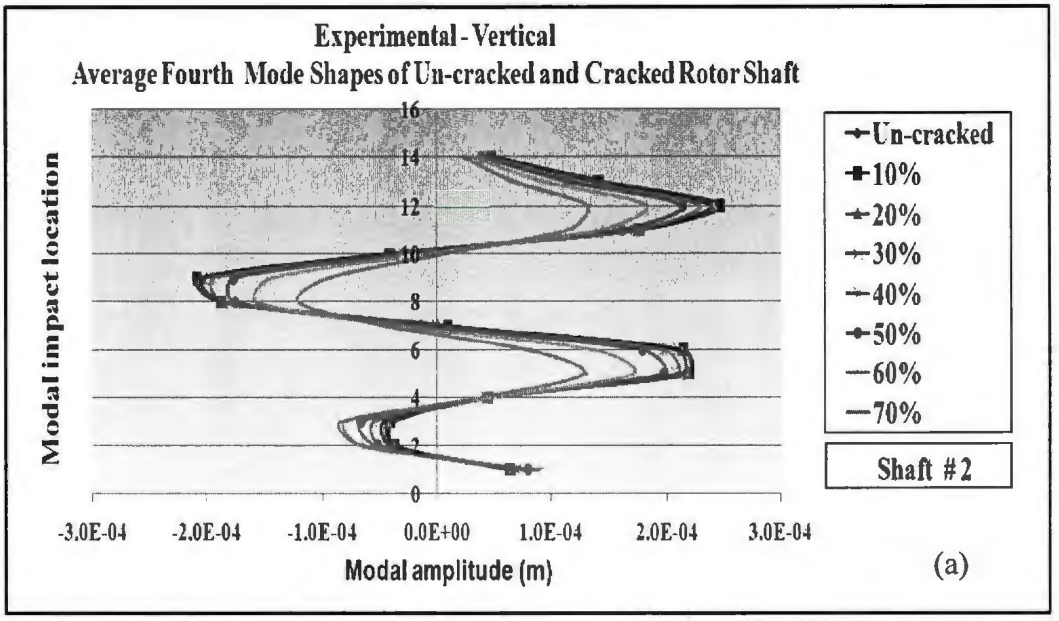

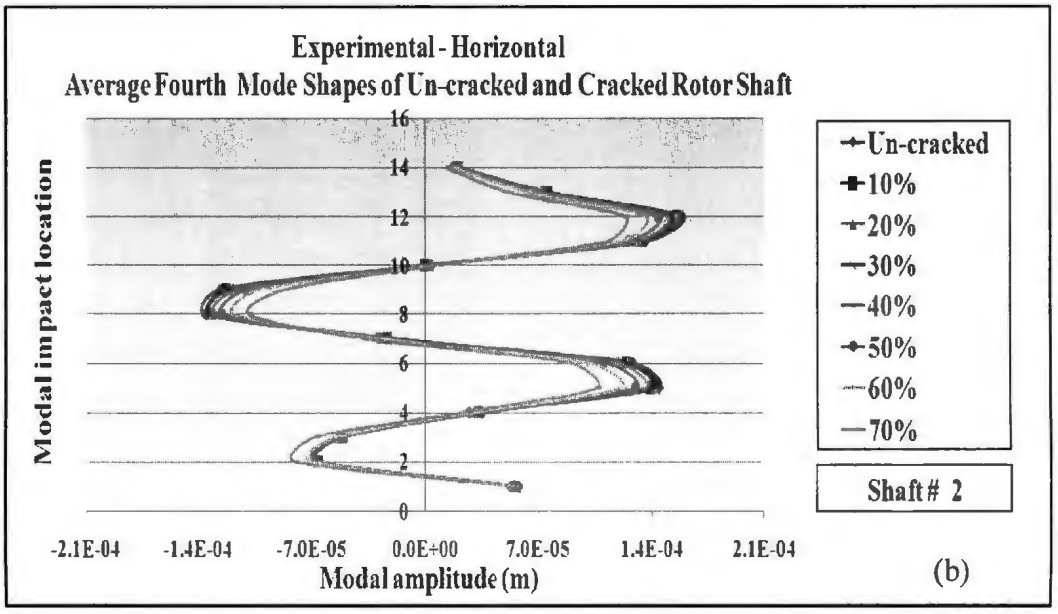

Figure 3.20 Fourth Mode Shapes of Un-Cracked and Cracked Rotor Shaft from Experimental Work (a) Vertical (b) Horizontal.

3.5.2 Rate of Change of Bending Frequencies with Respect to Crack Depth Ratio

Figure 3.21 shows the changes that occur in the experimental frequencies as the crack depth ratios change from 0 to 70% (with second order curve fit). In addition, Figure 3.22 shows the rate of change of frequencies as a function of crack depth ratios. In Figure 3.21, the changes that occur in frequencies are less than 2% till the crack depth ratio becomes larger than 50%. In contrast, when the rate of change of frequencies of a function of crack depth ratio is considered the presence of crack can be seen even from the crack depth ratio of 20%. This is similar to an earlier observation made by Hamidi et al. (1992) that the crack presence was observable from a crack depth ratio of 0.3, when the rate of change frequencies were considered. Hence the rate of change in bending frequencies for shaft # 2 (shown in Figure 3.22) becomes a better indicator of crack presence. When the rates of frequency change (with respect to crack depth ratio) are plotted as a function of crack depth ratio it is observed that between 20% and 30% crack depth ratio, the variation in rate of change of frequency is found to be 3% to 4%. Instead if frequency changes were used as the crack indicator, the changes between 20% and 30% crack depth ratio is around 0.5% to 1.0%; this is much less than that shown by the rate of change of frequency (with respect to crack depth). The results of the other shafts, viz., shaft # 1 and shaft # 3, are presented in appendix C.

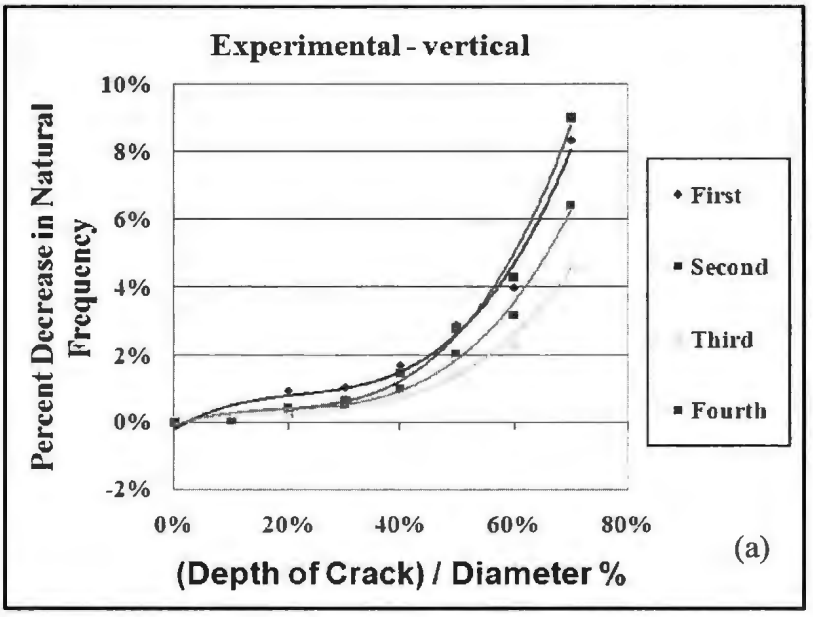

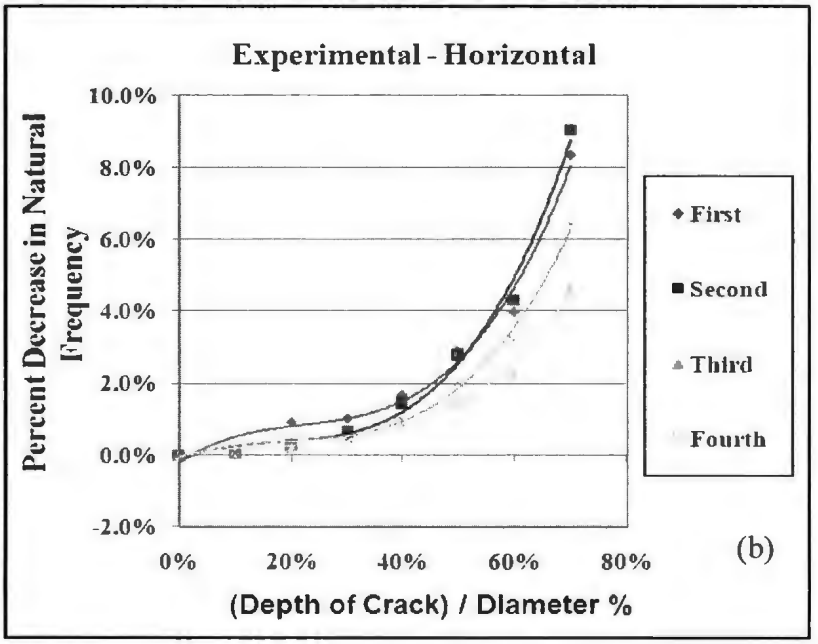

Figure 3.21 Depth of Crack vs. Percent Decrease in Natural Frequencies for Experimental Results: (a) Vertical (b) Horizontal.

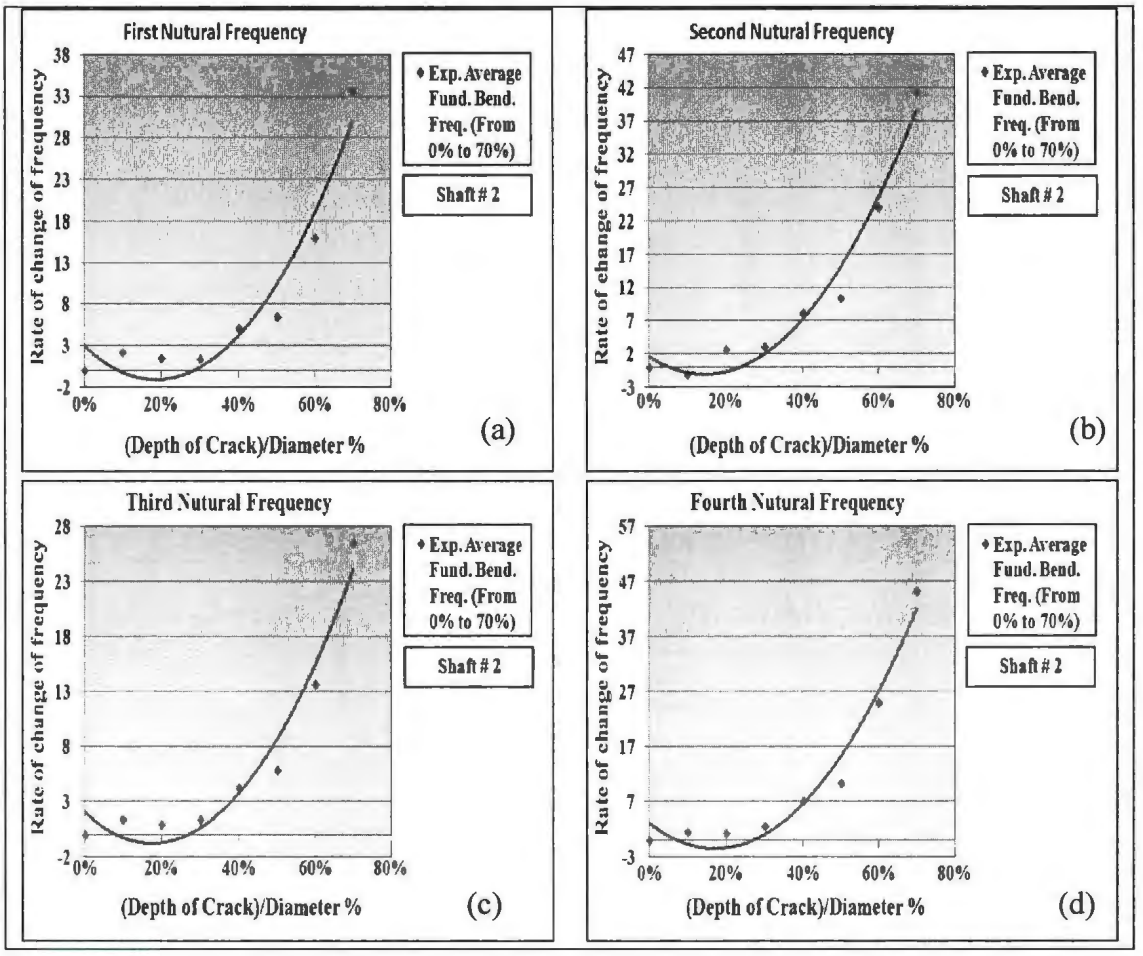

Figure 3.22 Rate of Change of Frequency (with Respect to Crack Depth Ratio) vs. Crack Depth Ratio of the First Four Frequencies; (a) Mode One; (b) Mode Two; (c) Mode Three; (d) Mode Four

3.5.3 Measured Natural Frequencies for Torsional Vibration

Figure 3.23 (a) shows the plot of the depth of crack and percent change (decrease) in torsional natural frequencies for experimental measurements. Figure 3.23 (a) shows that the changes in the first torsional frequency give a much better indication of the crack presence even during the starting of the crack. This is better shown through Figure 3.23 (b) which plots the rate of change of torsional frequency (with respect to crack depth ratio) vs. the crack depth ratio. It is seen that the rate of change in the first torsional

frequency (with respect to crack depth ratio) vs. crack depth ratio is much higher (at a crack depth ratio of 10%, the rate of change of frequency with respect to crack depth ratio is nearly 10.0%) whereas the rate of change of bending frequencies during the earlier stage of crack initiation and growth was much less (at a crack depth ratio of 10%, the rate of change of frequency with respect to crack depth ratio was only 1.0%); refer Figures 3.22 and 3.23 (b). This could be easily understood since the influence of cracking on torsional inertia (due to its larger influence along the skin surface of the cylindrical shaft than its depth) will be much higher than the bending inertia and the consequent changes in the rate of frequency change. Hence the rate of change of torsional frequency could very well be used as a very good indicator of the presence of any small crack.

Considering the values of torsional natural frequency of experimental measurements for un-cracked shaft shown in Table 3.3 it can be seen that the error between analytical and experimental values is less than 1.57%, indicating that the experimental measurements seem to have been done very carefully.

Table 3-3 Theoretical and Experimental Values of the Mass Moment of Inertia and the Torsional Natural Frequencies

Mass moment of inertia for platform, kg.m2		Mass moment of inertia for platform with propeller, kg.m2	Mass moment of inertia for propeller, kg.m2	Total mass moment of inertia (propeller + plate* + shaft**), kg.m2	Torsional natural frequency for un-cracked shaft *wn* , Hz	
Theoretical (a)	Experimental (b)	Experimental (c)	Experimental (d) = (c) – (b)	Theoretical and experimental	Theoretical	Experimental
7.746x10-3	7.571x10-3	1.163x10-2	4.057x10-3	5.639x10-3	43.04	43.72

* J_{plate} = 1.5232x10^{-3} kg. m^2 (by experimental measurments); ** J_{shaft} = 1.5232x10^{-3} kg. m^2 (by theory).

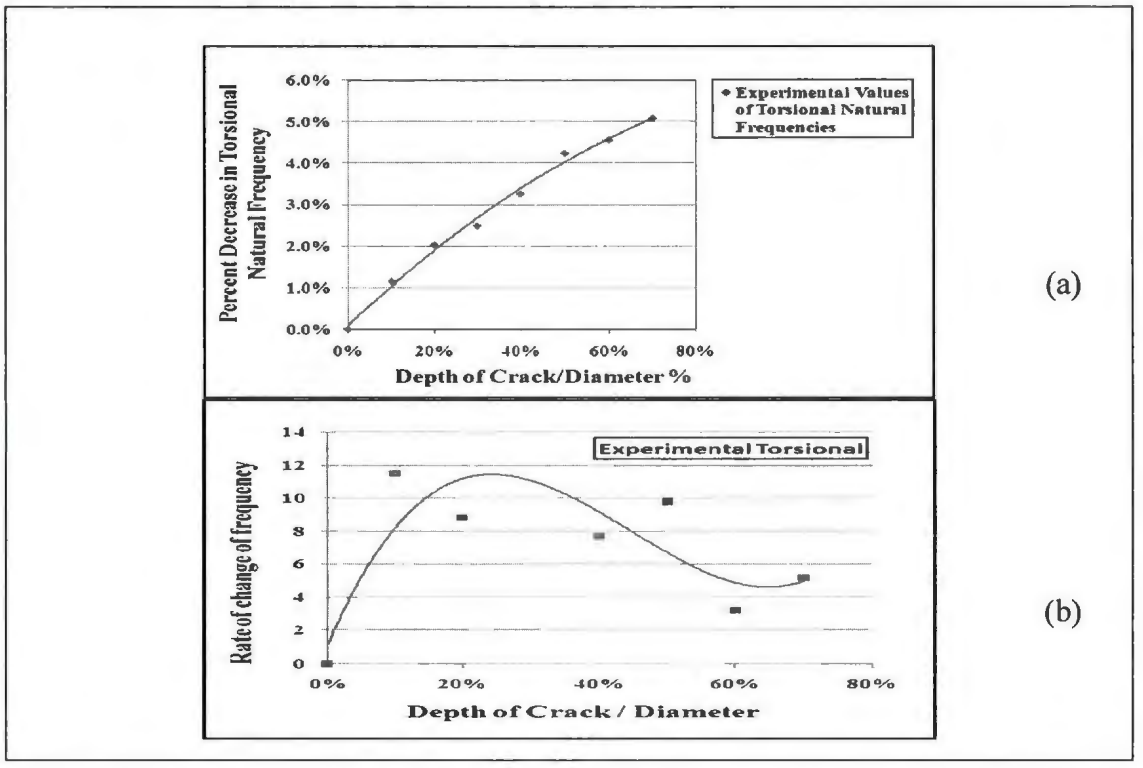

Figure 3.23 Depth of Crack and Percent Decrease in Torsional Natural Frequencies for Experimental Results; and (b) Rate of Change of the curve in part a vs. Crack Depth Ratio

3.6 Summary

The experimental fabrication and setup are described for the intact rotor shaft and the rotor shaft with different levels of crack severity (from 10% to 70%). The natural frequencies and mode shapes (lateral and torsional) were obtained by using the Engineering Innovation (LMS Test Lab ^{TM}) software package and three strain gages with five data acquisition channels (four were multi-plexed)

From the experimental results presented in this chapter, it is observed that the values of the natural frequencies for vertical and horizontal transverse vibrations were not the same for all the different pairs of (vertical and horizontal) modes for different shafts. This is

probably due to the inherent property variation and the different support and bearing stiffnesses provided. Also the third mode shape could be used as a good indicator of the presence of a crack in the shaft. This seems to give much higher variations in mode shapes than the frequency changes that occur due to the presence of the crack.

Analysis of experimental results shows that it is possible to detect the presence of a crack. These results showed that it was possible to detect a crack, around the crack depth ratio of 20% (or larger), when the rates of frequency change (as a function of crack depth ratio) were plotted as a function of crack depth ratio (between 20% and 30% crack depth ratios, the rate of change variation was found to be 3% to 4%). Instead if frequency changes were used as the crack indicator, then the changes were much smaller (between 20% and 30% crack depth ratios, the change in frequency ratio was around 0.5% to 1.0%) than that shown by the rate of change of frequency (with respect to crack depth).

For torsional vibration, monitoring the first torsional frequency [with regards to its rate of change (with respect to crack depth ratio)] gave a much better indication of the crack presence (at a 10% crack depth ratio, the rate of change of frequency was around 10%) than the monitoring of bending frequencies for its rate of change with respect to crack depth ratio (at a 10% crack depth ratio, the rate of change of bending frequency was around 1%).

These experimental results will be used later for the crack identification procedure presented in the subsequent chapters.

Chapter 4

Modeling of the Rotor Shaft System for Crack Detection Using Transverse Vibrations and Beam Elements

4.1 Introduction

It has been mentioned earlier in chapter two that various modelling efforts have been made to discretize rotor shafts using beam elements and three-dimensional elements (using Boolean operations) while carrying out dynamic analysis and testing for crack detection. In this chapter, numerical investigations were carried out to identify the transverse crack existence in a cylindrical shaft with a cantilever overhang, using beam elements and transverse vibration procedures. Effects of different crack depths were investigated numerically, and the results interpreted to give better comprehension of its vibratory behaviour. The shaft was fixed at one end to the test frame support and was continuous over the other frame support to end in a cantilevered end, carrying the propeller. The shaft was supported through ball bearings on the two supporting test frames, as shown in Figure 3.7. Initially the cylindrical rotor shaft, supported through roller bearings and test frame supports, had to be properly modeled for carrying out analysis using finite element procedures. The beam element, BEAM4 having six degrees of freedom, and available in ANSYS finite element program was used for: (i) Numerical prediction of the dynamic response of un-cracked and cracked shafts and (ii) Correlating the experimental results. In this study, a linear "three to six springs" model was used to represent the effects of each of the two ball bearings, supporting the shaft, over the (fixed) end and the other support near the cantilever end; these spring constants were

determined (using trial and error method) to achieve the best agreement between un-cracked experimental and numerical results. Since the BEAM4 elements did not include the stress intensity effects present in cracks, an equivalent crack effect, as described by Petroski (1981) and Rytter (1993) with the use of a short beam element, was used in the present study to include the stress intensity effects in cracks.

4.2 Theory and Modeling of the Bearing Support

One transverse open crack was considered to be present in the shaft in this study. The un-cracked shaft, shown in Figure 3.7, was modeled by replacing the bearing support effects by linear translational and rotational springs shown in Figure 4.1. The actual bearing support used in the experimental study is shown in Figure 3.8 (b) (see McMaster-Carr, 2011). In the ball bearing used during these experiments, the flange of the housing bearing was fixed to the steel support frame; the inner ball bearing was fixed to the cylindrical shaft by tightening two screws positioned at 90° to one another. The elasticity of these bearing connections of the test frame supports, and the cylindrical shaft, were replaced by orthogonal linear springs, located at the positions of the two orthogonal tight screws as shown in Figure 4.1. Hence the linear spring supports at right angles, used in this study, represent the elastic effects of these tight screws of the cylindrical shaft (along with the flange mount and inner bearing and support frame), on the vibration frequencies of the shaft. Figures 4.1 (a_1) to (e_1) show the five models used for modeling the ball bearing and test frame supports used in the study, viz., six, eight, ten and twelve springs, respectively.

From the results obtained (shown later in this chapter) it was observed that none of these five numerical models were fully sufficient to represent exactly the bearing support effects, but they did reasonably represent the effects of the bearing supports; as such they gave reasonably good results when compared with the measured experimental results. For each spring support location the restoring forces increased or decreased depending on the deformations at that location, which in turn depended on the elastic effects of the rotor shaft bearing and the test frame support at the same location. The best model that gave results very close to the experiment was identified in the subsequent computations given in a later section.

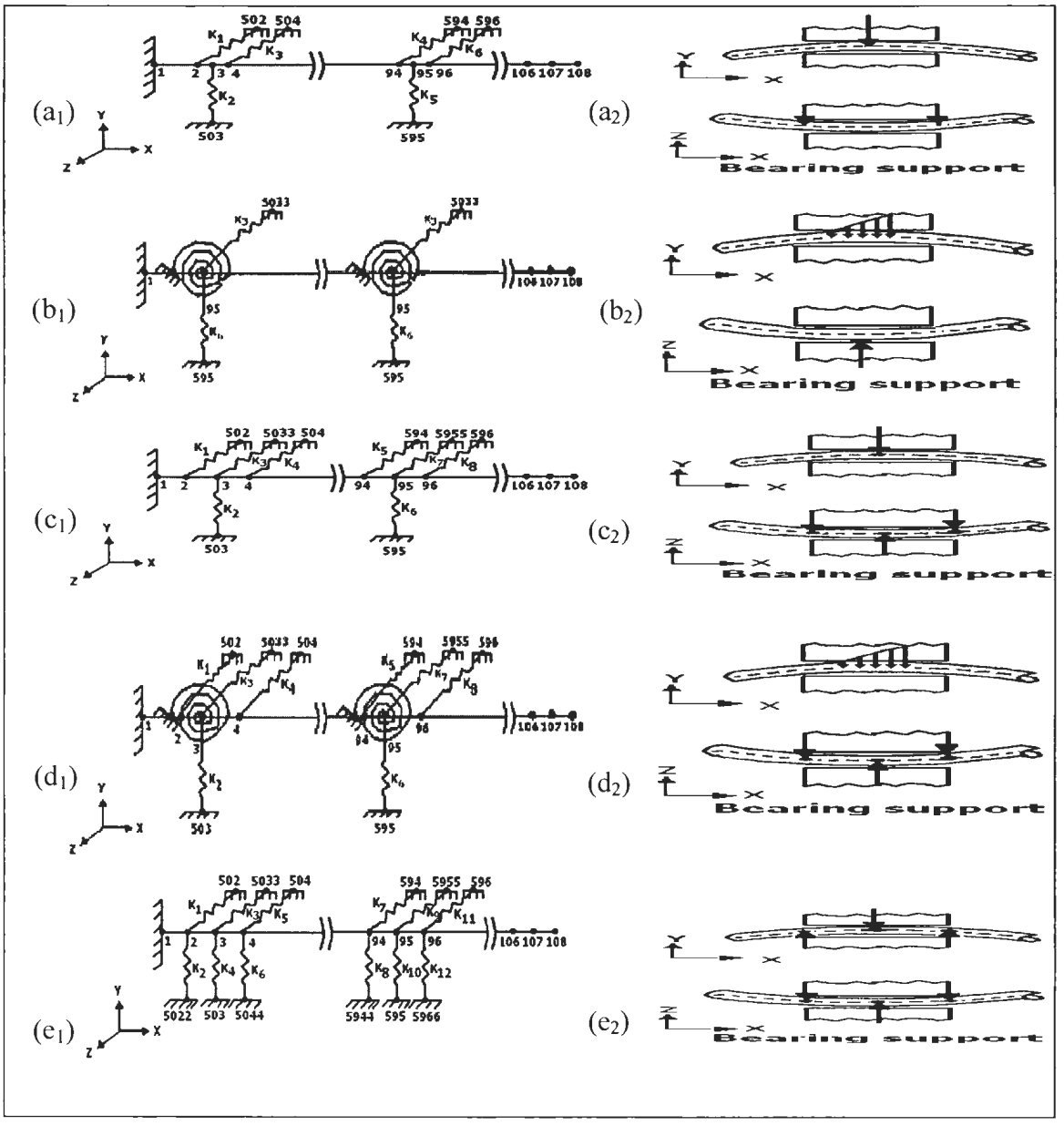

Figure 4.1 Finite Element Model for Cylindrical Shaft and Bearings: (a1) and (a2) Six Translational Springs Modeling; (b1) and (b2) Four Translational and Two Rotational Springs Modeling ;(c1) and (c2) Eight Translational Springs Modeling; (d1) and (d2) Eight Translational Springs and Two Rotational Springs Modelling; and (e1) and (e2) Twelve Translational Springs Modelling.

4.3 Description of the Numerical Model in ANSYS using Beam4 Element

In the present investigation, the general aim was to identify the dynamic system characteristics when the damage (crack) was present in the shaft. As mentioned above, the experimental investigations were carried out for a crack, only at one location, for three separate rotor shafts. In the numerical study, two finite element models were used; one was the un-cracked shaft and the other representing the cracked shaft with seven crack depths. The crack was located at the maximum bending moment position, viz., on the right of bearing support 2, as shown in Figure 4.2. Commercial ANSYS software (Appendix D.1 shows the ANSYS codes that were used in this chapter) was used to determine the dynamic characteristics so as to correlate with the experimental results. In the finite element model the shaft was continuous over two spans (having an overhanging span for propeller) with ball-bearing supports. A schematic sketch of the rotor shaft is shown in Figure 4.3. Its right end (carrying the propeller as a concentrated mass) was free, while the left one was clamped. The length and the diameter of the shaft were as given earlier, i.e., 1220 mm and 15.87 mm, respectively. The moment of inertia of the un-cracked cross section was $I = 3.217 \times 10^{-9}$ m^4 and the polar moment of inertia for each element was $J_p = 6.434 \times 10^{-9}$ m^4 The Young's modulus was $E = 2 \times 10^{11}$ N/m^2, Poisson's ratio was 0.3, shear modulus of elasticity was $G = 7.69 \times 10^{10}$ N/m^2 and the density was ρ = 7667 kg/m^3. Beam element (type 4) was used to model the shaft used for numerical analysis through ANSYS. This element is a uniaxial element with torsion, bending, shear tension, and compression capabilities. The element had six degrees of freedom at each node: axial, transverse and rotational motions are shown with numbering of its local

degrees of freedom as shown in Figure 4.4. While modeling the shaft it was assumed that all the elements had the same material properties and geometrical profile except at the cracked location, which had a different geometrical property due to the presence of crack at that location.

The moment of inertia about the y axis and z axis for a circular shaft with radius r and crack depth 'a' as shown in Figure 4.5 could be calculated (Das et al. 1994), as

$$I_{yy} = I_{yy}(\textit{fullcircle}) - I_{yy}(\textit{segment})$$

$$I_{yy} = \frac{\pi r^4}{4} - \frac{r^4}{12}(3\alpha - 2\sin^3\alpha\cos\alpha - 3\sin\alpha\cos\alpha) \qquad (4.1)$$

$$I_{zz} = I_{zz}(\textit{fullcircle}) - I_{zz}(\textit{segment})$$

$$I_{zz} = \frac{\pi r^4}{4} - \frac{r^4}{4}(\alpha + 2\sin^3\alpha\cos\alpha - \sin\alpha\cos\alpha) \qquad (4.2)$$

where α is the subtended half- angle, at the center, of the segment shown in Figure 4.5 (b).

In this modeling, it was assumed that neutral axis did not shift at the crack location, which was not proper; the crack was thus assumed to be symmetrical in this finite element assumption. Transverse vibration of the shaft occurred in the directions perpendicular to the length of the shaft. Generalized displacements (x_1, y_1 and z_1) and (x_2, y_2 and z_2) (see Figure 4.6) were longitudinal and transverse displacements of the shaft element at nodes 1 and 2, while the (θ_{x1}, θ_{y1} and θ_{z1}) and (θ_{x2}, θ_{y2} and θ_{z2}) were the corresponding rotations of the nodes 1 and 2. The length of the element was taken as *l*

and the general form of the mass and stiffness matrices were used in formulating the FE model for the un-cracked and cracked shafts (Chandrupatla and Belegundu 2002).

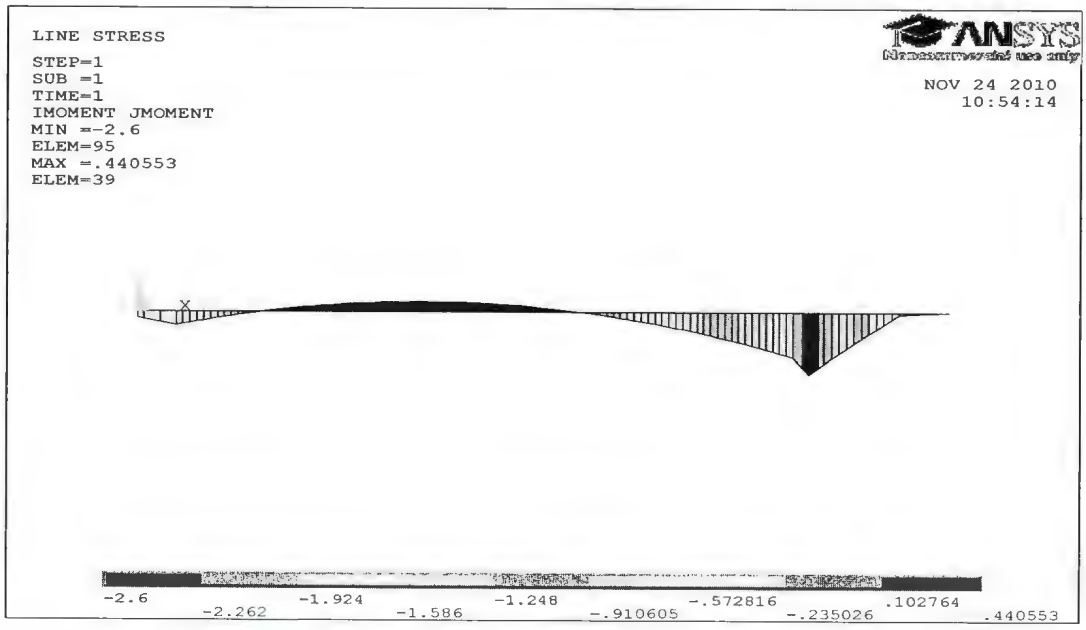

Figure 4.2 Bending Moment Diagram along the Rotor Shaft

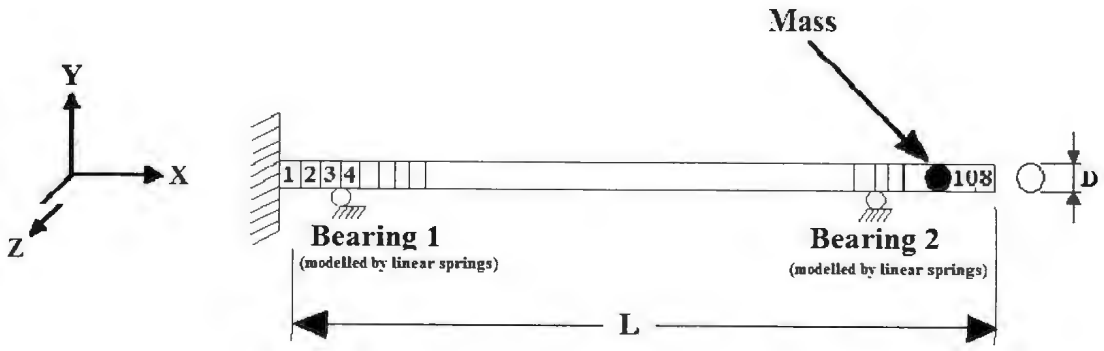

Figure 4.3 A Rotor Shaft Modeled and Discretized Using Beam Elements

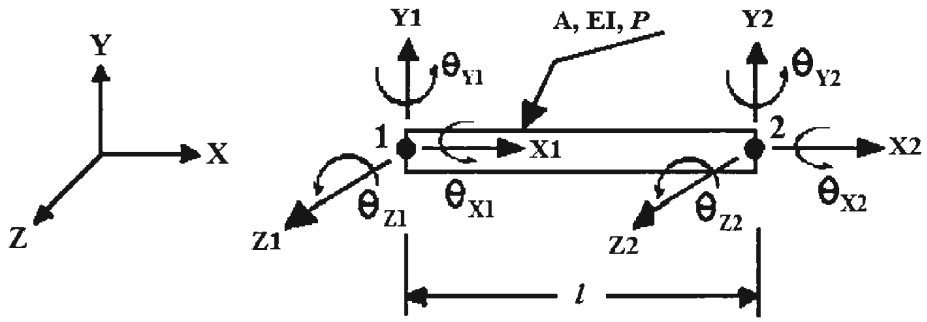

Figure 4.4 Degrees of Freedom Numbering for a Three-Dimensional Shaft Element

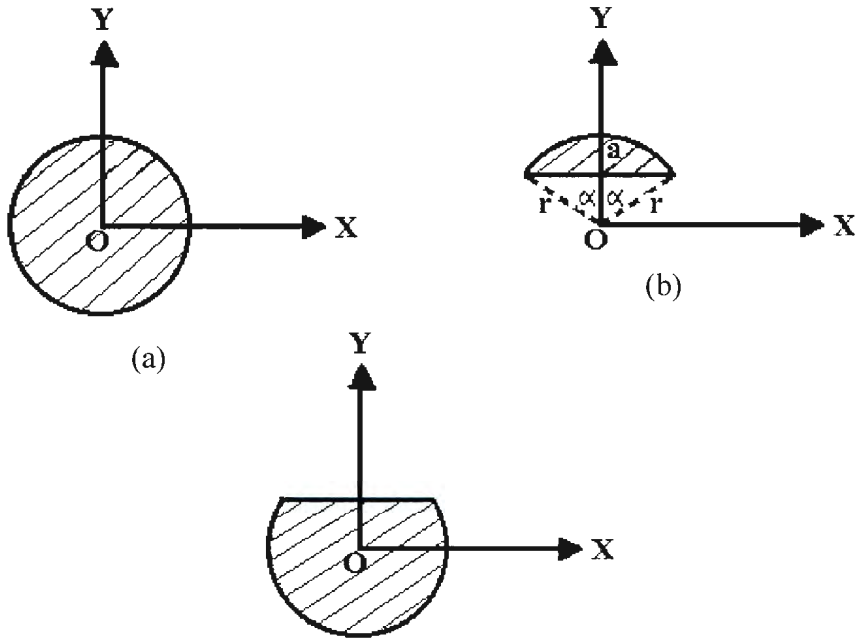

Figure 4.5 Sketch of the Moment of Inertia of: (a) Circle; (b) Circular Segment; and (c) Semi-Circle

4.4 Results from ANSYS - Beam4 and Discussions

In this part of the study the findings from results obtained experimentally and numerically are presented and discussed. For experimental and numerical studies, one crack position and various crack ratios (from 0% to 70% ratio) were examined. From a detailed comparison of numerical results, obtained for six, eight, ten and twelve springs modeling, with the experimental results for the uncracked rotor shaft, it was found that the six springs [shown in Figure 4.2 (b), with some area of contact near the screw contact of the inner bearing with the cylindrical shaft] model gave the smallest difference between the numerical and experimental frequency results (for six, eight and ten springs modeling the results are presented in Appendix D.2). Hence the model with six springs [Figure 4.1 (b)] was used as the proper model for subsequent studies; it was also observed from the ANSYS numerical results (using BEAM4 shaft elements) that the output did not contain any first mode torsional frequency component; it did contain a higher mode torsional frequency at 652.0 Hz (which could not be the correct lowest frequency value). The reason for this absence is that the support springs used did not permit the free torsional motion at the test frame supports 1 and 2 required for comparing torsional frequencies.). Table 4.1 shows the comparison of the first eight natural frequencies (four vertical and four horizontal) between the experimental and numerical values (uncracked and cracked), for the case of six springs [see Figure 4.1 (b)]. In this part of the study only one element, having a width of 0.65mm (equal to the width of the saw-cut crack), was used to represent the crack; and all the other elements, around the crack region were also similar to (but wider than) this element. It can be seen from Table 4.1 that the

experimental values showed comparatively larger changes for the crack present in the shaft; whereas the numerical analysis results showed almost no changes, as the crack depth increased from 0 to 70%. The numerical analysis seems to be insensitive to the presence of the crack. This was due to the fact that the flexibility introduced in the experimental model by the presence of a crack seems to be much higher than that provided by the single finite element used to represent the crack effect in the numerical model, as shown in Figure 4.6 (a). To improve the numerical results, the model shown in Figure 4.6 (b) was used to represent the crack effect. It was observed that even though a large number of smaller elements have been used to represent a single wider crack it was found to give the same accuracy as the finite element model with a number of variable length elements. Table 4.1 shows the comparison of the first eight natural frequencies between the experimental and numerical results (with six springs) with the simulated correction with a larger number of small beam elements to represent crack. It shows from this comparison that the results of corrected numerical analysis are much closer to the experimental results.

Taking into consideration the representation of the crack by a modeled short beam element [having the same depth as the un-cracked portion of shaft, at the cracked section, but with a larger element width - see Figure 4.6 (b)] in the studies of Petroski (1985) and Rytter (1993) and the crack influence zone cited by Yang et al. (2001), more studies were carried out by considering additional elements around the crack location to have the same moment of inertia of the shaft as that of the cracked section (to represent the longer short beam element).The results of these studies are shown later in Figure 4.7.

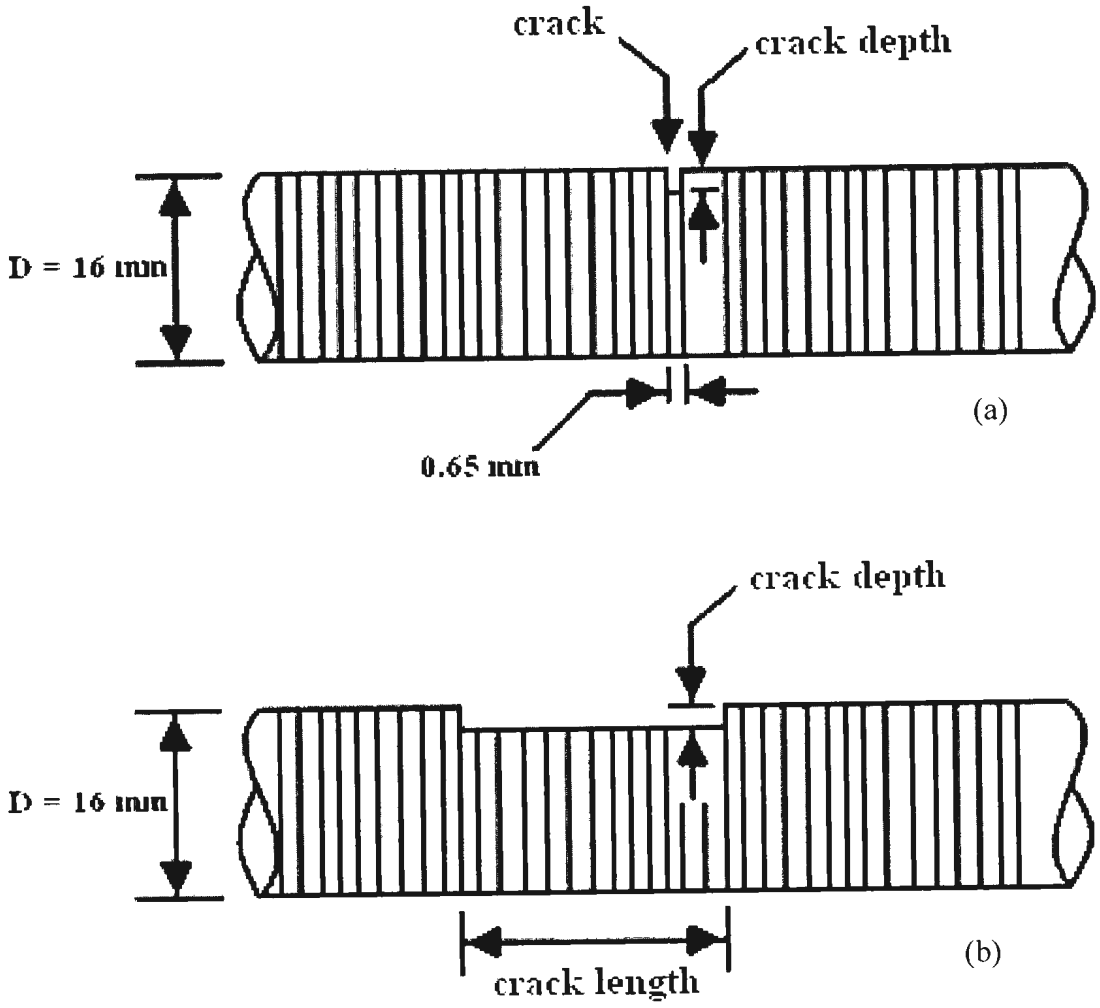

Figure 4.6 Schematic Diagram of; (a) One Element Representing Crack Effect; and (b) A Wider Element Representing the Crack Effect

Table 4-1 Experimental and Numerical Values of the Natural Frequencies for Various Crack Depth-Ratios (Uncorrected Numerical Values Shown within Brackets and Corrected Numerical Results are Shown with the Asterisk); V-Vertical and H-Horizontal.

Frequency	Crack depth ratios							
	0.0%		10%		20%		30%	
	V	H	V	H	V	H	V	H
First	34.134 (34.338) 34.338*	43.633 (43.858) 43.858*	34.125 (34.337) 34.262*	43.515 (43.855) 43.550*	33.816 (34.337) 34.286*	43.363 (43.849) 43.046*	33.778 (34.336) 34.176*	43.343 (43.844) 42.570*
Second	76.703 (78.269) 78.269*	78.792 (80.436) 80.436*	76.657 (78.265) 77.889*	78.806 (80.425) 79.481*	76.483 (78.266) 77.953*	78.424 (80.408) 78.054*	76.195 (78.260) 76.835*	78.382 (80.392) 77.398*
Third	191.652 (190.42) 190.42*	199.499 (196.13) 196.13*	191.491 (190.42) 189.99*	199.204 (196.12) 195.04*	191.256 (190.42) 190.05*	199.069 (196.10) 193.47*	190.859 (190.41) 189.42*	199.006 (196.08) 192.17*
Fourth	367.563 (366.26) 366.26*	383.139 (382.40) 382.40*	367.282 (366.26) 365.94*	379.423 (382.39) 380.85*	365.883 (366.26) 366.03*	379.213 (382.36) 378.62*	365.752 (366.26) 365.55*	379.109 (382.33) 376.84*
Frequency	Crack depth ratios							
	40%		50%		60%		70%	
	V	H	V	H	V	H	V	H
First	33.556 (34.334) 33.964*	43.185 (43.841) 42.964*	33.145 (34.329) 33.563*	42.947 (43.841) 42.300*	32.774 (34.320) 32.762*	42.862 (43.841) 42.274*	31.286 (34.300) 30.964*	42.069 (43.837) 41.962*
Second	75.572 (78.248) 76.240*	78.298 (80.384) 76.412*	74.553 (78.228) 74.743*	78.214 (80.382) 76.151*	73.401 (78.186) 71.921*	77.644 (80.381) 76.059*	69.774 (78.088) 67.206*	75.896 (80.370) 75.361*
Third	190.076 (190.40) 188.34*	198.671 (196.07) 191.55*	188.763 (190.38) 186.58*	198.299 (196.07) 191.46*	187.240 (190.33) 183.81*	197.993 (196.06) 191.37*	182.790 (190.22) 179.66*	194.457 (196.05) 190.66*
Fourth	363.809 (366.25) 364.68*	378.435 (382.32) 376.03*	359.989 (366.23) 363.21*	377.565 (382.32) 375.98*	355.839 (366.19) 360.84*	376.664 (382.32) 375.92	343.971 (366.10) 357.25*	373.689 (382.30) 375.03*

These numerical results plotted in Figure 4.7 were correlated by comparing them with the experimental results. The first three natural frequencies were calculated for several values of the crack depth ratios [0, 0.1, 0.2, 0.3, 0.4, 0.5, 0.6, and 0.7] and for the presence of crack represented by different (twenty-nine) short shaft element lengths [0.65 (case I0), 6.65 (case I3), 12.65 (I5), 18.65 (I7), 24.65 (I9), 30.65 (I11), 36.65 (I13), 42.65 (I15), 54.65 (I19), 60.65 (I21), 66.65 (I23), 72.65 (I25), and 84.65 (case I29)] mm. Figures 4.7 (a), (b), and (c) show the numerical and experimental results for the first, second and

third natural (non-dimensional) frequencies vs. crack depth ratios, respectively. Clearly, it can be seen from these figures that the first natural frequency needed a larger equivalent length shaft element to give a good agreement between numerical and experimental values. It can be seen from Figure 4.7 (a), that the curve (given by Num. V.I_{19}) determined from numerical calculations seems to be better coincident with the curve from the experimental test results (given by experimental values). For the second and third frequencies shown in Figures 4.7 (b) and (c), the curves (represented respectively by Num. V.I_{11} and Num. V.I_{9}) seem to be better coincident with the curves from the experimental values (represented by Exp. values). Therefore while the first frequency needs a longer equivalent shaft element, the second and third natural frequencies need shorter equivalent shaft element lengths to give good agreement with experimental results. The above modeling of the cracked shaft (by an equivalent short shaft) gives the best fit with the experimental results as follows: (i) For the first natural frequency, the equivalent cracked shaft length is around 54.65 mm; and (ii) For the second and third natural frequencies, the values are around 30.65 and 24.65 mm, respectively.

The differences between numerical and experimental frequencies for various crack depth ratios, before and after the correction with a short shaft element for the cracked section has been made, are also given in Table 4.1. For the first natural frequencies the numerical values used are obtained with a short shaft element length given by Num. V.I_{19}, for the second natural frequencies the numerical values used are for those given by the short shaft element Num. V.I_{11}, and for the third natural frequencies the numerical values used

are for those given by the short shaft element Num. V. I_9. It is clear from this table that the modeling of a cracked location by an equivalent short shaft element has considerably reduced the percentage differences, between the numerical and experimental values, and keeps the numerical values close to experimental values.

Figures 4.8 (a), (b), (c) and (d) show the comparison of changes that occurred in the experimental (shaft # 2) and numerical (using Beam4) frequencies as the crack depth ratios changed from 0 to 70% (with second order curve fit). As observed earlier by Hamidi et .al. (1992), the rate of change in bending natural frequencies (shown in Figure 4.8) become noticeable for all cases when the crack depth ratio becomes greater than 20% and in some cases Figures 4.8 (a) and (b) when the crack depth ratio becomes greater than 10%, indicating that the rates of change in natural frequencies (with respect to crack depth ratio) seem to be a better indicator of crack presence.

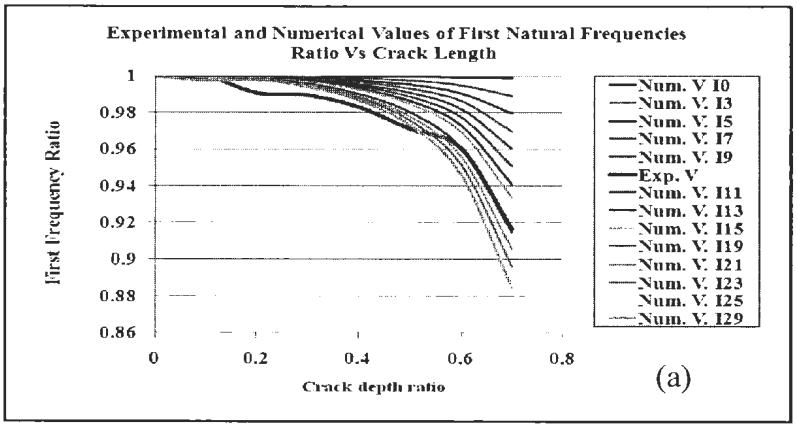

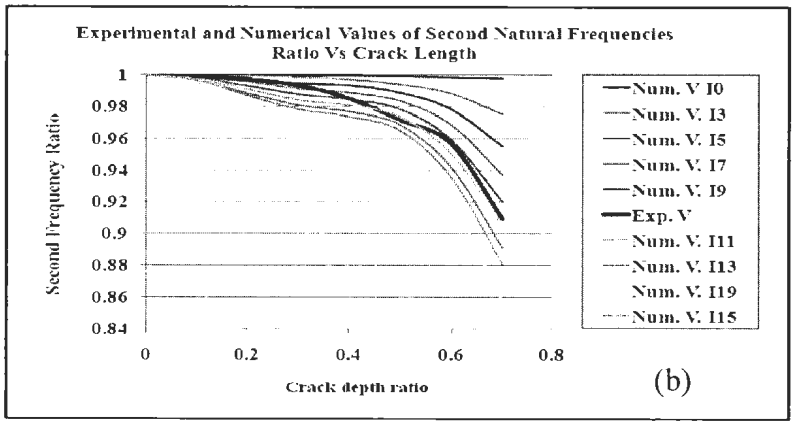

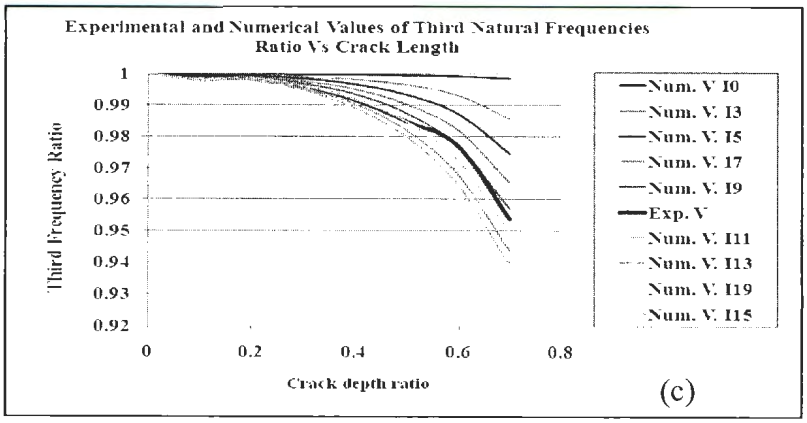

Figure 4.7 Experimental and Numerical Values of Non-Dimensionalized Vertical Natural Frequencies vs Crack Depth Ratios (a) First Natural Frequency (b) Second Natural Frequency; and (c) Third Natural Frequency

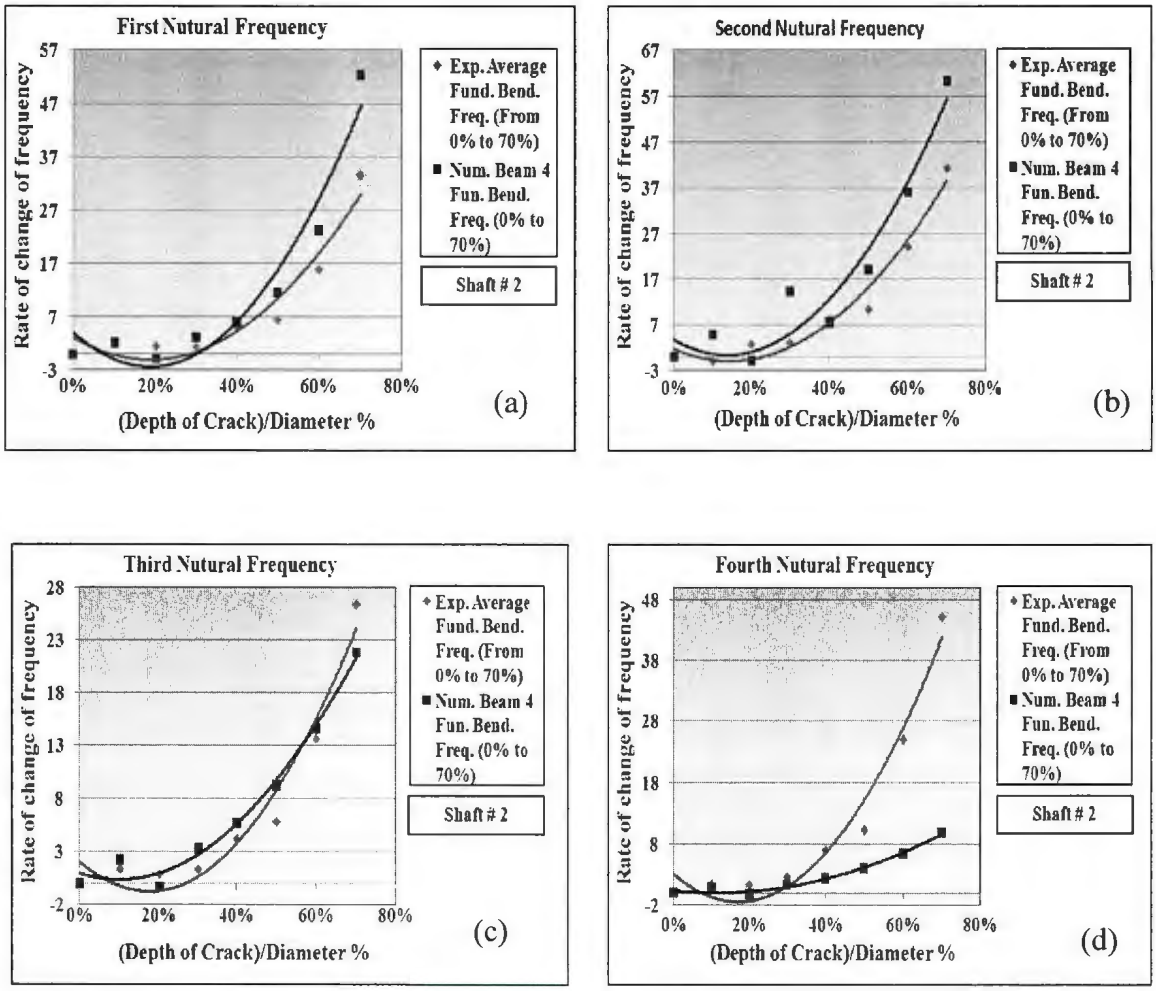

Figure 4.8 Rate of Change of Frequency (with Respect to Crack Depth Ratio) vs. Crack Depth Ratio of the First Four Frequencies; (a) Mode One; (b) Mode Two; (c) Mode Three; (d) Mode Four

Table 4.2 gives the percentage differences between the experimental and the corrected frequencies shown in Table 4.1. It is seen from Table 4.2, that the six springs' model [shown in Figure 4.1 (b)] does not seem to be a very good model for the second vertical bending frequency, since the differences are much larger than the first and third

frequencies. Considering the bending of the first three modes the bending curve shapes are similar for vertical bending modes I and III near the position of crack, where the support spring model of Figure 4.1 b_2 seems to work very well. For the III vertical bending mode, the support spring modal of Figure 4.1 a_2 may give better results.

Table 4-2 Differences between Numerically and Experimentally Obtained Frequencies, for Various Crack Depth-Ratios for the Equivalent Shaft Length Modeling (Values within Brackets before Correction).

Frequency	Crack depth ratios							
	0.0%	10%	20%	30%	40%	50%	60%	70%
	V	V	V	V	V	V	V	V
First	0.59% (0.59%)	0.40% (0.62%)	1.39% (1.54%)	1.18% (1.65%)	1.22% (2.32%)	1.26% (3.57%)	0.04% (4.72%)	1.03% (8.79%)
Second	2.00% (2.00%)	1.61% (2.09%)	1.92% (2.33%)	0.84% (2.71%)	0.88% (3.42%)	0.25% (4.93%)	2.02% (6.52%)	3.68% (11.92%)
Third	0.64% (0.64%)	0.78% (0.56%)	0.63% (0.44%)	0.75% (0.24%)	0.91% (0.17%)	1.16% (0.86%)	1.83% (1.65%)	1.71% (4.06%)

Using the experimental mode shapes shown in the previous chapter in the Figures 3.17 to 3.20, the effective bending lengths (between points of contra-flexures) can be taken as $((1/\sqrt{2})L_1)$ for the first mode, $((1/2)L_1)$ for the second mode and $(L_1/(2\sqrt{2}))$ for the third mode, where L_1 is the length between the two bearing supports. Taking L_1 to be equal to 0.97m (from Figure 3.7, which gives the actual span length between the two test frame supports), the effective bending lengths for the first three frequencies were obtained as 0.686m, 0.485m and 0.343m, respectively. This led to (*effective crack length /effective bending length for the mode*) ratios of 1/12.55 for first bending mode, 1/15.83 for second bending mode and 1/13.91 for third bending mode. Hence the ratio of 1/12 to 1/16 seems to give a better fit for the equivalent short length shaft ratio (= *effective crack length/ effective bending length)* for the different modes. The fourth mode shape (shown

in Figure 3.20) was not considered in the analysis owing to the following reasons, viz., (i) The node over the bearing support seems to have shifted outside its proper location, probably due to the curve fitting procedure; (ii) Measurements were made only at fourteen locations along the length of the shaft, and this has not provided enough plotting points to give the proper modal shape curve; and (iii) The presence of a crack seems to be indicated for all curves and thereafter appreciable change seems to occur in the plots (also see Appendix B).

The value of 1/12 to 1/16 for the equivalent short length shaft ratio can be given an alternate interpretation which will enable this ratio to be utilized in the first level crack identification scheme for shaft. When a shaft cracks, the average wave velocity in the cracked portion and the un-cracked portion should be the same. Hence

$$\Delta L/\Delta t = L/T_c \tag{4.3}$$

where ΔL is the effective crack length, Δt is the time taken by the considered bending wave (first record or third frequency) to cover the distance ΔL, L is the wave length of the considered wave (equal to twice the effective bending length) and T_c is the period of the considered wave in the cracked case. Rearranging Eqn. (4.3),

$$\Delta t/T_c = \Delta L/L = \Delta L/2L_{eff} \tag{4.4}$$

Hence,

$$\Delta L/L_{eff} = 2\ (\Delta t/T_c) \tag{4.5}$$

According to Rao (1995) in a time-domain numerical integration procedure using finite-difference schemes, the solution becomes unconditionally stable and reasonably accurate when the $\Delta t/T_{uc}$ ratio is smaller than 1/20 to 1/40. From Table 4.1, it can be seen that when crack depth ratio is around 40%, the T_{uc}/T_c is approximately 1.02 for the first mode, and 1.01 for the second and third modes. Hence $\Delta t/T_{uc}$ ratio can be expected to be smaller than 1/19.6 to 1/39.6. Hence Eqn. (4.5) can be expressed as

$$1/9.8 < \Delta L/L_{eff} < 1/19.8 \tag{4.6}$$

which is approximately the ratio obtained from the experimental values. Consequently a finite element analysis could be carried out with the ratio of (effective crack length / effective bending length) of (1/12.0) to (1/16) and the cracked frequency of rotor shafts can be obtained for a crack depth ratio 40%. When the measured frequency of the rotor shaft reduces below this value for the first three modes, then one can be invariably sure to say that there is a crack or damage in the rotor shaft and carry out a detailed inspection on the rotating shaft to locate the crack.

Figure 4.9 and Figure 4.10 show (LMS system given) the mode shapes comparison for first eight natural frequencies of (four vertical and four horizontal) experimental and numerical analyses (Beam4). As could be observed from the plots shown in Figure 4.9 and Figure 4.10, the experimental measurements closely correspond with the numerical computations.

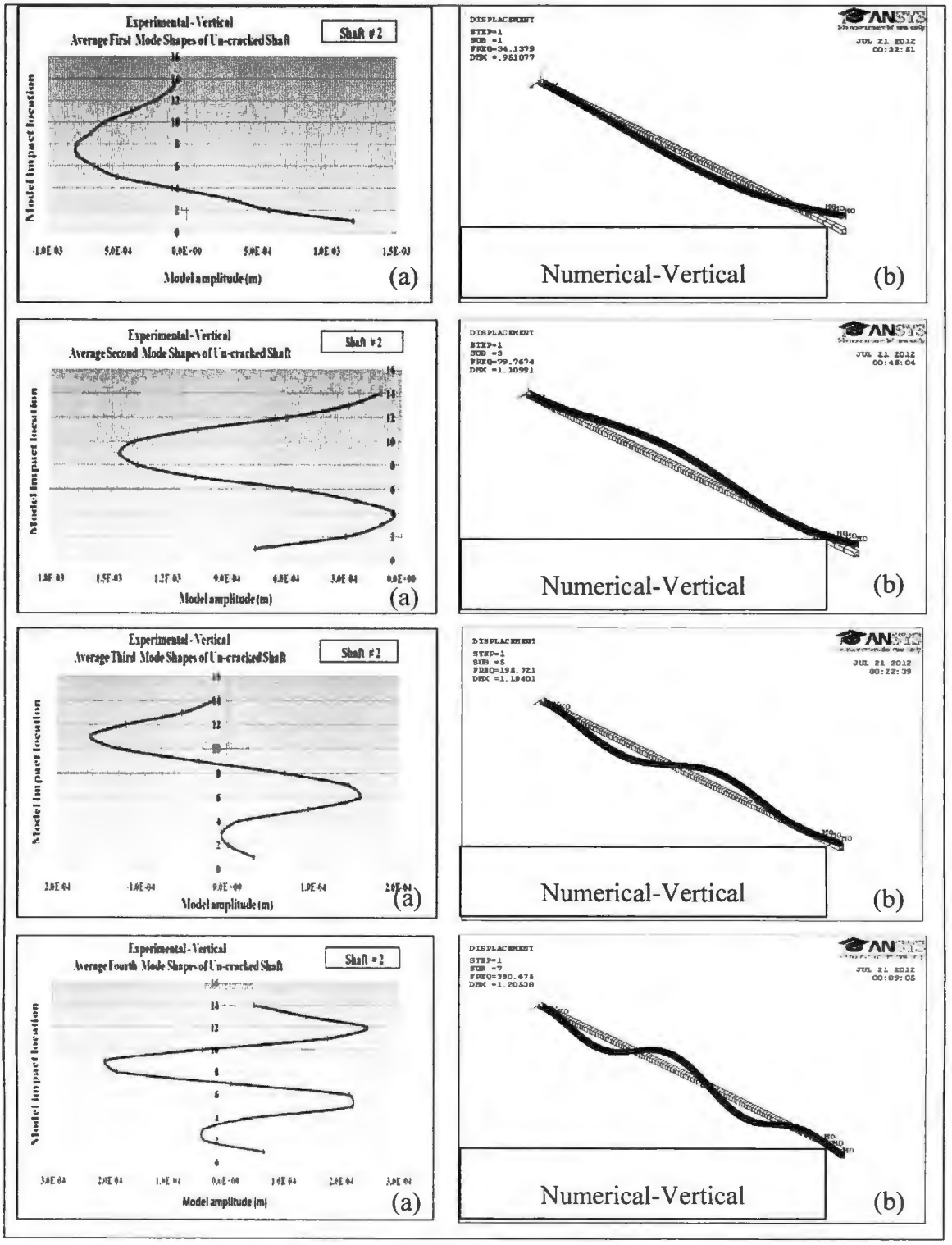

Figure 4.9 Mode Shapes Comparison for First Four Vertical Frequencies a) Experimental and b) Numerical

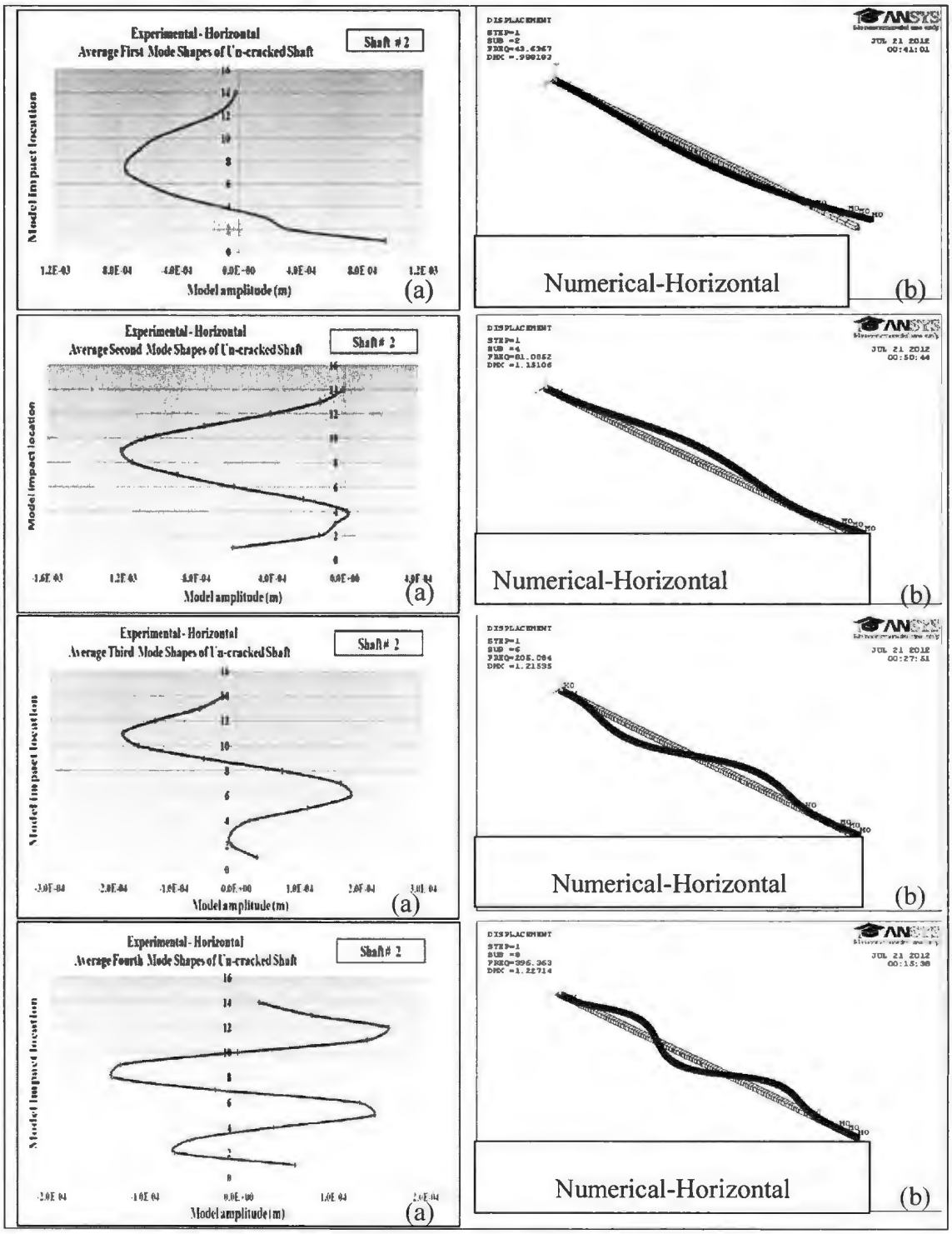

Figure 4.10 Mode Shapes Comparison for First Four Horizontal Natural Frequencies a) Experimental and b) Numerical

4.5 Summary

In this chapter, results were obtained from the finite element software program ANSYS 13, using the beam element, BEAM4, for the numerical prediction of the dynamic response of un-cracked and cracked shafts. Five support spring models were developed to represent the ball bearing and from support effect, viz., six, eight and twelve springs. It is seen that the rotor shaft with six support springs, shown in Figure 4.1 (b), gives the best agreement between experimental and numerical results. This is due to the fact that this model closely represents the elasticity effects that exist between the two tight screws that connect the inner bearing to the cylindrical shaft and elasticity of the support provided by the two frame supports 1 and 2.

When the crack was modeled by a very slender beam element the experimental values shows comparatively larger changes for the crack present in the shaft; whereas the numerical analysis results showed almost no changes, as the crack depth increased from 0 to 70%. The numerical analysis seemed to be insensitive to the presence of the crack in this modelling. This was due to the fact that the flexibility introduced in the experimental model by the presence of a crack was much higher than that provided by the single slender finite element used to represent the crack effect in the numerical model. To improve the numerical results, the model shown in Figure 4.6 (b) (a wider element) was used to represent the crack effect. The results obtained with this wider "crack width" modal were much closer to the experimental results.

From the modeling of a crack, in a cracked shaft, by an equivalent short beam, the best fit for the length of a short rotor shaft element for first natural frequency was about 54.65 mm, while the best fit for second and third natural frequencies were between 30.65mm and 24.65mm, respectively. This gave an approximate ratio (= *effective crack length/ effective bending length for the mode*) of 1/12 to 1/16 for different modes. This also seems to be corroborated by the digitized time interval requirements for accuracy in finite-difference related numerical integration. The above relationship could be used as a first level inspection scheme for determining the presence of cracking in a rotating shaft.

Chapter 5

Crack Detection in Rotor Shafts Using Vibration Measurements and Numerical Analyses using Three-Dimensional Isoperimetric Elements

5.1 Introduction

Cracking of cylindrical shafts is an important area for research, since the changes observed in their vibration characteristics even during large-sized cracking are much smaller than those observed for rectangular beams; hence early identification of crack existence becomes essential to prevent sudden failures in rotating shafts. In this chapter numerical investigations (3-D) were carried out to identify the presence of a crack in a cylindrical overhanging shaft with a propeller at the free end. Three-dimensional iso-parametric elements (element types 186 and 187) available in the ANSYS FEM program were used in the analysis to model the rotor shaft and the embedded crack. The open crack was embedded in the rotor shaft and the mesh generation was suitably modified to incorporate the stress intensity effects present at the crack tip.

Instead of the beam elements used in the earlier numerical study reported in Chapter 4, the study reported herein used 3-D iso-parametric elements (20-noded, 15-noded, 12-noded and 10-noded) for modeling the shaft, bearings, supports, propeller, torque loading arm and other accessories. Moreover in the earlier study only support springs were used to represent the elastic effects of bearings, supports and other attachments present in the cylindrical shaft system. Hence in the present chapter a detailed modeling of the bearing connections to the shaft, as well as to the supporting frames, were done to properly

include the total effect of the support elasticity. This detailed modeling of the shaft-propeller system using FEM procedures has given extensive insights into the behavior of the shaft-propeller system including the overall shaft behavior, the support bending, the local bending of the propeller blades, and the presence of combined modes.

Vibratory responses of the un-cracked and cracked shaft were obtained numerically using the finite element method and were compared with the results obtained from experimental testing. Finite element results were used to generate numerical frequency response functions that were used to detect the crack occurrence in the shaft propeller-bearings system and to compare the numerical results with experimental results.

5.2 Modeling of Rotor Shaft-Bearing-Propeller System with ANSYS Workbench

The shaft was supported over two roller bearings supported on two fixed steel supports; the fixed steel supports were fixed-welded to the large steel base plate as shown in Figure 5.1 (a). The steel base plate was fixed to the table at bottom. The bearing model used for the present study was the Flange Mounted McMaster-Carr Ball bearing (5967k81) shown in Figure 5.1 (McMaster-Carr, 2011) shown in Figure 5.1 (b). It contained two main parts, viz., the inner and outer housing bearing surfaces connected together through some balls, and two tight screws that connected the shaft to the inner bearing, as shown in Figure 5.1 (c).

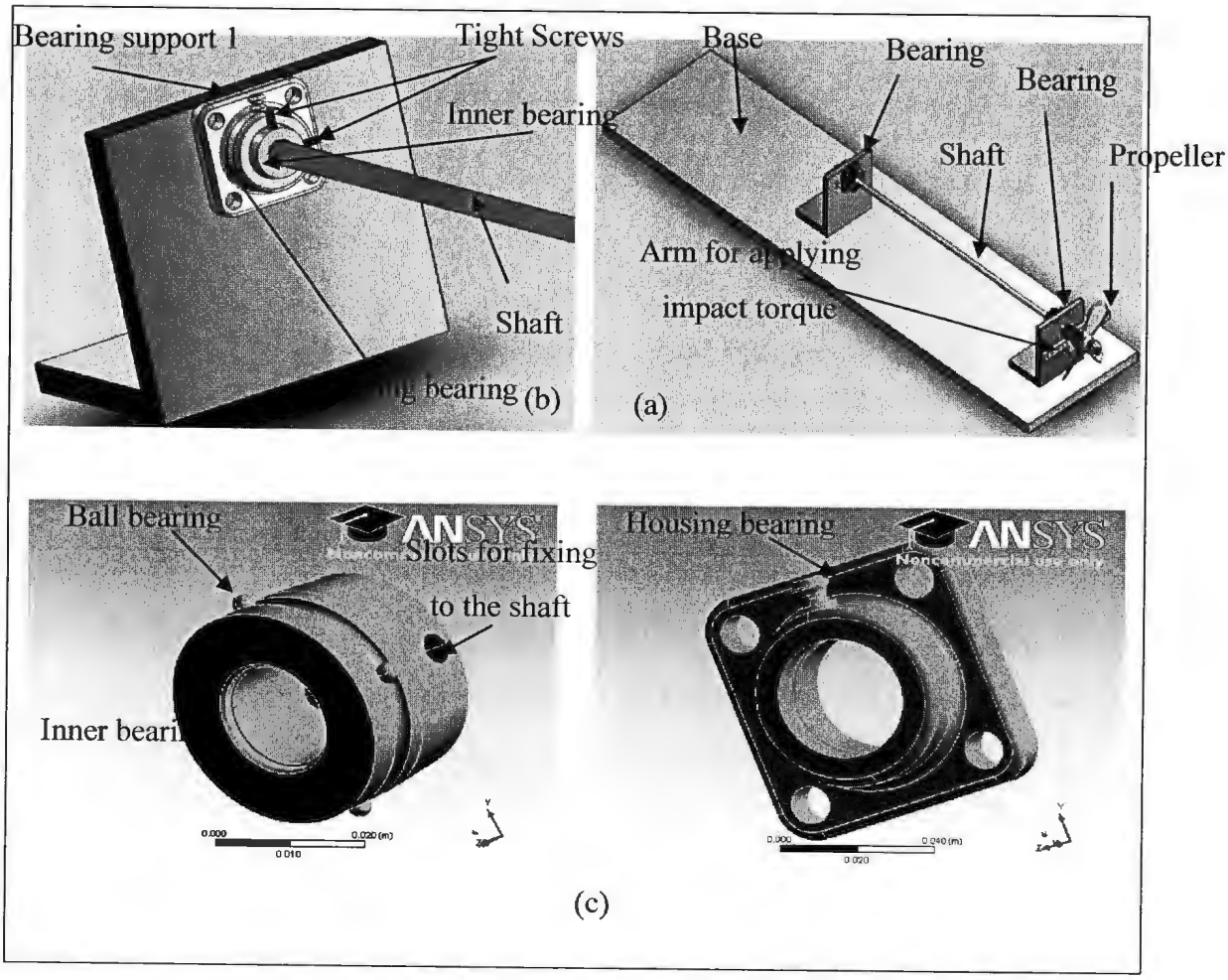

Figure 5.1 a) Details of Bearing Support; b) Schematic Diagram of Shaft-Propeller-Bearing; and c) Inner and Outer Bearing.

5.2.1 Elements Used in Analysis

In this study, the Finite element software program ANSYS Workbench 13 was used to create 3-D analytical models of the shaft-propeller system. The element types used for the 3-D model were chosen automatically (Huei, 2011) by default from the element library by the Workbench according to the types of the structural elements used in the analysis. It uses two types of elements (see Figure 5.2), viz., (i) Solid 186, which is a second order 3-D, 20-node element which can degenerate to a hexahedral triangle-based prism, or a

quadrilateral-based pyramid, or a tetrahedron; and (ii) Solid 187, which is a 3-D 10-node tetrahedral second order structural solid element. Each node for both types of element has three degrees of freedom (translations in the x, y, and z directions).

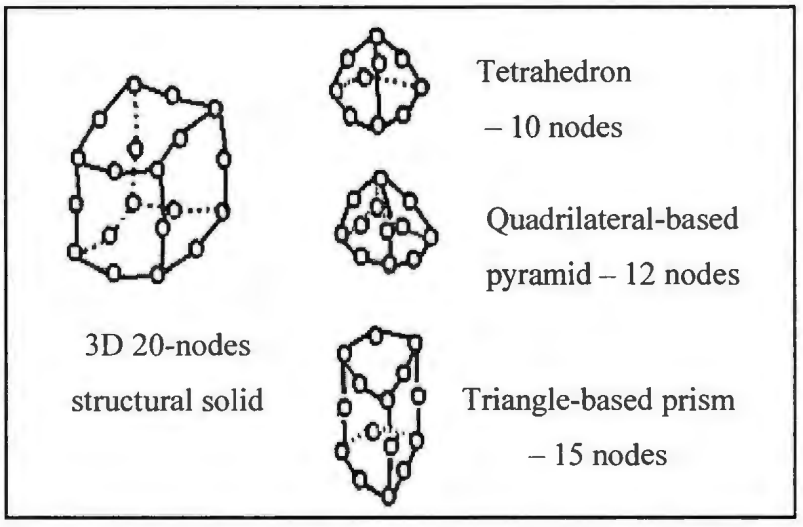

Figure 5.2 Geometries of the Elements.

5.2.2 Mesh Convergence Study and Geometry

Commercial FE software ANSYS with Workbench was utilized to carry out the modeling and frequency analysis of circular shafts supported on bearings. A mesh convergence study was carried out earlier so as to ensure that the values of the experimental natural frequencies for lateral and torsional were convergent with numerical results. Several mesh sizes (with maximum element dimensions varying from 0.7cm to 2.0 cm) of the model were utilized in this study. The shaft-propeller-bearing configuration and mesh generation are shown in Figure 5.3 (a). The mesh convergent study carried out (given in Table 5.1) showed that the frequency responses were very close to the experimental results for a mesh size of 1.0 cm for the shaft system. The model had 39731 elements and

78580 nodes for the un-cracked shaft. For the cracked shaft the same mesh was used with refinement of the mesh around the crack front giving a much higher number of elements and nodes for the vibrating system. The mesh around the crack region is shown in Figure 5.3 (b).

Table 5-1 Numerical Values of the Natural Frequencies for Various Crack Depth-Ratios, V - Vertical and H - Horizontal.

Frequency	Crack depth ratios							
	0.0%		10%		20%		30%	
	V	H	V	H	V	H	V	H
First	35.577	41.182	35.594	41.113	35.551	41.173	35.471	41.107
Second	75.247	78.245	75.113	78.102	75.021	78.017	74.933	78.129
Third	187.880	199.22	187.51	198.97	187.43	198.82	187.4	199.4
Fourth	360.1	381.49	358.72	380.75	358.99	380.58	362.09	383.3
First natural frequency for torsion	43.453	43.422	43.111	42.92	43.453	43.422	43.111	42.92
Frequency	Crack depth ratios							
	40%		50%		60%		70%	
	V	H	V	H	V	H	V	H
First	35.402	41.575	34.922	41.002	34.23	40.497	33.706	40.583
Second	74.27	77.997	73.48	77.79	71.832	76.594	69.705	76.879
Third	186.4	198.66	185.56	198.76	183.36	197.05	179.87	196.46
Fourth	379.14	360.66	360.66	380.83	341.77	376.87	338.83	366.55
First natural frequency for torsion	42.739	42.599	42.353	41.877	42.739	42.599	42.353	41.877

5.2.3 Contact Behaviour

In ANSYS workbench the contact between two bodies were represented by two contact surfaces, one specified as a contact surface and the other as a target surface. The contact between these bodies can be represented by one of the following types, viz., bonded,

frictional, frictionless, rough, and no separation. Bonded contact means that the two bodies were integral with one another and act as a single body. Frictional contact applies only to surfaces in contact and the value of friction varies from a low value to a high value (only positive values were permitted). Rough contact represents the surfaces which have a very large friction coefficient between the contacting bodies. In the present shaft-propeller system, all the three types of contact have been used. It can be explained as follows: (i) The parts which were bonded together are, viz., two tight screws to inner bearing and to shaft, housing bearing to inner connection (a part that is made to fill the space between the bearing surfaces and the steel supports, to avoid unwanted zero modes), housing bearing to balls, shaft to small nut, shaft to big nut, shaft to fixed aluminum, propeller to small nut, small nut to big nut, and fixed aluminum to support 1; (ii) The parts which had frictional contacts were, viz., aluminum arm to shaft (friction coefficient is 0.2), aluminum arm to propeller (friction coefficient is 0.1), inner connection to support (friction coefficient is 0.001), and shaft to propeller (friction coefficient is 0.1); and (iii) The parts which had frictionless contacts were, viz., housing bearing to inner bearing, balls to inner bearing, balls to inner connections, inner bearing to inner connections, inner bearing to shaft, inner connections to shaft, fixed aluminum to support 1 and shaft to support 1. The frictional coefficient became important in determining the correct torsional frequency since the propeller was not welded to the shaft, but joined rigidly through a slotted keyway system. The frictional coefficients that gave frequencies close to the experimental values were used to get the correct numerical

frequency values. The same consideration was used in identifying the frictional coefficient for the torque arm.

5.2.4 Materials

The shaft-bearing-system model contained different type of materials. As mentioned in the previous section the model had several interconnecting parts such as shaft, propeller, bearings, nuts, tight screws, aluminum arm, fixed aluminum, support, and inner connection. The material properties of these parts used in the analysis are summarized in Table 5.2.

Table 5-2 Material Properties Used in the Numerical Modal

Type	Material	Density Kg/m^3	Modulus of elasticity Pa	Poisson's ratio	Bulk Modulus Pa	Shear Modulus Pa
shaft	Steel	7850	2e+11	0.3	1.67e+11	7.69e+10
Propeller	Bronze	8800	1.14e+11	0.34	1.19e+11	4.25e+10
Support	steel	7850	2e+11	0.3	1.67e+11	7.69e+10
Housing bearing	Gray cast iron	7200	1.1e+11	0.28	8.33e+10	4.29e+10
Inner bearing	Structural steel	7850	2e+11	0.3	1.67e+11	7.69e+09
Fixed aluminum	Aluminum Alloy	2770	7.1e+10	0.33	6.96e+10	2.67e+10
Aluminum arm	Aluminum Alloy	2770	7.1e+10	0.33	6.96e+10	2.67e+10
Inner connection	Artificial polyethylene	50	1.1e+05	0.42	2.29e+05	38732
Tight screws	steel	7850	2e+11	0.3	1.67e+11	7.69e+10
Small and big nut	steel	7850	2e+11	0.3	1.67e+11	7.69e+10

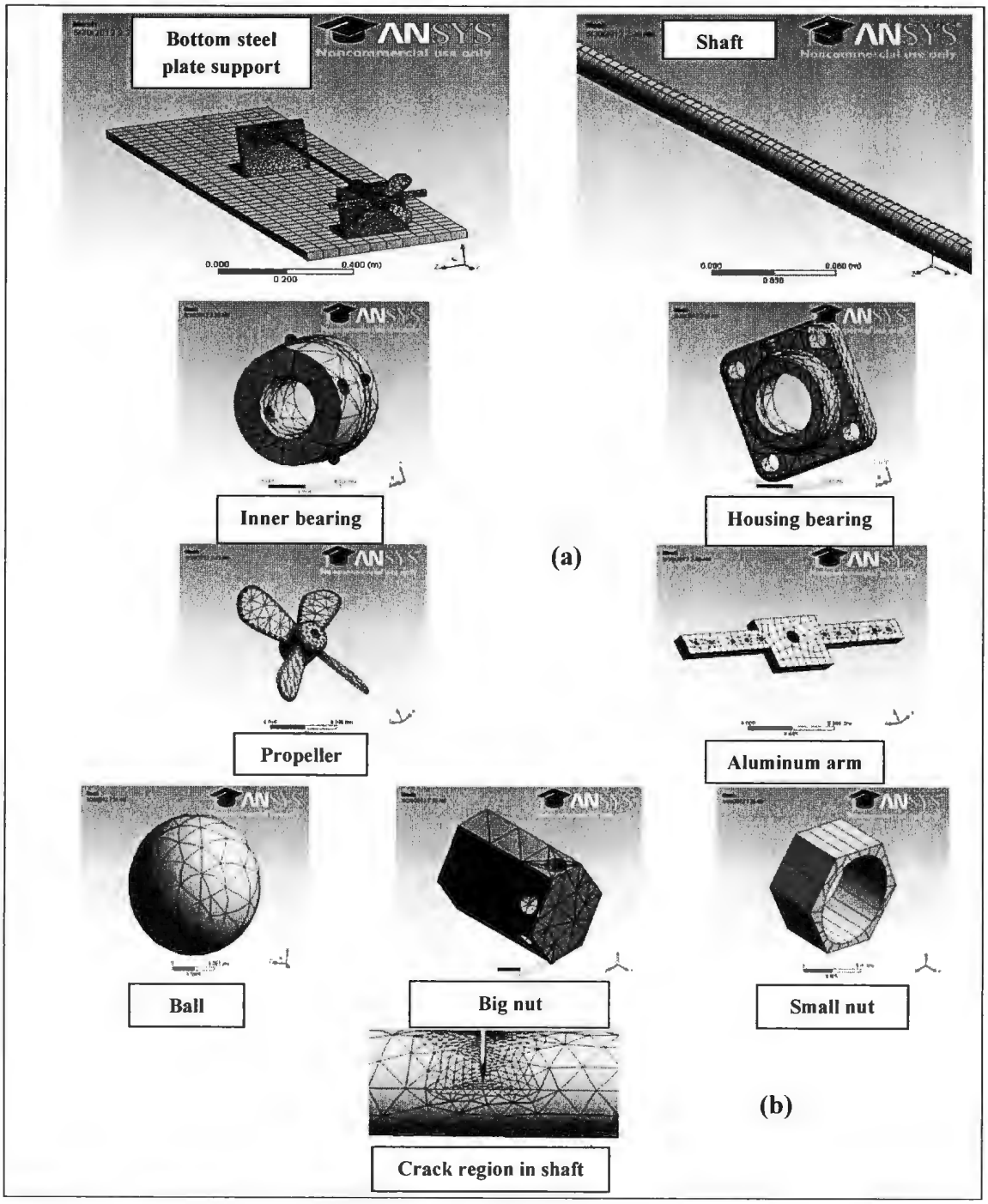

Figure 5.3 Finite Element Mesh Used for the Various Components of the Rotating Shaft System; and b) Mesh Around the Crack Region.

5.3 Presentation of the Results and Discussion

In this part, results obtained from the finite element software program (using ANSYS workbench 13) and from experimental program are presented. The twenty frequencies obtained from a prior study and the mode shapes obtained are given in Table 5.3 and Figures 5.4 and 5.5 (also see Appendix F). It can be seen from Figure 5.4, that the lower propeller blade frequencies are clustered between the third and fourth vertical bending frequencies. In addition it can also be seen that the support bends due to shaft vibration as shown for the modes shapes of frequency 343.95 Hz and 424.85 Hz. In order to relate them to the earlier experimental results, only the eight lowest bending frequencies (four vertical and four horizontal) and mode shapes of the un-cracked and cracked shafts will be highlighted hereafter. For experimental and numerical studies, one crack position and various crack ratios (from 0% to 70% ratio) were examined.

Table 5.3 shows the results of the first eight natural bending frequencies (four vertical and four horizontal); it also gives the computed torsional frequency. These experiments were repeated for three different shaft-bearing systems, viz., shaft No. 1, shaft No.2 and shaft No. 3. The three shafts were of almost of the same diameter (average measured diameter values were 0.01588 m, 0.01586 m, 0.01589 m, respectively). For each crack depth three independent tests were carried out and the results processed through the LMS Test Lab system. Then the results were added and averaged (see Appendix A) to get the final results reported herein.

Table 5-3 Experimental and Numerical Values of the Natural Frequencies (Hz) for Various Crack Depth-Ratios (V - Vertical and H - Horizontal and Torsional).

Frequency		Crack depth ratios							
		0.0%		10%		20%		30%	
		V	H	V	H	V	H	V	H
First	Exp. Shaft 1 *	34.768	41.344	34.417	41.544	34.119	41.182	34.325	41.196
	Exp. Shaft 2 *	36.395	42.980	36.315	42.959	36.262	42.904	36.212	42.91
	Exp. Shaft 3 *	33.855	40.629	33.774	40.656	33.751	40.615	33.736	40.550
	Num. Comp.	35.577	41.182	35.594	41.113	35.551	41.173	35.471	41.107
Second	Exp. Shaft 1 *	76.78167	78.279	76.413	78.57567	76.05867	78.31	75.205	78.02033
	Exp. Shaft 2 *	75.975	80.034	76.056	79.985	75.852	79.903	75.617	79.309
	Exp. Shaft 3 *	74.614	79.914	74.593	79.809	74.487	79.844	74.215	79.826
	Num. Comp.	75.247	78.245	75.113	78.102	75.021	78.017	74.933	78.129
Third	Exp. Shaft 1 *	190.634	199.089	190.757	197.944	189.998	197.769	189.865	197.829
	Exp. Shaft 2 *	196.119	199.544	195.849	199.462	195.667	199.503	195.398	199.424
	Exp. Shaft 3 *	192.190	197.813	191.962	197.817	191.742	197.771	191.298	197.652
	Num. Comp.	187.880	199.22	187.51	198.97	187.43	198.82	187.4	199.4
Fourth	Exp. Shaft 1 *	365.8	335.241	364.3547	335.2313	362.3233	335.7223	365.426	336.0583
	Exp. Shaft 2 *	367.423	369.148	366.861	368.992	366.391	368.896	365.457	368.605
	Exp. Shaft 3 *	352.959	355.931	353.392	355.628	352.642	355.315	349.39	353.132
	Num. Comp.	360.1	381.49	358.72	380.75	358.99	380.58	362.09	383.3
First natural frequency for torsion	Exp. Shaft 1	43.716		43.213		42.826		42.628	
	Num. Comp.	43.453		43.422		43.111		42.92	

Frequency		Crack depth ratios							
		0.40%		50%		60%		70%	
		V	H	V	H	V	H	V	H
First	Exp. Shaft 1 *	33.80933	41.09267	33.79633	40.815	32.64033	40.52267	30.60033	39.84867
	Exp. Shaft 2 *	36.02723	42.77933	35.791	42.70067	35.21133	42.23533	33.98633	41.728
	Exp. Shaft 3 *	33.54967	40.47867	33.335	40.339	32.80367	40.03433	31.67467	39.535
	Num. Comp.	35.402	41.575	34.922	41.002	34.23	40.497	33.706	40.583
Second	Exp. Shaft 1 *	75.48633	77.35933	74.19133	76.54333	72.79567	76.23	67.299	74.95233
	Exp. Shaft 2 *	74.99833	79.09533	74.20733	79.09067	72.38067	79.03467	69.24733	77.91233
	Exp. Shaft 3 *	73.44333	79.603	72.554	79.372	70.73833	78.92633	67.54433	77.9527
	Num. Comp.	74.27	77.997	73.48	77.79	71.832	76.594	69.705	76.879
Third	Exp. Shaft 1 *	189.449	197.708	188.0927	197.1897	186.1117	196.4363	178.986	195.956
	Exp. Shaft 2 *	194.5687	199.3333	193.421	199.0703	190.7537	198.4617	185.5763	197.3003
	Exp. Shaft 3 *	190.0337	197.4143	188.644	197.0687	185.412	196.3743	180.0857	195.0663
	Num. Comp.	186.4	198.66	185.56	198.76	183.36	197.05	179.87	196.46
Fourth	Exp. Shaft 1 *	358.8217	335.4333	355.349	333.2633	345.0703	331.14	327.8163	321.8417
	Exp. Shaft 2 *	362.876	367.6683	359.1237	366.059	349.9673	362.3057	333.337	354.9043
	Exp. Shaft 3 *	344.4017	350.252	339.052	347.5507	328.8137	343.1973	315.164	336.204
	Num. Comp.	379.14	360.66	360.66	380.83	341.77	376.87	338.83	366.55
First natural frequency for torsion	Exp. Shaft 1	42.292		41.864		41.723		41.497	
	Num. Comp.	42.739		42.599		42.353		41.877	

* Average of three independent measurements

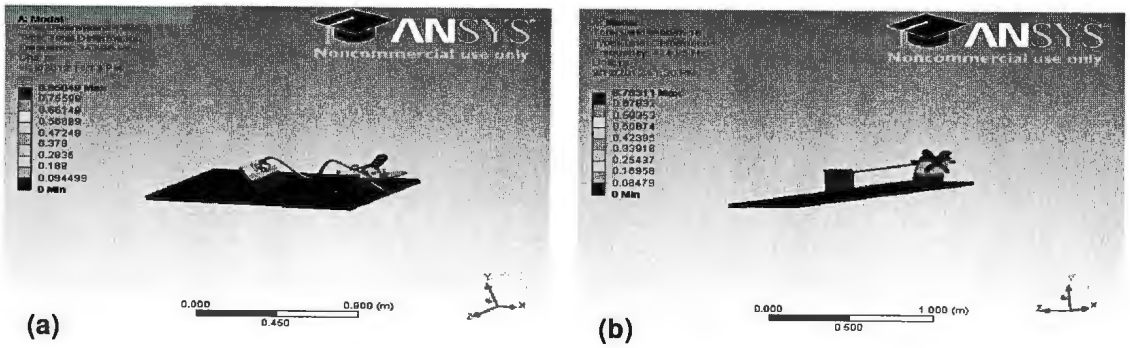

Figure 5.4 Bending Mode Shapes for: a) Coupled Vertical Bending of Rotor Shaft and Support # 1; and b) Bending of Support # 2

The experimental and numerical results seem to be agreeing very well (in a non-dimensional manner) with one another as the crack depth increases in the shaft-propeller-bearing system; in both experimental and numerical results, the frequencies of the cracked shaft clearly decrease as the crack depth increases. Also the estimated numerical values of frequencies have been observed to be higher than the measured experimental ones for the fundamental frequency. The experimental and numerical results are extremely consistent as the crack depth increases in the shaft-propeller system; the frequencies of the cracked shaft progressively decreases as the crack depth increases, in both experimental measurements and numerical computations. Also the experimental measurements of frequency changes have been observed to be higher than the numerically estimated values for all the frequencies. One probable reason for this difference is that the numerical changes shown by FE procedure seems to under estimate the changes taking place at the crack location.

Also the measured frequency differences between successive crack profiles used in the study were many times less than 0.1 to 0.2 Hz. It has also been estimated from the given

digitization rate of the experiments, that the accuracy of frequency measurements was around 0.25 Hz. This is in correspondence with the limitations in the ANSYS software for FRF computations where the minimum frequency difference that could be achieved was 0.25 Hz. Hence the measured changes would reflect these limitations in the changes that occur in measuring the successive cracks profiles used in the study.

Figure 5.5 and 5.6 shows the mode shapes comparison for first eight natural frequencies of (four vertical and four horizontal) experimental and numerical analyses for un-cracked shaft (for cracked shaft the results are presented in Appendix E). As could be observed from the plots shown in Figures 5.5 and 5.6, the experimental measurements closely correspond with the numerical computations. In the numerical computations the local propeller blade responses were observed to lie between the 3^{rd} and 4^{rd} vertical bending frequencies. In addition the support bending vibrations were observed to be above the 4^{rd} horizontal bending frequency (also for rotor shaft-support-propeller bending, see Figures F.1 to F.7 in Appendix F).

Figure 5.7 shows the changes that occur in the experimental bending and torsional frequencies as the crack depth ratios change from 0 to 70% (cubic curve fit). It can be seen that the frequency changes become appreciable only when the crack depth ratio is more than 50%. This would lead to a precipitous cracking of the shaft unless it is noticed in a timely manner. Hence another type of measure is required to detect the presence of cracking damage in cylindrical shafts. When the rate of change of frequency is plotted as a function of crack depth ratio, as shown in Figure 5.8 (a) – (d) (also the Appendix C

shows the details of the rate of the changes of the other shafts), the abrupt changes in plots can be observed even for a crack depth ratio of 20% or greater. This was observed earlier by (Hamidi, Piaud, & Massoud, 1992), who stated that the rate of change in natural frequencies becomes observable when the crack depth ratio becomes greater than 0.30.

Also in Figure 5.8 (a) the plot of the depth of crack and rate of change in torsional frequency shows a significant difference from that of the bending frequencies. It shows that the rate of change in the torsional frequency gives a much better indication of the crack presence, especially during the starting point of the crack. It is seen that the rate of change of the expt. torsional frequency vs. crack depth ratio is much higher (at the crack depth ratios of 10%, 20% and 30%, the rate of change of frequency with respect to crack depth ratios are correspondingly 8%, 12% and 11%) whereas the rate of change of bending frequencies during the earlier stage of crack initiation and growth is much less (at the above crack depth ratios the rate of change of frequency with respect to crack depth ratio are varying between 2% to 5% - see Figure 5.8 (a)). This could be easily understood since the influence of cracking on torsional inertia (due to its larger influence along the skin surface of the cylindrical shaft than its depth) will be much higher than the bending inertia and the consequent changes in the rate of frequency change. Hence the rate of change of torsional frequency (with respect to crack depth ratio) could very well be used as a very good indicator of the presence of any small crack. More experimental measurements are needed to confirm the above findings.

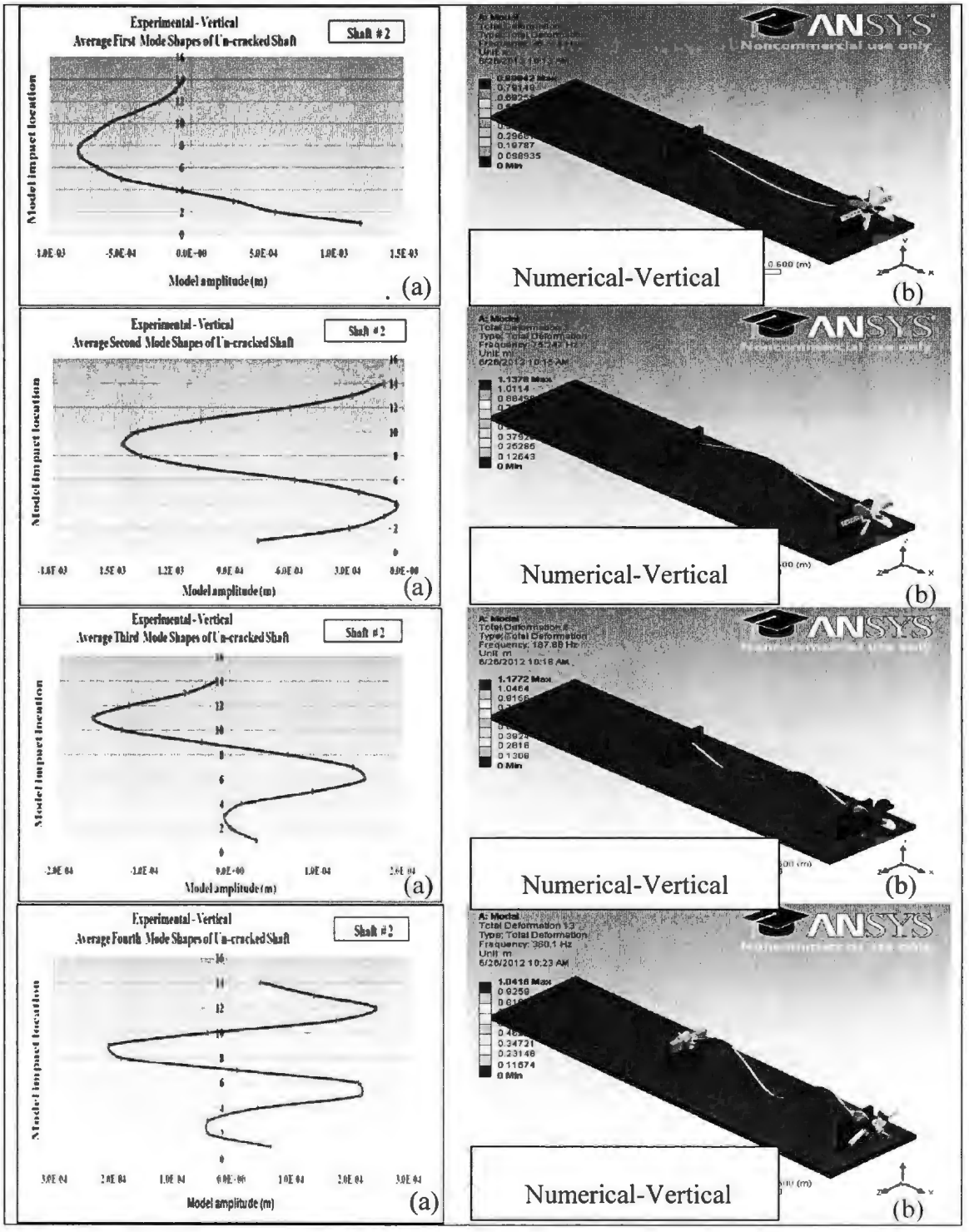

Figure 5.5 Mode Shapes Comparison for First Four Vertical Frequencies a) Experimental and b) Numerical.

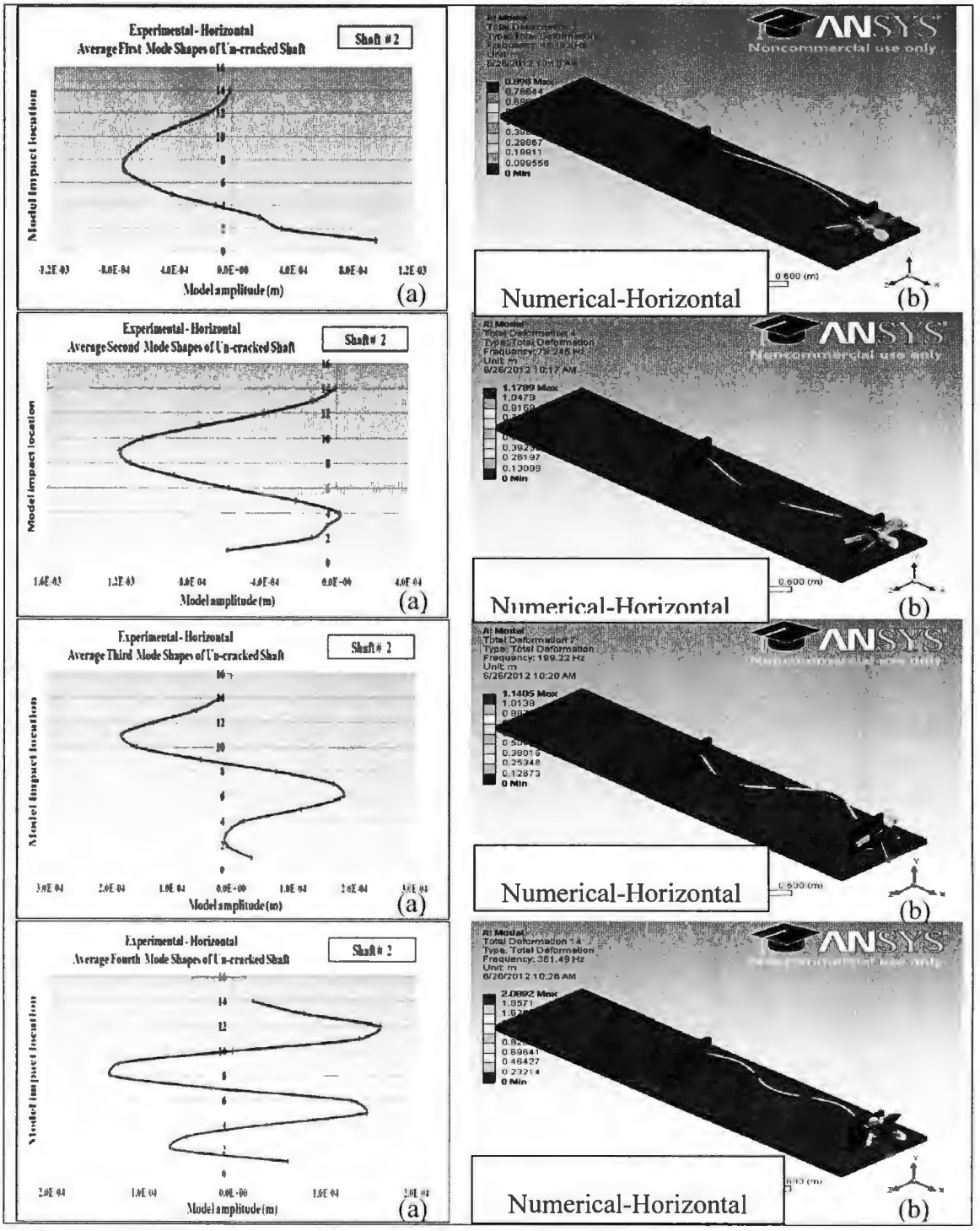

Figure 5.6 Mode Shapes Comparison for First Four Horizontal Natural Frequencies a) Experimental and b) Numerical.

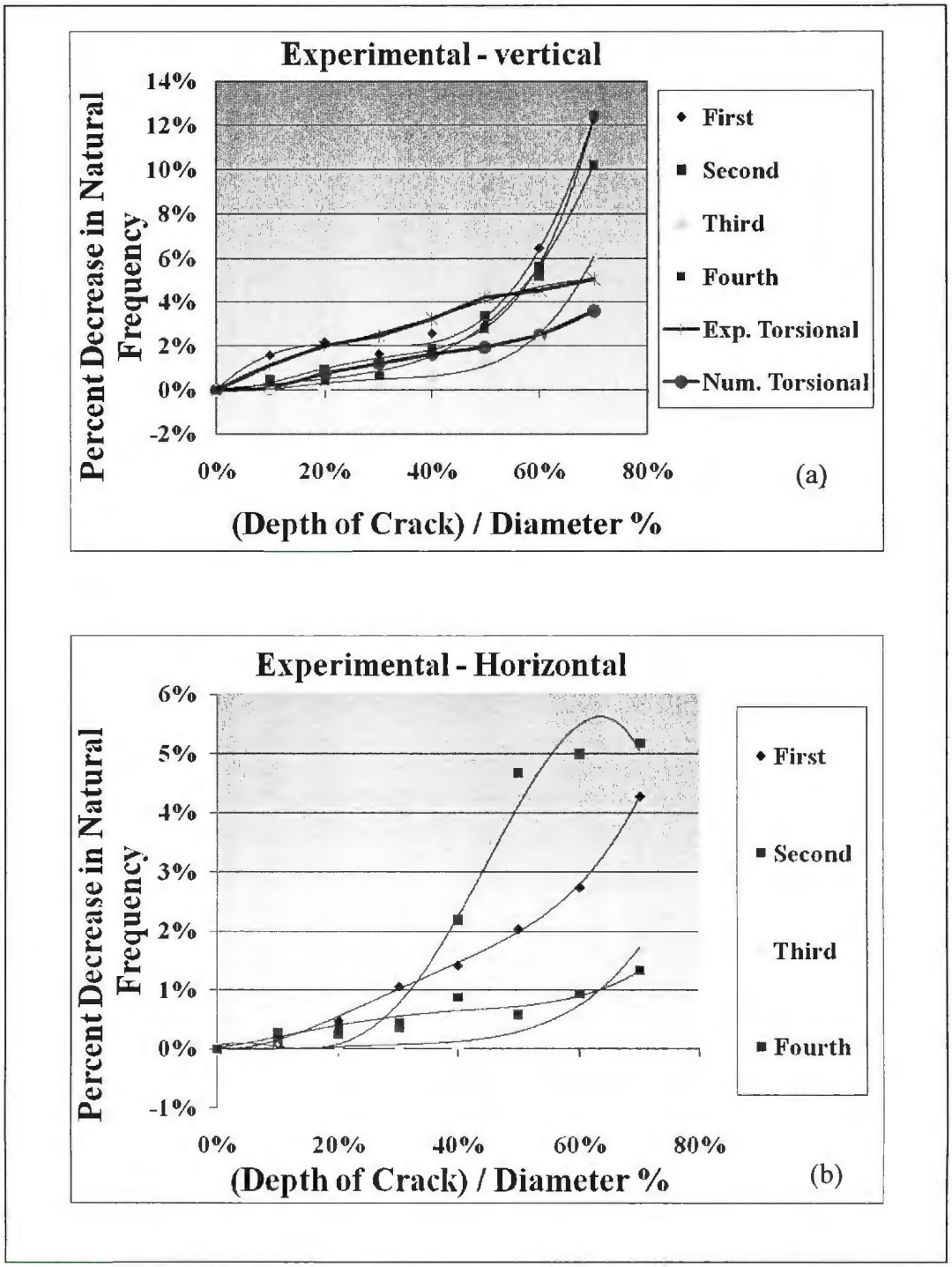

Figure 5.7 Depth of Crack vs. Percent Decrease in Bending and Torsion Natural Frequencies for Experimental Results a) Vertical; b) Horizontal.

Figure 5.9 shows the vertical bending responses of the system under test (impact excitation) and the corresponding response functions (acceleration FRFs, velocity FRFs, displacement FRFs) for experimental and numerical results for shaft # 1 (the results were almost similar for shaft # 1 and shaft # 3, which are presented in Appendix G). Frequency response functions for various crack depth ratios (from 0% to 70% ratio) were obtained for all cases. All figures illustrate the frequency shifts that occur due to the increased cracking in the shaft. It is also observed for all cases (experimental and numerical), reasonable agreements exist between numerical and experimental results. It can be seen from these figures, that the acceleration, velocity and displacement response functions (ARFs, VRFs and DRFs) can also be used as another tool for crack identification. Figure 5.10 shows individual comparisons for all cases (intact ARFs, VRFs and DRFs; cracked 10% ARFs, VRFs and DRFs; cracked 20% ARFs, VRFs and DRFs; cracked 30% ARFs, VRFs and DRFs; cracked 40% ARFs, VRFs and DRFs; cracked 50% ARFs, VRFs and DRFs; cracked 60% ARFs, VRFs and DRFs; and cracked 70% ARFs, VRFs and DRFs.) for vertical bending response functions of experimental and numerical computations. It can be seen more clearly that the shifts of acceleration, velocity and displacement response peaks are dependent on the change in natural frequencies and are directly proportional to the severities of the crack. The results are presented here for shaft # 2 while the rest of results, shaft # 1 and shaft # 3 are presented in Appendix H.

It is essential to point out two limitations in all the numerical computations reported above: (i) It can be seen from the curves given in Figures 5.9 and 5.10 respectively, in this study there is an extra frequency observable (around 35.0 to 45.0 Hz) in the

experimental results, which is not observed in the numerical computations. This extra frequency was determined to be due to the presence of the effect of torsional rotation (especially at the fixed end near support 1) in the measurement of vertical displacements. In the numerical computations, the torsional and bending frequencies (as well as their response functions) could not be computed in a single numerical computation for the indeterminate shaft. It had to be computed in two separate computations where the shaft was permitted to either bend or rotate freely (over the support 2 near the overhang) by the provision of zero friction (boundary condition for torsion) at the support near the overhang; this led to two different systems. The torsional frequencies were obtained correctly, when zero friction was provided at bearing support 2 and the bending frequencies were correctly obtained when friction of bearing # 2 was greater than zero (> 10^{-14}); and (ii) Also in the numerical computation for response functions the desired accuracy for computations could not be achieved with the provided computer memory size in the computing system. The accuracy with which the researcher could obtain response results was 0.25Hz (one could solve results up to 1000 steps for the frequency range of zero to 250Hz). These two restrictions prevented better comparison to be obtained between experimental and numerical results.

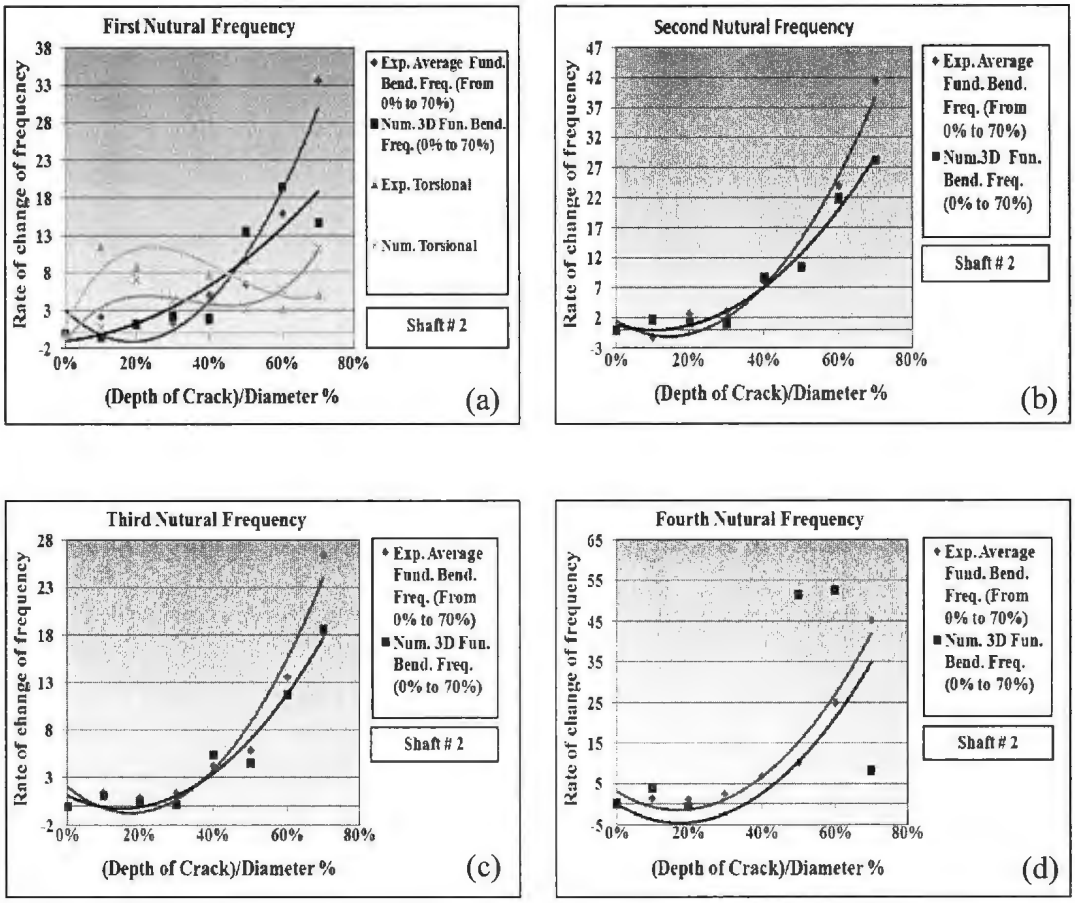

Figure 5.8 Comparison of Rate of Change of Frequency (with Respect to Crack Depth Ratio) vs. Crack Depth Ratio of the First Four Frequencies; (a) Mode One; (b) Mode Two; (c) Mode Three; (d) Mode Four.

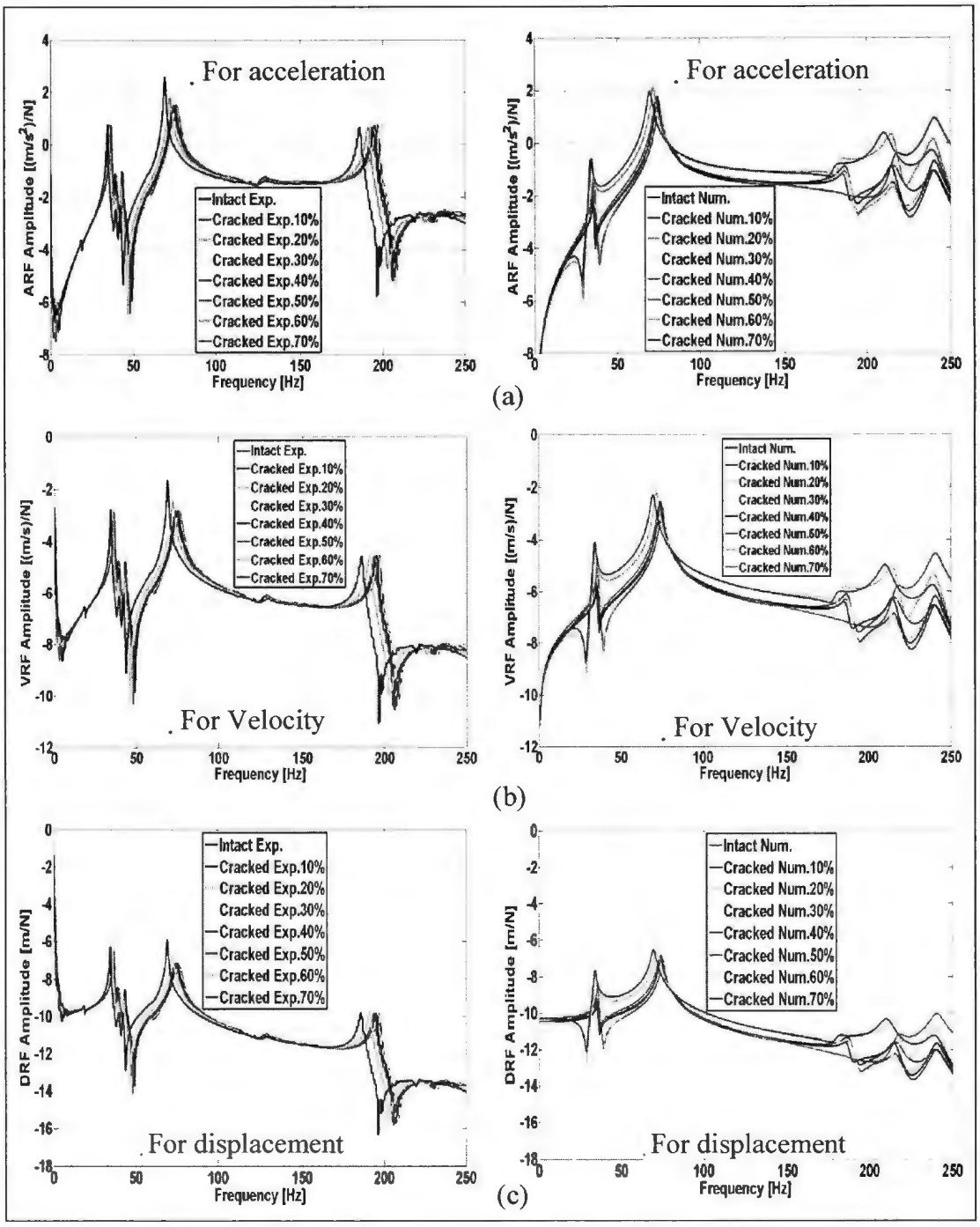

Figure 5.9 Experimental and Numerical Vertical Bending Frequency Response Functions of: a) Accelerations (ARFs); b) Velocities (VRFs) and (c) Displacements (DRFs) for Shaft # 2.

Figure 5.11 (a), (c) and (e) shows the changes that occur in the vertical amplitude response and the slope (of amplitude response) for resonant frequencies (experimental results) as the crack depth ratio increases from 0.0 to 0.7. Plots of the two other shafts are presented in Appendix I.1 and I.2. Figure 5.11 (a) shows the changes that occur in acceleration vertical amplitude response vs. crack depth ratio. It is observed from this figure that the identifier of the mode shape change due to crack is shown better by the first mode shape than the second mode; the crack presence can be identified above a crack depth ratio of 0.2. Similarly, Figure 5.11 (c) shows the changes that occur in velocity amplitude vs. crack depth ratio. In this figure the second mode gives a much better indication for the presence of crack than the first mode. Once again the crack presence can be identified beyond a crack depth ratio of 0.2. Also Figure 5.11 (e) shows the changes that occur in displacement amplitude response vs. crack depth ratio. These responses look like acceleration amplitude responses but may be less sensitive for crack. It can be seen from Figures 5.11 (a) to (f) that the identification of crack can be observed with much better sensitivity from the velocity amplitude responses shown in Figure 5.10 (c) and (d) (since the variation is much higher for velocity). In this case the crack can be identified after 0.2. Figure 5.11 (b), (d) and (f) show the slope of the modal amplitudes for acceleration, velocity and displacement responses, respectively vs. crack depth ratio. Figure 5.11 (b) and (d) show that beyond the crack depth ratio of 0.2, presence of the crack can be easily identified.

Figure 5.12 (a) to (f) show the changes that occur in the amplitude and the slope (of amplitudes) for anti-resonant frequencies (experimental results) as the crack depth ratio

increases from 0.0 to 0.7. Figures 5.12 (a) and (e) show the changes that occur in acceleration amplitudes and displacement amplitudes vs. crack depth ratio, respectively. It is observed from the two figures that the crack can be identified after a crack depth ratio of 0.4; mode shape change due to crack is shown better by the third mode amplitude shape than the first mode amplitude shape. By comparing these anti-resonant figures and the previous ones, it is clear that the resonant frequency gives a much better indicator for the crack presence than the anti-resonant frequency. On the other hand Figure 5.12 (c) for first mode gives a very good indicator for the crack presence than all other figures; hence the changes that occur in velocity amplitudes vs. crack depth ratio is much better than acceleration or displacement amplitudes. Figure 5.12 (b), (d) and (f) show the slope of the anti-resonant modal amplitude for acceleration, velocity and displacement, respectively vs. crack depth ratio. Figure 5.12 (b) shows that beyond a crack depth ratio of 0.3, presence of the crack could be identified; and the third mode seems to be better than first mode. Whereas Figure 5.12 (d) gives better results [than Figure 5.12 (b)] since it can sense the crack presence even from an earlier stage of crack (when crack depth ratio is > 0.0) for both modes. For all crack cases are presented in Appendix I.3 and I.4.

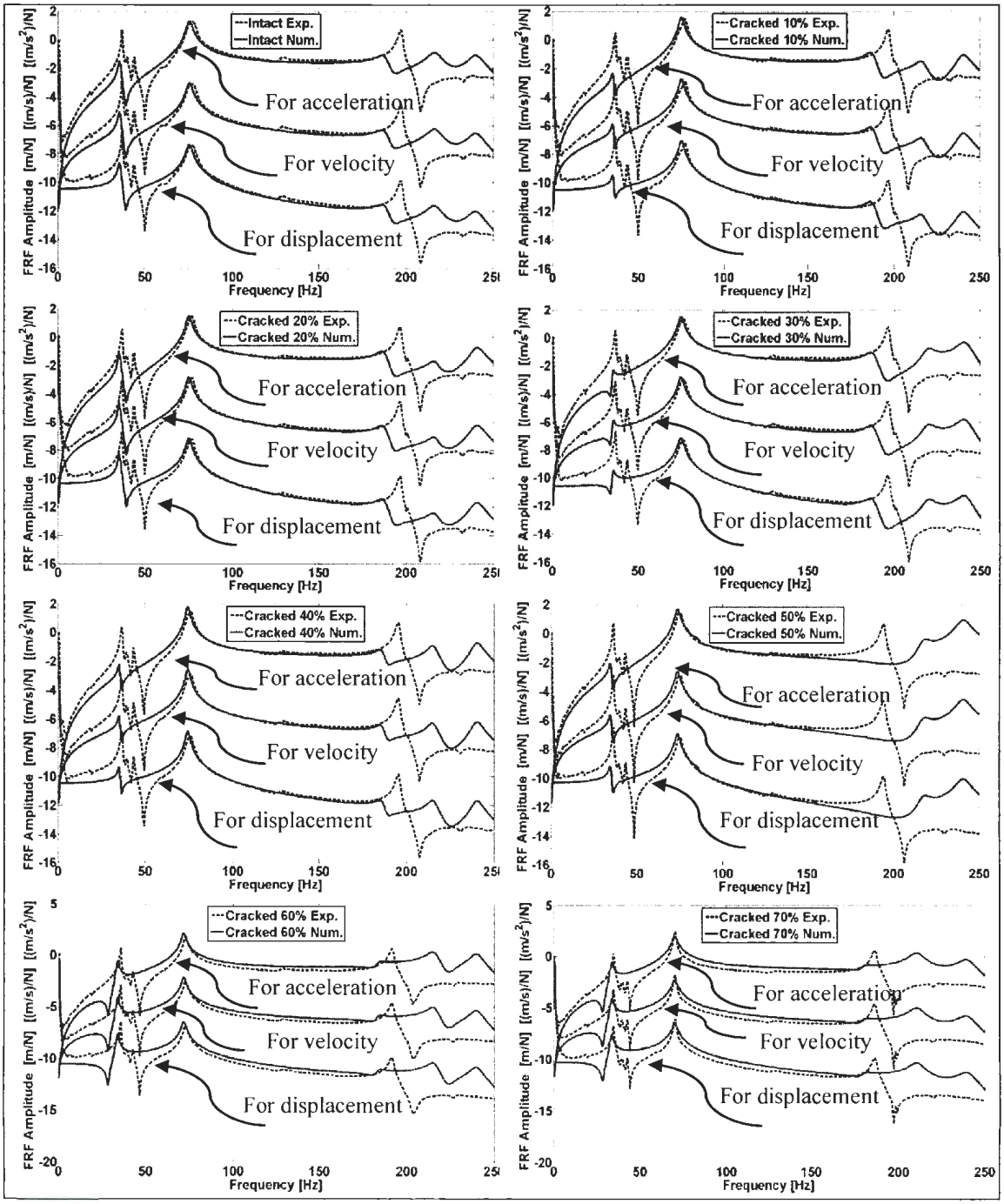

Figure 5.10 Schematic of Vertical Bending Frequency Response Functions for Different Depth of Crack of Experimental and Numerical Computations. Shaft # 2.

Figure 5.13 shows experimental and numerical comparison for first and second modes for acceleration, velocity and displacement amplitudes. It can be observed from the amplitude curves of Figure 5.13 that the amplitude ratios of all the modes increase for the resonant frequencies as the crack depths ratio increases. The trend of agreement between experimental and numerical values is very good, especially for all the first modes; however only a small change occurs in amplitudes values at all the second modes. Also it can be seen from numerical acceleration results that it gives a much better indication of the crack presence for mode 2 even from the beginning stages of the crack but the sensitivity seems to be much higher for velocity amplitude ratios (also see Figures I.5 and I.6 in Appendix I.)

Figure 5.14 shows the slope of the first and second experimental and numerical modal amplitudes. These figures show that velocity and displacement slopes give a much better indication of the crack presence than the slope of acceleration. It can be observed from Figure 5.13 (b) and (c) that the crack is present even from beginning stages (since the sensitivity at lower crack depths is much higher) while Figure 5.13 (a) shows a definite presence of the crack beyond a crack depth ratio of 0.2 (also see Figures I.7 and I.8 in Appendix I).

Figure 5.15 (a) to (c) show the changes that occur in the resonant frequencies (experimental and numerical results) as the crack depth ratio increases from 0.0 to 0.7. Figure 5.15 (a) shows the changes that occur in the non-dimensional frequency ratios ($\omega_{cracked}/\omega_{un\text{-}cracked}$) for the first four vertical bending frequencies as the crack depth ratio

increases. It is observed that the changes in non-dimensional frequency ratios are not appreciable for a crack depth ratio less than 0.5 (in this range the non-dimensional frequency ratio is greater than 0.98). This crack depth ratio is quite large for crack detection since the structure may tend to fail catastrophically beyond this crack depth. Hence for these types of shafts, we need to obtain another type of measure that could indicate the crack presence much earlier. Figure 5.15 (b) shows the relationships that exist between experimental measurements and numerical computations of non-dimensional frequency ratios for all crack depths (for different modes). At lower crack depth ratios (<0.4) the relationship is almost linear; as crack depth ratio increases beyond this, the relationship tends to become slightly nonlinear. This seems to imply that the nonlinear effect on the resonant frequencies is marginal at crack depth ratios are less than 0.4; even beyond this crack depth ratio the nonlinear effect is not significant (also see Figures J.1 and J.2 in Appendix J).

Considering the results presented for amplitude measurement in Figures 5.11 to 5.14, it appears that measurements and comparisons made at resonant frequencies seem to be more reliable for both amplitude measurements and its slope than those at anti-resonant frequencies. Moreover sensitivity of prediction seems to be better for slopes of normalized amplitude vs. crack depth ratio than that for normalized amplitude ratio vs. crack depth ratio [since it could be observed from Figure 5.11 that change in normalized amplitude ratios vary from 1.0 to 1.2 (for first mode) between a crack depth ratio of 0.0 to 0.4; whereas the change in slopes is much higher, varying from 0.0 to 5.0 (for first mode) between a crack depth ratio of 0.2 to 0.5]. Also the velocity amplitude comparisons seem

to give much better results than the acceleration and displacement amplitude comparisons. In addition the use of results at the second resonant frequency seems to be much superior to that at first frequency.

A better crack detection method is obtained when the slope of the frequency ratio vs. crack depth ratio curve is plotted against the crack depth ratio, as shown in Figure 5.15 (c). The whole process of determining the slope of the non-dimensional curve vs. crack depth ratio was cast in a mathematical format. First the curves shown in Figure 5.15 (a) were curve-fitted and the algebraic equations that relate very closely the non-dimensional frequency ratio (y) to crack depth ratio (x = d/D) was determined for all the four modes. Then these equations were differentiated with respect to crack depth ratio (= x) to obtain the slope equation for the curve. These relationships are indicated in Table 5.4, given below. From the slope curves shown in Figure 5.15 (c), it can be observed that when the crack depth ratio is greater than 0.2 to 0.25, one can definitely say that there is a well-defined crack that is present in the structure (for both experimental and numerical results). Thus this gives a better indicator of crack presence in the rotor shaft. Incidentally, the mathematical equations given in Table 5.4 can also be used to estimate the unknown crack depth ratio, if the different experimental frequency ratios are known for different modes.

Table 5-4 Mathematical Equations Obtained for the Frequency Ratio Curve and Its Slope as a Function of Crack Depth-Ratio [Y = ($\Omega_{cracked}/\Omega_{un\text{-}Cracked}$); X = (D/D)]

Mode #	Non-dimensional frequency ratio curve	Slope of non-dimensional frequency ratio curve
Mode 1	y_1 = -0.519x3 + 0.330x2 - 0.070x + 1.000	dy_1/dx = -1.557x^2+0.66x-0.07
Mode 2	y_2 =-0.555x3 + 0.280x2 - 0.050x + 1.000	dy_2/dx = -1.665x^2+0.56x-0.05
Mode 3	y_3 =-0.387x3 + 0.229x2 - 0.046x + 1.000	dy_3/dx = -1.161x^2+0.458X-0.046
Mode 4	y_4 =-0.656x3 + 0.371x2 - 0.070x + 1.000	dy_4/dx = -1.968x^2+0.742x-0.070

In a similar manner, the relationships that exist between the non-dimensional anti-resonant frequencies and crack depth ratio are shown in Figure 5.15(a), (b) and (c). Anti-resonant frequency is the frequency at which the mechanical impedance of the shaft has the largest magnitude (or the mobility has the lowest magnitude). The results are similar to that at resonant frequencies; but the sensitivities seem to be better for anti-resonant frequencies as indicated earlier by (Afolabi, 1987). See Figures J.3 and J.4 in Appendix J for shaft # 1 and Shaft # 3.

Comparing the results shown in Figures 5.15 and 5.16 for the change in frequency ratios as a function of crack depth ratios at resonant and anti-resonant frequencies, respectively, sensitivity of measurements seem to be better for the first resonant and first anti-resonant frequencies than that for the higher frequencies. Also use of slopes of the plots seems to be the most efficient method for detecting the crack presence in the rotating shaft much early. Moreover the use of the results shown in Figure 5.11 to 5.16, would give a better procedure for carrying out a first level robust crack measurement and prediction procedure for rotor shafts.

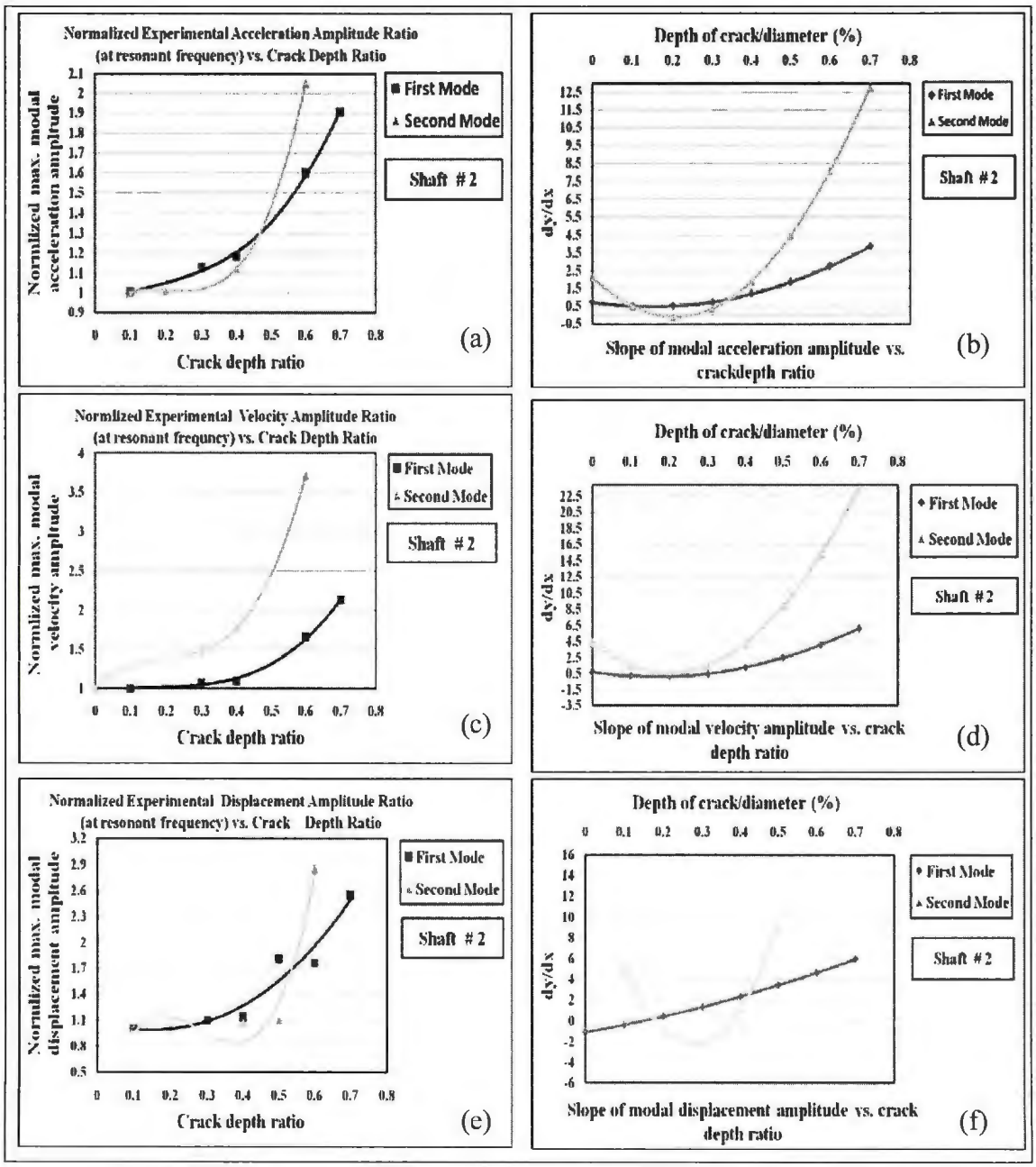

Figure 5.11 Comparison of Experimental Results for Resonant Frequency Vertical Amplitudes: a) Acceleration Amplitude Versus Crack Depth Ratio; b) Slope of Modal Acceleration Amplitude Versus Crack Depth Ratio; c) Velocity Amplitude Versus Crack Depth Ratio; d) Slope of Modal Velocity Amplitude Versus Crack Depth Ratio; e) Displacement Amplitude Versus Crack Depth Ratio; and f) Slope of Modal Displacement Amplitude Versus Crack Depth Ratio

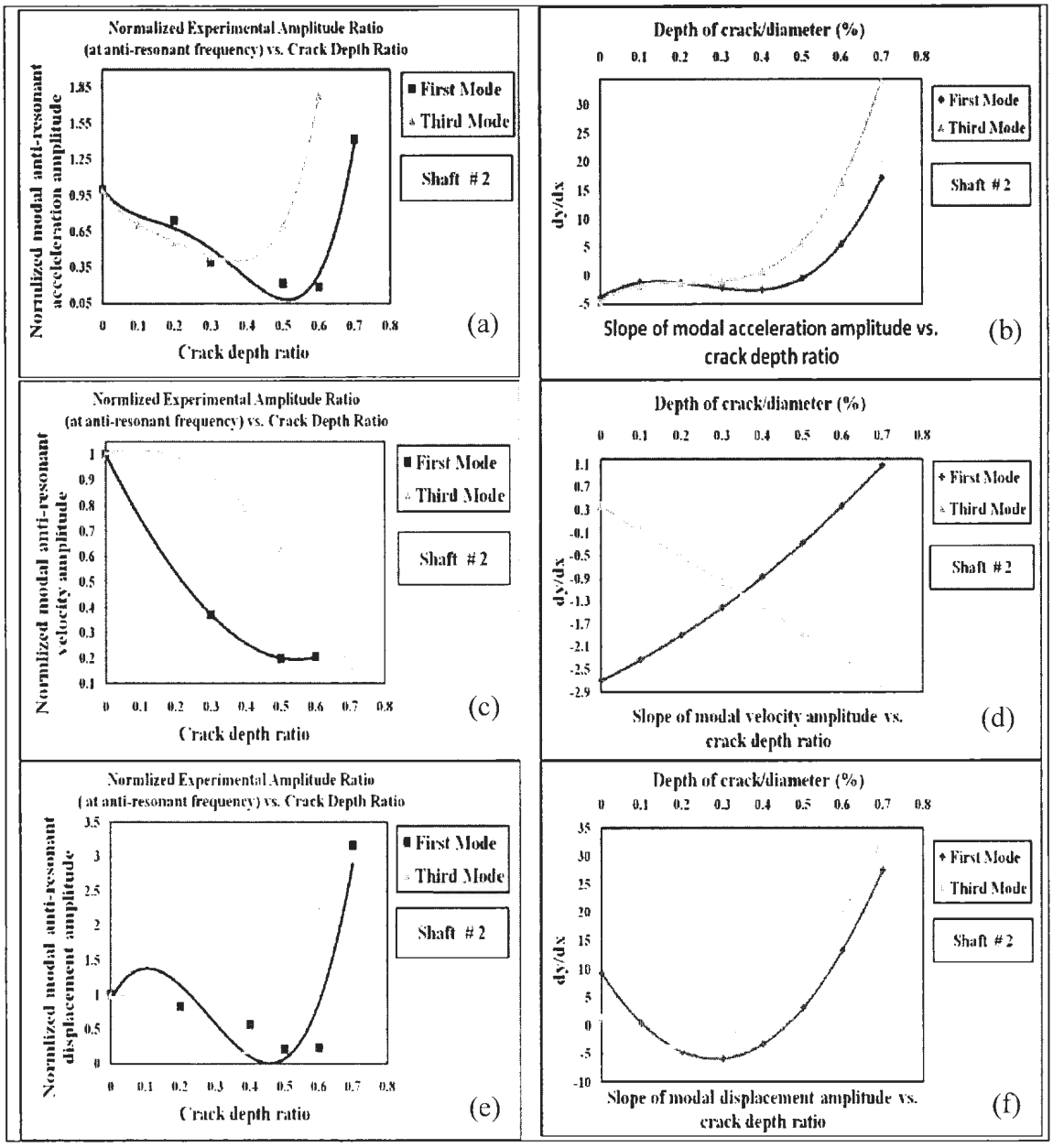

Figure 5.12 Comparison of Experimental Results For Anti-Resonant Frequency Amplitude Response: a) Acceleration Amplitude Versus Crack Depth Ratio; b) Slope of Modal Acceleration Amplitude Versus Crack Depth Ratio; c) Velocity Amplitude Versus Crack Depth Ratio; d) Slope of Modal Velocity Amplitude Versus Crack Depth Ratio; e) Displacement Amplitude Versus Crack Depth Ratio; and f) Slope of Modal Displacement Amplitude Versus Crack Depth Ratio.

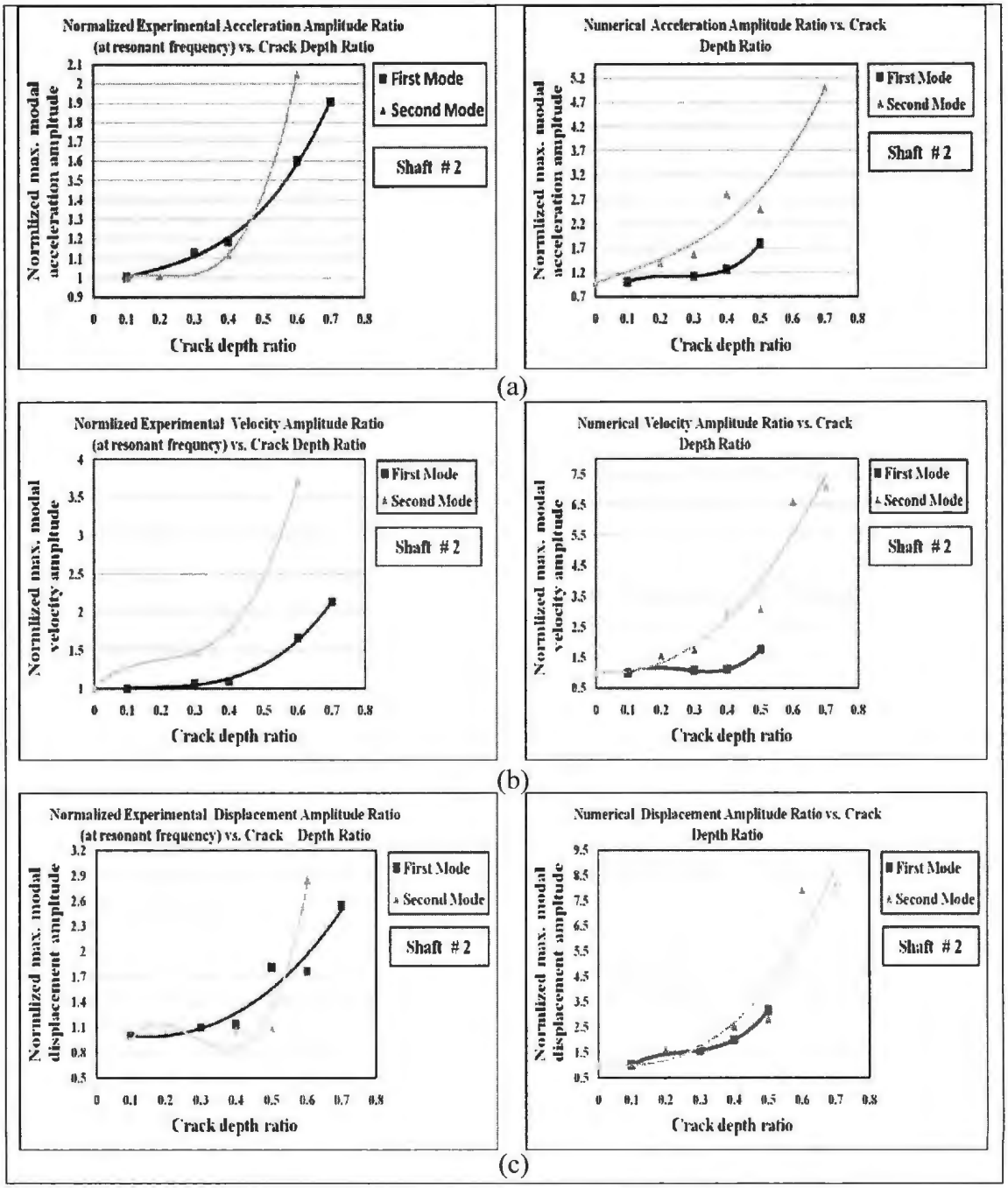

Figure 5.13 Comparison of Experimental and Numerical Results for Resonant Frequency of Shaft # 2 for (First and Second Modes): a) Acceleration Amplitude Versus Crack Depth Ratio; b) Velocity Amplitude Versus Crack Depth Ratio; and c) Displacement Amplitude Versus Crack Depth Ratio

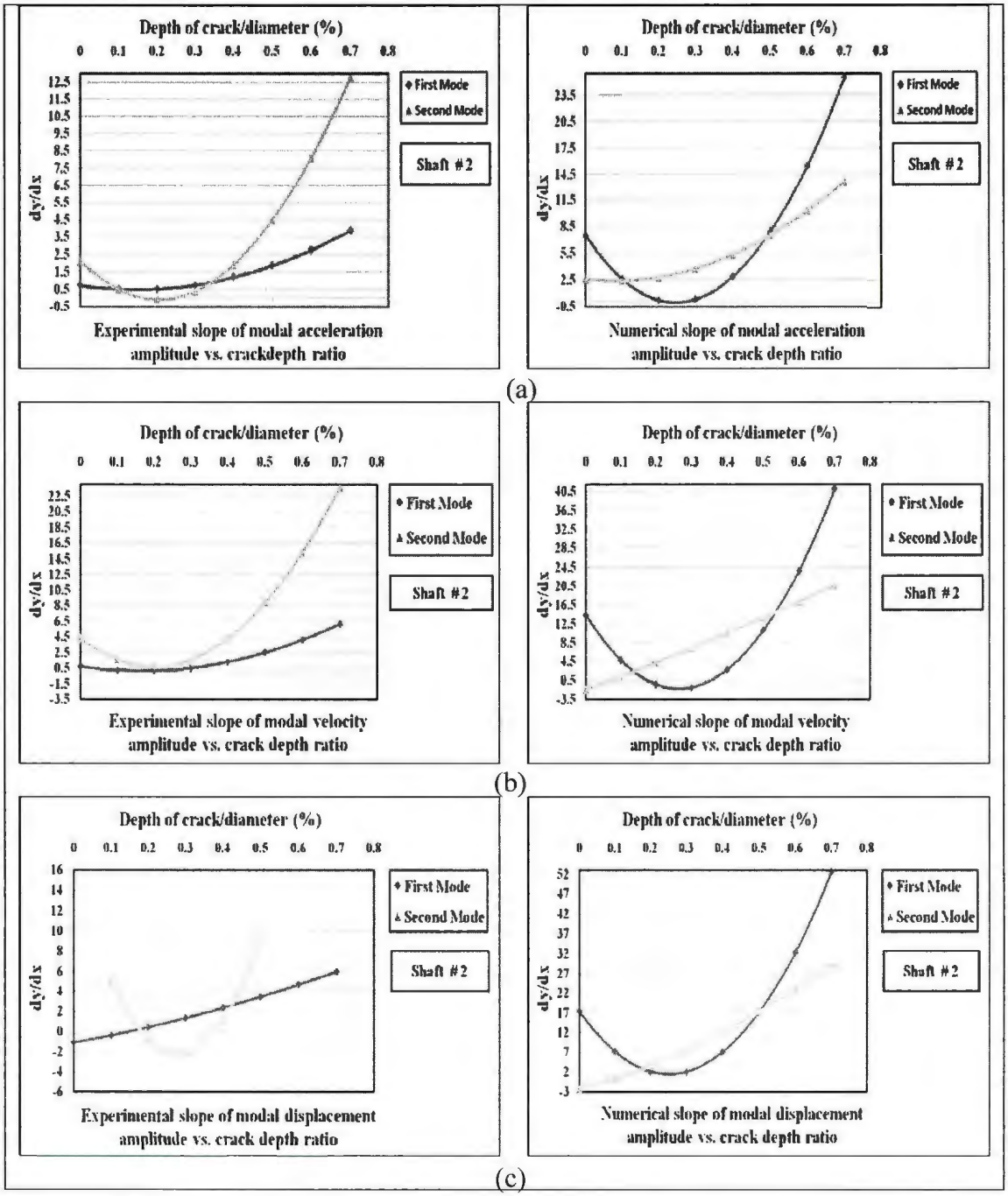

Figure 5.14 Comparison of Experimental and Numerical Results for Slopes of Resonant Frequency Amplitudes of Shaft # 2 for (First and Second Modes): a) Slope of the Modal Acceleration Amplitude vs. Crack Depth Ratio; b) Slope of the Modal Velocity Amplitude vs. Crack Depth Ratio; and c) Slope of the Modal Displacement Amplitude vs. Crack Depth Ratio.

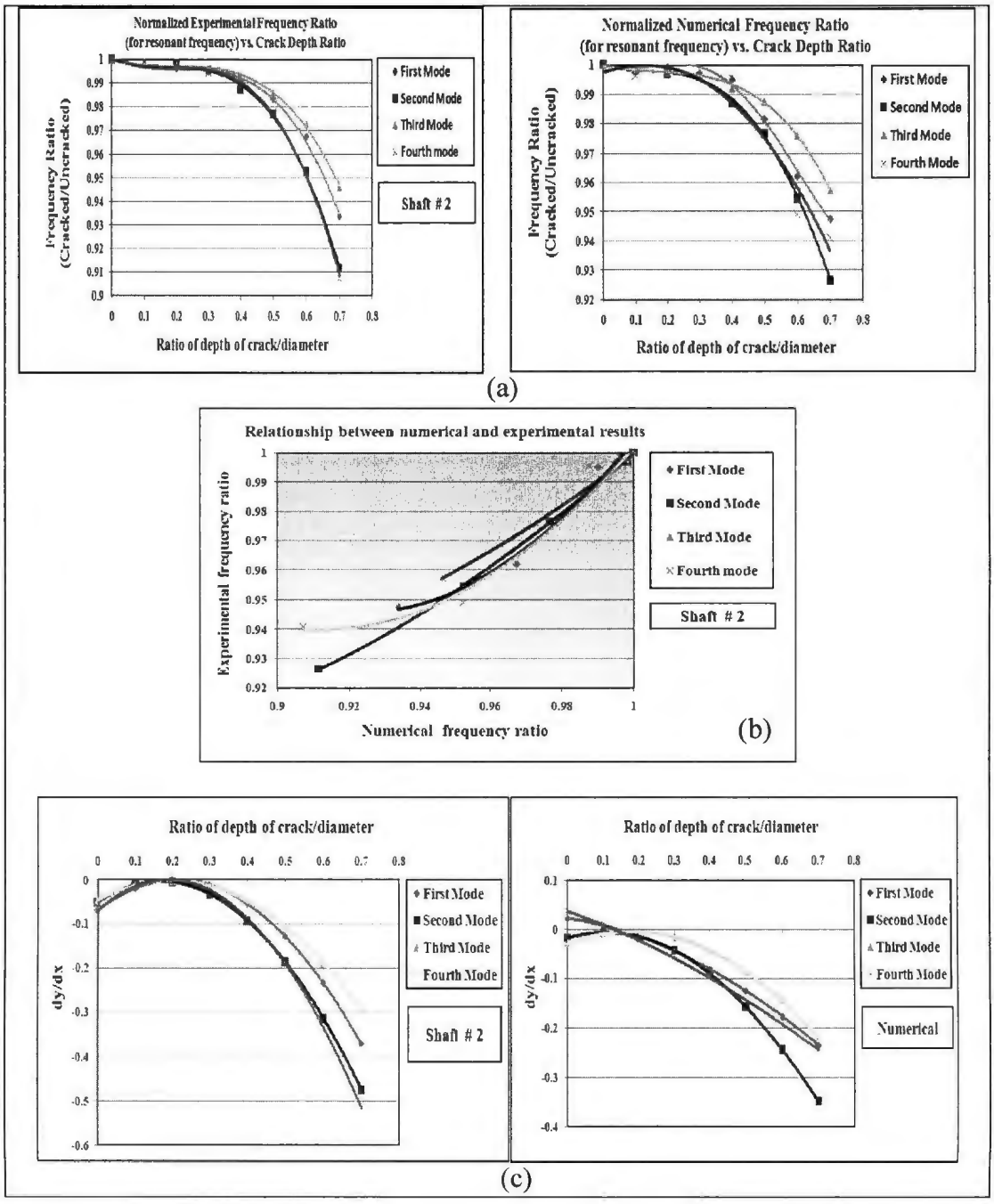

Figure 5.15 Comparison of Experimental and Numerical Results of Shaft # 2 for (at Four Resonant Modes): a) Experimental and Numerical Frequency Ratio versus Crack Depth Ratio; b) Relationship between Numerical and Experimental Results of Frequency Ratio; and c) Experimental and Numerical Slope of the Frequency Ratio vs. Crack Depth Ratio Curves.

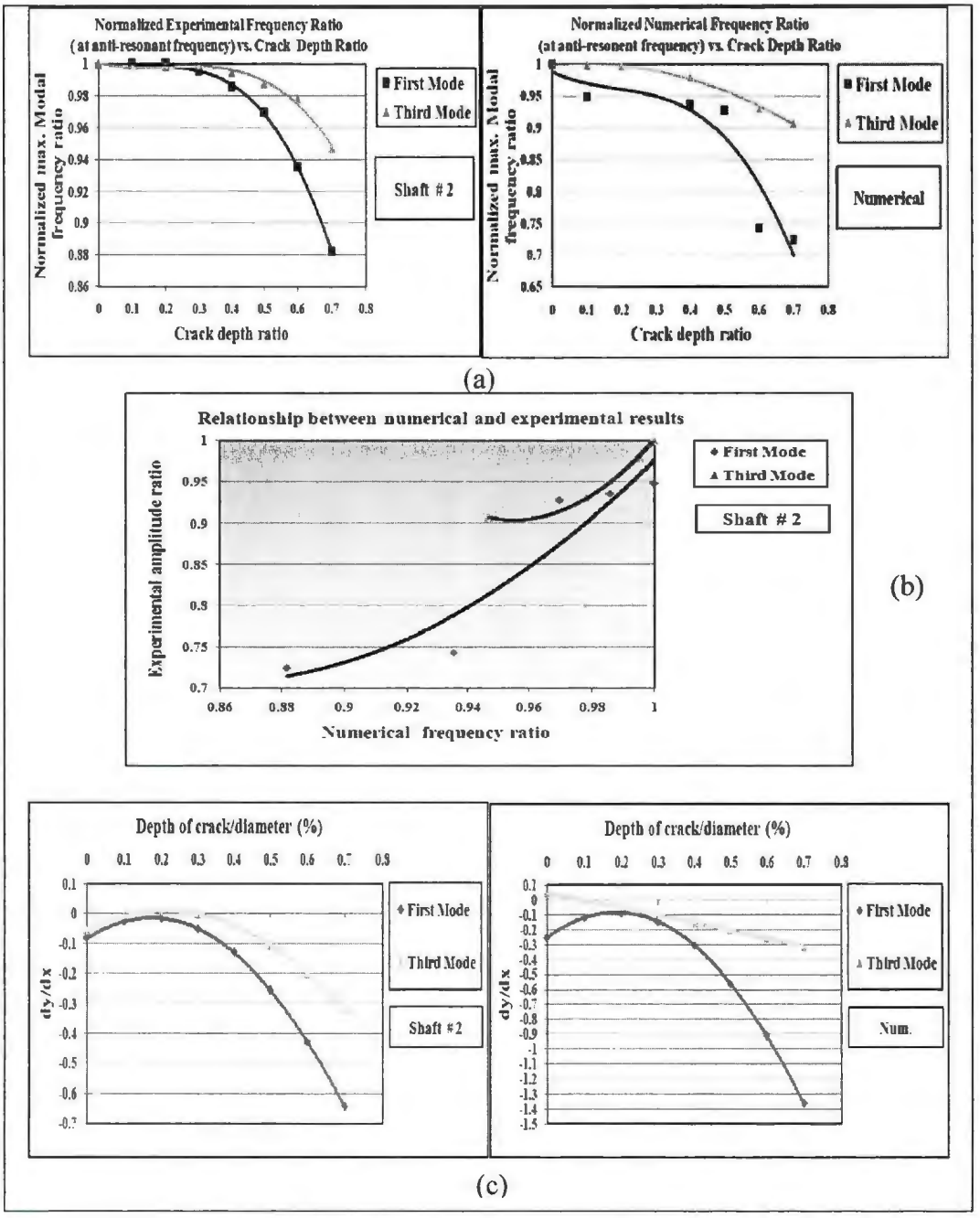

Figure 5.16 Comparison of Experimental and Numerical Results for (First and Third Modal Frequencies): a) Experimental and Numerical Ant-Resonant Frequency Ratio Versus Crack Depth Ratio; b) the Relationship between Numerical and Experimental Results Of Anti-Resonant Frequency Ratio and c) Experimental and Numerical Slope of the Frequency Ratio vs. Crack Depth Ratio.

5.4 Summary

In this chapter numerical investigations (using 3-D elements) are carried out to identify the presence of a crack in a cylindrical overhanging rotor shaft with a propeller at the free end. The three-dimensional iso-parametric elements (element types 186 and 187) available in the ANSYS FEM program were utilized for this purpose; the open crack was embedded in the shaft and the mesh generation was suitably modified to incorporate the stress intensity effects present at the crack tip.

The propeller-bearing-shaft system has been holistically modeled using FE procedure with the actual in-situ profiles for the propeller, bearings, supports and torque loading aluminum arm. Also vibration analysis for experimental results has been successfully correlated with the finite element results. These results show that it is possible to detect the crack presence beyond the crack depth ratio of 20%.

The following are some of the highlights of results obtained from this chapter: When the rates of changes of bending or torsional frequencies were plotted as a function of crack depth ratio, it was possible to detect the presence of crack in a rotor shaft above a crack depth ratio of 0.2. This will be a very good procedure for detecting the presence of a crack in the rotor shaft; the examination of the change of torsional frequencies of a rotating shaft was able to predict the presence of obtained crack even from its beginning stages. This conclusion has to be firmed up by additional experimental and numerical results on a number of shaft configurations.

The changes that take place in the vibrational amplitudes of the rotating shaft, in terms of its maximum accelerations/velocities/displacements and its slope gave a better and more sensitive predictive technique for crack presence when the crack depth ratio was greater than 0.20. It is seen that the monitoring of the rate of changes that occur in the velocity amplitudes (or its inverse impedance amplitudes) would prove to be a better predictive tool in the frequency range considered in this thesis. The curve-fitted equations obtained for the variations of modal frequencies and modal amplitudes, and as well the derivatives of the above equations would give a very good predictive method for the identification of an existing crack in the shaft. In addition the linearity of results between experimental measurements and numerical predictions indicate that the relationship between experimental and numerical results did not become nonlinear till the crack depth ratio was greater than 0.40. Even up to a crack depth ratio of 0.60 (from a crack 0.40 depth ratio) the nonlinearity between experimental measurements and theoretical analysis did not seem to be significant.

Chapter 6

Crack Detection in Shafts Using Mechanical Impedance from Experimental Measurements and Numerical Computations

6.1 Introduction

In this chapter, we will describe the analytical investigations which were carried out using an overhanging cylindrical shaft carrying a propeller at the cantilever end, in order to identify the crack existence in shafts using the mechanical impedance approach. Also the earlier experimental study given in Chapter 3, used the modal analysis software, LMS Test Lab^{TM}, for measuring and analyzing the response results from un-cracked and cracked shafts. The main objective of the part of experimental study reported in this chapter was to examine the effect of cracks on the lateral vibrations of a shaft using mechanical impedance measurements.In the numerical study, both the un-cracked and the cracked shafts (with varying crack depths) were modeled using a finite element procedure. 3-D iso-parametric elements (element types 186 and 187), available in the ANSYS FEM program, were utilized to model the system. The impedance and the previously obtained velocity frequency response functions were used to identify the crack depth in the rotor shaft system. Impedance and mobility were measured and simulated numerically in the vertical direction for the resonant frequencies and anti-resonant frequencies. The experimental results were used to validate the numerical results. From these results crack identification parameters were determined.

6.2 Definition of Mechanical Impedance

Mechanical impedance is defined as the structure's capability to resist motion when it is subjected to the effect of a given force. Mechanical impedance represents the relationship between forces and velocities acting on a given structure. Some researchers preferred to use the inverse of the mechanical impedance, the mobility (or admittance). The mechanical impedance can be expressed as a function of the forcing frequency ω, it is highly dependent on the frequency. The peak of the impedance occurs when the system has almost a zero velocity response, this occurs at the resonance frequencies.

The mechanical impedance at a point of the structure can be analytically defined as the ratio of the harmonic force, F (ω), to the velocity response V (ω) of that point on the structure. If the value of the harmonic response is V (ω), then the impedance, Z (ω) (Tapio and Jukka, 1989) is given by

$$Z(\omega) = F(\omega)/V(\omega) \tag{6.1}$$

6.3 Mechanical Impedance and Multi-Degree-of-Freedom Systems

The matrix equation for the motion of a multi-degree-of-freedom system can be expressed as

$$[m]\{\ddot{X}(t)\}+[c]\{\dot{X}(t)\}+[k]\{X(t)\}=\{F(t)\} \tag{6.2}$$

where [m], [c] and [k] are the mass, damping, and stiffness matrices of the system, respectively. X(t) is the response of the system in terms of the system displacement and

F(t) is the external force vector applied to the system. Expressing equation (6.2) in a summation form (On, 1967)

$$\sum_{\beta=1}^{N}\left[m_{\alpha\beta}\frac{d}{dt}+c_{\alpha\beta}+k_{\alpha\beta}\int dt\right]\frac{dx}{dt}=f_{\alpha}(t),\cdots\alpha=1,2,\ldots,N. \tag{6.3}$$

where N, α, and β represent the degrees of freedom of the system and coordinates, respectively. The Fourier transform of Equation (6.3) leads to,

$$\sum_{\beta=1}^{N}\left(iwm_{\alpha\beta}+c_{\alpha\beta}+\frac{k_{\alpha\beta}}{iw}\right)V_{\beta}(w)=F_{\alpha}(w),\cdots\alpha=1,2,\ldots,N. \tag{6.4}$$

where $V_\beta(\omega)$is the Fourier transform of the velocity (= dx/dt) response and $F_\alpha(\omega)$ is the Fourier transform of the excitation force. If the term within the bracket can be expressed as,

$$Z_{\alpha\beta}(w)=\left(iwm_{\alpha\beta}+c_{\alpha\beta}+\frac{k_{\alpha\beta}}{iw}\right) \tag{6.5}$$

which characterizes the frequency dependent properties of the system, then Eqn. (6.4) may be expressed as

$$\sum_{\beta=1}^{N}Z_{\alpha\beta}V_{\beta}=F_{\alpha} \tag{6.6}$$

In a proper matrix format, eqn. (6.6) can be rewritten as

$$\left[Z_{\alpha\beta}\right]\left\{V_{\beta}\right\}=\left\{F_{\alpha}\right\} \tag{6.7}$$

In eqn. (6.7), $Z_{\alpha\beta}$ is termed the point impedance parameter of the system (when $\alpha = \beta$). When $\alpha \neq \beta$ it is termed as the transfer impedance parameter. Equation (6.7) gives results in terms of the mechanical impedances of the vibrating system. Once the impedances (or its inverse, mobility) are known, the corresponding complements of dynamic stiffness (or displacements) and apparent mass (or accelerations) can be obtained by the use of proper numerical integration or differentiation of the impedance functions.

6.4 Relationship between Input and Output in the Dynamic Response of a Rotating Shaft

This section illustrates the relationship that exists between the input and output obtained from a vibrating system (in this case, a rotating shaft). The relationship can be expressed by the block diagram given in Figure 6.1, which relates the input and the output of a structural system in a direct manner. The inverse of the relationship shown in Figure 6.1 is shown in Figure 6.2 (Schwarz & Richardson, 1999). In the direct (or forward) manner, the relationship between the input and output shown in Figure 6.1 can be expressed as

$$\begin{bmatrix} H_{displacement}(\omega) \\ H_{Velocity}(\omega) \\ H_{acceleration}(\omega) \end{bmatrix} = \begin{Bmatrix} 1/X(\omega) \\ 1/V(\omega) \\ 1/A(\omega) \end{Bmatrix} \{F(\omega)\} \tag{6.8}$$

In the indirect (or inverse) manner, the input and output shown in Figure 6.2 can be expressed as

$$\begin{bmatrix} {}_{inv}H_{displacement}(\omega) \\ {}_{inv}H_{Velocity}(\omega) \\ {}_{inv}H_{acceleration}(\omega) \end{bmatrix} = \begin{Bmatrix} X(\omega) \\ V(\omega) \\ A(\omega) \end{Bmatrix} \{1/F(\omega)\} \tag{6.9}$$

The transfer functions $H_{disp.}$ (ω) are called receptance (or dynamic compliance) function for displacement or, mobility function for velocities or accelerance function for accelerations. The inverse transfer functions, $_{inv.}H_{disp.}$ (w) are called dynamic stiffness (for displacement input) or mechanical impedance (for velocity input) or apparent mass (for acceleration input) functions. The LMS system gave the real and imagery components of the accelerance data of the tested rotor shaft; using the Matlab provisions the velocity and displacement information were obtained. Similarly the inverses of the above functions were obtained by using Matlab provisions.

The characteristic features of these matrix functions can be suitably utilized to monitor and detect cracks (or damages) in structures. If the system frequencies are very low (in the case of massive structures), better sensitivity will be obtained for monitoring and detection by the use of displacement response function $H_{disp.}$ (w) or its inverse $_{inv.}H_{disp.}$ (w). If the frequencies are in the intermediate range, the use of velocity response function $H_{vel.}$ (w) or its inverse $_{inv.}H_{vel.}$ (w) (or mechanical impedance) will give better sensitivity for monitoring cracks (or damages) in the structural system. For higher frequencies (in the case of very stiff structures) the use of acceleration-related response functions $H_{accl.}$ (w) or its inverse $_{inv.}H_{accl.}$ (w) (or apparent mass) will give better sensitivity in monitoring cracks (or damages) in the structural system. In the present study, attention will be focused more on deriving information from velocity-related impedance response functions.

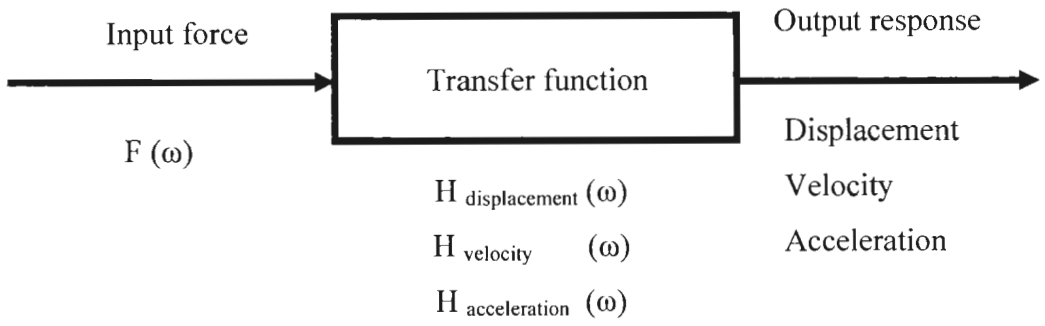

Figure 6.1 Block Diagram for Input-Output Relationship in Frequency Domain

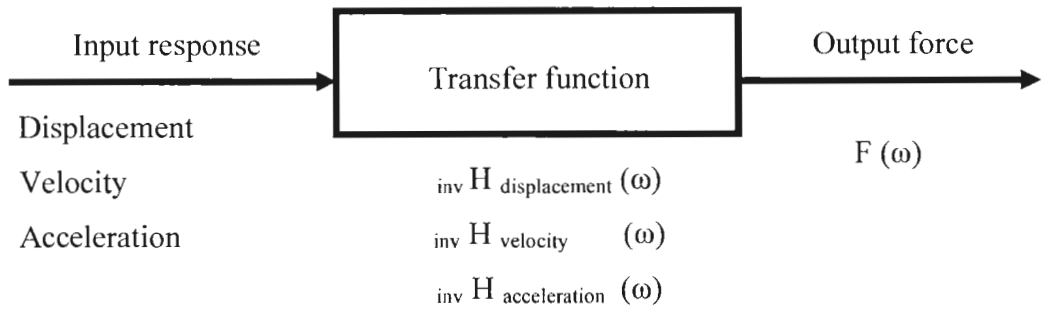

Figure 6.2 Block Diagram for the Inverse Input-Output Relationship in Frequency Domain

6.5 Presentation of Results and Discussion

Figure 6.3 shows the velocity responses of the system under applied force (impact excitation) indicating the experimental and numerical computation for velocity FRFs. All figures illustrate the frequency shifts that occur due to the increased cracking in the shaft. It is also observed that for all cases (experimental and numerical), reasonable agreements exist between numerical and experimental results. It can be seen from these figures, that the velocity response functions (VRFs) can also be used as a good tool for crack

identification. Also Figure 6.4 shows individual comparisons for some cases (intact VRFs, cracked 10% VRFs, cracked 20% VRFs, cracked 30% VRFs, cracked 40% VRFs, cracked 50% VRFs, cracked 60% VRFs, and cracked 70% VRFs.) for response functions of experimental and numerical computations. It can be seen more clearly that the shift of velocity response peaks is dependent on the change in natural frequencies and is directly proportional to the severity of the crack.

It is essential to point out two limitations in all the numerical computations reported: (i) It can be seen from the curves given in Figure 6.3 that the experimental results show an additional frequency which is not seen in the numerical computations. This additional frequency was determined to be due to the presence of a torsional frequency in the measurement of vertical displacements. In the numerical computations, the torsional and bending frequencies (as well as their response functions) could not be computed in a single numerical computation for the indeterminate shaft. Torsional and bending vibrations were calculated separately where, the shaft was permitted to either bend or rotate freely (over the support near the overhang) by the provision of zero friction (boundary condition for torsion) at the support near the overhang. The torsional frequencies were obtained correctly, when zero friction was provided at the bearing located at support # 2; and (ii) This approach was used also because of the limited capacity of the computing system. The accuracy with which the researcher could obtain response results was 0.25Hz (one could solve results up to 1000 steps for the frequency range of zero to 250Hz). These two restrictions prevented better comparison to be obtained between experimental and numerical computations.

See Figures K.1.1, K.1.2, K.1.3 and K.1.4 in Appendix K for shaft # 1 and Shaft # 3.

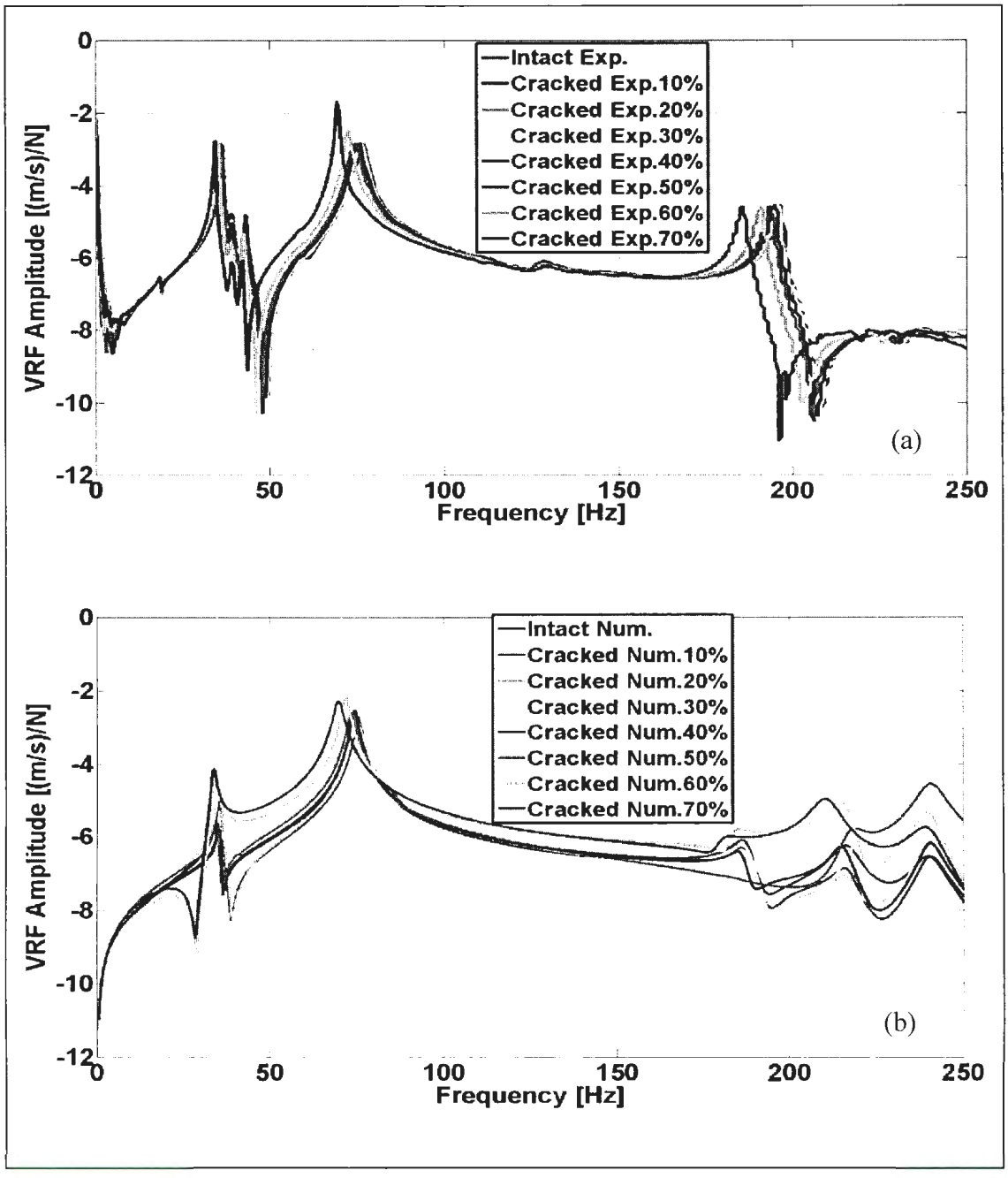

Figure 6.3 Responses of the System for; a) Experimental; and b) Numerical Computations of Velocity Response Functions (VRFs) for Shaft #2.

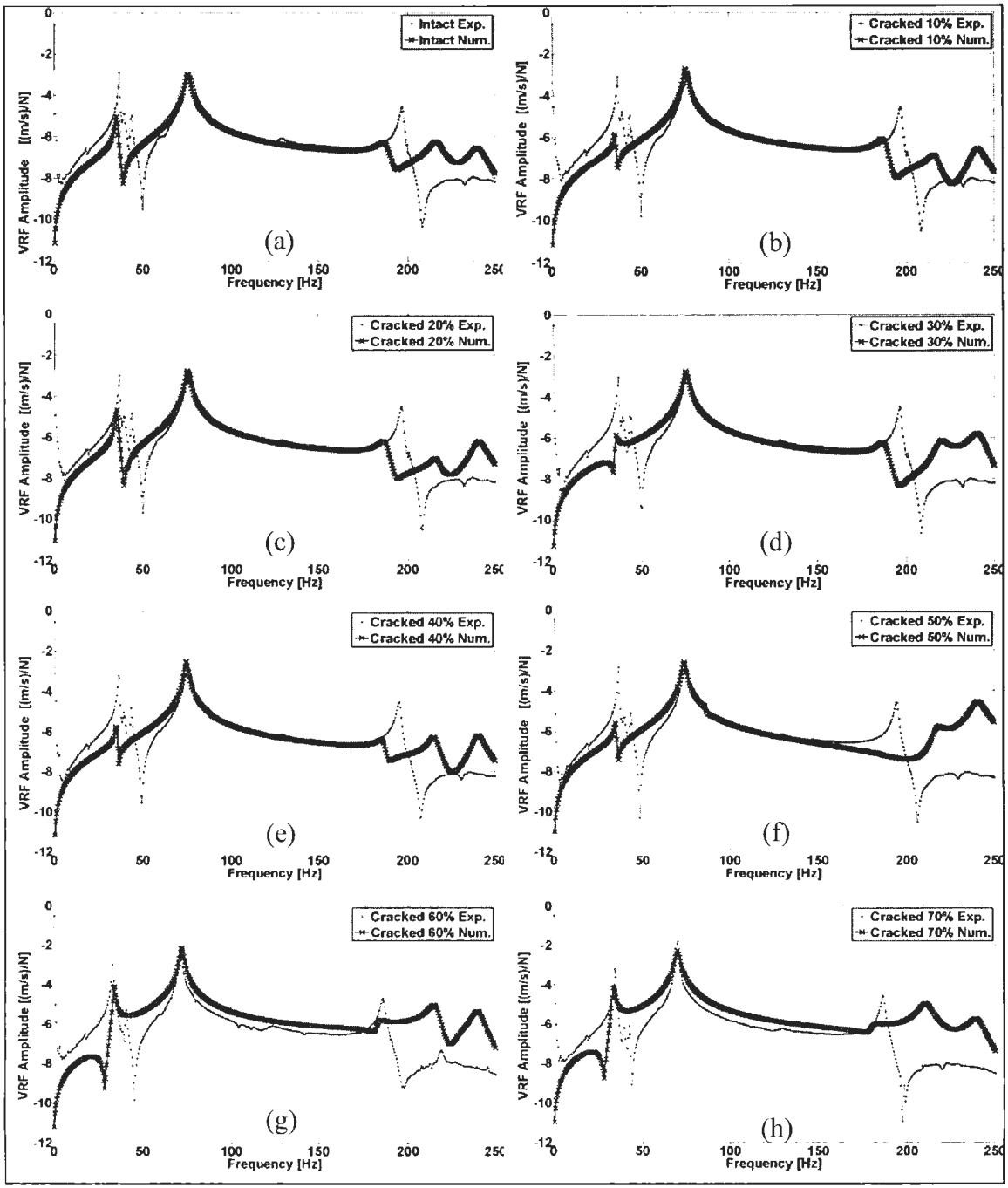

Figure 6.4 Comparison of Velocity Responses Functions (VRF) in Experimental and Numerical Computations a) Intact VRFs; b) Cracked 10% VRFs; c) Cracked 20% VRFs; d) Cracked 30% VRFs; e) Cracked 40% VRFs; f) Cracked 50% VRFs; g) Cracked 60% VRFs; and h) Cracked 70% VRFs; for Shaft # 2

Figures 6.5 and 6.6 give the experimental and numerical plots obtained by LMS Test Laboratory software and ANSYS Workbench software, respectively. The plots show the mechanical impedances of a cylindrical rotor shaft-propeller-bearing system obtained for vertical vibrations. Figure 6.5 shows the computed mechanical impedances of the cylindrical shaft for the various crack depth ratios (0.0 to 0.7). The impedance values peak when the cylindrical rotor shaft system has almost a zero velocity response. These impedance peaks are obtained at what are traditionally called as anti-resonant frequencies (where the velocity responses are almost zero) of the vibrating system. In this case the experimental anti-resonant frequencies for the un-cracked experimental rotor shaft are located at 49.51 Hz and 207.5 Hz for the first and third anti-resonances (the second anti-resonance was missing); the corresponding numerical values were 39.0 Hz and 194.0 Hz (the large differences are due to the difficulties in modeling and the limitations in the provided computational memory size). In contrast the impedance values are almost zero at the resonant frequencies. The near-zero anti-resonance frequency observed in the experimental results [see Figure 6.5 (a)] are probably due to the vibration of the foundation support to which the steel base plate of the experimental test setup is attached.

Figure 6.7 shows experimental and numerical changes in impedance and mobility for intact and 70% crack depths. Impedance and mobility were measured and simulated in the vertical direction. It can be observed from the mobility curves of Figure 6.7 (a) that the amplitudes of all the mobility carves increase for the resonant frequencies for increasing crack depths. In contrast, the amplitudes of impedance at all the experimental anti-resonant frequencies either decrease (at the first anti-resonance) or increase (at the

third anti-resonance) as crack depth increases. This trend seems to be reversal for the numerically computed impedances. At the first anti-resonant frequency the impedance amplitude seems to increase as the crack depth increases; whereas at the third anti-resonant frequency, the impedance amplitude seems to decrease as the crack depth increases. This difference between experimental and numerical computations may once again be attributed to the difficulty in combining bending and torsional motions of the rotor shaft. The trend of agreement between experimental and numerical values is very good; however only a small change occurs in mobility amplitudes at the first resonant frequency.

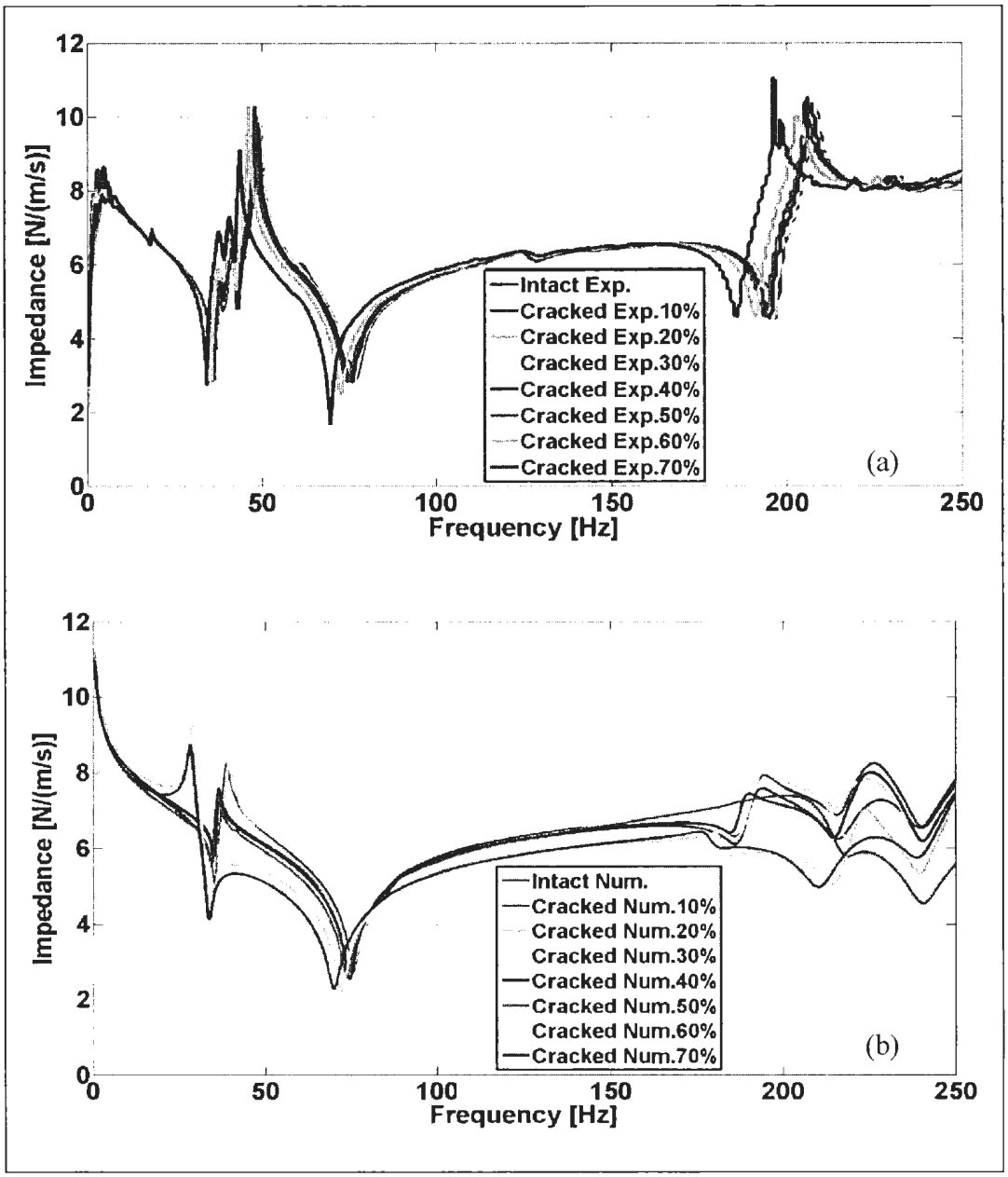

Figure 6.5 Change of the Impedances with Crack Depth for both Experimental and Numerical Results for Shaft # 2

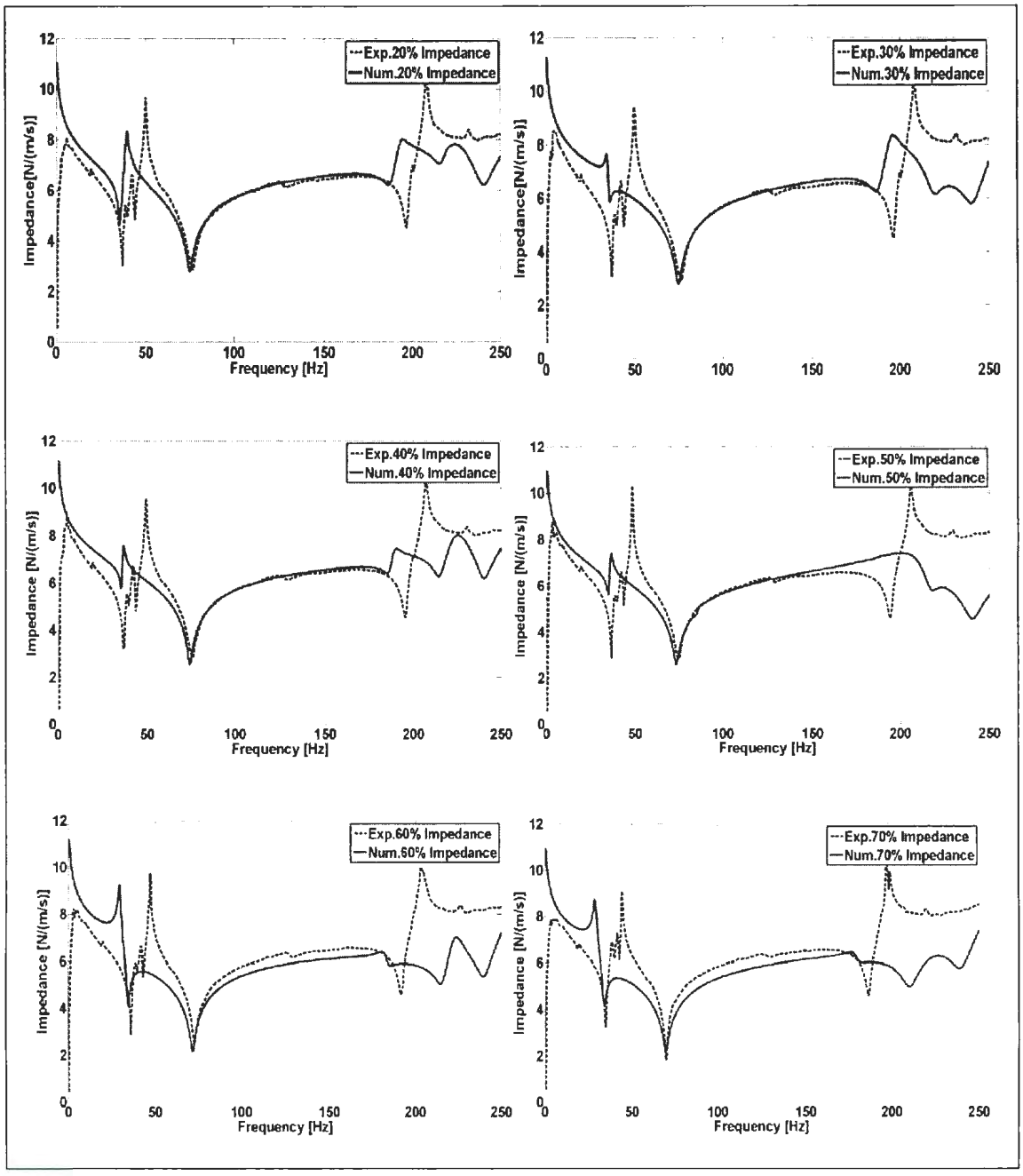

Figure 6.6 Variation of Experimental and Numerical Impedance for Different Crack Depths for Shaft # 2

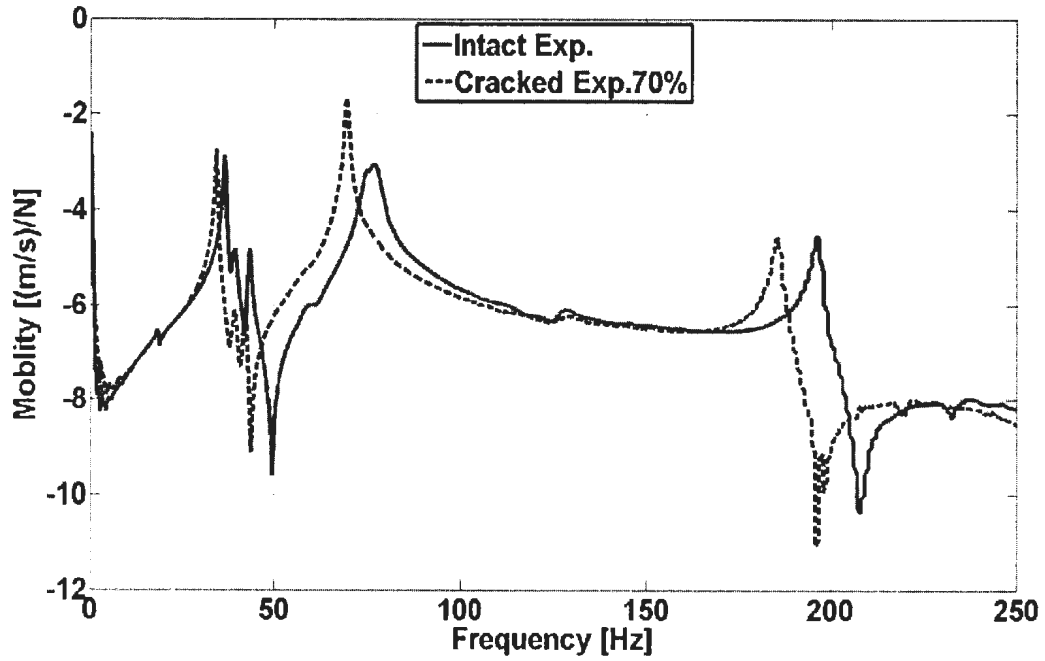

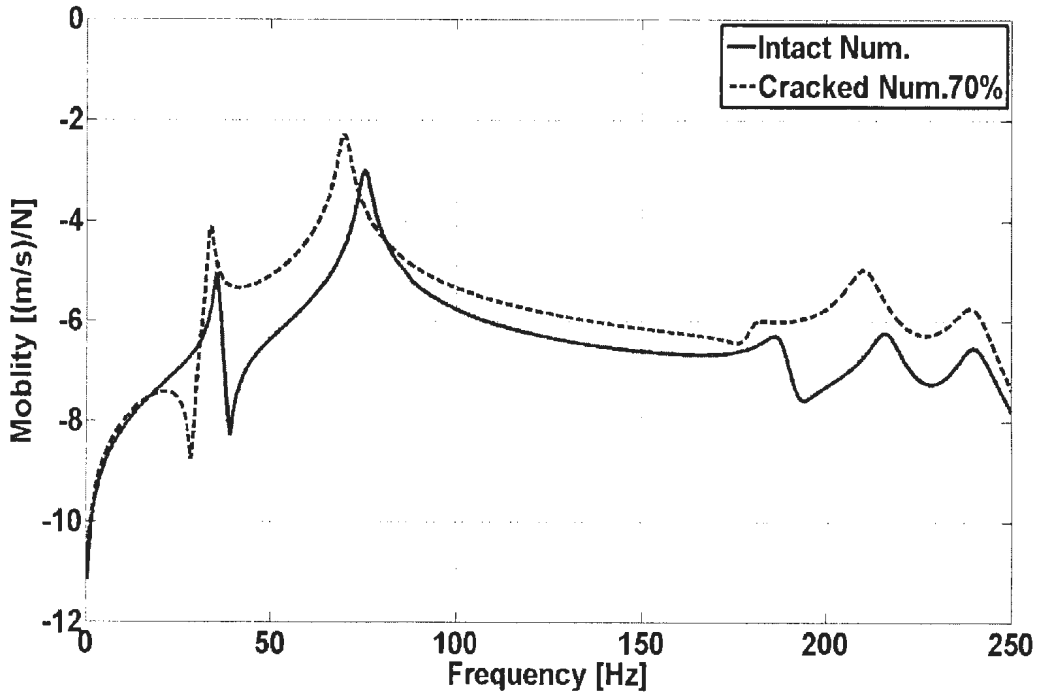

Figure 6.7 (a) Changes in the Mobility between Intact and 70% Crack Depth Ratio for Experimental and Numerical Results for Shaft # 2

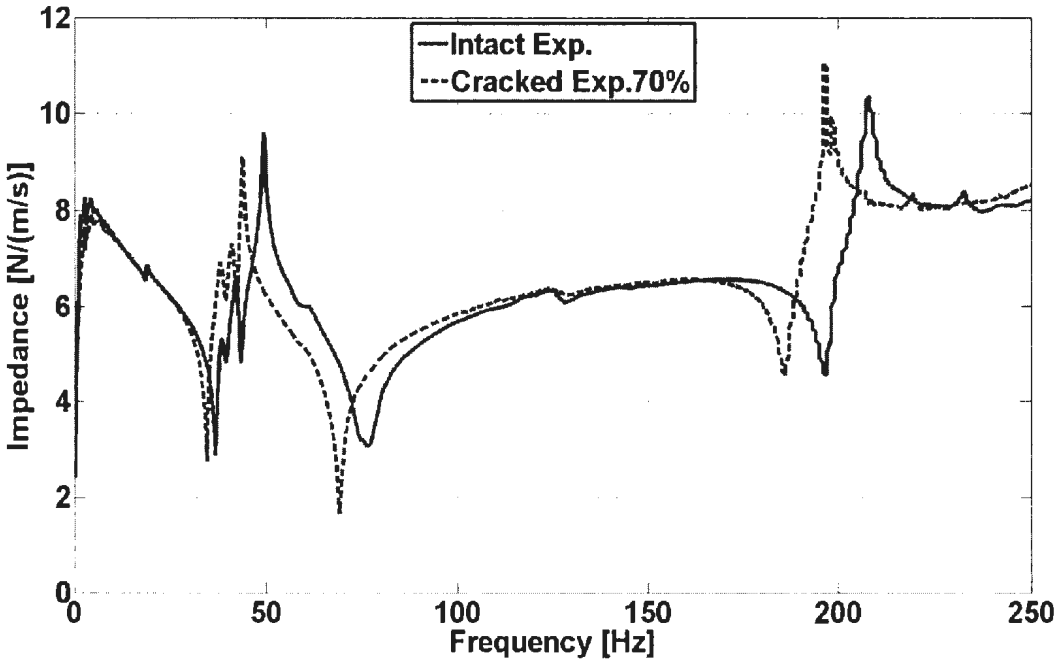

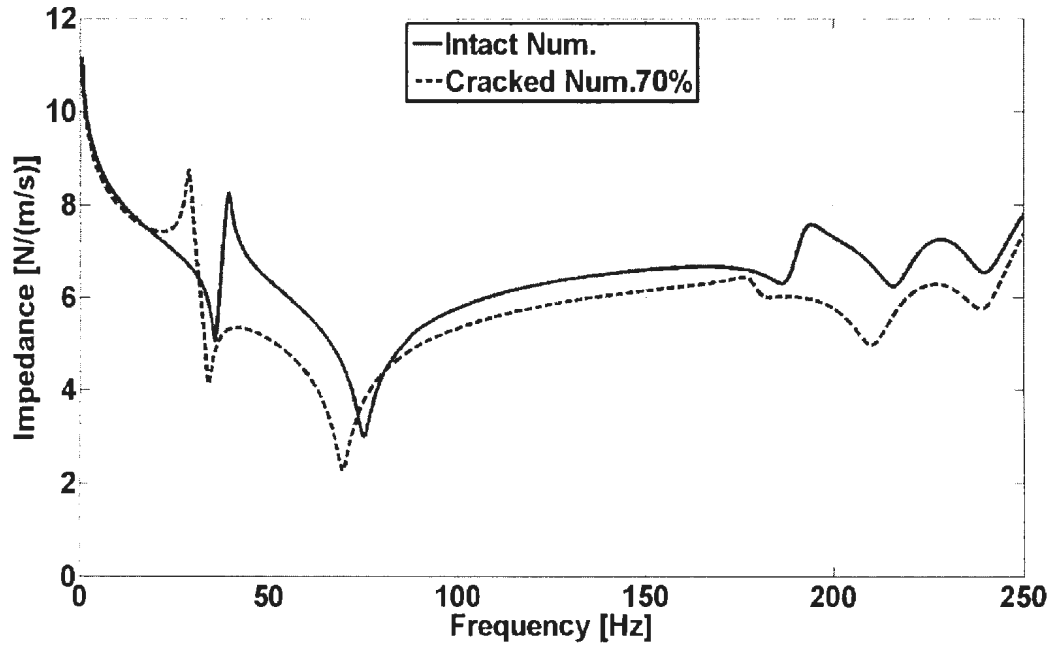

Figure 6.7 (b) Changes in the Impedance between Intact and 70% Crack Depth Ratio for Experimental and Numerical Results for Shaft # 2

Figure 6.8 (a) shows the plot of the torsional frequency ratio and crack depth ratio for experimental and numerical analysis. It shows that the change in the frequency ratio gives a much better indication of the crack presence even from the beginning stages of the crack. Figure 6.8 (b) shows the slope of the torsional frequency ratio for first experimental and numerical mode. Figure 6.8 (b) shows that beyond a crack depth ratio of 0.2 (for torsion), it shows a definitive presence of the crack. More studies need to be carried out to confirm this conclusion in a definite manner (only one shaft – shaft # 1 was strain-gaged to measure the torsional frequency).

Figure 6.9 gives the experimental impedance amplitude ratio [(maximum impedance amplitude at zero crack)/ (maximum impedance amplitude at different crack depths)] plots and slope of impedance as a function of crack depth ratio at resonant frequency. It is seen from Figures 6.9 (a) and (b) that the identifier of the mode shape change due to crack is shown better by the second mode shape than the first mode. In addition, the crack presence is indicated from the beginning when the impedance amplitude is used as the crack indicator, as seen in Figure 6.9 (a). It should also be noticed that the changes in second mode amplitudes shown in Figure 6.9 (b) are higher than that for the second model amplitude shown in Figure 6.9 (a); it is also much higher than the frequency ratio changes shown in Figures 5.14, 5.15 and 6.8. Consequently the use of impedance amplitudes seems to give more sensitive indications regarding the presence and severity of crack. Also from Figure 6.9 (b) the definitive presence of a crack is indicated beyond a crack depth ratio of 0.25 or more. The results are presented here for shaft # 2 while the rest of results, shaft # 1 and shaft # 3 are presented in Appendix L.

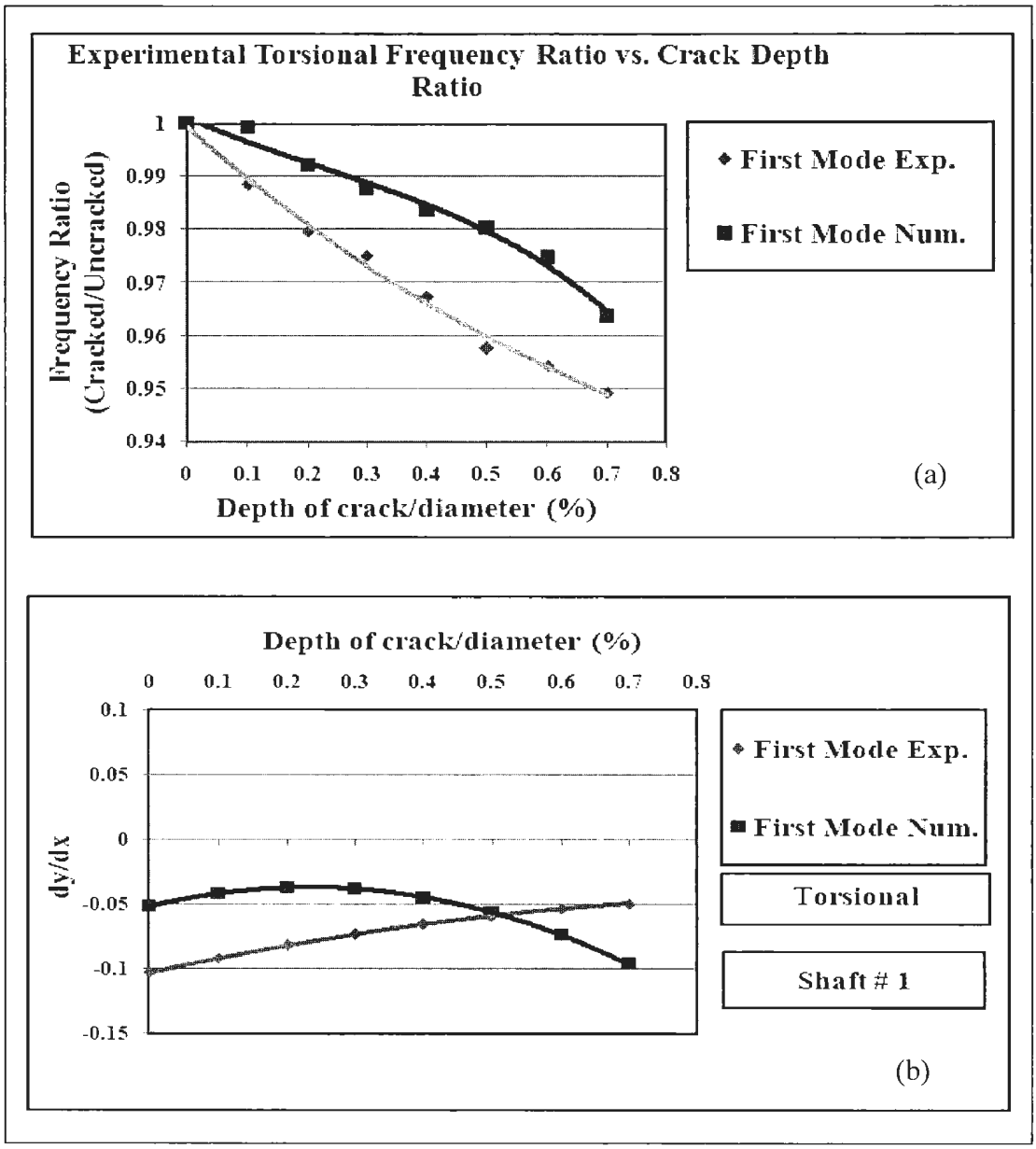

Figure 6.8 Comparison of Experimental and Numerical Results for: a) Experimental and Numerical Torsional Frequency Ratio versus Crack Depth Ratio; and b) Experimental and Numerical Torsional Slope of the Frequency Ratio for First Mode.

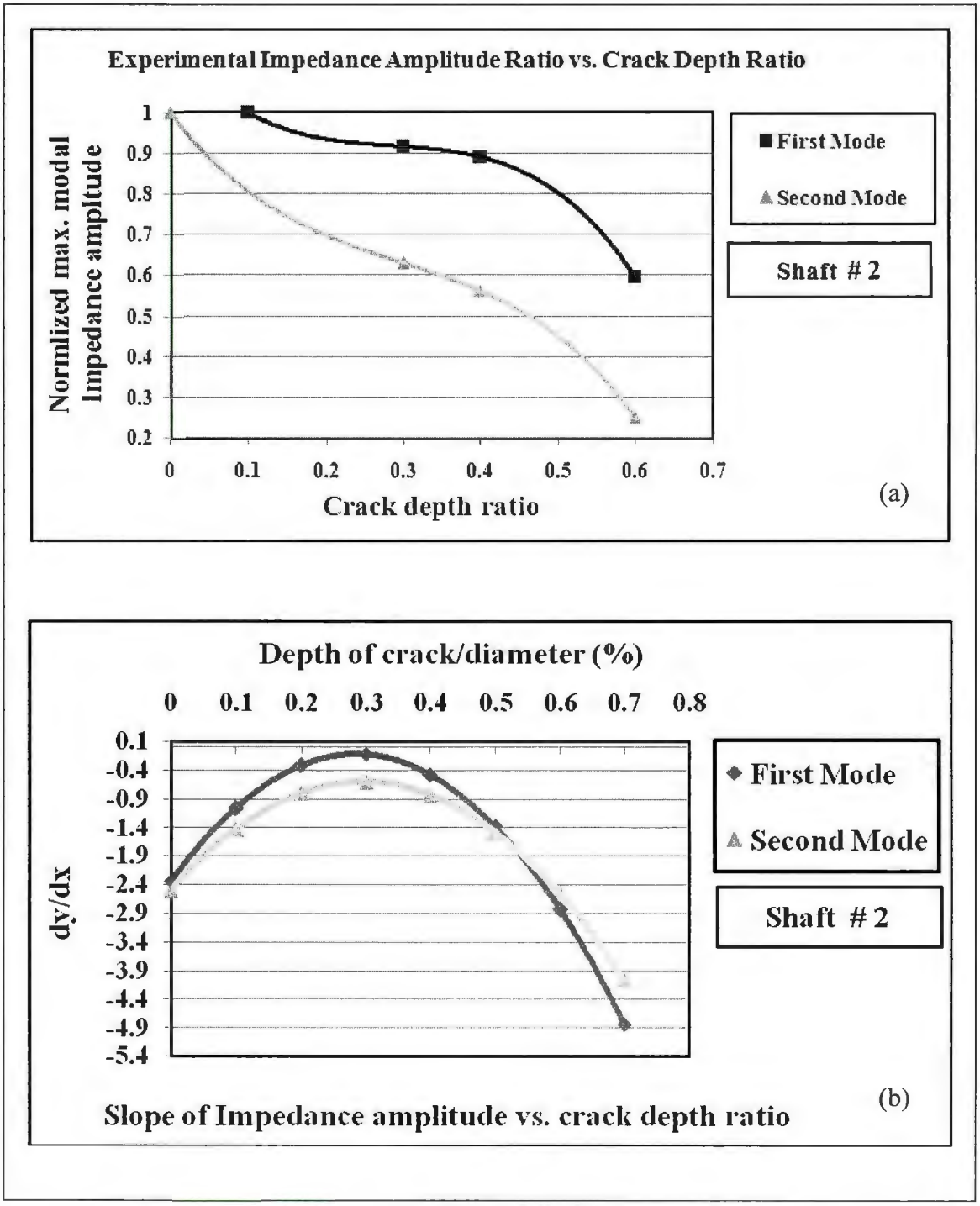

Figure 6.9 Comparison of Experimental and Numerical Results for: a) Amplitude Ratio versus Crack Depth Ratio; and b) Slope of Impedance Amplitude versus Crack Depth Ratio

6.6 Summary

In this chapter, the results of analytical investigations which were carried out, on an overhanging cylindrical rotor shaft carrying a propeller at the cantilever end, in order to identify the crack existence in shafts using the mechanical impedance approach are reported.

In the numerical study, both the un-cracked and the cracked shafts (with varying crack depths) were modeled by finite element procedure. 3-D iso-parametric elements (element types 186 and 187), available in the ANSYS FEM program, were utilized to model the system. The impedance and velocity frequency response functions were used to identify the crack depth in the shaft system. Impedance and mobility were measured and simulated in the vertical direction for the resonant frequencies and anti-resonant frequencies.

Impedance and mobility were measured and simulated in the vertical direction. The amplitudes of all the mobility curves increase for the resonant frequencies for increasing crack depth. In contrast, the amplitudes of impedance at all the anti-resonant frequencies either decrease (at the first anti-resonance) or increase (at the third anti-resonance). The trend of agreement between experimental and numerical values is very good; however only a small change occurs in mobility at the first response frequency. The use of impedance amplitudes seems to give more sensitive indications regarding the presence and severity of a crack. When impedance amplitudes at non-resonant frequencies are

plotted as a function of crack depth ratios, it can be seen that the crack presence is indicated even from the beginning of the crack shown [Figure 6.9 (a)].

A better crack detection measure is obtained when the slope of the frequency ratio vs. crack depth ratio curve is plotted against the crack depth ratio. In this case it can be observed that when the crack depth ratio is greater than 0.2 to 0.25, one can definitely say that there is a well-defined crack that is existing in the structure from the large changes that occur in the slopes of the curves (for both experimental and numerical results.

The torsional frequency ratio vs. crack depth ratio for experimental and numerical analysis shows that the change in the frequency ratio gives a much better indication of the crack presence even from the beginning stages of the crack.

Chapter 7

Conclusions and Recommendations

7.1 Conclusions

The present study consisted of two main parts: an experimental program and a numerical analysis to develop a methodology that can be used to identify the existence of cracks on a cylindrical rotor shaft with a cantilevered span. A testing rig was designed and fabricated to investigate the characteristics of the vibrating un-cracked and cracked shafts using modal testing techniques. The finite element analysis was performed using the software program ANSYS.

The experimental program consisted of two components. In the first, an off-line, experimental modal analysis was performed to determine the vertical and horizontal transverse vibrations of the shaft using a software package, LMS Test Lab ^{TM}. The second component used an off-line, experimental modal analysis technique to study the torsional vibration of the rotor shaft system. In both cases, dynamic characteristics such as natural frequencies, damping factor, and mode shapes were recorded and determined to correlate with the analytical and numerical method results. These experiments were repeated for three different rotor shaft-bearing systems the shafts were labelled, shaft No. 1, shaft No.2 and shaft No. 3. The three shafts had almost the same diameter (measured average values were 0.01588 m, 0.01586 m, 0.01589 m respectively). For each crack depth three separate tests were carried out and the results processed through the LMS

Test Lab system. Then the results were added and averaged to get the final result reported herein.

In the numerical part, investigations were carried out to identify the existence of transverse cracks on the shaft using lateral and torsional vibrations. The effects of having cracks with different depths were investigated numerically, and the results interpreted to give better understanding of the shaft's vibratory behaviour. Two different numerical models were used in the numerical computations. Following the earlier literature, the beam element, BEAM4, available in ANSYS finite element program was used for the numerical prediction of the dynamic response of un-cracked and cracked shafts as well as to verify the experimental results. In this part, a linear "three to six springs" model was used to represent the effects of each of the two ball bearings, supporting the shaft, over the (fixed) end and the other support near the cantilever end. These spring constants were determined to achieve the best agreement between un-cracked experimental and numerical results. Whereas in the second part, 3-D iso-parametric elements (20-noded, 15-noded, 12-noded and 10-noded) were used for modeling the shaft, bearings, supports, propeller, torque loading arm and the other components of the test rig. This provided a detailed modeling of the bearing connections to the shaft, as well as to the supporting frames. This detailed modeling of the shaft-propeller system using FEM procedures has given extensive insights into the behavior of the shaft-propeller system including the overall shaft behavior, the support bending, the local bending of the propeller blades, and the presence of combined modes. Vibration responses of an un-cracked and cracked shaft were obtained numerically using the finite element method and related to the

experimental results. Finite element results were used to generate numerical frequency response functions that were used to detect the crack occurrence in the rotor shaft propeller-bearings system and to compare the numerical results with experimental results.

The following contributions and conclusions have been made from the previous study:

1. In this study, five spring models were developed to represent the ball-bearing support effect, namely, six, eight, and twelve springs. It was seen that bearings with six springs, shown in Figure 4.2 (b), gave the best agreement between experimental and numerical results. This was due to the fact that that this model closely represented the elasticity effects that exist between the two tight screws that connect the inner bearing to the cylindrical shaft and the elasticity of the support provided by the two frame supports 1 and 2.
2. Even though the shaft was uniformly cylindrical, the values of the experimental and numerical natural frequencies for vertical and horizontal transverse vibrations were not the same for all the different pairs of (vertical and horizontal) modes. This was primarily due to the difference in behaviour of the supporting system such as bearings and frame supports in the vertical and horizontal directions. Consequently the difference in modeling the two orthogonal bearing support contacts by linear springs became very important so as to make the numerical values closer to the measured experimental values; this has to be done very carefully.

3. From the modeling of a crack, in a cracked shaft, by an equivalent short beam, the best fit for the length of a shaft element for first natural frequency was about 54.65mm while the best fit for second and third natural frequencies was between 30.65mm and 24.65 mm, respectively. This gave an approximate ratio (effective crack length/effective bending length for the mode) of 1/12 to 1/16 for different modes. This also seemed to be corroborated by the digitized time interval requirements for accuracy in finite-difference-related numerical integration. The above relationship could be used as a first-level inspection scheme for determining the presence of cracking in a rotating shaft.
4. The third-mode shape of this beam bending model could be used as a good indicator of the presence of a crack on the shaft. This gave a much higher variation in mode shapes than the changes in frequencies that occur due to the presence of the crack.
5. Vibration analysis for experimental results was successful in detecting the presence of a crack. These results showed that it was possible to detect a crack, around the crack depth ratio of 20% and beyond, when the rates of frequency change (as a function of crack depth ratio) were plotted as a function of crack depth ratio (between 20% and 30% crack depth ratios, the rate of change variation was found to be 3% to 4%). This is an improvement on the conclusions made by Hamidi et al (1992) where he stated that it was possible to detect cracks in rotor shafts beyond crack depth ratio of 0.3 to 0,35. However, if frequency changes were used as the crack indicator, then the changes were much smaller (between

20% and 30% crack depth ratios, the change in frequency ratio was around 0.5% to 1.0%) than that shown by the rate of change of frequency (with respect to crack depth).

6. The first torsional frequency gave a much better indication of the crack presence than the bending frequencies. The rate of change of frequency as a function of crack-to-depth ratio was higher for torsional frequency than bending frequency. For example, at 10 percent crack-to-depth ratio, the rates of change were 10 percent and 1 percent for torsional and bending cases, respectively.
7. When the rates of changes of bending or torsional frequencies were plotted as a function of crack depth ratio, it was possible to detect the presence of crack in a rotating shaft above a crack depth ratio of 0.2. This will be a very good procedure for detecting the presence of a crack on the rotating shaft.
8. Using the change of torsional frequencies of a rotating shaft one is able to predict the presence of obtained crack in its early stages of development. This conclusion has to be further investigated by additional experimental and numerical results on a number of shaft configurations.
9. The changes in the vibrational amplitudes of the rotating shaft can be used as good indices for detecting cracks having depth ratio greater than 0.2.
10. It was concluded that the rate of change of the velocity amplitude (or its inverse: impedance amplitude) can be used as a predictive tool for crack presence in the frequency range considered in this thesis.

11. The curve-fitted equations obtained for the variations of modal frequencies and modal amplitudes, as well the derivatives of the above equations, gave a very good predictive method for the identification of an existing crack in the shaft.
12. The linearity of results of the experimental measurements and the numerical predictions indicated that the nonlinear effects of the crack did not show up until the crack-depth ratio exceeded 0.40. Nonlinearity effects were not appreciable in the range of crack-depth ratios between 0.4 and 0.6.
13. There is a good agreement between the experimental and numerical results. Both the experimental and numerical results show that the frequencies of the cracked shaft decreased as the crack depth increased.
14. Impedance and mobility were measured and simulated in the vertical direction. It was found that the amplitudes of the mobility curves, measured at resonant frequencies, increased with increasing crack depth. In contrast, the amplitudes of impedance measured at all the anti-resonant frequencies either decreased (at the first anti-resonance) or increased (at the third anti-resonance) as the crack depth increased. The trend of agreement between experimental and numerical values was very good; however only a small change occurred in mobility at the first response frequency. The use of impedance amplitudes seems to give more sensitive indications regarding the presence and severity of crack.
15. Changes occurred in the non-dimensional frequency ratios ($\omega_{cracked}/\omega_{un\text{-}cracked}$) for the first four vertical bending frequencies as the crack depth ratio increased. It was observed that the changes in non-dimensional frequency ratios were not

appreciable for a crack depth ratio less than 0.5 (in this range the non-dimensional frequency ratio was greater than 0.98). This frequency ratio was very large compared to the crack depth ratio for crack detection since the structure may tend to fail catastrophically beyond this crack depth.

16. At lower crack depth ratios (<0.4) the relationship between experimental and numerical non-dimensional frequencies was almost linear; as crack depth increased beyond this, the frequency ratio tended to become slightly nonlinear. This seemed to imply that the nonlinear effect on the resonant frequencies was marginal at crack depth ratios less than 0.4; even beyond this crack depth ratio the effect was not significant.
17. A better crack detection measure was obtained when the slope of the frequency ratio vs. crack depth ratio curve was plotted against the crack depth ratio. In this case it can be observed that when the crack depth ratio was greater than 0.2 to 0.25, one can definitely say that there was a well-defined crack that was existing in the structure from the large changes that occurred in the slopes of the curves (for both experimental and numerical results).
18. Conclusions derived for anti-resonant frequencies were almost similar to the ones that were made for the resonant frequencies.
19. The torsional frequency ratio vs. crack depth ratio for experimental and numerical analysis showed that the change in the frequency ratio gave a much better indication of the crack presence even from the beginning stages of the crack.

7.2 Recommendations

For any time-limited graduate study, it is difficult to claim that the study has covered all the relevant areas of the investigation pertinent to this research. In order to complete this work, the following suggestions are recommended for future research:

a) As mentioned in the experimental work, only 14 points were used on the circular shaft to measure the lateral vibration by using LMS software and computer system. In order to ensure that there were enough points to get the best mode shapes, should be increased the measurement points. Moreover the moving of the crack location to different points of the beam would have given a crack prediction methodology for the overhanging shaft.

b) Also for measured lateral vibration only two simultaneous channels of data acquisition were used (accelerometer and impact hammer). In order to ensure more accurate measurements of the dynamic response of the cylindrical rotor shaft more simultaneous channels should be used.

c) As mentioned earlier the LMS device in the structural Lab in Memorial University was used only for measuring the lateral vibrations. In general the LMS software can be used to measure the torsional vibrations also but due to funding issues additional extension to measure the torsional vibration were not possible. The author recommends the purchase of this software addition to LMS device to measure torsional vibration in the future studies.

d) During torsional and strain gage modal tests only one shaft was used. For this part of experimental study, more experimental measurements are needed to confirm the very significant findings reported in this report.

e) The beam element, BEAM4, available in ANSYS finite element program was used for the numerical prediction of the dynamic response of un-cracked and cracked shafts as well as to verify the experimental results. Five spring models were developed to represent the ball bearing support effect, viz., six, eight and twelve springs. Consequently, better results would be obtained in future studies if other spring models containing the effect of damping were used.

f) Also in the numerical computation for response functions the desired accuracy for computations could not be achieved with the provided computer memory size in the computing system. The accuracy with which the researcher could obtain response results was 0.25Hz (one could solve results up to 1000 steps for the frequency range of zero to 250Hz). If it is possible to avoid these two restrictions (for the student research by providing on-line extra accessing computer memory space) better comparison can be obtained between experimental and numerical results.

g) In the 3D modal testing and analysis, studies could be extended to include different type of bearings instead of ball bearings alone; different type of crack shapes also instead of vertical crack alone could be used to find the results of lateral and torsional vibrations.

h) A better computational model which would combine the bending and torsional vibrations motion for an indeterminate multi-span rotor system would provide a better computational asset for these studies.

Bibliography

Adewusi, S. and Al-Bedoor, B. 2002, "Detection of Propagating Cracks in Rotors Using Neural Networks," *American Society of Mechanical Engineers, Pressure Vessels and piping Division*, Vancouver, Canada, Vol. 447, pp. 71-78.

Adewusi, S., 2000, "Detection of a Transverse Crack in a Rotating Shaft Using Wavelet Transform", Ph.D. Thesis, Submitted to The Department of Mechanical Engineering, University of Petroleum & Minerals, Saudi Arabia.

Afolabi, D., 1987, "An anti-resonance technique for detecting structural damage," *Proceedings of Fifth International Model Analysis Conference*. London, Vol. 1, pp. 491-495.

Allemang, R., J., 1990, "Vibrations: Experimental Modal Analysis," UC-SDRL-CN-20-263-692, Department of Mechanical, Industrial and Nuclear Engineering, University of Cincinnati, Ohio, pp. 18 – 21.

Bachschmid, N., Pennacchi, P., and Tanzi, E., "Torsional Behavior of Cracked Rotors," *IMECHE Conference Transactions*, Swansea, Wales, Issn 1356-1448, pp. 553-562.

Bamnios, G. and Trochidis, A., 1995, "Mechanical Impedance of a Cracked Cantilever Beam," *Acoustical Society of America* Vol. 97, No. 6. Bamnios, Y., Douka, E., and Trochidis, A., 2002, "Crack Identification in Beam Structures Using Mechanical Impedance," *Journal of Sound And Vibration*, Vol. 256, No. 2, pp. 287-297.

Bieryla, D., Trethewey, M., Lissenden, C. M. Lebold, and Maynard, K., 2005, "Shaft Crack Monitoring Via Torsional Vibration Analysis; Part 1 - Laboratory Tests," 23nd *International Modal Analysis Conference*, Orlando, FL, USA.

Calibration chart for impact hammer, Type 8206-002, Bruel & Kjaer Calibration system No: 150157.1 and is traceable to the national institute of standards and Technology, USA and Physikalisch-Technische Bundesanstalt, Germany. 2009.

Chandrupatla, T., Belegundu, A., 2002, "Introduction to Finite Elements in Engineering," *Third Edition, Prentice Hall, Upper Saddle River*, New Jersey, pp. 240 and 244.

Chen,Y., 1996, "Crack Detection in Plated T· Joints through Vibration Techniques," Ph.D. Thesis, Faculty of Engineering and Applied Science Memorial University of Newfoundland, St John's, Canada, 165p.

Chenea, P., 1952. "On Application of Impedance Method to Continuous Systems," *American Society of Mechanical Engineers*, pp. 233-236

Cho, S. Han, S. Park, C. and Kim, Y., 2006, "Noncontact Torsional Wave Transduction in A Rotating Shaft Using Oblique Magnetostrictive Strips," *Journal of Applied Physics*, Vol. 100, No.10, pp. 104903-6.

Das, B., Kassimali, A., and Sami, S., 1994, "Engineering Mechanics Statics," Richard D. Irwin, Boston, Massachusetts, Inc., pp. 562-564.

Dimarogonas, A., 1996, "Vibration of Cracked Structures: A State of the Art Review," *Engineering Fracture Mechanics*, Vol. 55, No. 5, pp.831.

Doebling, S. W., Farrar, C. R., Prime, M. W., and Shevitz, D. W., 1996, "Damage Identification and Health Monitoring of Structural and Mechanical Systems from Changes in Their Vibration Characteristics," *Los Alamos National Laboratory is operated by the University of California for the United States Department of Energy under contact* W-7405-ENG-36, LA – 13070-MS, UC-900, Issued: May 1996.

Doosan, Components in turbines and generators for nuclear and thermal power plants, (7:20 PM, Saturday August, 25 2012). Dorfman LS.,Trubelja M., 1999, " Torsional monitoring of turbine-generators for incipient failure detection," *Proceedings of the Sixth EPRI Steam Turbine/Generator Workshop*, St. Louis, Missouri, August 17–20,. pp. 1–6.

Downer, L., 2010, "Detecting Damage in Beams and Structures through Modal Analysis,", Master of Engineering thesis, Memorial University, St. John's, NL, Canada, 262p.

Elshafey, A., Marzouk, H., and Haddara, M., 2011, "Experimental Damage Identification Using Modified Mode Shape Difference," *Journal of Marine Science*, Vol. 10, pp. 1-3.

Fayyadh, M., and AbdulRazak, H., 2011, "Application of weighted average on modal parameters for damage detection algorithms: Case study on steel beam," *International Journal of the Physical Sciences,* Vol. 6, No. 25, pp. 5912-5921.

Ferfecki, P., and Ondrouch, J., 2007, "Computation of the Steady-State Response of a Rotor System to the Presence of a Transverse Crack," *Centre of advanced innovation technologies.*

Ganeriwala, S. Kanakasabai, V. and Richardson, M., 2011, "Modes Indicate Cracks in Wind Turbine Blades," *Presented at IMAC XXIX*, Jacksonville, FL. Garrett, P., Guindon, E., Trethewey, M., Lissenden, C., Lebold, M., and Maynard, K., 2005, "Shaft Crack Monitoring via Torsional Vibration Analysis; Part 2-Field Applications," *23rd International Modal Analysis Conference*, Orlando, FL, USA.

Gounaris, G., and Papadopoulos, C., 2002, "Crack Identification in Rotating Shafts by Coupled Response Measurements," *Engineering Fracture Mechanics*, Vol. 69, pp. 339-352.

Hamidi, L., Piaud, J. and Massoud, M., 1992, "A Study of Crack Influence on the Modal Characteristics of Rotors," *International Conference on Vibrations in Rotating Machinery*, Bath, UK, No. C432/066, pp. 283-288.

Jian-bin, L., Hai-feng, Z., and Di, S., 2012., " Research for the Crack Dynamic Monitoring of Crank Shaft of Marine Diesel Engine Based on Magnetic Memory Technology," *Information Technology Journal*, Vol. 11 (4), pp. 516-519. Kane, J., and McGoldrick, R., 1949, "Longitudinal Vibrations of Marine Propulsion-Shafting Systems," *Society of Naval Architects and Marine Engineers*, Vol. 57, pp. 193-232.

Kisa, M., and Arif, M., 2006, "Modal Analysis of Multi-Cracked Beams with Circular Cross Section," *Engineering Fracture Mechanics*, Vol. 73, No. 8, pp. 963-977.

Kumar, C., and Rastogi, V., 2009, "A Brief Review on Dynamics of a Cracked Rotor," *International Journal of Rotating Machinery*. Volume 2009 (2009), Article ID 758108, 6 pages,.

Lahti, T., and Linjama, J., 1989, "Measurement of reflection and impedance in a beam by the structural intensity technique," *Technical Research Centre of Finland*, Research Reports 625.60.

Larry, S., Dorfman, and Trubelja, M., 1999, "Torsional Monitoring of Turbine-Generators for Incipient Failure Detection," *Structural Integrity Associates*.

Li, X., Yao, H., Ren, Z., and Wen, B., 2008, "Simulation of Dynamic Characteristics of Faulty Multi-Span Rotor System through FEA," *15thInternational Congress on Sound and Vibration*, Daejeon, Korea. Vol. 29, No. 2, pp. 250-253.

Lissenden, C., Tissot, S., Trethewey, M., and Maynard, K., 2007, "Torsion Response of a Cracked Stainless Steel Shaft," *Journal of compilation Blackwell Publishing Ltd. Fatigue Fracture Engineering Mater Structure*, Vol. 30, pp. 734–747.

Liu, D., 2004, "Damage Detection In Mechanical Structures Through Coupled Response Measurements", Ph.D. Thesis, Submitted to The Division of Mechanical Engineering, University of Queensland, Brisbane, Australia.

Manley, R., 1941, "Mechanical Impedance of Damped Vibrating Systems," *Journal of the Royal Aeronautical Society*, Vol. 45, No. 371, pp. 342-348.

McMaster-Carr (Princeton, New Jersey, USA) supplies products (including bearings) used to maintain manufacturing plants and large commercial facilities worldwide. Details available in www.mcmaster.com website on September 15, 2011.

Nautic, Boat propeller shaft, (7:45 PM, Saturday August, 25 2012). http:// www. Nauticexpo.com/boat-manufacturer/propeller-shaft-17046.html

On, F. J., 1967, "Mechanical Impedance Analysis for Lumped Parameter Multi-Degree of Freedom/Multi-Dimensional Systems," NASA TN D-3865, spring field, Virginia. Owolabi, G., M., 2001, "Crack identification Procedures in Beams Using Experimental Modal Analysis," Master of Engineering Thesis, Faculty of Engineering and Applied Science Memorial University of Newfoundland, St John's, Canada, 191p.

Owolabi, G., M., Swamidas, A. S. J. And Seshadri, R., 2003, "Crack detection in beams using changes in frequencies and amplitudes of frequency response functions," *Journal of Sound and Vibration*, Volume 265, Issue 1, p. 1-22. Pennacchi, P. and Vania, A., 2008, "Diagnostics of a Crack in a Load Coupling of a Gas Turbine Using the Machine Model and the Analysis of the Shaft Vibrations," *Mechanical Systems and Signal Processing*, Vol. 22, No. 5, pp. 1157-1178. Petroski, H., J., 1981, "Simple Static and Dynamic Models for the Cracked Elastic Beams," *International Journal of Fracture*, Vol. 17, No. 4, pp. R71–R76.

Ping, H., 1997, "Coupled Axial and Bending Vibrations of a Uniform Beam-Column with an Oblique Crack," Ph.D. Thesis, Submitted to the Department of Mechanical Engineering, University of Washington, United States.

Prabhakar, S. Sekhar, A. and Mohanty, A., 2001, "Detection and Monitoring of Cracks Using Mechanical Impedance of Rotor-Bearing System," *Journal of the Acoustical Society of America*, Vol. 110, No. 5, pp. 2351-2359.

Prabhakar, S., Mohanty, A., and Sekhar, A., 2002 "Crack Detection by Measurement of Mechanical Impedance of A Rotor-Bearing System," *Acoustical Society of America*, Vol. 112, No. 6, pp. 2825-2830.

Ramesh, T. and Sekhar, A. 2008, "Detection of Two Cracks in a Rotor-Bearing System Using Amplitude Deviation Curve," *Journal of Sound and Vibration*, Vol. 314, No. 3, pp.457-464.

Rao, S., 1995, "Mechanical Vibrations," Addison Wesley, New York, p. 688.

Rolls-Royce plc, 2012, Hybrid Shaft Generator (HSG) http://www.rolls-royce. com/ marine/ship_design_systems/prop_sys/hsg/.

Rytter, A., 1993, "Vibrational Based Inspection of Civil Engineering Structures," Ph.D. thesis, Department of Building Technology and Structural Engineering, University of Aalborg, Aalborg, Denmark.

Sabnavis, G., Gordon, R., Kasarda, M., and Quinn, D., 2004, "Cracked Shaft Detection and Diagnostics: A Literature Review," *The Shock and Vibration Digest*, 36(4), pp. 287-296.

Schwarz, B. & Richardson, M. (1999), "Experimental modal analysis," CSI Reliability Week, Orlando, FL, 12p. Sekhar, A., and Srinivas, B., 2003, "Dynamics of Cracked Composite Shafts," *Journal of Reinforced Plastics and Composites*, 22(7), pp. 637-653.

Shen, I., 1995, "Vibration of Three- Dimensional, Finite, Linear, Elastic Solid Containing Cracks," *Journal of Applied Mechanics*, Vol. 62, No. 2, pp.282-288.

Sinou J. J. and Lees A.W., 2007, "A Non-Linear Study of A Cracked Rotor," *European Journal of Mechanics and Solids*, Vol. 26, pp. 152–170.

Sudhakar, G., and Sekhar, A., 2010, "Model Based Shaft Crack Identification in Rotating Machinery," *Turbine Technical Conference and Exposition presented by ASME International Gas Turbine Institute*, 6(23812), pp. 473-480.

Thompson, K., 1991, "Fatigue Crack Growth from Surface Flaws in Smooth and Notched Shafts Subjected to Axial and Torsional Loads," Ph.D. Thesis, Submitted to The Department of Mechanical Engineering, University of Stanford, United States.

Wang, P., Davies, P., Starkey, J., and Routson, R., 1992, "A Torsional Vibration Measurement System," *Transactions on Instrumentation and Measurement*, Vol. (41), No. 6, pp. 661-666.

Wauer, J., 1990, "On the Dynamics of Cracked Rotors: A Literature Survey," *Applied Mechanics Reviews*, Vol. 43(1), pp. 13-17.

Yang, B. and Suh, C., 2005, "Non-Linear Characteristics of a Cracked Rotor–Journal Bearing System", *Proceeding of the Institution of Mechanical Engineers, Part K: Journal of Multi-Body Dynamics*, Vol. 219, No. 1/2005, pp. 87-108.

Yang, X., 2001, " Vibration Based Crack Analysis and Detection in Beam Using Energy Method," Ph.D. Thesis Submitted to Faculty of Engineering, Memorial University, St. John's, NL, , pp. 71-74 and 106.

Zakhezin, A., and Malysheva, T., 2001, "Modal Analysis Rotor System for Diagnostic of the Fatigue Crack," *Condition Monitoring Conference, St. Catherine's College*, Oxford, UK.

Zhinong, L., Sun, J., Han, J., Chu, F., and He, Y., 2006, "Parametric Bispectrum Analysis of Cracked Rotor Based on Blind Identification of Time Series Models," *Proceedings of the 6th World Congress on Intelligent Control and Automation*, Dalian, China.

APPENDIX

Appendix A – "Measured Natural Frequencies for Lateral Vibration" "Numerical Values for Beam Type of Modelling Shown within Brackets"

A.1 Measured Natural Frequencies for Lateral Vibration

Table A.1.1 (a) Experimental Values (Shaft # 1) of Natural Frequencies for Various Crack Depth-Ratios (Numerical Values Shown Within Brackets –V- Vertical and H – Horizontal and Torsional).

0	Crack depth ratios							
	0.0%		10%		20%		30%	
	V	H	V	H	V	H	V	H
First	34.9 (35.577)	41.626 (41.182)	34.505 (35.594)	41.546 (41.113)	34.137 (35.551)	41.427 (41.173)	34.32 (35.471)	41.187 (41.107)
Second	76.8 (75.247)	78.284 (78.245)	76.426 (75.113)	78.204 (78.102)	76.067 (75.021)	78.09 (78.017)	75.838 (74.933)	77.991 (78.129)
Third	190.617 (187.88)	197.9 (199.22)	190.824 (187.51)	197.934 (198.97)	190.012 (187.43)	197.82 (198.82)	189.882 (187.4)	197.81 (199.4)
Fourth	365.75 (360.1)	338.874 (381.49)	364.380 (358.72)	335.279 (380.75)	364.209 (358.99)	336.490 (380.58)	363.309 (362.09)	336.507 (383.3)
First natural frequency for torsion	43.716 (43.453)		43.213 (43.422)		42.826 (43.111)		42.628 (42.92)	
Frequency	Crack depth ratios							
	40%		50%		60%		70%	
	V	H	V	H	V	H	V	H
First	33.989 (35.402)	41.036 (41.575)	33.848 (34.922)	40.78 (41.002)	32.647 (34.23)	40.486 (40.497)	30.614 (33.706)	39.849 (40.583)
Second	75.483 (74.27)	76.564 (77.997)	74.191 (73.48)	74.625 (77.79)	72.808 (71.832)	74.376 (76.594)	67.27 (69.705)	74.232 (76.879)
Third	189.431 (186.4)	197.684 (198.66)	188.099 (185.56)	197.174 (198.76)	186.108 (183.36)	196.551 (197.05)	178.965 (179.87)	194.45 (196.46)
Fourth	358.797 (358.5)	335.525 (379.14)	355.610 (360.66)	332.950 (380.83)	345.149 (341.77)	330.605 (376.87)	328.424 (338.83)	321.935 (366.55)
First natural frequency for torsion	42.292 (42.739)		41.864 (42.599)		41.723 (42.353)		41.497 (41.877)	

Table A.1.1 (b) Experimental Values of the Natural Frequencies for Various Crack Depth-Ratios for Shaft # 1 (Numerical Values Shown Within Brackets –V- Vertical and H – Horizontal and Torsional).

00	Crack depth ratios							
	0.0%		10%		20%		30%	
	V	H	V	H	V	H	V	H
First	34.701 (35.577)	41.374 (41.182)	34.441 (35.594)	41.541 (41.113)	34.131 (35.551)	41.021 (41.173)	34.322 (35.471)	41.187 (41.107)
Second	76.709 (75.247)	78.268 (78.245)	76.425 (75.113)	78.745 (78.102)	76.067 (75.021)	78.389 (78.017)	73.939 (74.933)	78.008 (78.129)
Third	190.617 (187.88)	201.461 (199.22)	190.824 (187.51)	197.964 (198.97)	190.012 (187.43)	197.704 (198.82)	189.83 (187.4)	197.83 (199.4)
Fourth	365.75 (360.1)	333.187 (381.49)	364.380 (358.72)	335.041 (380.75)	361.451 (358.99)	335.152 (380.58)	369.66 (362.09)	335.276 (383.3)
First natural frequency for torsion	43.716 (43.453)		43.213 (43.422)		42.826 (43.111)		42.628 (42.92)	
Frequency	Crack depth ratios							
	40%		50%		60%		70%	
	V	H	V	H	V	H	V	H
First	33.667 (35.402)	41.163 (41.575)	33.848 (34.922)	40.80 (41.002)	32.647 (34.23)	40.523 (40.497)	30.614 (33.706)	39.849 (40.583)
Second	75.483 (74.27)	77.761 (77.997)	74.191 (73.48)	77.496 (77.79)	72.808 (71.832)	77.153 (76.594)	67.271 (69.705)	75.308 (76.879)
Third	189.431 (186.4)	197.721 (198.66)	188.099 (185.56)	197.213 (198.76)	186.108 (183.36)	196.551 (197.05)	178.965 (179.87)	194.45 (196.46)
Fourth	358.797 (358.5)	335.404 (379.14)	355.610 (360.66)	333.026 (380.83)	345.149 (341.77)	331.017 (376.87)	327.224 (338.83)	321.715 (366.55)
First natural frequency for torsion	42.292 (42.739)		41.864 (42.599)		41.723 (42.353)		41.497 (41.877)	

Table A.1.1 (c) Experimental Values of the Natural Frequencies for Various Crack Depth Ratios for Shaft # 1 (Numerical Values Shown Within Brackets –V- Vertical and H – Horizontal and Torsional).

00	Crack depth ratios							
	0.0%		10%		20%		30%	
	V	H	V	H	V	H	V	H
First	34.704 (35.577)	41.033 (41.182)	34.306 (35.594)	41.545 (41.113)	34.089 (35.551)	41.098 (41.173)	34.335 (35.471)	41.213 (41.107)
Second	76.836 (75.247)	78.285 (78.245)	76.388 (75.113)	78.778 (78.102)	76.042 (75.021)	78.451 (78.017)	75.838 (74.933)	78.062 (78.129)
Third	190.668 (187.88)	197.905 (199.22)	190.624 (187.51)	197.934 (198.97)	189.969 (187.43)	197.782 (198.82)	189.882 (187.4)	197.849 (199.4)
Fourth	365.9 (360.1)	333.662 (381.49)	364.304 (358.72)	335.374 (380.75)	361.31 (358.99)	335.525 (380.58)	363.309 (362.09)	336.392 (383.3)
First natural frequency for torsion	43.716 (43.453)		43.213 (43.422)		42.826 (43.111)		42.628 (42.92)	
Frequency	Crack depth ratios							
	40%		50%		60%		70%	
	V	H	V	H	V	H	V	H
First	33.772 (35.402)	41.079 (41.575)	33.693 (34.922)	40.865 (41.002)	32.627 (34.23)	40.559 (40.497)	30.573 (33.706)	39.848 (40.583)
Second	75.493 (74.27)	77.753 (77.997)	74.192 (73.48)	77.509 (77.79)	72.771 (71.832)	77.161 (76.594)	67.356 (69.705)	75.317 (76.879)
Third	189.485 (186.4)	197.719 (198.66)	188.08 (185.56)	197.182 (198.76)	186.119 (183.36)	196.207 (197.05)	179.028 (179.87)	198.968 (196.46)
Fourth	358.871 (358.5)	335.371 (379.14)	354.827 (360.66)	333.814 (380.83)	344.913 (341.77)	331.798 (376.87)	327.801 (338.83)	321.875 (366.55)
First natural frequency for torsion	42.292 (42.739)		41.864 (42.599)		41.723 (42.353)		41.497 (41.877)	

Table A.1.2 (A) Experimental Values of the Natural Frequencies for Various Crack Depth-Ratios for Shaft # 2 (Numerical Values Shown Within Brackets –V- Vertical and H – Horizontal and Torsional).

0	Crack depth ratios							
	0.0%		10%		20%		30%	
	V	H	V	H	V	H	V	H
First	36.381 (35.577)	42.962 (41.182)	36.366 (35.594)	42.938 (41.113)	36.283 (35.551)	42.918 (41.173)	36.231 (35.471)	42.914 (41.107)
Second	75.987 (75.247)	80.049 (78.245)	75.981 (75.113)	79.969 (78.102)	75.838 (75.021)	79.965 (78.017)	75.582 (74.933)	79.887 (78.129)
Third	196.117 (187.88)	199.587 (199.22)	195.816 (187.51)	199.462 (198.97)	195.626 (187.43)	199.506 (198.82)	195.386 (187.4)	199.382 (199.4)
Fourth	367.458 (360.1)	369.215 (381.49)	366.862 (358.72)	369.019 (380.75)	366.35 (358.99)	368.92 (380.58)	365.421 (362.09)	368.502 (383.3)
First natural frequency for torsion	43.716 (43.453)		43.213 (43.422)		42.826 (43.111)		42.628 (42.92)	
Frequency	Crack depth ratios							
	40%		50%		60%		70%	
	V	H	V	H	V	H	V	H
First	36.028 (35.402)	42.772 (41.575)	35.782 (34.922)	42.723 (41.002)	35.222 (34.23)	42.207 (40.497)	34.042 (33.706)	41.721 (40.583)
Second	74.931 (74.27)	79.766 (77.997)	74.187 (73.48)	79.375 (77.79)	72.369 (71.832)	79.207 (76.594)	69.258 (69.705)	78.010 (76.879)
Third	194.531 (186.4)	199.321 (198.66)	193.387 (185.56)	199.059 (198.76)	190.769 (183.36)	198.459 (197.05)	185.636 (179.87)	197.291 (196.46)
Fourth	362.804 (358.5)	367.671 (379.14)	359.056 (360.66)	366.089 (380.83)	349.926 (341.77)	362.248 (376.87)	333.436 (338.83)	354.892 (366.55)
First natural frequency for torsion	42.292 (42.739)		41.864 (42.599)		41.723 (42.353)		41.497 (41.877)	

Table A.1.2. (b) Experimental Values of the Natural Frequencies for Various Crack Depth-Ratios for Shaft # 2 (Numerical Values Shown Within Brackets –V- Vertical and H – Horizontal and Torsional).

Frequency	Crack depth ratios							
	0.0%		10%		20%		30%	
	V	H	V	H	V	H	V	H
First	36.385 (35.577)	43.026 (41.182)	36.287 (35.594)	42.976 (41.113)	36.24 (35.551)	42.893 (41.173)	36.204 (35.471)	42.891 (41.107)
Second	75.931 (75.247)	80.036 (78.245)	76.093 (75.113)	80.054 (78.102)	75.866 (75.021)	79.940 (78.017)	75.639 (74.933)	78.324 (78.129)
Third	196.111 (187.88)	199.547 (199.22)	195.856 (187.51)	199.465 (198.97)	195.713 (187.43)	199.488 (198.82)	195.391 (187.4)	199.426 (199.4)
Fourth	367.403 (360.1)	369.194 (381.49)	366.881 (358.72)	368.976 (380.75)	366.41 (358.99)	368.847 (380.58)	365.443 (362.09)	368.653 (383.3)
First natural frequency for torsion	43.716 (43.453)		43.213 (43.422)		42.826 (43.111)		42.628 (42.92)	
Frequency	Crack depth ratios							
	40%		50%		60%		70%	
	V	H	V	H	V	H	V	H
First	36.041 (35.402)	42.779 (41.575)	35.795 (34.922)	42.686 (41.002)	35.216 (34.23)	42.255 (40.497)	33.974 (33.706)	41.715 (40.583)
Second	75.015 (74.27)	78.003 (77.997)	74.231 (73.48)	78.561 (77.79)	72.395 (71.832)	79.001 (76.594)	69.247 (69.705)	77.875 (76.879)
Third	194.587 (186.4)	199.333 (198.66)	193.436 (185.56)	199.077 (198.76)	190.732 (183.36)	198.472 (197.05)	185.554 (179.87)	197.300 (196.46)
Fourth	362.935 (358.5)	367.662 (379.14)	359.182 (360.66)	366.013 (380.83)	349.957 (341.77)	362.343 (376.87)	333.306 (338.83)	354.891 (366.55)
First natural frequency for torsion	42.292 (42.739)		41.864 (42.599)		41.723 (42.353)		41.497 (41.877)	

Table A.1.2 (C) Experimental Values of the Natural Frequencies for Various Crack Depth Ratios for Shaft # 2 (Numerical Values Shown Within Brackets –V- Vertical and H – Horizontal and Torsional).

Frequency	Crack depth ratios							
	0.0%		10%		20%		30%	
	V	H	V	H	V	H	V	H
First	36.421 (35.577)	42.953 (41.182)	36.291 (35.594)	42.964 (41.113)	36.264 (35.551)	42.902 (41.173)	36.201 (35.471)	42.925 (41.107)
Second	76.008 (75.247)	80.017 (78.245)	76.094 (75.113)	79.933 (78.102)	75.852 (75.021)	79.805 (78.017)	75.629 (74.933)	79.717 (78.129)
Third	196.131 (187.88)	199.497 (199.22)	195.876 (187.51)	199.459 (198.97)	195.662 (187.43)	199.516 (198.82)	195.418 (187.4)	199.463 (199.4)
Fourth	367.407 (360.1)	369.036 (381.49)	366.841 (358.72)	368.982 (380.75)	366.414 (358.99)	368.92 (380.58)	365.506 (362.09)	368.66 (383.3)
First natural frequency for torsion	43.716 (43.453)		43.213 (43.422)		42.826 (43.111)		42.628 (42.92)	
Frequency	Crack depth ratios							
	40%		50%		60%		70%	
	V	H	V	H	V	H	V	H
First	36.0127 (35.402)	42.787 (41.575)	35.796 (34.922)	42.693 (41.002)	35.196 (34.23)	42.244 (40.497)	33.943 (33.706)	41.748 (40.583)
Second	75.049 (74.27)	79.517 (77.997)	74.204 (73.48)	79.336 (77.79)	72.378 (71.832)	78.896 (76.594)	69.237 (69.705)	77.852 (76.879)
Third	194.588 (186.4)	199.346 (198.66)	193.44 (185.56)	199.075 (198.76)	190.76 (183.36)	198.454 (197.05)	185.539 (179.87)	197.31 (196.46)
Fourth	362.889 (358.5)	367.672 (379.14)	359.133 (360.66)	366.075 (380.83)	350.019 (341.77)	362.326 (376.87)	333.269 (338.83)	354.93 (366.55)
First natural frequency for torsion	42.292 (42.739)		41.864 (42.599)		41.723 (42.353)		41.497 (41.877)	

Table A.1.3 (A) Experimental Values of the Natural Frequencies for Various Crack Depth Ratios for Shaft # 3 (Numerical Values Shown Within Brackets –V- Vertical and H – Horizontal and Torsional).

Frequency	Crack depth ratios							
	0.0%		10%		20%		30%	
	V	H	V	H	V	H	V	H
First	33.861 (35.577)	40.648 (41.182)	33.815 (35.594)	40.680 (41.113)	33.719 (35.551)	40.654 (41.173)	33.750 (35.471)	40.559 (41.107)
Second	74.559 (75.247)	79.937 (78.245)	74.622 (75.113)	79.811 (78.102)	74.407 (75.021)	79.816 (78.017)	74.237 (74.933)	79.825 (78.129)
Third	192.141 (187.88)	197.821 (199.22)	191.984 (187.51)	197.833 (198.97)	191.729 (187.43)	197.791 (198.82)	191.295 (187.4)	197.651 (199.4)
Fourth	352.23 (360.1)	356.036 (381.49)	353.499 (358.72)	355.740 (380.75)	352.623 (358.99)	355.639 (380.58)	347.419 (362.09)	353.123 (383.3)
First natural frequency for torsion	43.716 (43.453)		43.213 (43.422)		42.826 (43.111)		42.628 (42.92)	
Frequency	Crack depth ratios							
	40%		50%		60%		70%	
	V	H	V	H	V	H	V	H
First	33.557 (35.402)	40.462 (41.575)	33.344 (34.922)	40.353 (41.002)	32.814 (34.23)	40.017 (40.497)	31.682 (33.706)	39.532 (40.583)
Second	73.413 (74.27)	79.615 (77.997)	72.564 (73.48)	79.369 (77.79)	70.733 (71.832)	78.947 (76.594)	67.587 (69.705)	77.896 (76.879)
Third	190.034 (186.4)	197.427 (198.66)	188.679 (185.56)	197.064 (198.76)	185.399 (183.36)	196.36 (197.05)	180.197 (179.87)	195.073 (196.46)
Fourth	344.186 (358.5)	350.337 (379.14)	339.04 (360.66)	347.542 (380.83)	328.718 (341.77)	343.369 (376.87)	315.593 (338.83)	336.402 (366.55)
First natural frequency for torsion	42.292 (42.739)		41.864 (42.599)		41.723 (42.353)		41.497 (41.877)	

Table A.1.3 (B) Experimental Values of the Natural Frequencies for Various Crack Depth Ratios for Shaft # 3 (Numerical Values Shown Within Brackets –V- Vertical and H – Horizontal and Torsional).

Frequency	Crack depth ratios							
	0.0%		10%		20%		30%	
	V	H	V	H	V	H	V	H
First	33.842 (35.577)	40.606 (41.182)	33.754 (35.594)	40.660 (41.113)	33.768 (35.551)	40.603 (41.173)	33.746 (35.471)	40.540 (41.107)
Second	74.603 (75.247)	79.924 (78.245)	74.516 (75.113)	79.816 (78.102)	74.519 (75.021)	79.805 (78.017)	74.241 (74.933)	79.829 (78.129)
Third	192.167 (187.88)	197.799 (199.22)	191.936 (187.51)	197.815 (198.97)	191.727 (187.43)	197.767 (198.82)	191.275 (187.4)	197.654 (199.4)
Fourth	353.571 (360.1)	354.825 (381.49)	353.314 (358.72)	355.777 (380.75)	352.537 (358.99)	355.223 (380.58)	350.492 (362.09)	353.115 (383.3)
First natural frequency for torsion	43.716 (43.453)		43.213 (43.422)		42.826 (43.111)		42.628 (42.92)	
Frequency	Crack depth ratios							
	40%		50%		60%		70%	
	V	H	V	H	V	H	V	H
First	33.535 (35.402)	40.471 (41.575)	33.333 (34.922)	40.340 (41.002)	32.791 (34.23)	40.041 (40.497)	31.672 (33.706)	39.527 (40.583)
Second	73.454 (74.27)	79.623 (77.997)	72.569 (73.48)	79.384 (77.79)	70.757 (71.832)	78.949 (76.594)	67.542 (69.705)	78.0671 (76.879)
Third	190.034 (186.4)	197.413 (198.66)	188.6 (185.56)	197.069 (198.76)	185.451 (183.36)	196.385 (197.05)	180.078 (179.87)	195.06 (196.46)
Fourth	344.309 (358.5)	350.243 (379.14)	339.21 (360.66)	347.540 (380.83)	328.87 (341.77)	343.262 (376.87)	315.226 (338.83)	336.080 (366.55)
First natural frequency for torsion	42.292 (42.739)		41.864 (42.599)		41.723 (42.353)		41.497 (41.877)	

Table A.1.3 (C) Experimental Values of the Natural Frequencies for Various Crack Depth Ratios for Shaft # 3 (Numerical Values Shown Within Brackets –V- Vertical and H – Horizontal and Torsional).

Frequency	Crack depth ratios							
	0.0%		10%		20%		30%	
	V	H	V	H	V	H	V	H
First	33.862 (35.577)	40.635 (41.182)	33.754 (35.594)	40.628 (41.113)	33.765 (35.551)	40.587 (41.173)	33.711 (35.471)	40.552 (41.107)
Second	74.679 (75.247)	79.882 (78.245)	74.640 (75.113)	79.801 (78.102)	74.535 (75.021)	79.911 (78.017)	74.167 (74.933)	79.823 (78.129)
Third	192.262 (187.88)	197.818 (199.22)	191.967 (187.51)	197.803 (198.97)	191.77 (187.43)	197.756 (198.82)	191.324 (187.4)	197.65 (199.4)
Fourth	353.078 (360.1)	356.932 (381.49)	353.364 (358.72)	355.367 (380.75)	352.765 (358.99)	355.084 (380.58)	350.259 (362.09)	353.157 (383.3)
First natural frequency for torsion	43.716 (43.453)		43.213 (43.422)		42.826 (43.111)		42.628 (42.92)	
Frequency	Crack depth ratios							
	40%		50%		60%		70%	
	V	H	V	H	V	H	V	H
First	33.557 (35.402)	40.503 (41.575)	33.328 (34.922)	40.324 (41.002)	32.806 (34.23)	40.045 (40.497)	31.67 (33.706)	39.546 (40.583)
Second	73.463 (74.27)	79.571 (77.997)	72.529 (73.48)	79.363 (77.79)	70.725 (71.832)	78.883 (76.594)	67.504 (69.705)	77.895 (76.879)
Third	190.033 (186.4)	197.403 (198.66)	188.653 (185.56)	197.073 (198.76)	185.386 (183.36)	196.378 (197.05)	179.982 (179.87)	195.066 (196.46)
Fourth	344.71 (358.5)	350.176 (379.14)	338.906 (360.66)	347.570 (380.83)	328.853 (341.77)	342.961 (376.87)	314.673 (338.83)	336.130 (366.55)
First natural frequency for torsion	42.292 (42.739)		41.864 (42.599)		41.723 (42.353)		41.497 (41.877)	

Appendix B – "The Experimental Mode Shapes for the Various Crack Depth Ratios

B.1 Mode Shapes for Shaft # 1

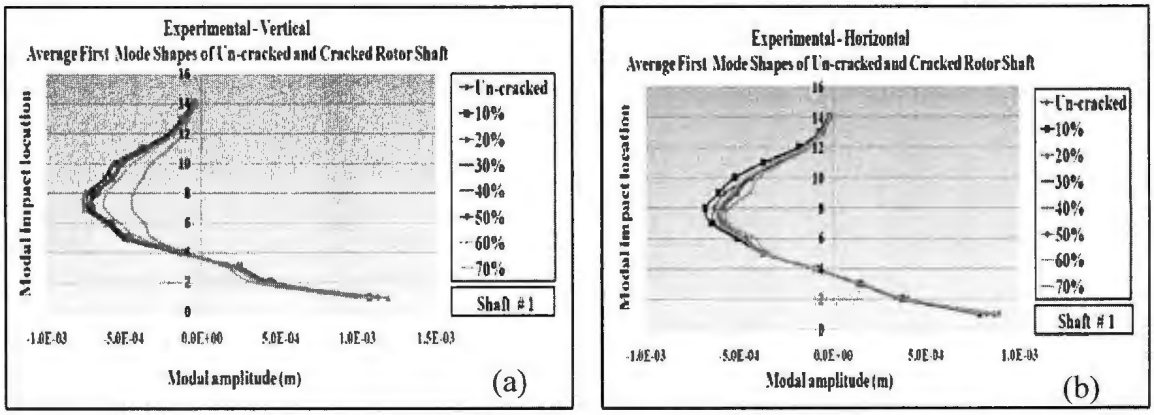

Figure B.1.1 First Mode Shapes of Un-Cracked and Cracked Rotor Shaft from Experimental Work (a) Vertical (b) Horizontal.

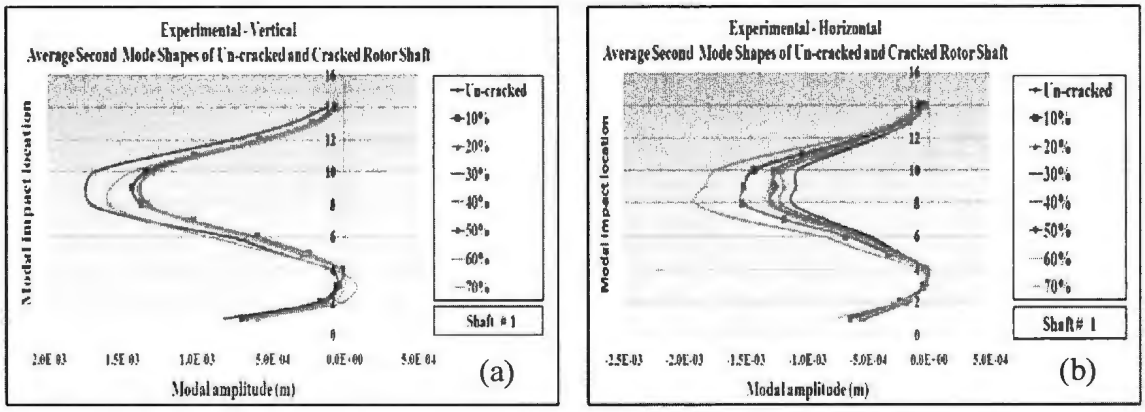

Figure B.1.2 Second Mode Shapes of Un-Cracked and Cracked Rotor Shaft from Experimental Work (a) Vertical (b) Horizontal.

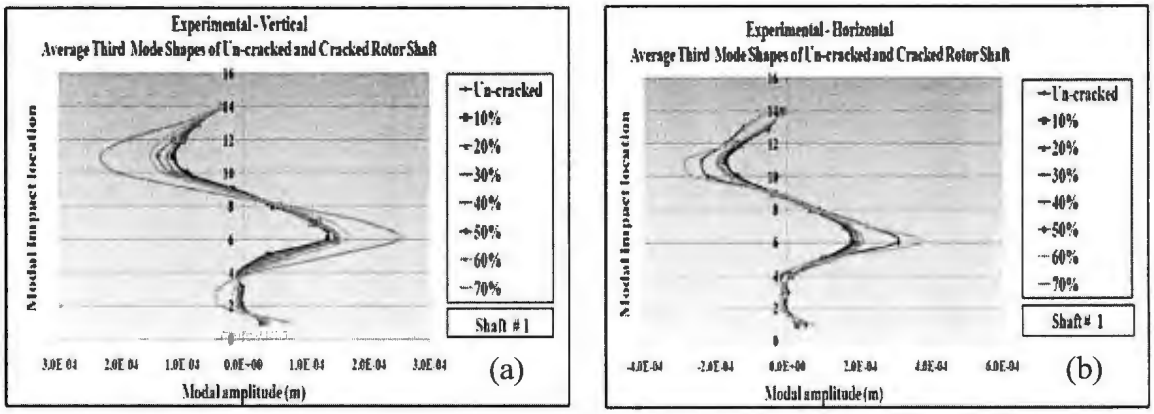

Figure B.1.3 Third Mode Shapes of Un-Cracked and Cracked Rotor Shaft from Experimental Work (a) Vertical (b) Horizontal.

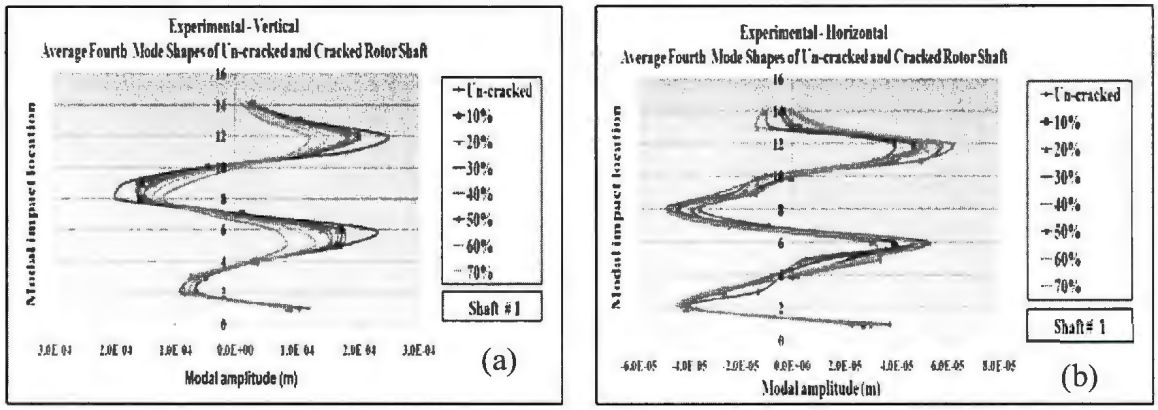

Figure B.1.4 Fourth Mode Shapes of Un-Cracked and Cracked Rotor Shaft from Experimental Work (a) Vertical (b) Horizontal.

B.2 Mode Shapes for Shaft # 3

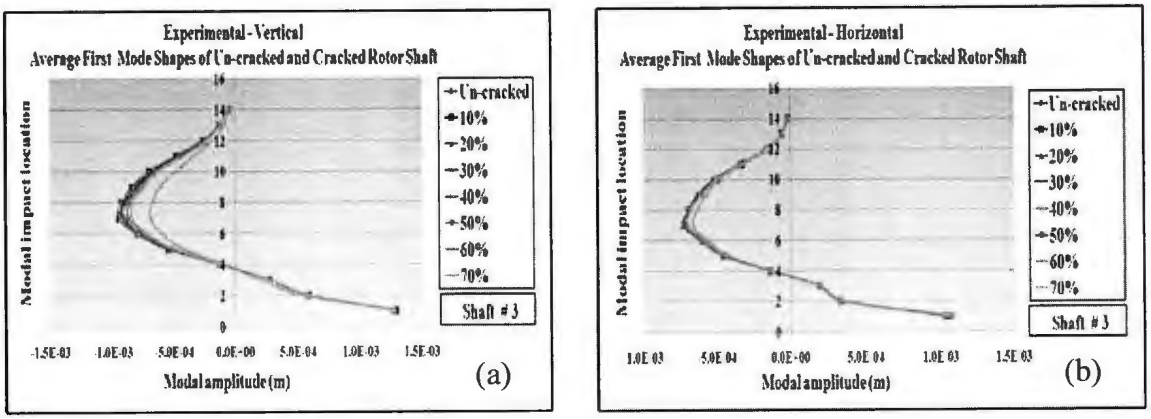

Figure B.2.1 First Mode Shapes of Un-Cracked and Cracked Rotor Shaft from Experimental Work (a) Vertical (b) Horizontal.

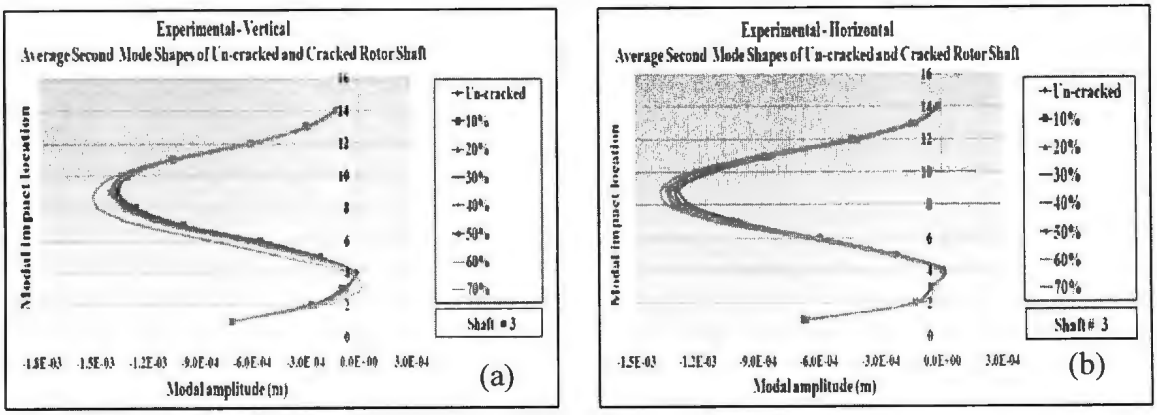

Figure B.2.2 Second Mode Shapes of Un-Cracked and Cracked Rotor Shaft from Experimental Work (a) Vertical (b) Horizontal.

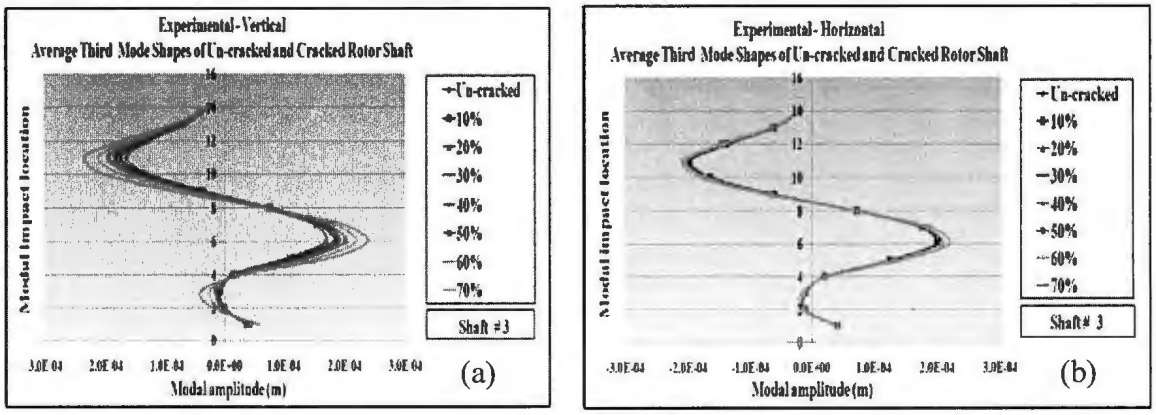

Figure B.2.3 Third Mode Shapes of Un-Cracked and Cracked Rotor Shaft from Experimental Work (a) Vertical (b) Horizontal.

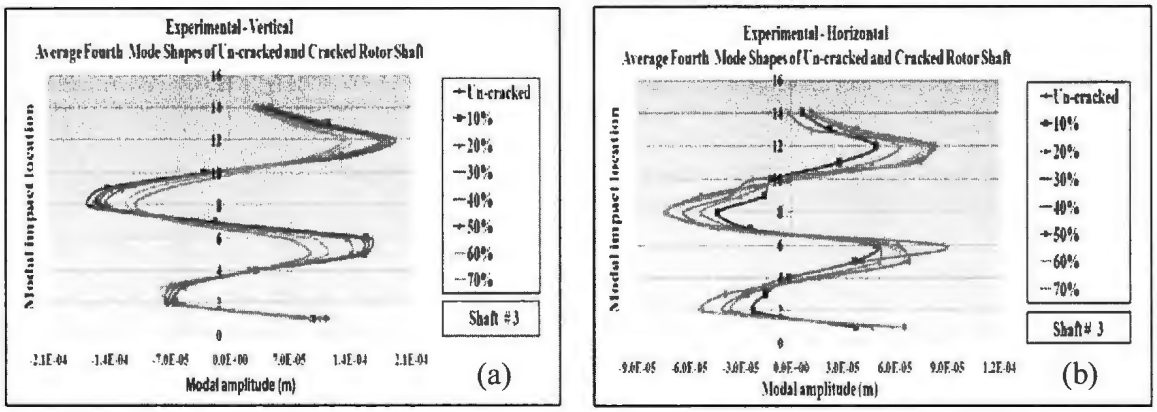

Figure B.2.4 Fourth Mode Shapes of Un-Cracked and Cracked Rotor Shaft from Experimental Work (a) Vertical (b) Horizontal.

Appendix C – "Rate of Change of Frequencies for Experimental Results for All the Rotor Shaft"

C.1 Rate of Change of Frequencies for Shaft # 1

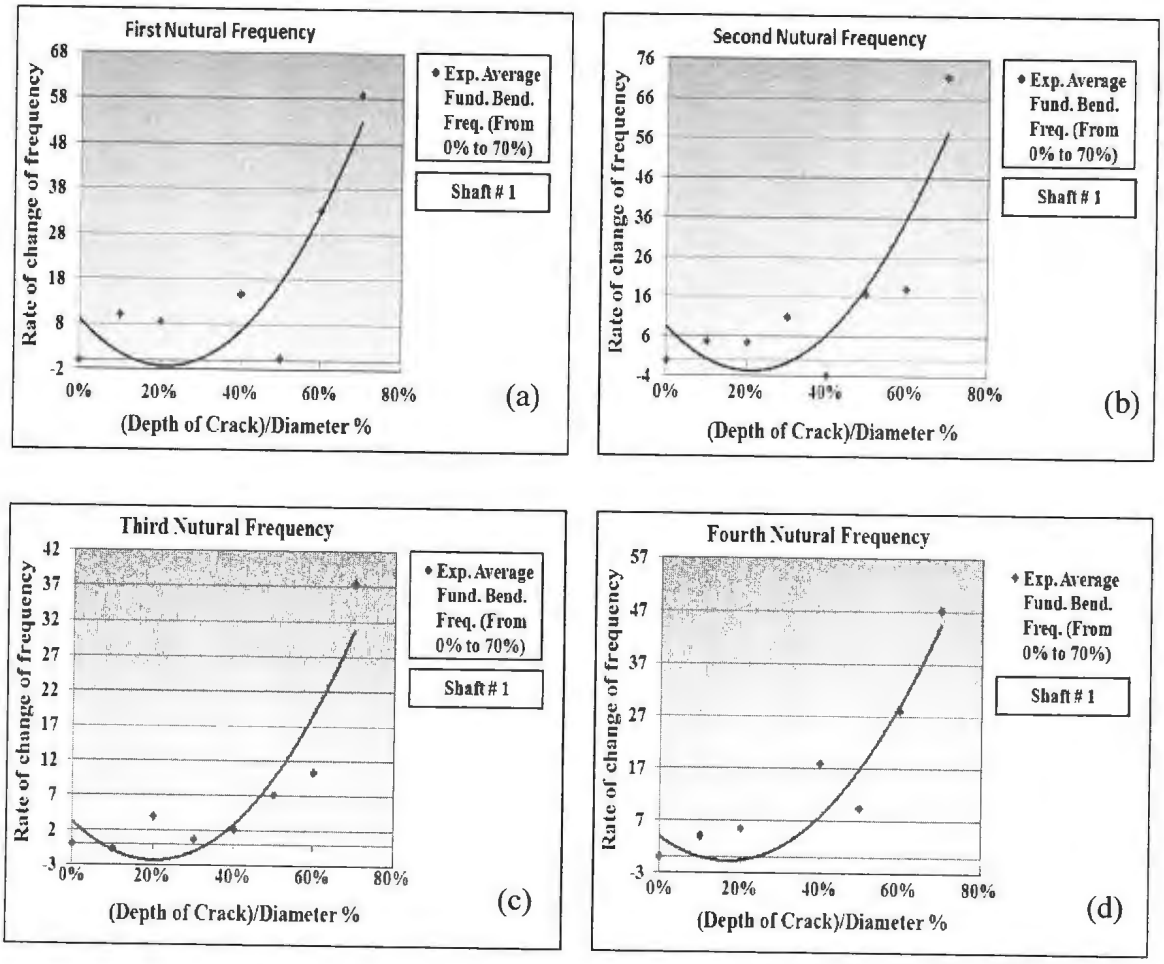

Figure C.1.1 Rate of Change of Frequency (with Respect to Crack Depth Ratio) vs. Crack Depth Ratio of the First Four Frequencies; (a) Mode One; (b) Mode Two; (c) Mode Three; (d) Mode Four

C.2 Rate of Change of Frequency for Shaft # 3

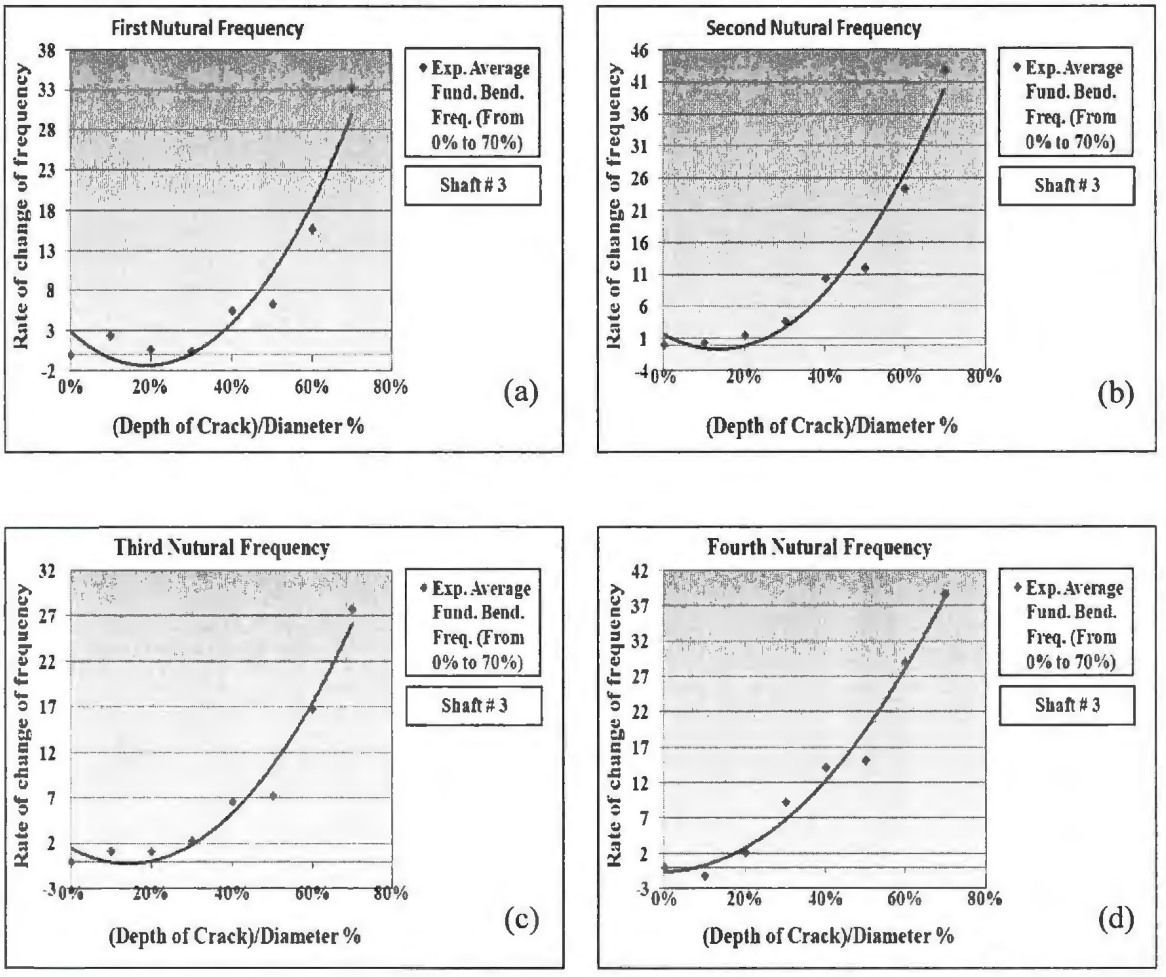

Figure C.2.1 Rate of Change of Frequency (with Respect to Crack Depth Ratio) vs. Crack Depth Ratio of the First Four Frequencies; (a) Mode One; (b) Mode Two; (c) Mode Three; (d) Mode Four

C.3 The Comparison of Changes that occur in the Experimental (shaft # 1 and shaft # 3) and Numerical (using Beam4) Frequencies as the Crack Depth Ratios Change from 0 To 70% (with second order curve fit)

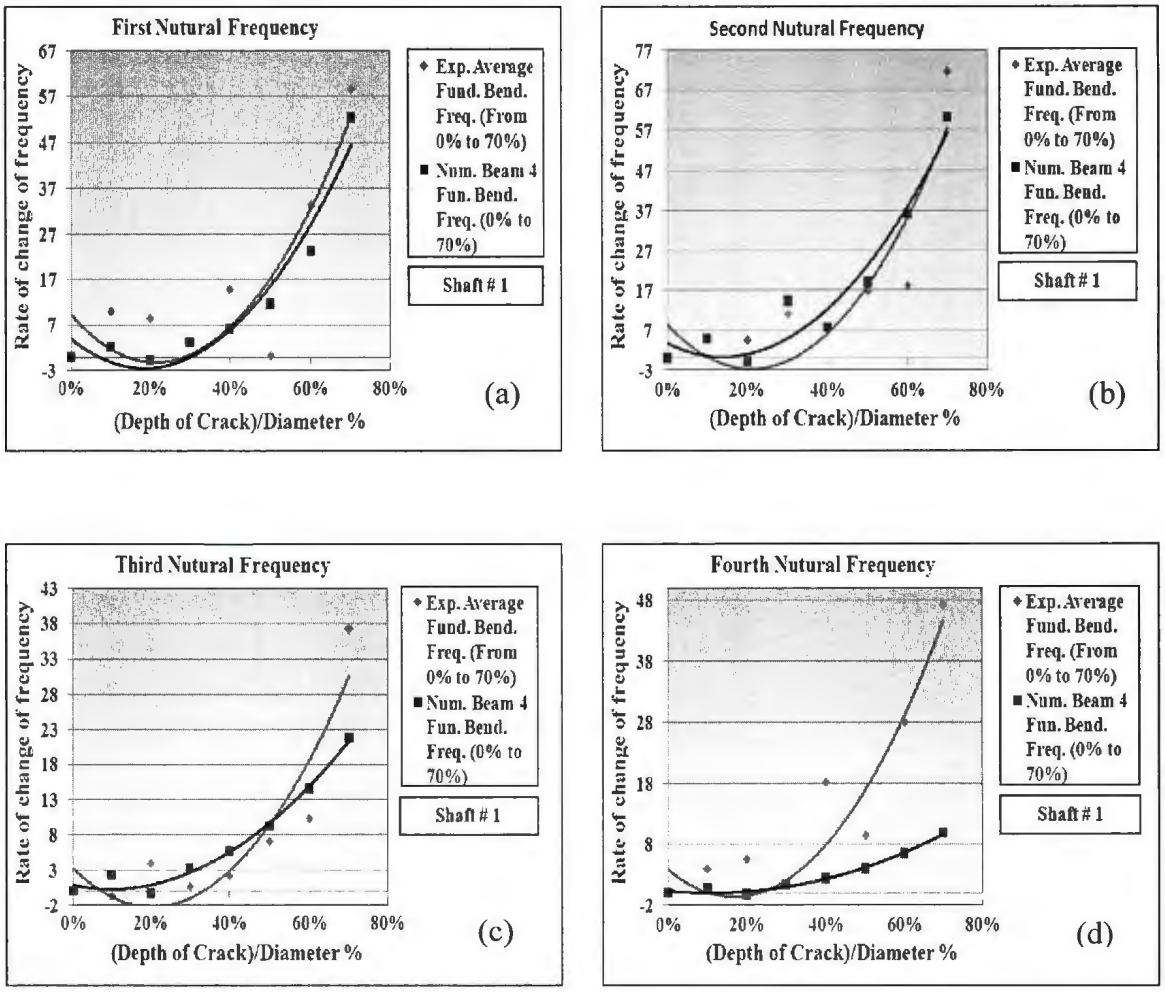

Figure C.3.1 Rate of Change of Frequency (with Respect to Crack Depth Ratio) vs. Crack Depth Ratio of the First Four Frequencies; (a) Mode One; (b) Mode Two; (c) Mode Three; (d) Mode Four

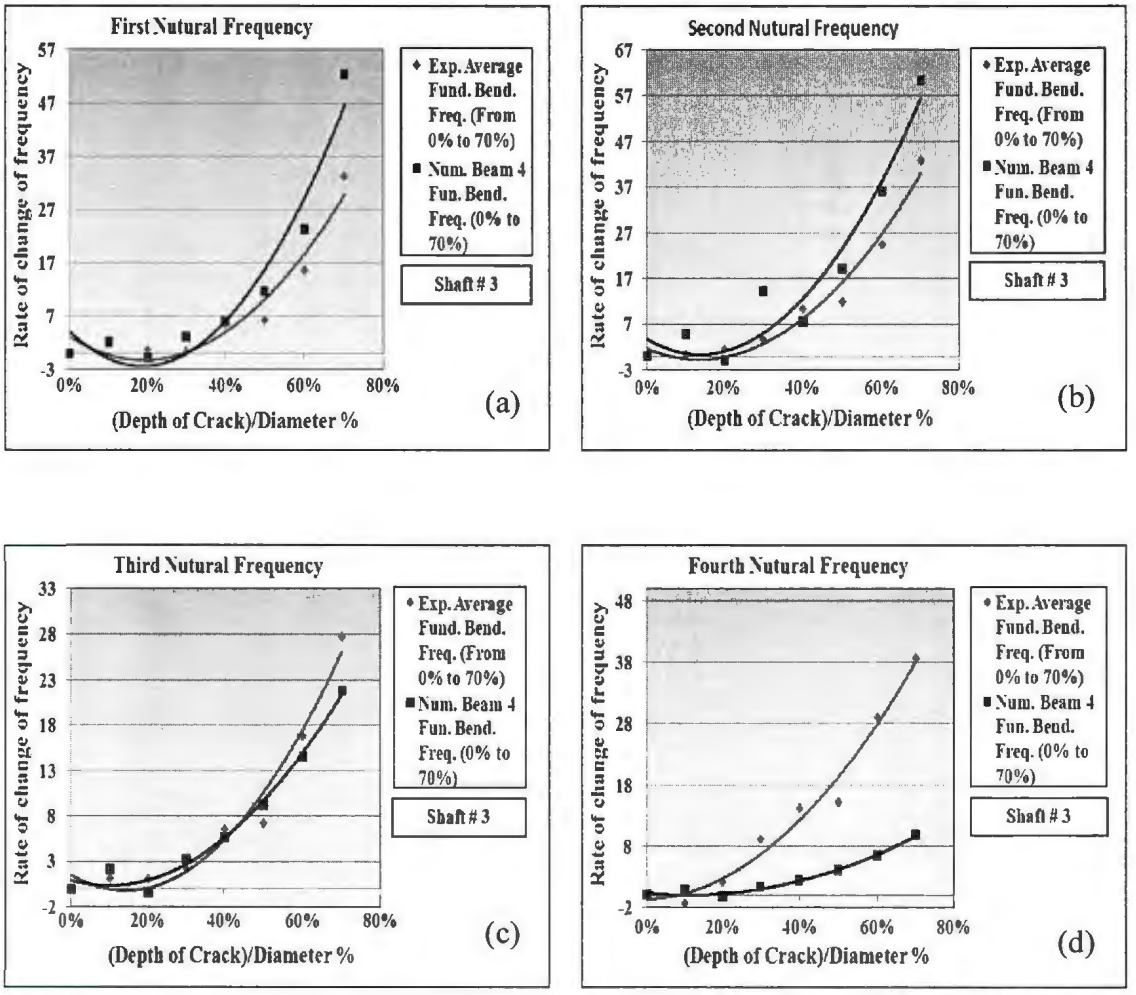

Figure C.3.2 Rate of Change of Frequency (with Respect to Crack Depth Ratio) vs. Crack Depth Ratio of the First Four Frequencies; (a) Mode One; (b) Mode Two; (c) Mode Three; (d) Mode Four

C.4 the comparison changes that occur in the experimental (shaft # 1 and shaft # 3) and numerical (using 3-D) frequencies as the crack depth ratios change from 0 to 70% (with second order curve fit)

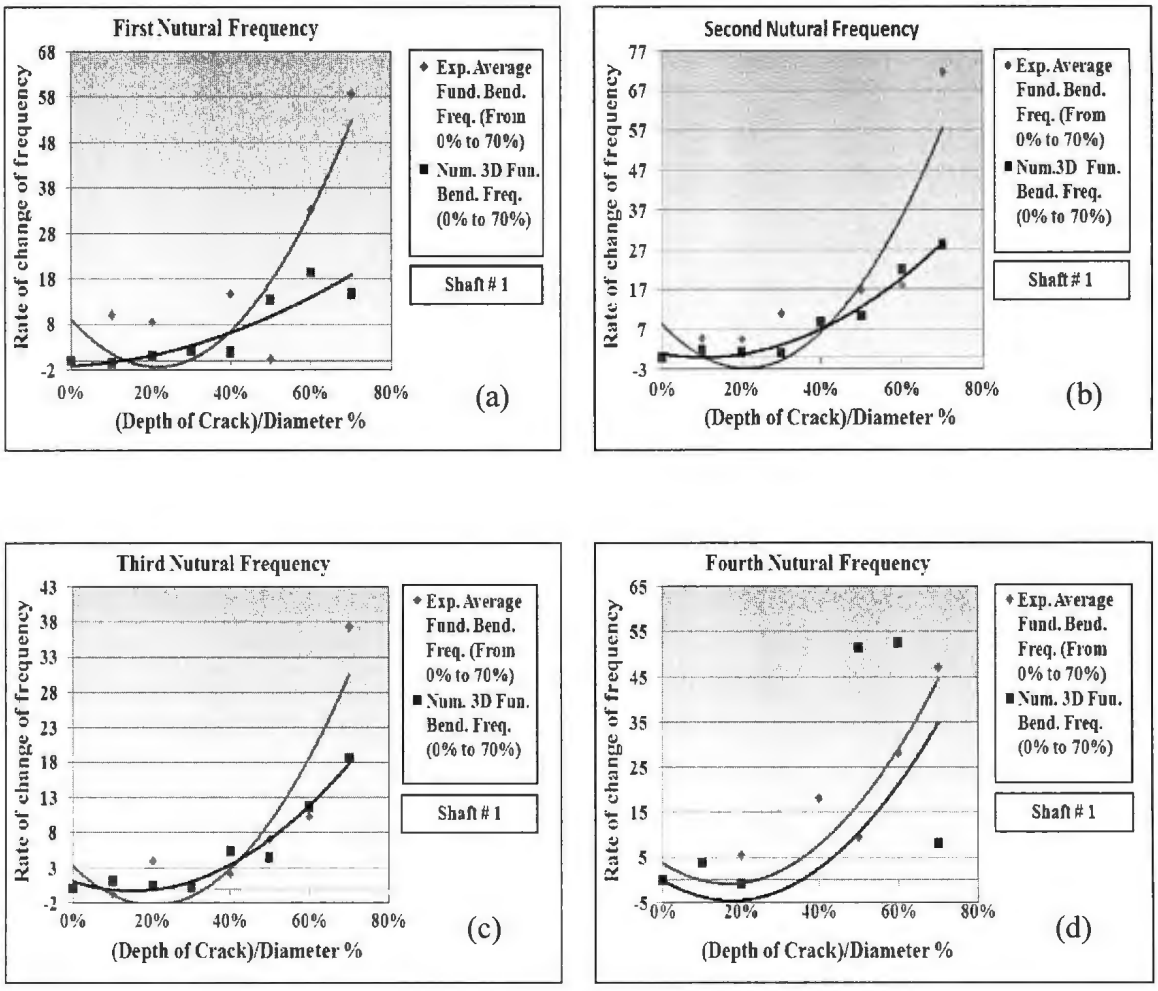

Figure C.4.1: Rate of Change of Frequency (with Respect to Crack Depth Ratio) vs. Crack Depth Ratio of the First Four Frequencies; (a) Mode One; (b) Mode Two; (c) Mode Three; (d) Mode Four

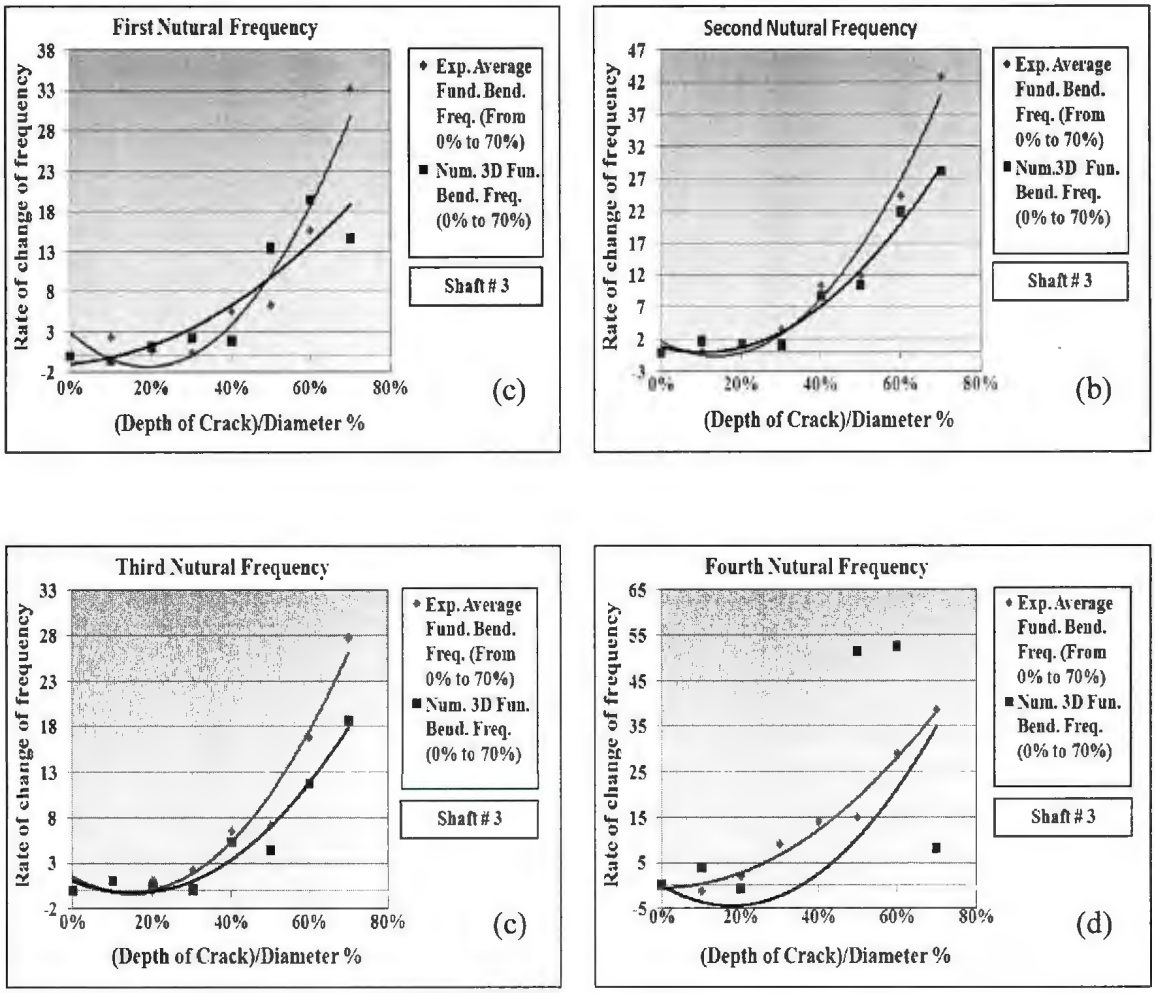

Figure C.4.2: Rate of Change of Frequency (with Respect to Crack Depth Ratio) vs. Crack Depth Ratio of the First Four Frequencies; (a) Mode One; (b) Mode Two; (c) Mode Three; (d) Mode Four

Appendix D – "Shows the ANSYS Codes that were used to find the Values of Natural Frequencies"

D.1 Shows the ANSYS codes are used to find the values of natural frequencies

```
FINISH
/CLEAR, NOSTART
/PREP7
!***************DEFINING ELEMENT TYPES*****************************
!ET,1,pipe16
ET,1,Beam4
ET,2,MASS21
ET,3,COMBIN14
!***************REAL CONSTANTS*************************************
R,1,2.01062e-4,3.217e-9,3.217e-9,1.6e-2,1.6e-2
                                                                    !
Real constant for beam4
!*******MASS REAL CONSTANTS ***************************************
R,2,0.072,0.072,0.072,!5.51e-6,5.51e-6,5.51e-6          !Mass 2
R,3,0.016,0.016,0.016,!1.224e-6,1.224e-6,1.224e-6       !Mass 3
!R,4,1.572,1.572,1.572,!0.013825,0.013825,0.013825      !Mass 4
 R,4,1.45,1.45,1.45
!******* COMBIN14 REAL CONSTANTS *********************************
R,5,4.25e6   !Z     $ R,6,7e9     !Y     $ R,7,1.46e6     !z     $ R,8,9e15     !z
R,9, 2e8     !Y     $ R,10, 9e15  !z
!************ REAL CONSTANTS FOR NEW FIVE ELEMENTS *************
R,11,2.01062e-4,3.217e-9,3.217e-9,1.6e-2,1.6e-2          ! Un-cracked
```

```
!R,11,2.86272e-5,2.12982e-9,2.96868e-9,1.28e-2,0.32e-2
                                        ! Area, Izz, Iyy, TKz, TKy, Theta about x-axis
R,12,2.01062e-4,3.217e-9,3.217e-9,1.6e-2,1.6e-2
R,13,2.01062e-4,3.217e-9,3.217e-9,1.6e-2,1.6e-2
R,14,2.01062e-4,3.217e-9,3.217e-9,1.6e-2,1.6e-2
R,15,2.01062e-4,3.217e-9,3.217e-9,1.6e-2,1.6e-2
!*************** MATERIALS*********************************************
EX,1,2e11              $ PRXY,1,0.3          $ Dens,1,7667.01
!*************** NODES ************************************************
N,1,        $ N,2,0.01    $ N,3,0.0335    $ N,4,0.057    $ N,94,0.98       $ N,95,1.0035
N,96,1.027    $ N,99,1.047    $ N,100,1.04765    $ N,101,1.057    $ N,102,1.067
N,103,1.077    $ N,104,1.087    $ N,106,1.13915    $ N,107,1.1733    $ N,108,1.2133
FILL,4,94      $ Fill,96,99       $ Fill,104,106
!**********************ELEMENT CONNECTIVITY************************
TYPE,1   $ REAL,1   $ EN,1,1,2   $ EN,2,2,3   $ EN,3,3,4   $ EGEN,96,1,-1
TYPE,1 $ REAL,11    $ EN,99,99,100   $  TYPE,1     $ REAL,12    $ EN,100,100,101
TYPE,1   $ REAL,13    $ EN,101,101,102   $ TYPE,1 $ REAL,14    $ EN,102,102,103
TYPE,1    $ REAL,15    $ EN,103,103,104   $ TYPE,1 $ REAL,1   $ EN,104,104,105
EN,105,105,106   $ EN,106,106,107   $ EN,107,107,108
!**********************SPRINGS*************************************
N,502,0.01,0 ,-.01   $ N,503,0.0335,-.01,  $ N,504,0.057,0,-.01    $ N,594,0.98,0,-0.01
N,595,1.0035,-0.01   $ N,596,1.027,0,-0.01    $ TYPE,3    $ REAL,5       $ E,94,594
REAL,6      $ E,95,595     $ REAL,7      $ E,96,596       $ REAL,8       $ E,2,502
REAL,9      $ E,3,503       $ REAL,10     $ E,4,504
!**********************SUPPORT*************************************
D,1,ALL          $ D,502,ALL        $ D,503,ALL       $ D,504,ALL     $ D,594,ALL
D,595,ALL        $ D,596,ALL
```

```
!***********************MASSES*************************************

TYPE,2    $ REAL,4    $ E,106    $ REAL,3    $ E,107    $ REAL,2    $ E,108

!***********************GRAVITY************************************

ACEL,0,9.81,0

!***********************SOLUTION***********************************

FINISH
/SOL
ANTYPE,2
MODOPT,LANB,20
EQSLV,SPAR
MXPAND,20, , ,0
MODOPT,LANB,20,0.05,5000, ,OFF
Solve
**********************************************************************
```

D.2 Experimental and Numerical Results of Natural Frequencies for Six, Eight and Ten Springs Modeling.

Table D.2.1 Experimental and Numerical Values of the Natural Frequencies for Various Crack Depth-Ratios (the Numerical Values of the Six, Eight and Ten Springs Modeling Shown Within Brackets, Respectively.); V - Vertical and H – Horizontal.

Frequency	Crack depth ratios							
	0.0%		10%		20%		30%	
	V	H	V	H	V	H	V	H
First	34.134 (33.909) (33.909) (34.423)	43.633 (43.616) (43.616) (43.658)	34.125 (33.908) (33.908) (34.421)	43.515 (43.615) (43.615) (43.657)	33.816 (33.905) (33.905) (34.419)	43.363 (43.615) (43.615) (43.657)	33.778 (33.903) (33.903) (34.416)	43.343 (43.613) (43.613) (43.654)
Second	76.703 (77.666) (77.666) (77.998)	78.792 (80.127) (80.127) (80.101)	76.657 (77.658) (77.658) (77.993)	78.806 (80.122) (80.122) (80.092)	76.483 (77.644) (77.644) (77.993)	78.424 (80.123) (80.123) (80.077)	76.195 (77.631) (77.631) (77.986)	78.382 (80.115) (80.115) (80.063)
Third	191.652 (188.23) (188.23) (188.92)	199.499 (195.36) (195.36) (195.93)	191.491 (188.22) (188.22) (188.91)	199.204 (195.35) (195.35) (195.91)	191.256 (188.20) (188.20) (188.92)	199.069 (195.36) (195.36) (195.89)	190.859 (188.19) (188.19) (188.91)	199.006 (195.35) (195.35) (195.87)
Fourth	367.563 (364.33) (364.33) (363.42)	383.139 (380.33) (380.33) (381.00)	367.282 (364.32) (364.32) (363.42)	379.423 (380.32) (380.32) (380.98)	365.883 (364.29) (364.29) (363.42)	379.213 (380.33) (380.33) (380.95)	365.752 (364.27) (364.27) (363.42)	379.109 (380.31) (380.31) (380.92)

Frequency	Crack depth ratios							
	40%		50%		60%		70%	
	V	H	V	H	V	H	V	H
First	33.556 (33.902) (33.902) (34.415)	43.185 (43.608) (43.608) (43.650)	33.145 (33.902) (33.902) (34.415)	42.947 (43.600) (43.600) (43.642)	32.774 (33.901) (33.901) (34.414)	42.862 (43.583) (43.583) (43.625)	31.286 (33.900) (33.900) (34.413)	42.069 (43.544) (43.544) (43.585)
Second	75.572 (77.624) (77.624) (77.973)	78.298 (80.100) (80.100) (80.056)	74.553 (77.623) (77.623) (77.949)	78.214 (80.073) (80.073) (80.055)	73.401 (77.621) (77.621) (77.900)	77.644 (80.020) (80.020) (80.054)	69.774 (77.613) (77.613) (77.785)	75.896 (79.894) (79.894) (80.044)
Third	190.076 (188.18) (188.18) (188.90)	198.671 (195.33) (195.33) (195.86)	188.763 (188.17) (188.17) (188.88)	198.299 (195.30) (195.30) (195.86)	187.240 (188.17) (188.17) (188.83)	197.993 (195.24) (195.24) (195.86)	182.790 (188.16) (188.16) (188.74)	194.457 (195.11) (195.11) (195.85)
Fourth	363.809 (364.26) (364.26) (363.40)	378.435 (380.29) (380.29) (380.91)	359.989 (364.26) (364.26) (363.38)	377.565 (382.25) (382.25) (380.91)	355.839 (364.26) (364.26) (363.35)	376.664 (380.17) (380.17) (380.90)	343.971 (364.24) (364.24) (363.25)	373.689 (379.97) (379.97) (380.89)

Appendix E – "The Mode shapes Comparison for First Eight Natural Frequencies of (four vertical and four horizontal) Experimental and Numerical analyses for cracked shaft"

E.1: Mode Shapes Comparison for First Four Vertical and Horizontal Frequencies (10%): (a) Experimental and (b) Numerical

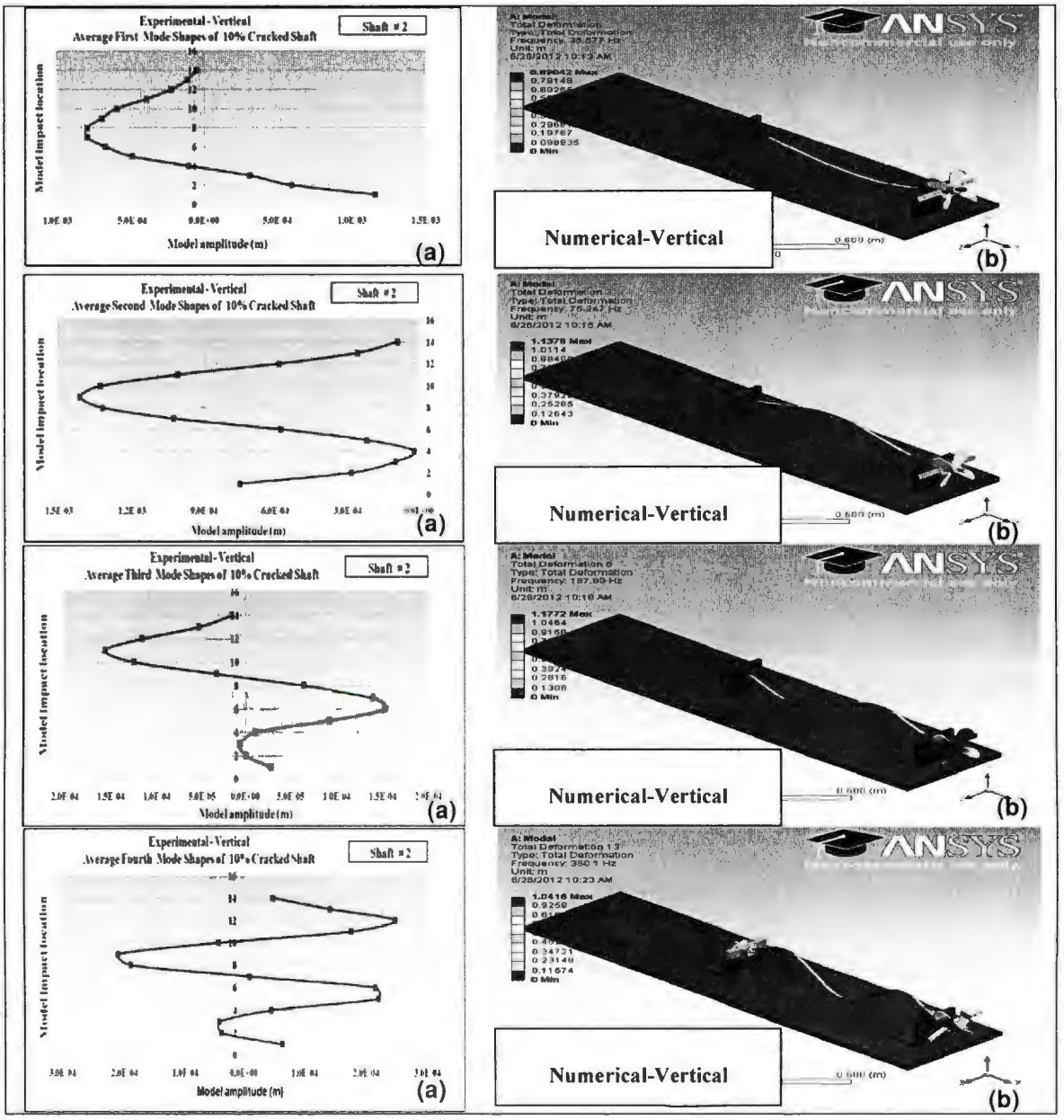

Figure E.1.1 Mode Shapes Comparison for First Four Vertical Frequencies (10%) a) Experimental and b) Numerical

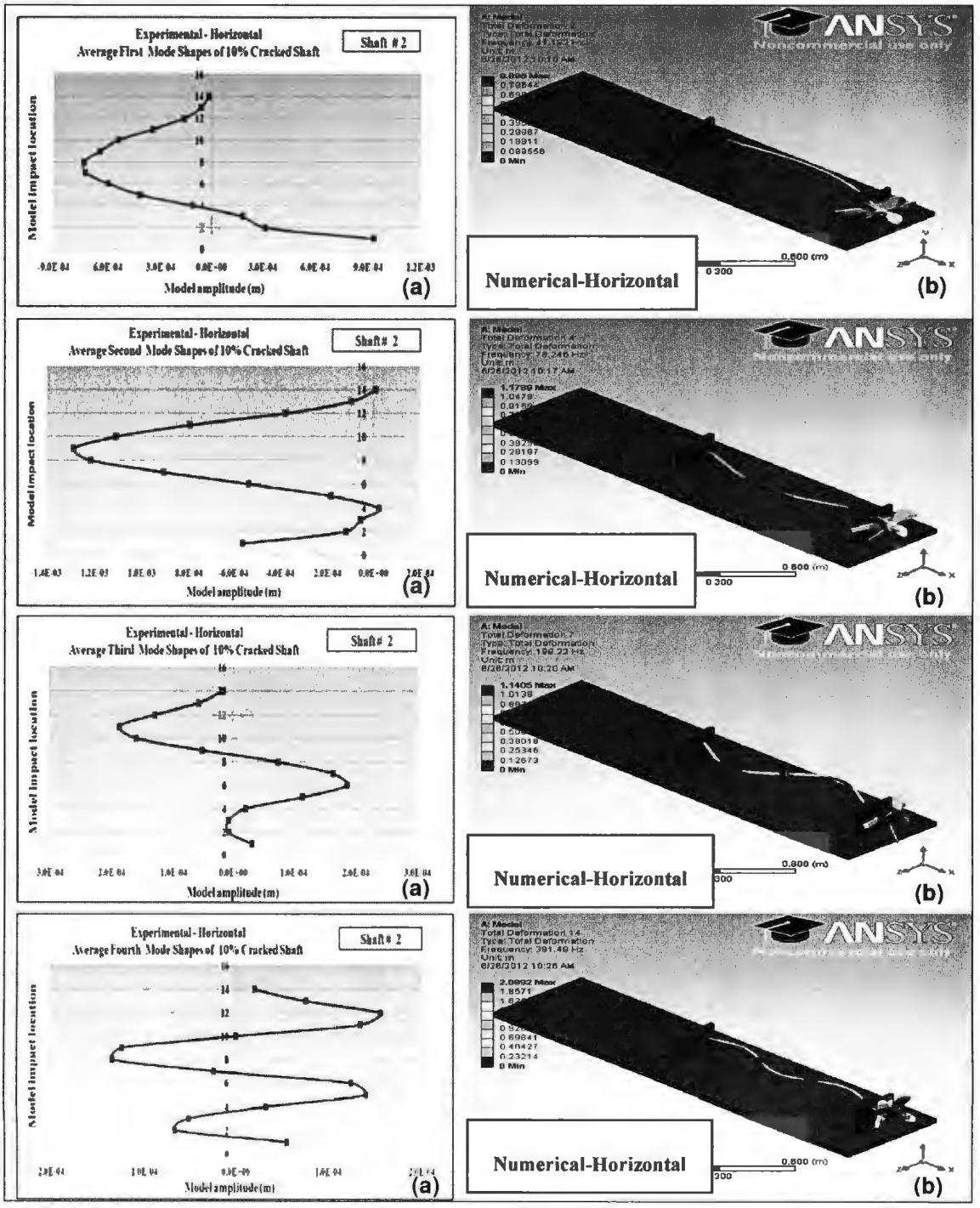

Figure E.1.2 Mode Shapes Comparison for First Four Horizontal Frequencies (10%) a) Experimental and b) Numerical

E.2: Mode Shapes Comparison for First Four Vertical and Horizontal Frequencies (20%): (A) Experimental and (B) Numerical

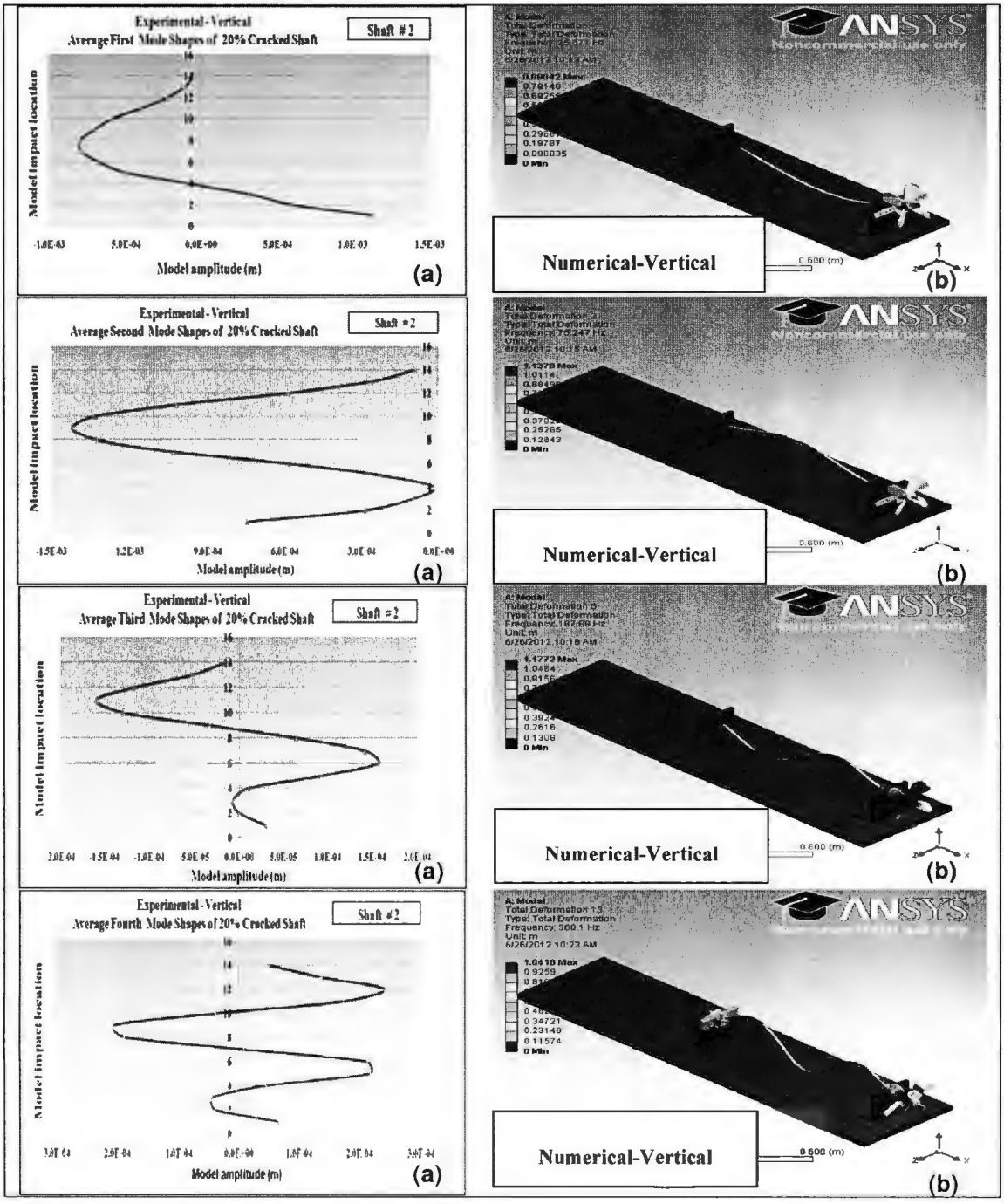

Figure E.2.1 Mode Shapes Comparison for First Four Vertical Frequencies (20%) a) Experimental and b) Numerical

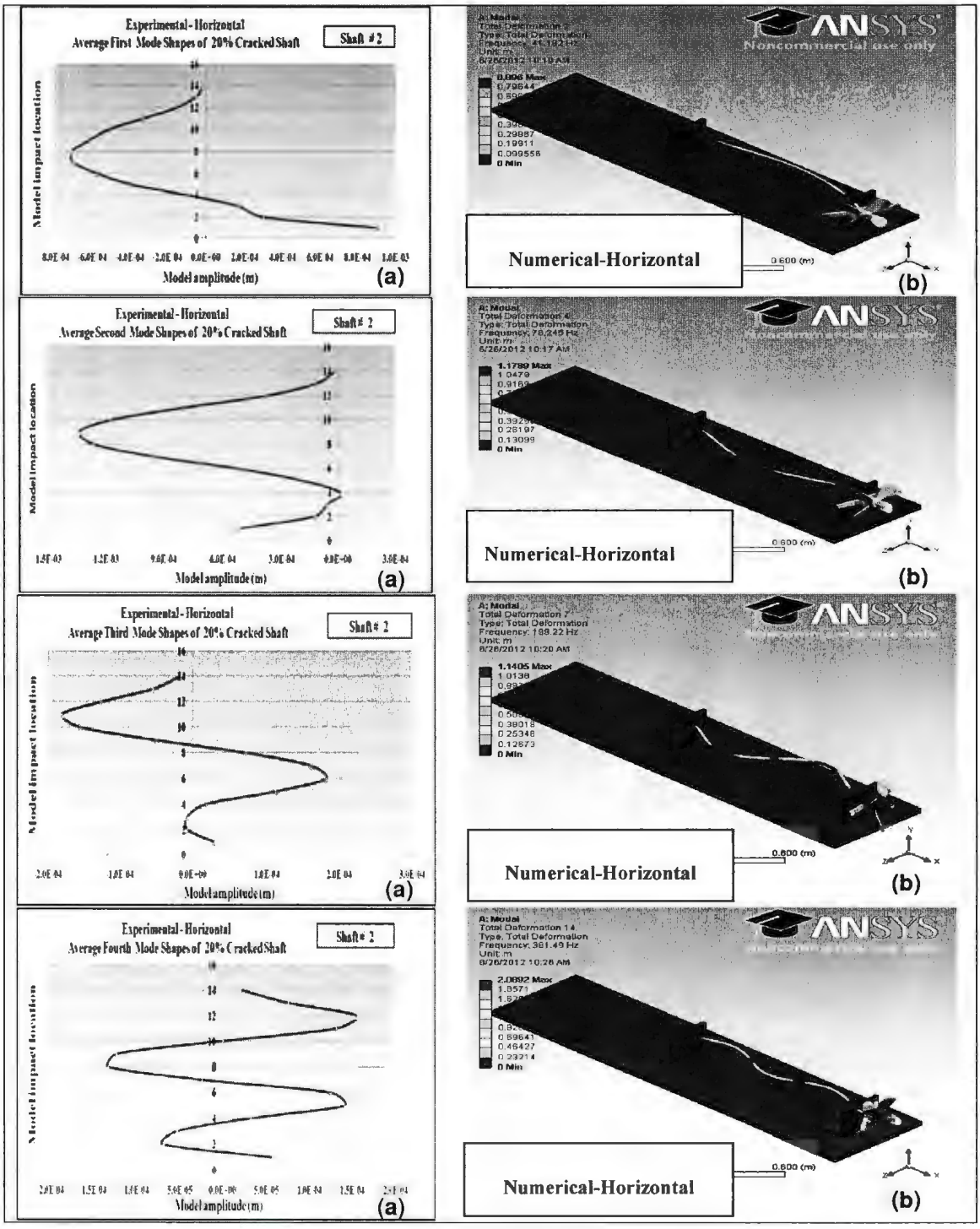

Figure E.2.2 Mode Shapes Comparison for First Four Horizontal Frequencies (20%) a) Experimental and b) Numerical

E.3: Mode Shapes Comparison for First Four Vertical and Horizontal Frequencies (30%): (A) Experimental and (B) Numerical

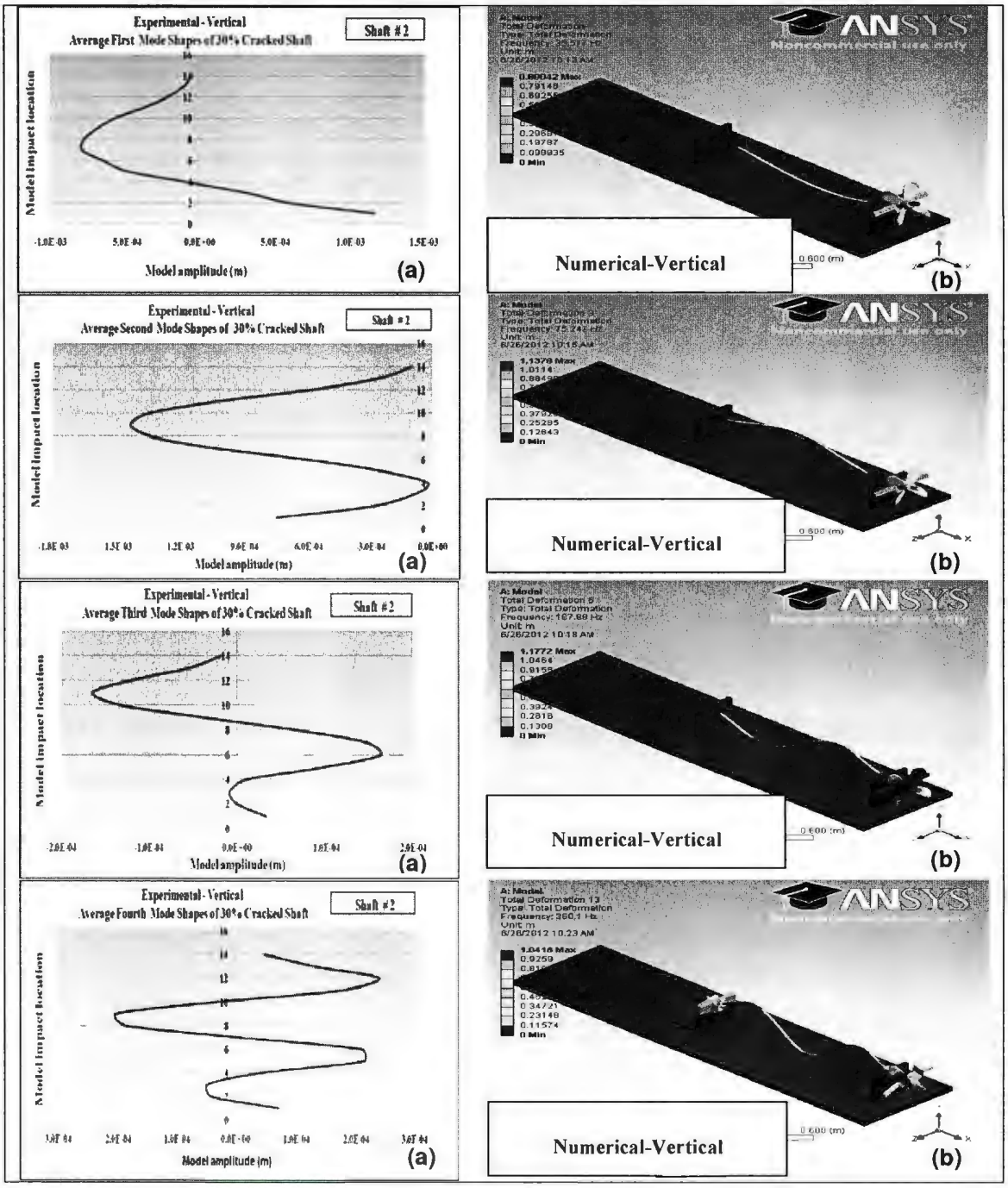

Figure E.3.1 Mode Shapes Comparison for First Four Vertical Frequencies (30%) a) Experimental and b) Numerical

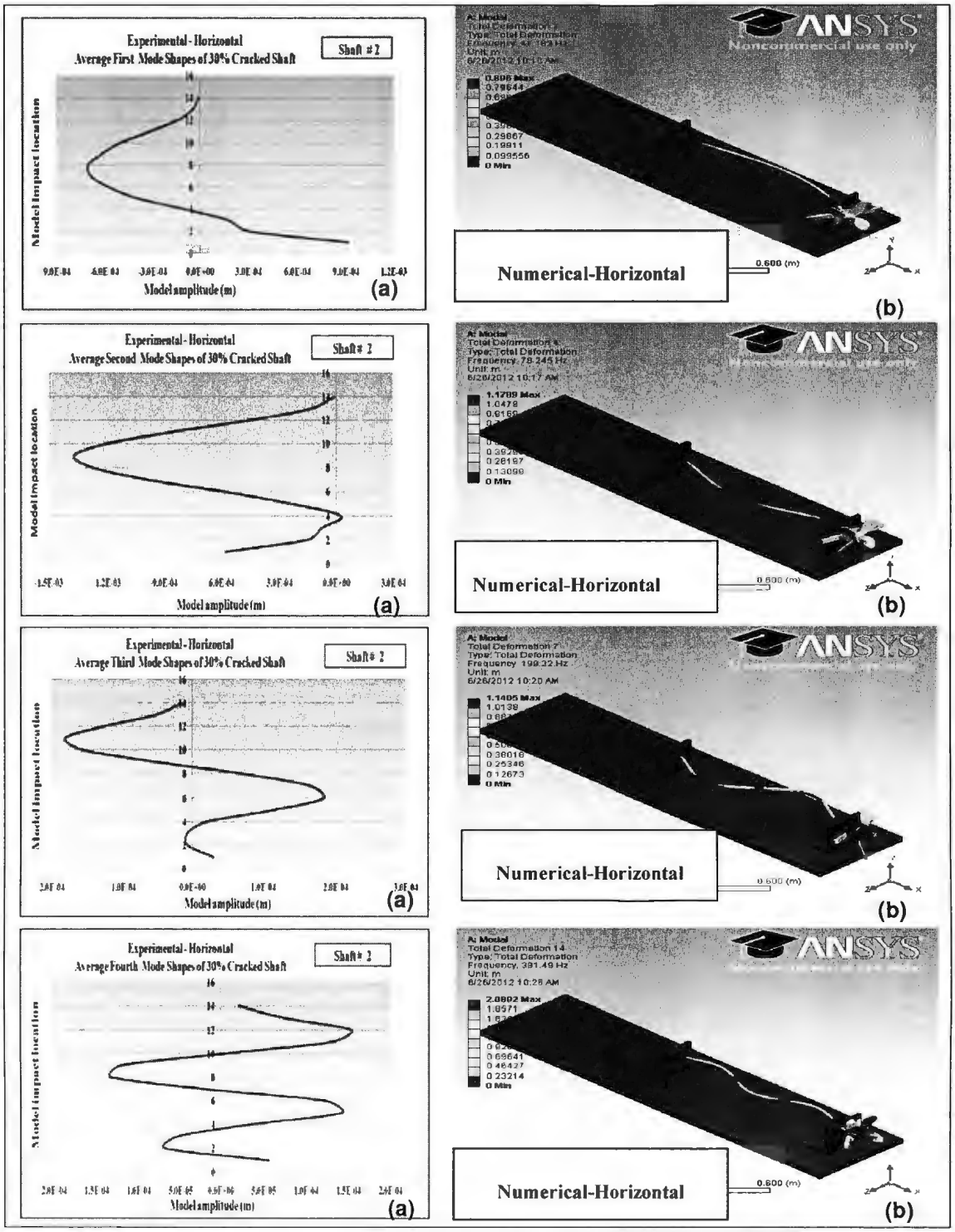

Figure E.3.2 Mode Shapes Comparison for First Four Horizontal Frequencies (30%) a) Experimental and b) Numerical

Appendix F – "Mode Shapes for Local and Coupled Vertical and Horizontal Numerical Computations for Uncracked Rotor Shaft-Propeller-Supports-Torque Bar"

F.1 First Vertical and Horizontal Bending Modes

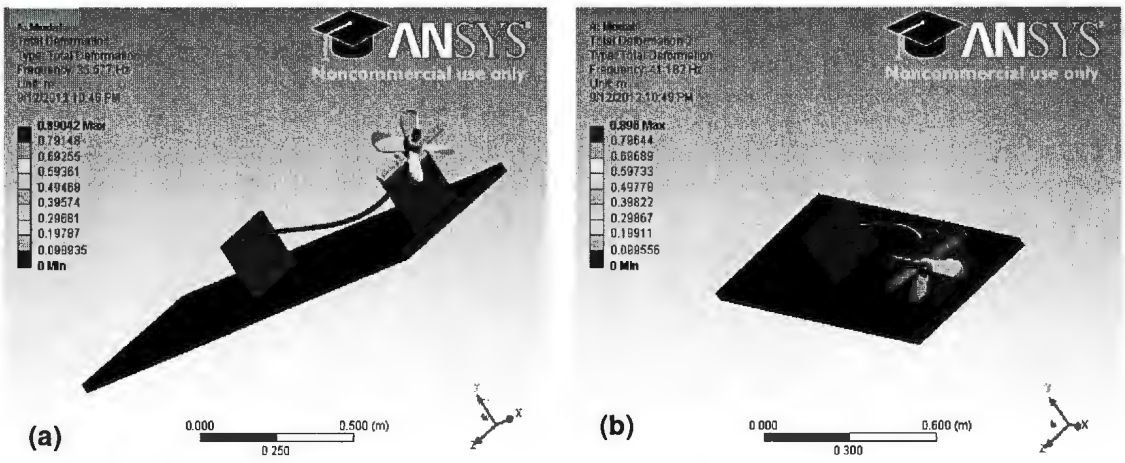

Figure F.1 Bending Mode Shapes for First: a) Vertical; and b) Horizontal

F.2 Second Vertical and Horizontal Bending Modes

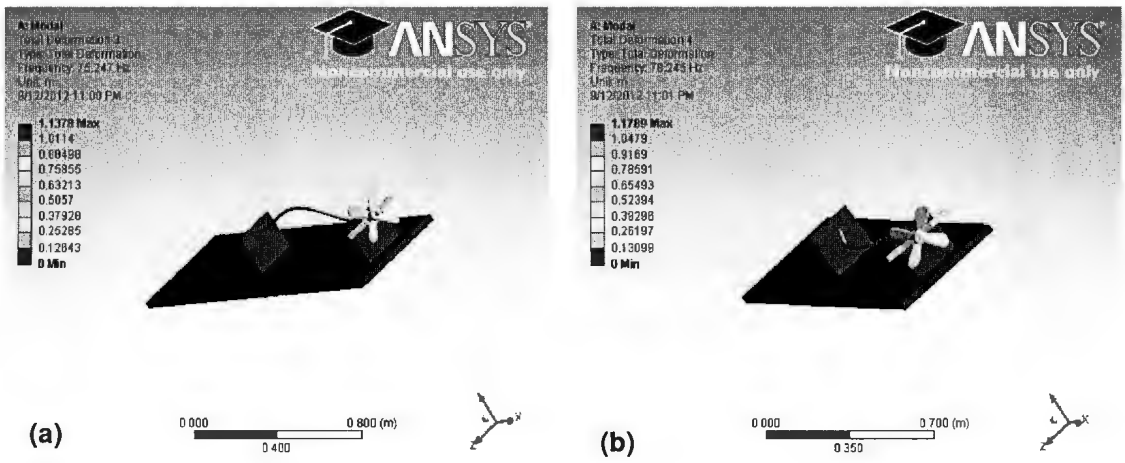

Figure F.2 Bending Mode Shapes for Second: a) Vertical; and b) Horizontal Modes

F.3 Third Vertical and Horizontal Bending Modes

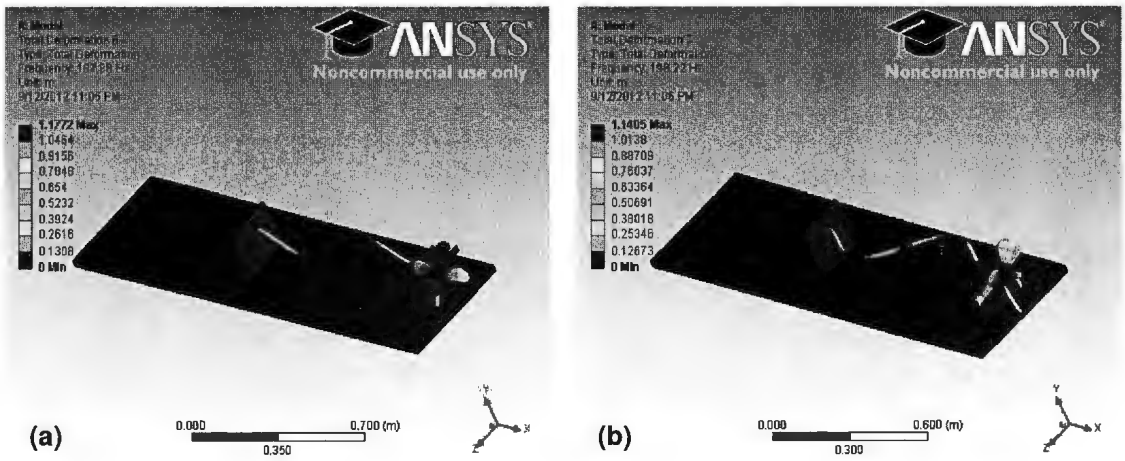

Figure F.3 Bending Mode Shapes for Third: a) Vertical; and b) Horizontal

F.4 Bending Mode Shapes for Rotor Shaft-Propeller-Support

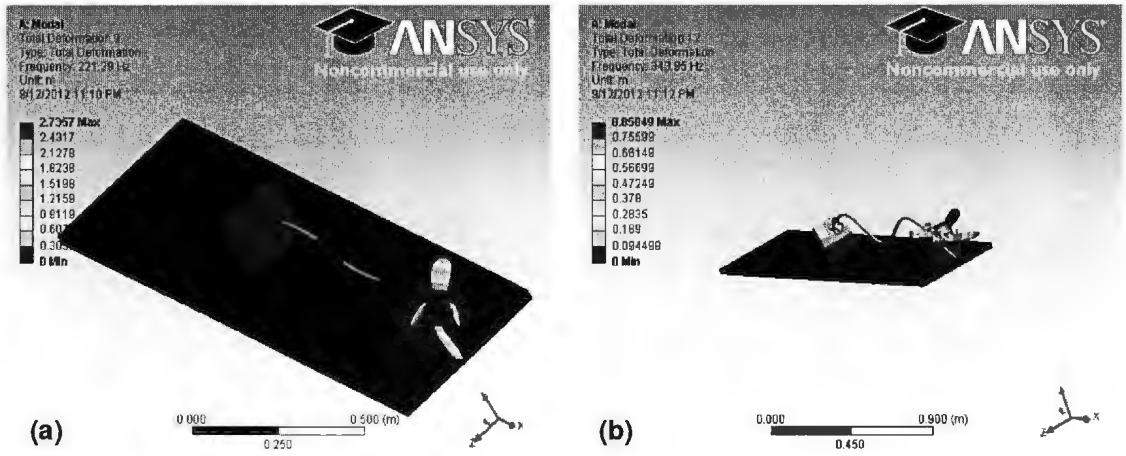

Figure F.4 Bending Mode Shapes for Bending of: a) Rotor Shaft-Propeller; and b) Rotor Shaft-Support #1

F.5 Fourth Vertical and Horizontal Bending Modes

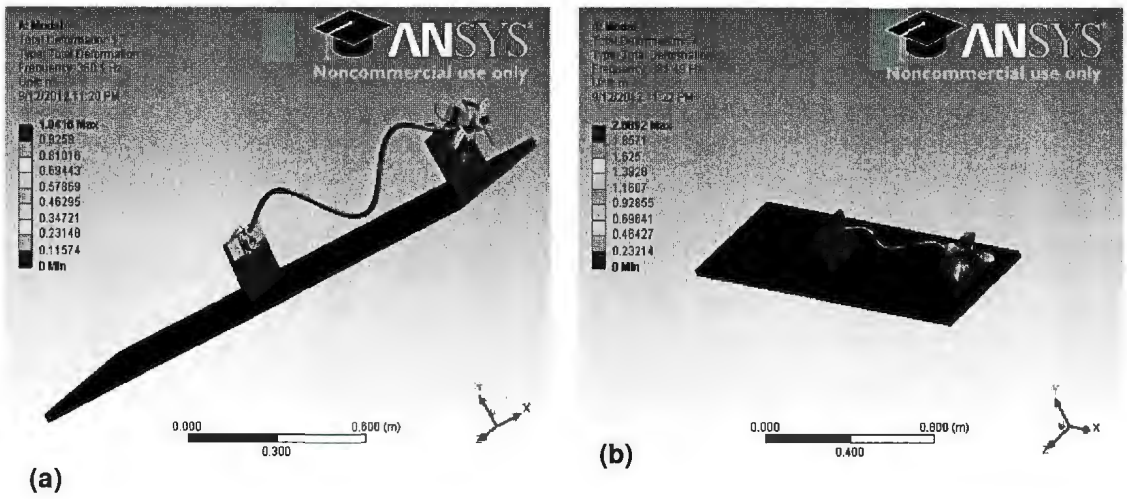

Figure F.5 Bending Mode Shapes for Fourth: a) Vertical; and b) Horizontal Modes

F.6 Coupled Horizontal Bending of Rotor Shaft and Torque Bar; also Mode Shape for Bending of Support # 2

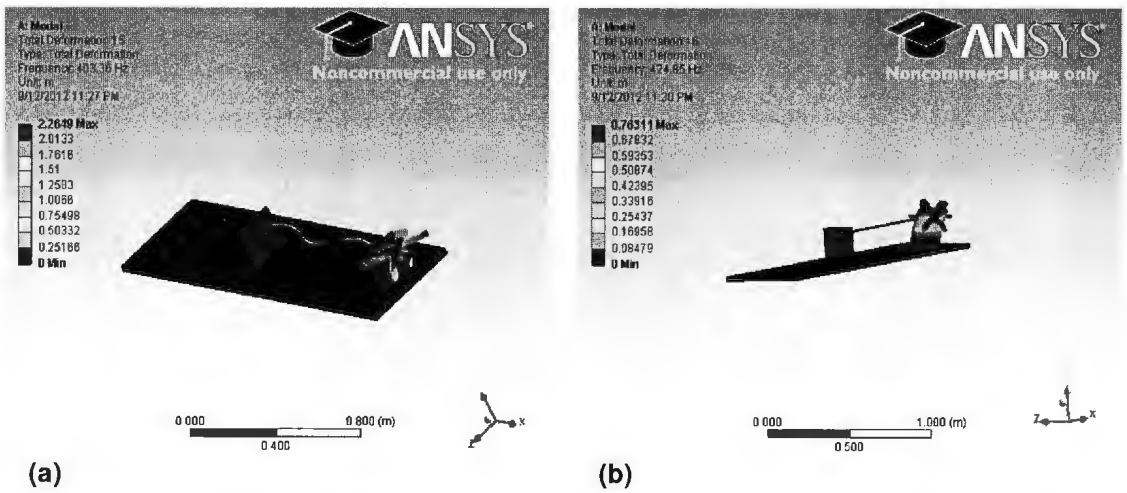

Figure F.6 Bending Mode Shapes for: a) Coupled Horizontal Bending of Rotor Shaft and Torque Bar; and b) Bending of Support # 2

F.7 Coupled of Vertical and Horizontal Bending of the Rotor Shaft and Propeller-Torque Bar

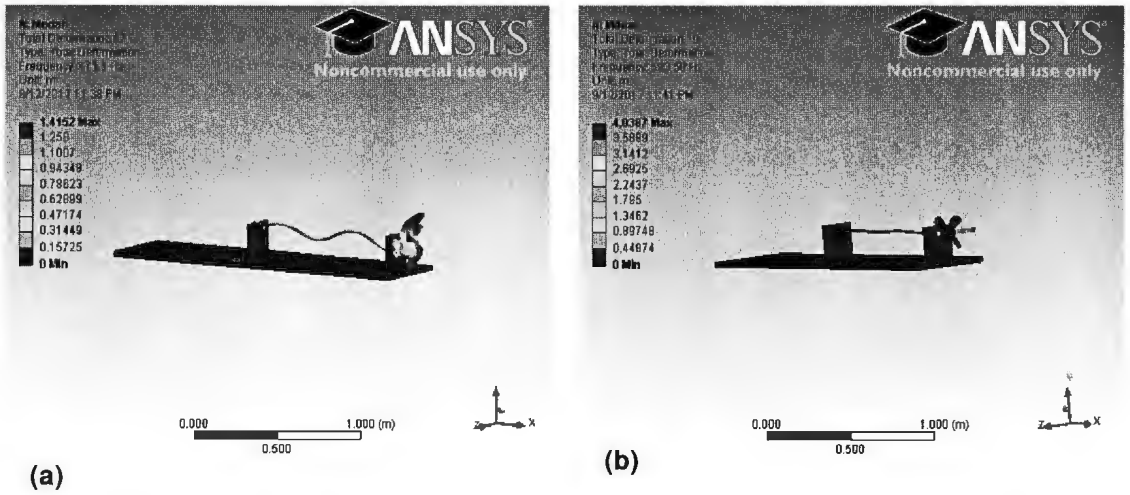

(a) (b)

Figure F.7 Coupled of Vertical and Horizontal Bending of the Rotor Shaft with: a) Propeller and Torque Bar; and b) Torque Bar

Appendix G – "Frequency Responses of the Rotor Shaft system"

G.1 The Responses of the System Under Test (impact excitation) and the Corresponding Responses Functions (Acceleration FRFs, Velocity FRFs, Displacement FRFs) for Experimental and Numerical Results

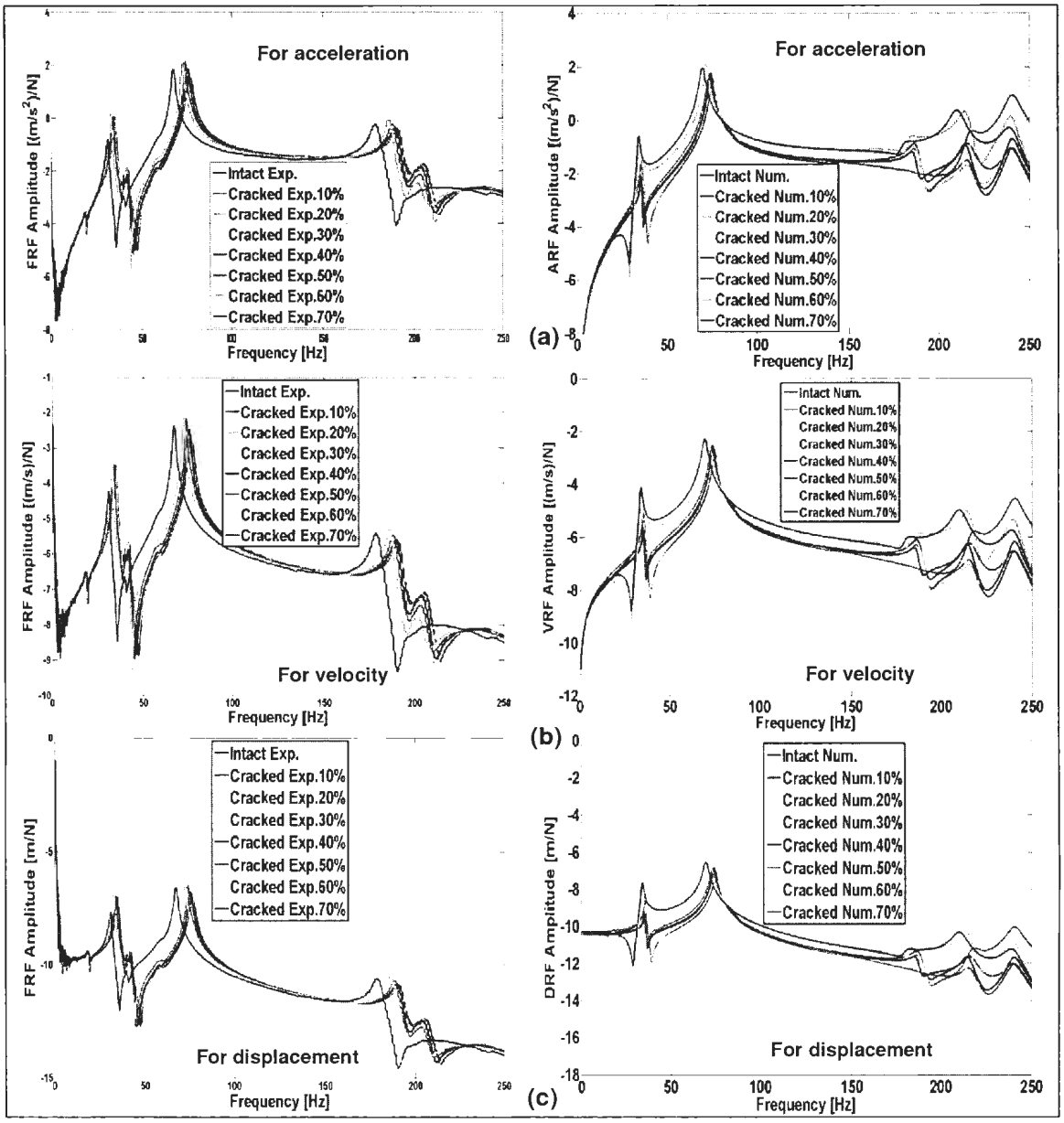

Figure G.1.1 Schematic of Experimental and Numerical Frequency Response Functions of: a) Accelerations (ARFs); b) Velocities (VRFs) and (c) Displacements (DRFs) for Shaft # 1.

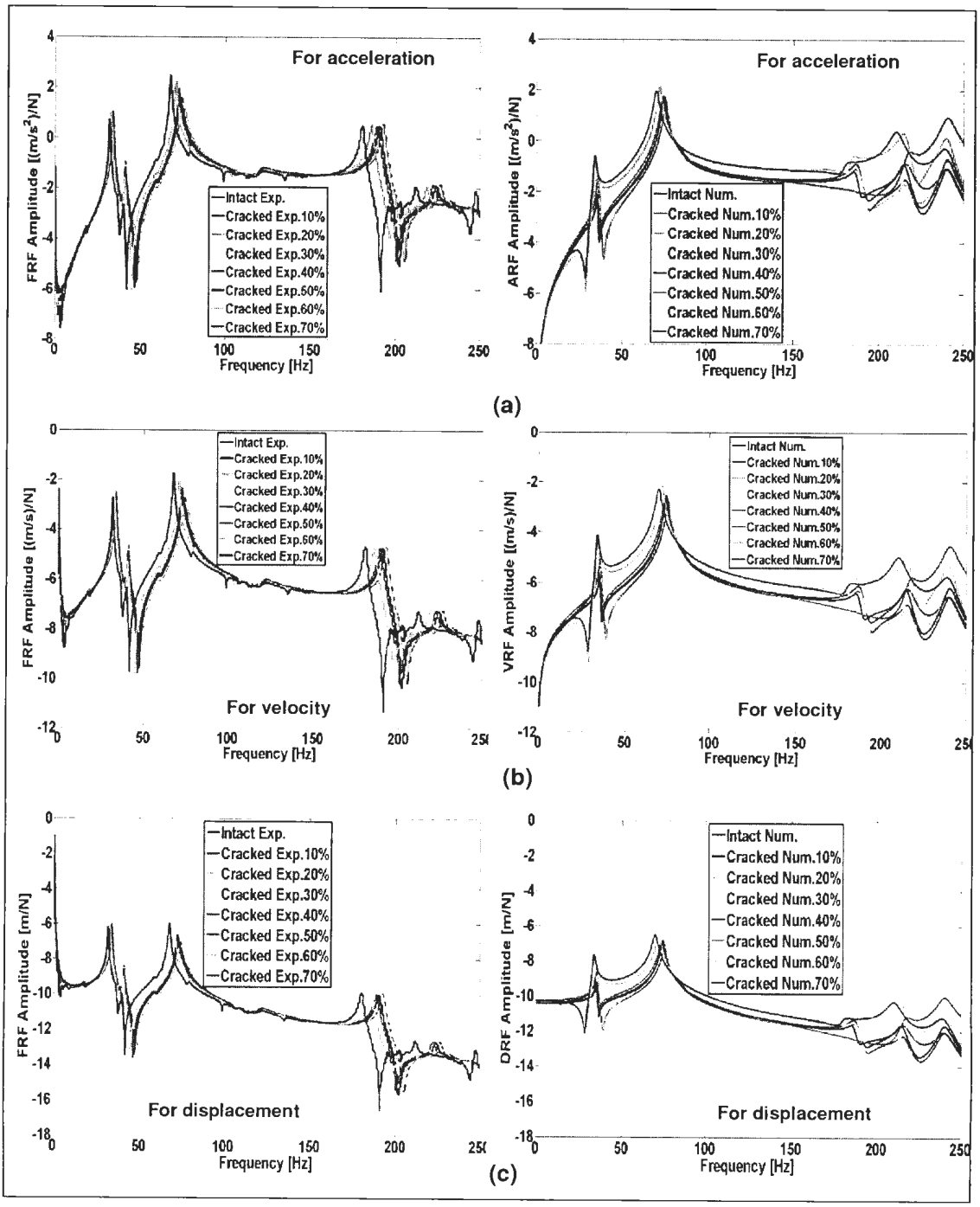

Figure G.1.2 Schematic of Experimental and Numerical Frequency Response Functions of: a) Accelerations (ARFs); b) Velocities (VRFs) and (c) Displacements (DRFs) for Shaft # 3.

Appendix H – "Comparison Frequency Response Function for Experimental and Numerical Computations"

H.1 Frequency Response Functions for Different Depth of Crack of Experimental and Numerical Computations: shaft # 1 & shaft # 3

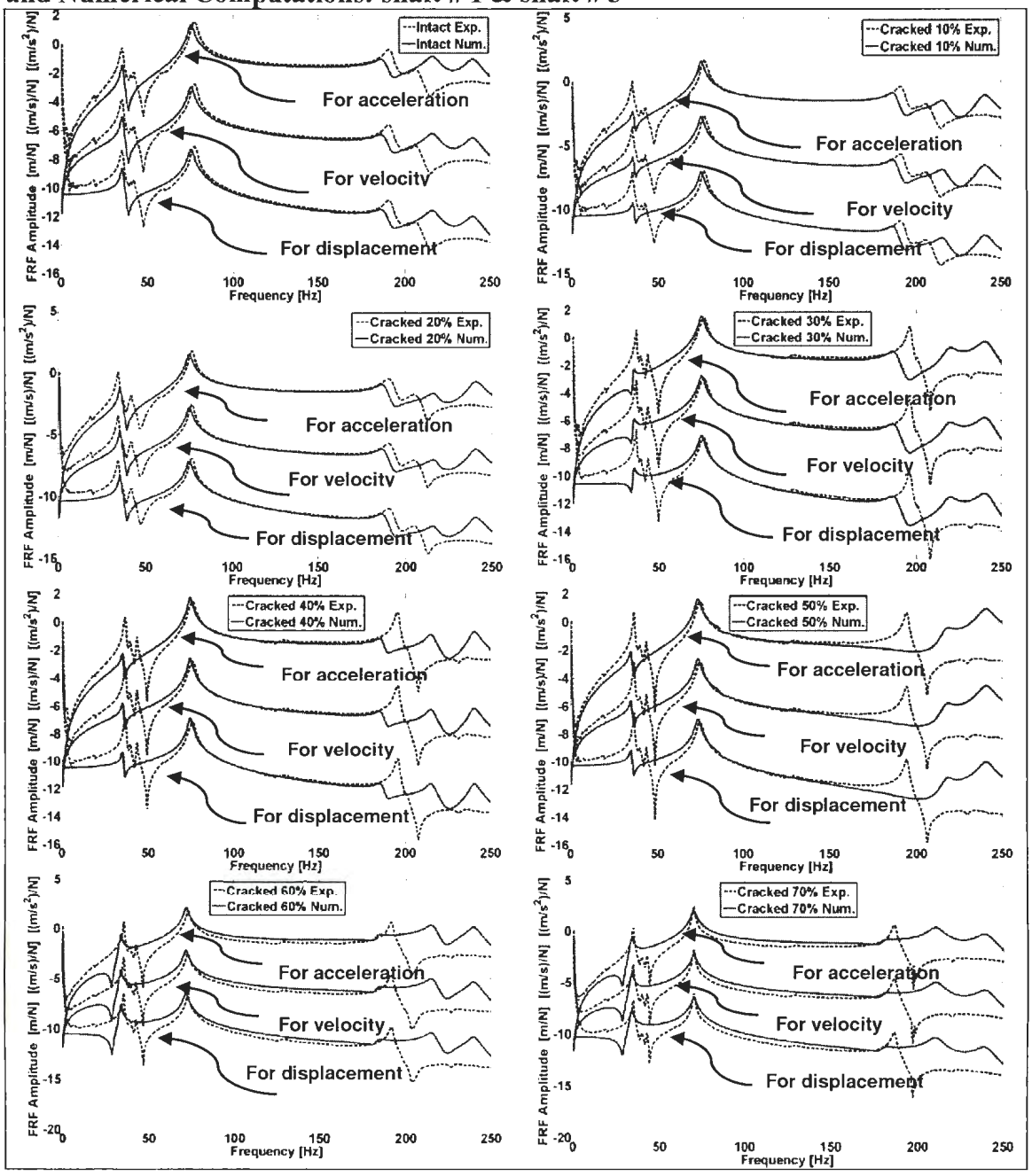

Figure H.1.1 Schematic of Frequency Response Functions for Different Depth of Crack of Experimental and Numerical Computations: Shaft # 1

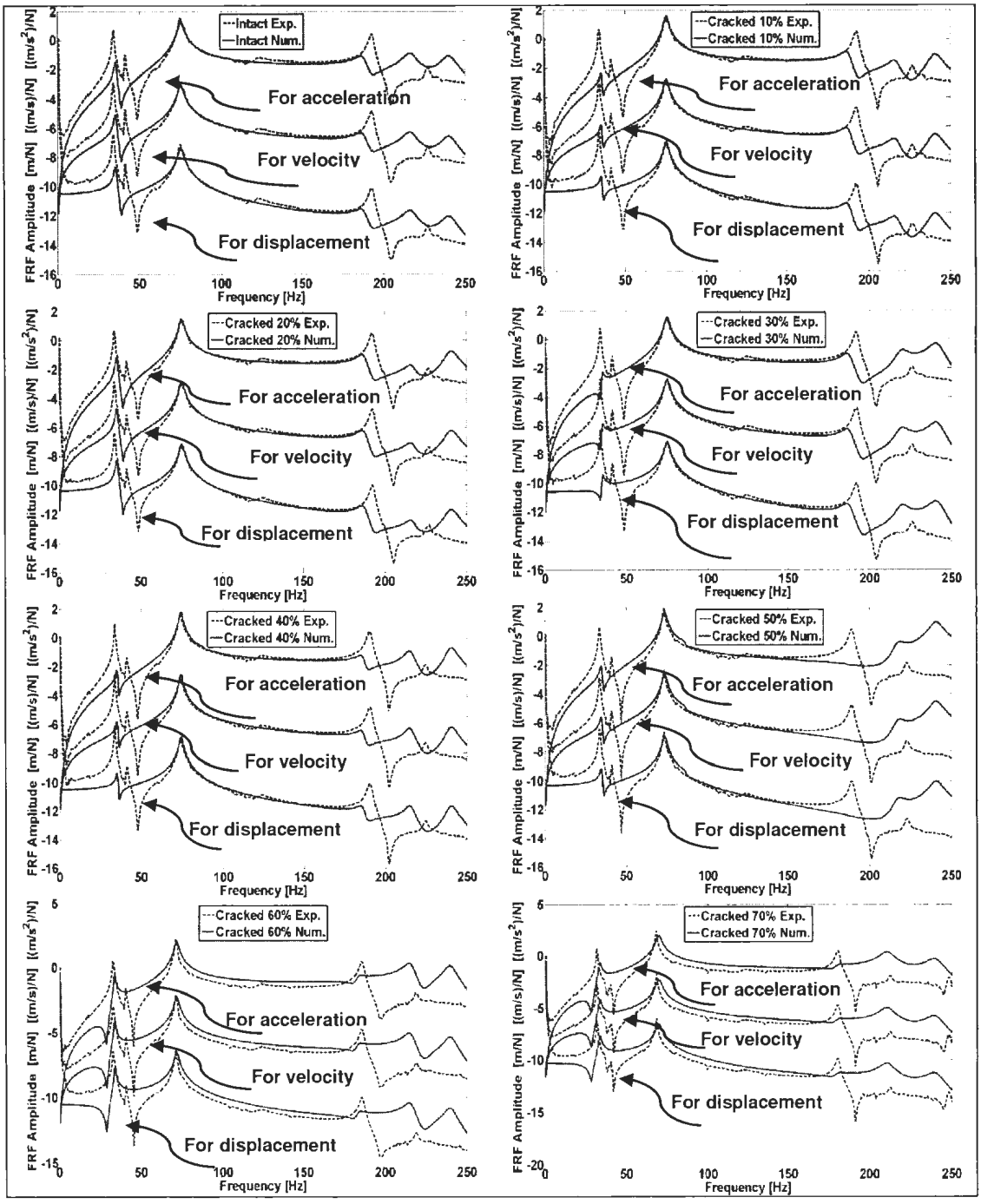

Figure H.1.2 Schematic of Frequency Response Functions for Different Depth of Crack of Experimental and Numerical Computations: Shaft # 3

Appendix I – "Comparison of Experimental Results of Resonant and Anti-Resonant Frequency Amplitudes"

I.1.1: Comparison of Experimental Results for Resonant Frequency Amplitudes shaft # 1

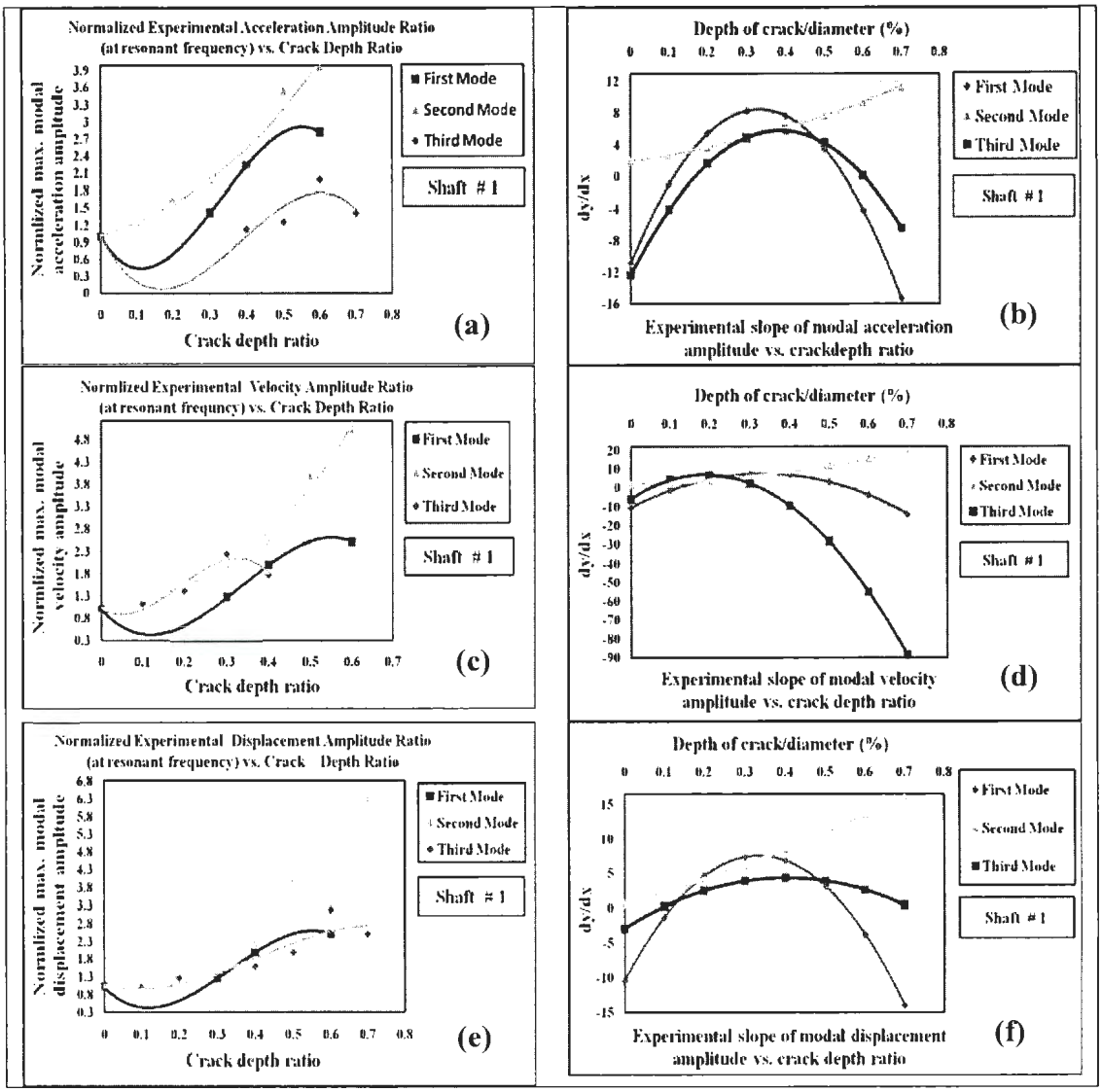

Figure I.1.1 Comparison of Experimental Results for Resonant Frequency Amplitudes: a) Acceleration Amplitude versus Crack Depth Ratio; b) Slope of Modal Acceleration Amplitude versus Crack Depth Ratio; c) Velocity Amplitude versus Crack Depth Ratio; d) Slope of Modal Velocity Amplitude versus Crack Depth Ratio; e) Displacement Amplitude versus Crack Depth Ratio; and f) Slope of Modal Displacement Amplitude versus Crack Depth Ratio; Shaft # 1

I.1.2: Comparison of Experimental Results for Resonant Frequency Amplitudes shaft # 3

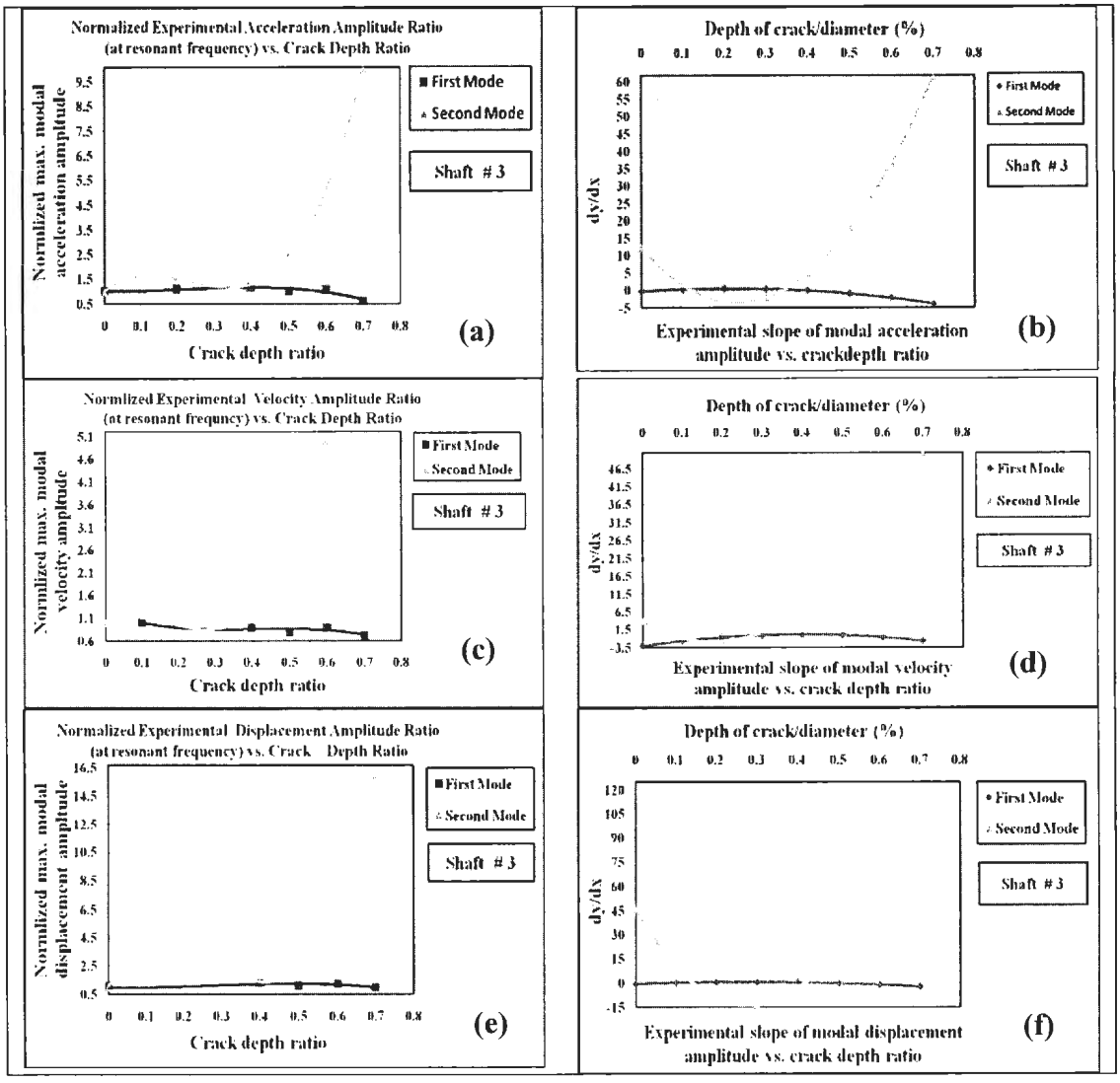

Figure I.1.2 Comparison of Experimental Results for Resonant Frequency Amplitudes: a) Acceleration Amplitude versus Crack Depth Ratio; b) Slope of Modal Acceleration Amplitude versus Crack Depth Ratio; c) Velocity Amplitude versus Crack Depth Ratio; d) Slope of Modal Velocity Amplitude versus Crack Depth Ratio; e) Displacement Amplitude versus Crack Depth Ratio; and f) Slope of modal Displacement Amplitude versus Crack Depth Ratio; Shaft # 3

I.1.3: Comparison of Experimental Results for Anti-Resonant Frequency Amplitudes-shaft # 1

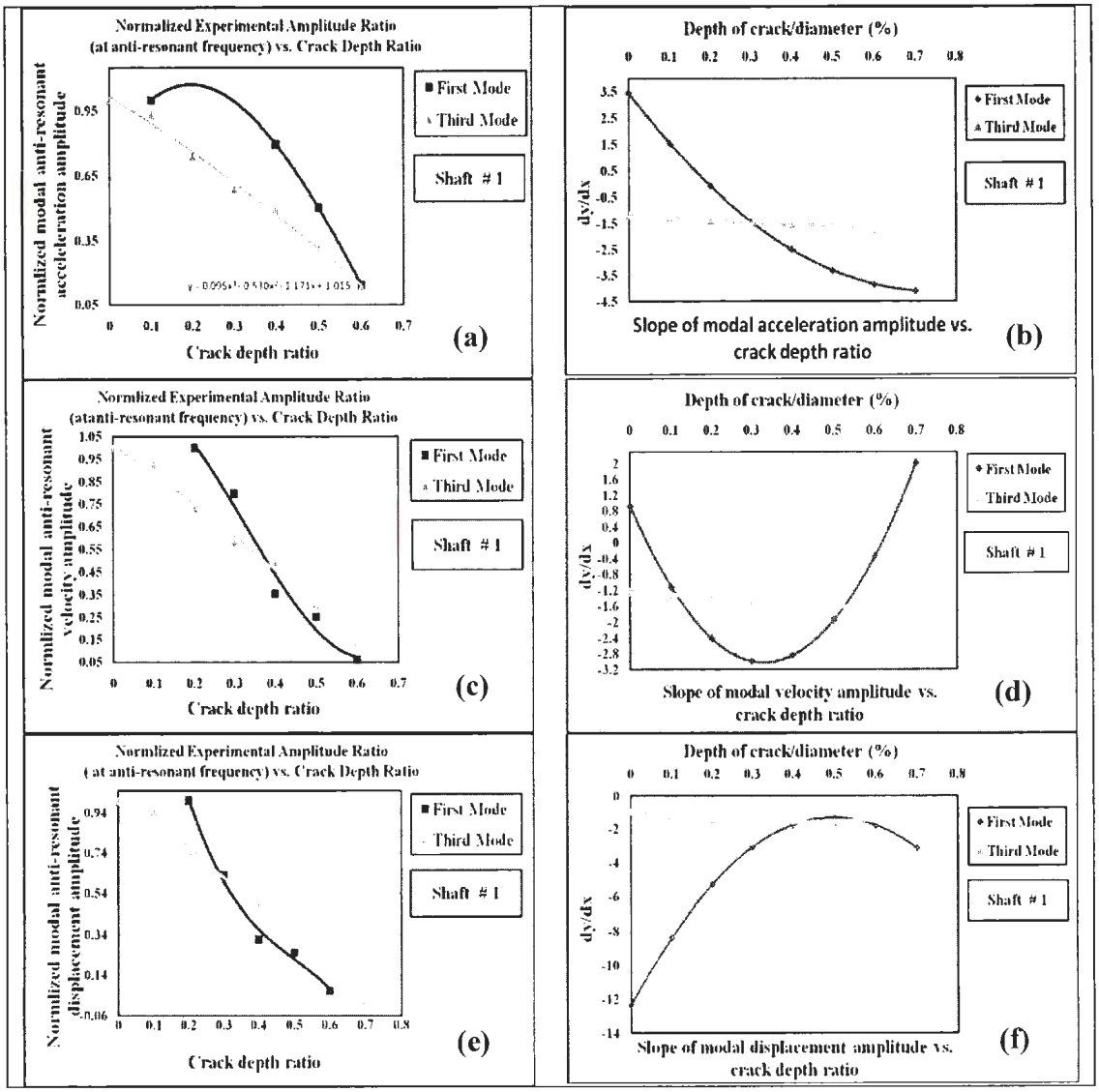

Figure I.1.3 Comparison of Experimental Results for Anti-Resonant Frequency Amplitude Response: a) Acceleration Amplitude versus Crack Depth Ratio; b) Slope of Modal Acceleration Amplitude versus Crack Depth Ratio; c) Velocity Amplitude versus Crack Depth Ratio; d) Slope of Modal Velocity Amplitude versus Crack Depth Ratio; e) Displacement Amplitude versus Crack Depth Ratio; and f) Slope of modal Displacement Amplitude versus Crack Depth Ratio; Shaft # 1

I.1.4: Comparison of Experimental Results for Anti-Resonant Frequency Amplitudes - shaft # 3

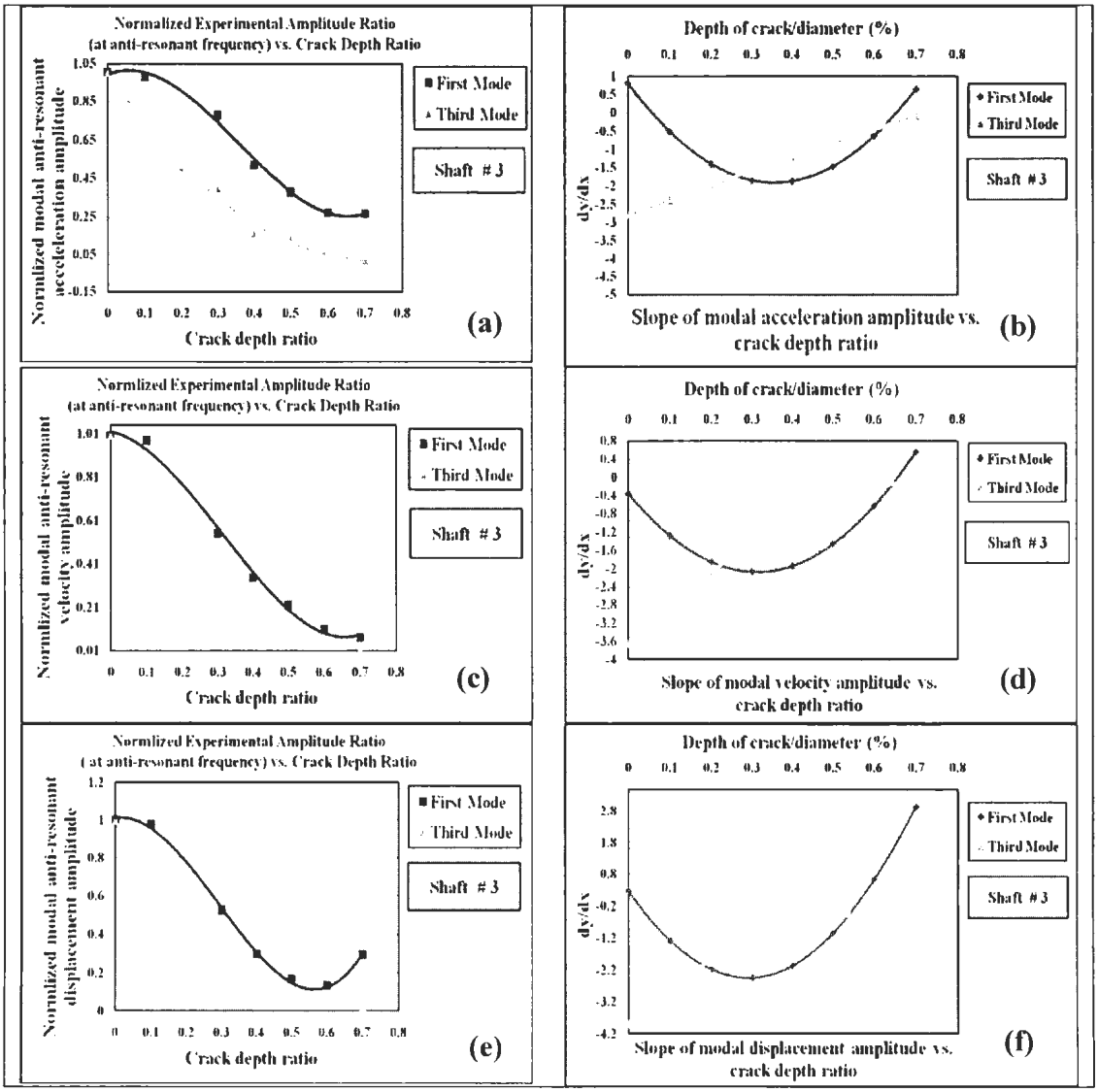

Figure I.1.4 Comparison of Experimental Results for Anti-Resonant Frequency Amplitude Response: a) Acceleration Amplitude versus Crack Depth Ratio; b) Slope of Modal Acceleration Amplitude versus Crack Depth Ratio; c) Velocity Amplitude versus Crack Depth Ratio; d) Slope of Modal Velocity Amplitude versus Crack Depth Ratio; e) Displacement Amplitude versus Crack Depth Ratio; and f) Slope of modal Displacement Amplitude versus Crack Depth Ratio; Shaft # 3

I.1.5: Comparison of Experimental and Numerical Results for Resonant Frequencies of Shaft # 1 (for First and Second Modes).

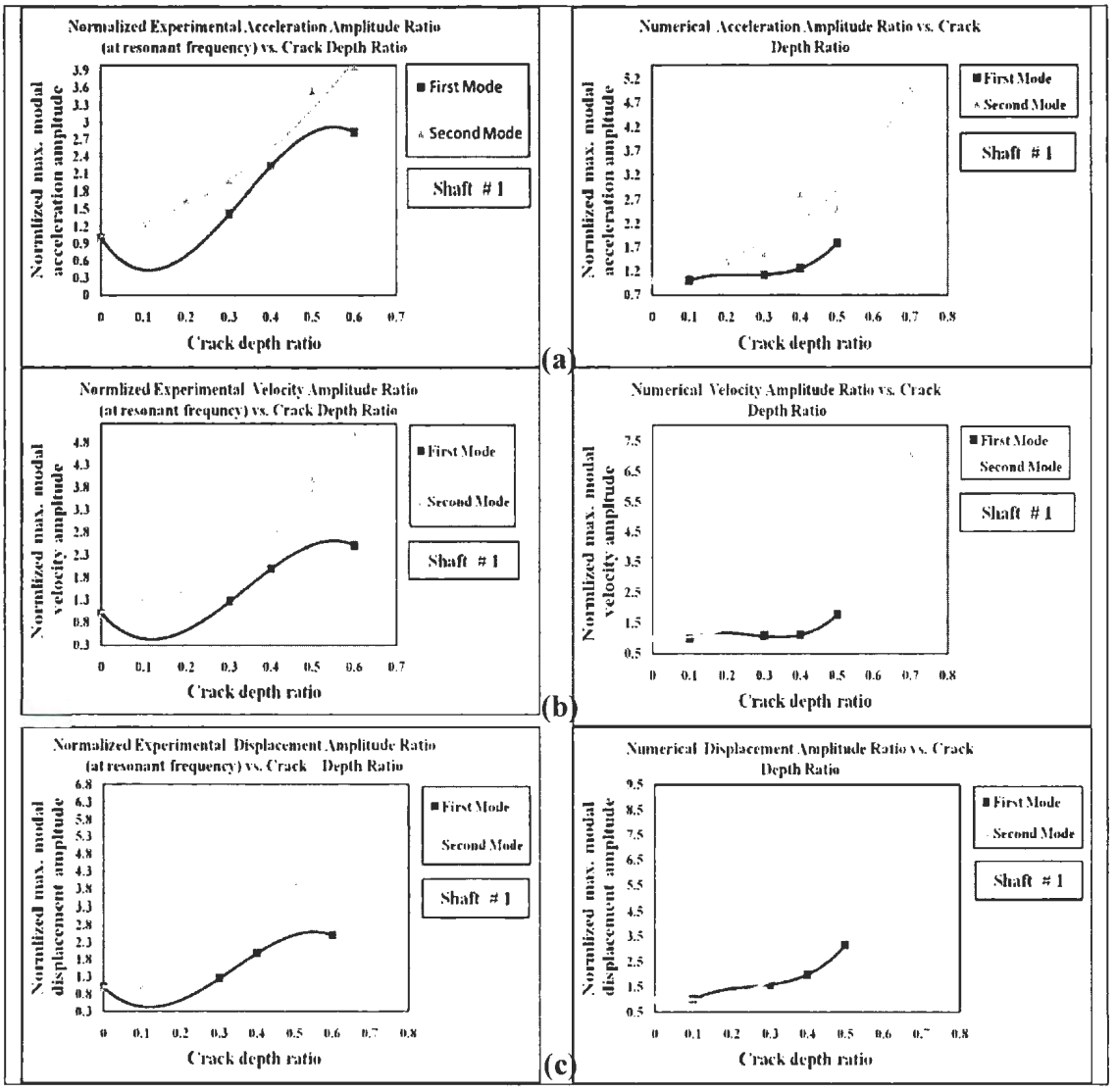

Figure I.1.5 Comparison of Experimental and Numerical Results for Resonant Frequency of Shaft # 1 for (First and Second Modes): a) Acceleration Amplitude versus Crack Depth Ratio; b) Velocity Amplitude versus Crack Depth Ratio; and c) Displacement Amplitude versus Crack Depth Ratio

I.1.6: Comparison of Experimental and Numerical Results for Resonant Frequencies of Shaft # 3 (for First and Second Modes)

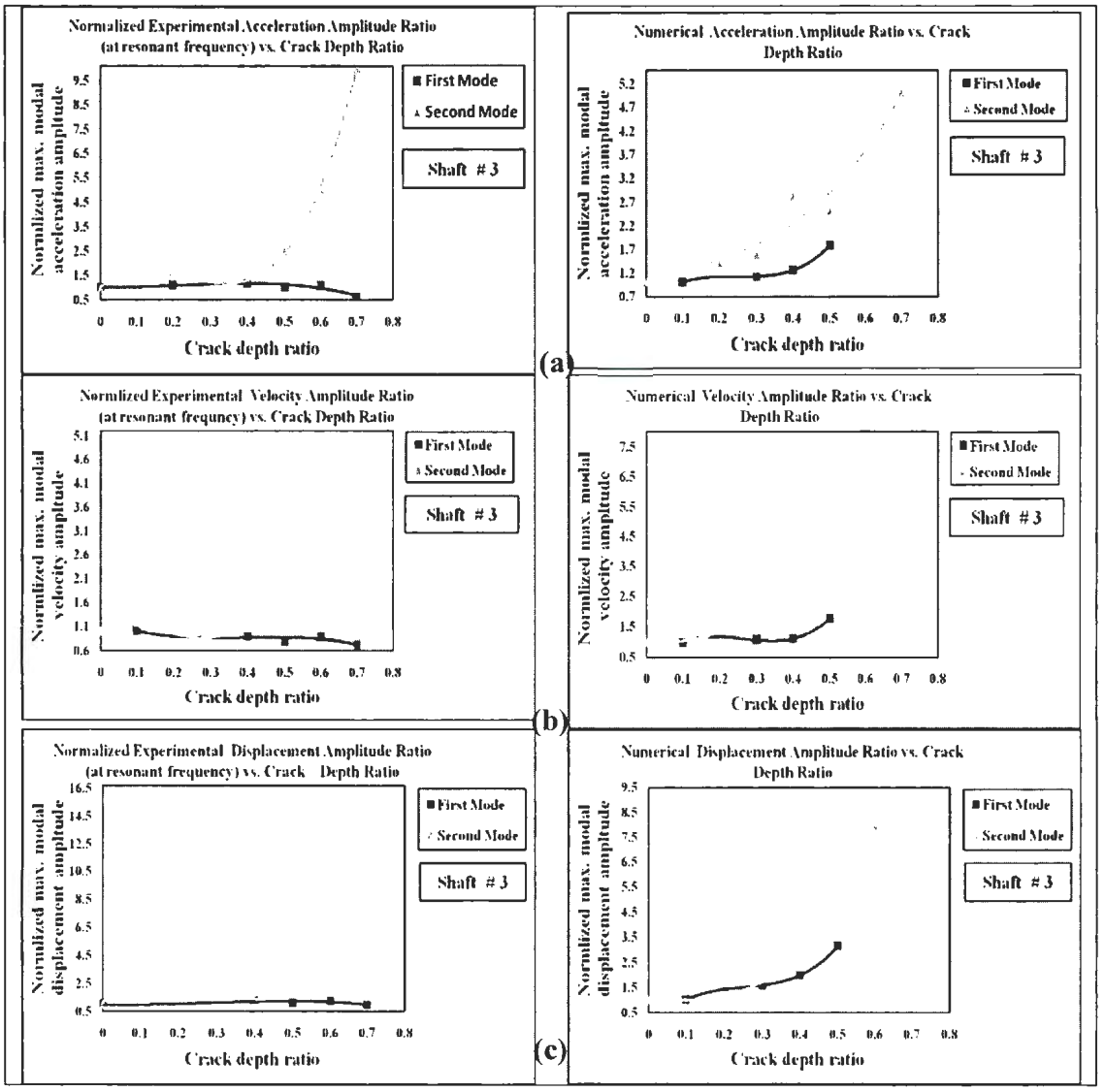

Figure I.1.6 Comparison of Experimental and Numerical Results for Resonant Frequency of Shaft # 3 for (First and Second Modes): a) Acceleration Amplitude versus Crack Depth Ratio; b) Velocity Amplitude versus Crack Depth Ratio; and c) Displacement Amplitude versus Crack Depth Ratio

I.1.7: Comparison of Experimental and Numerical Results for Slopes of Resonant Frequency Amplitudes of Shaft # 1 (for First and Second Modes)

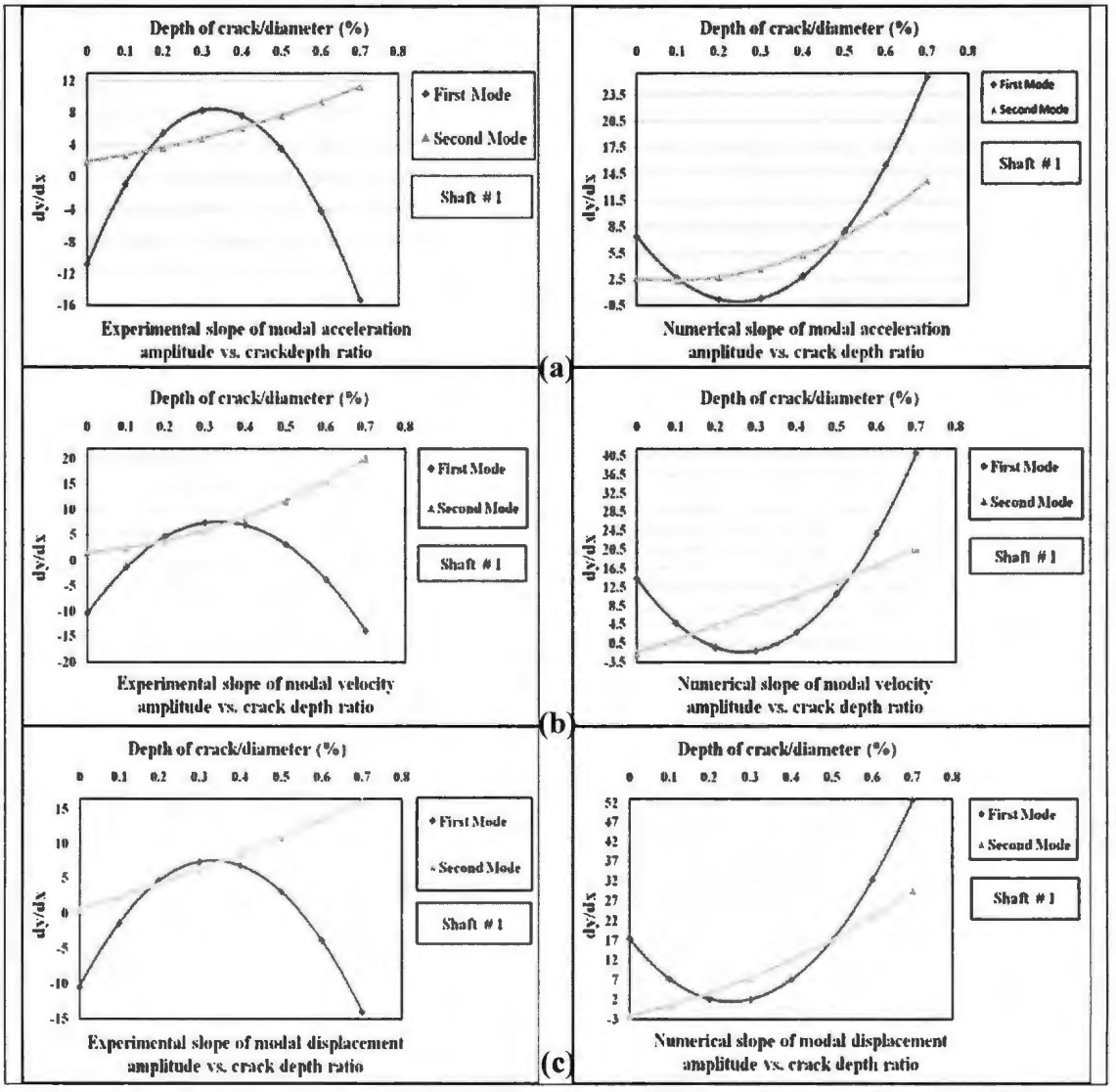

Figure I.1.7 Comparison of Experimental and Numerical Results for Slopes of Resonant Frequency Amplitudes of Shaft # 1 for (First and Second Modes): a) Slope of the Modal Acceleration Amplitude vs. Crack Depth Ratio; b) Slope of the Modal Velocity Amplitude vs. Crack Depth Ratio; and c) Slope of the Modal Displacement Amplitude vs. Crack Depth Ratio.

I.1.8: Comparison of Experimental and Numerical Results for Slopes of Resonant Frequency Amplitudes of Shaft # 3 (for First and Second Modes)

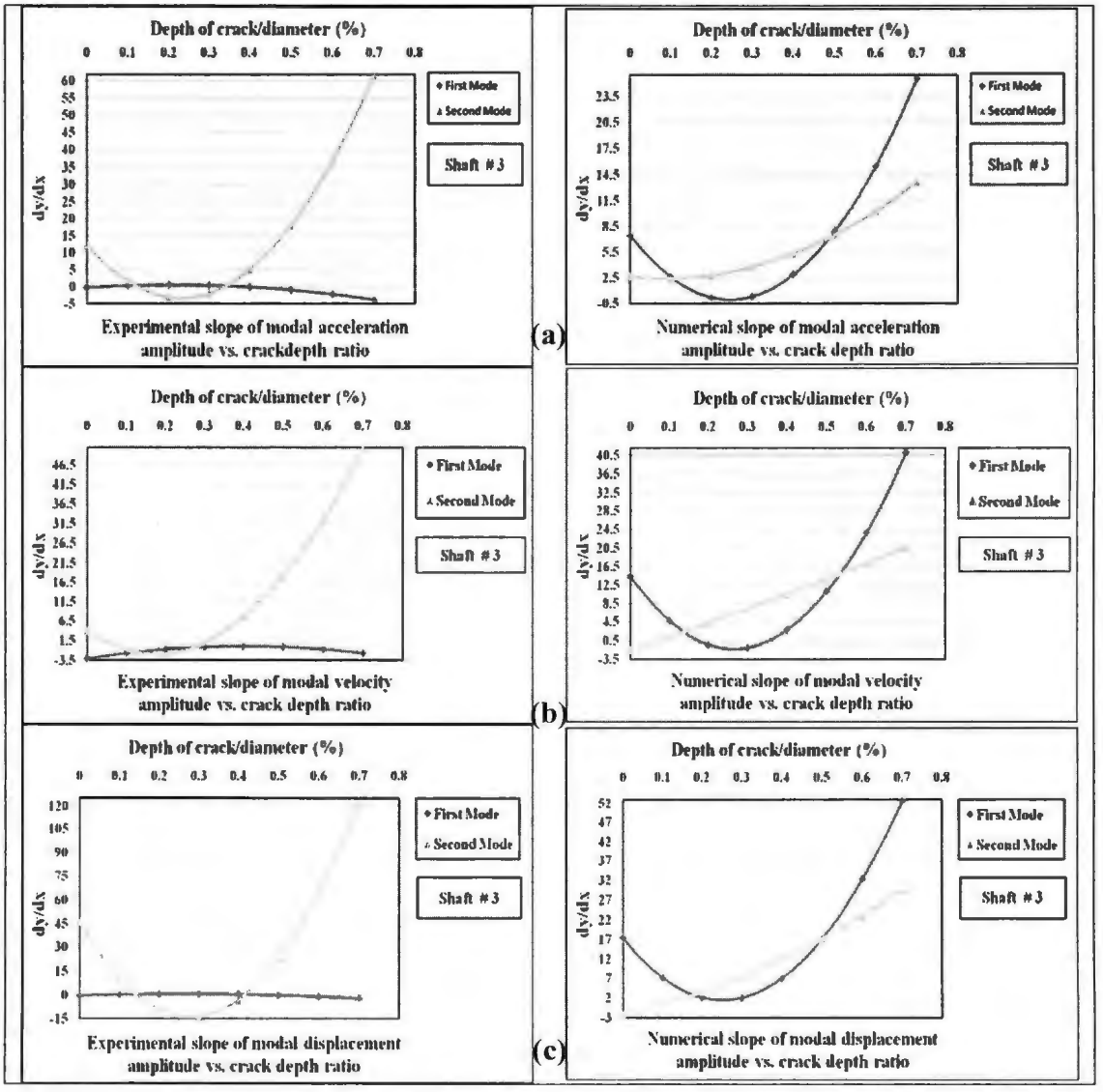

Figure I.1.8 Comparison of Experimental and Numerical Results for Slopes of Resonant Frequency Amplitudes of Shaft # 3 for (First and Second Modes): a) Slope of the Modal Acceleration Amplitude vs. Crack Depth Ratio; b) Slope of the Modal Velocity Amplitude vs. Crack Depth Ratio; and c) Slope of the Modal Displacement Amplitude vs. Crack Depth Ratio.

Appendix J – "Comparison of Experimental and Numerical Results of Resonant Frequency Shaft

J.1.1: Comparison of Experimental and Numerical Results of Shaft # 1 for (at Four Resonant Frequencies Ratios)

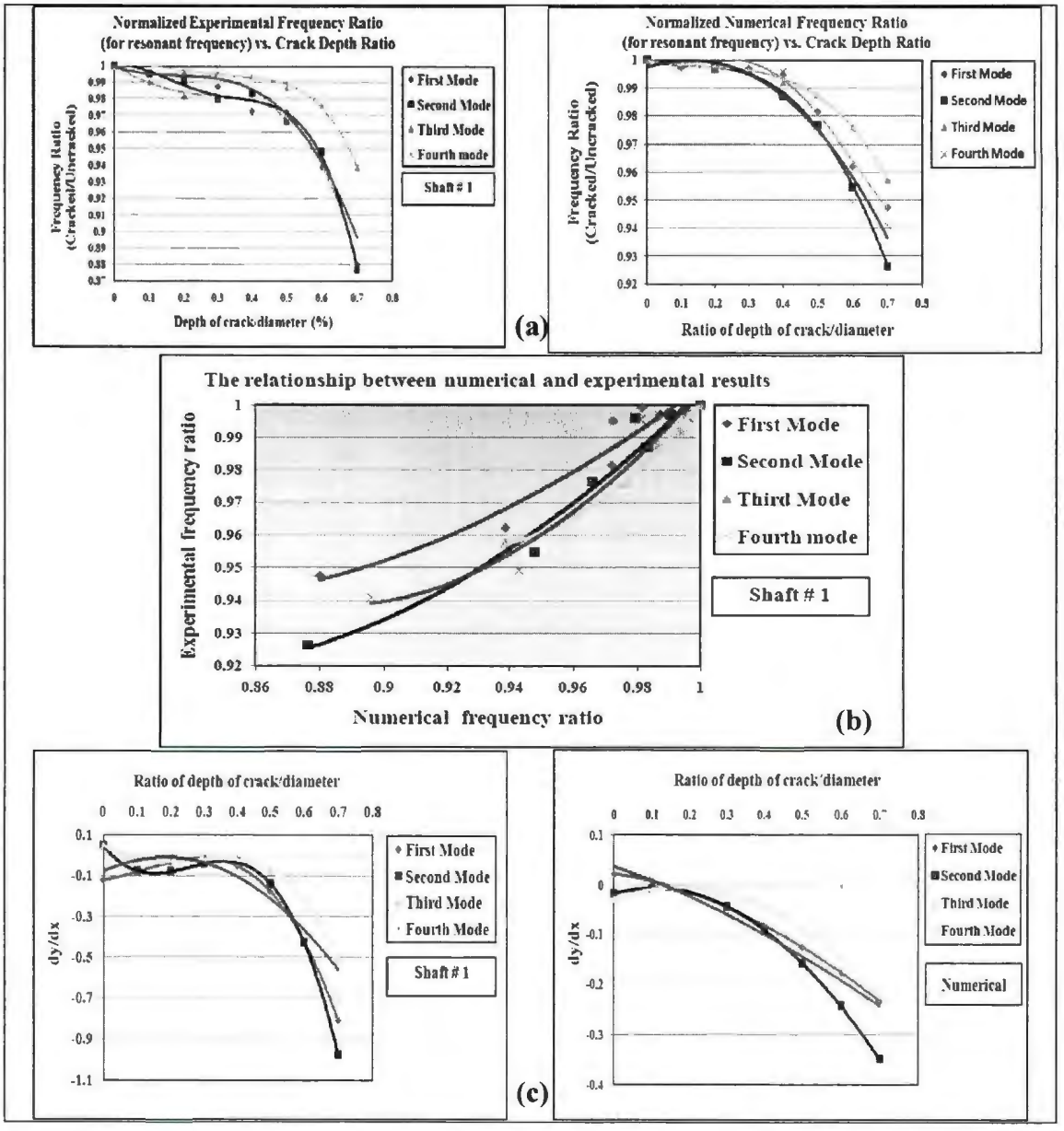

Figure J.1.1 Comparison of Experimental and Numerical Results of Shaft # 1 for (at Four Resonant Modes): a) Experimental and Numerical Frequency Ratio versus Crack Depth Ratio; b) Relationship between Numerical and Experimental Results of Frequency Ratio; and c) Experimental and Numerical Slope of the Frequency Ratio vs. Crack Depth Ratio Curves.

J.1.2: Comparison of Experimental and Numerical Results Resonant Frequencies of Shaft # 3 for (at Four Resonant Frequencies Ratios)

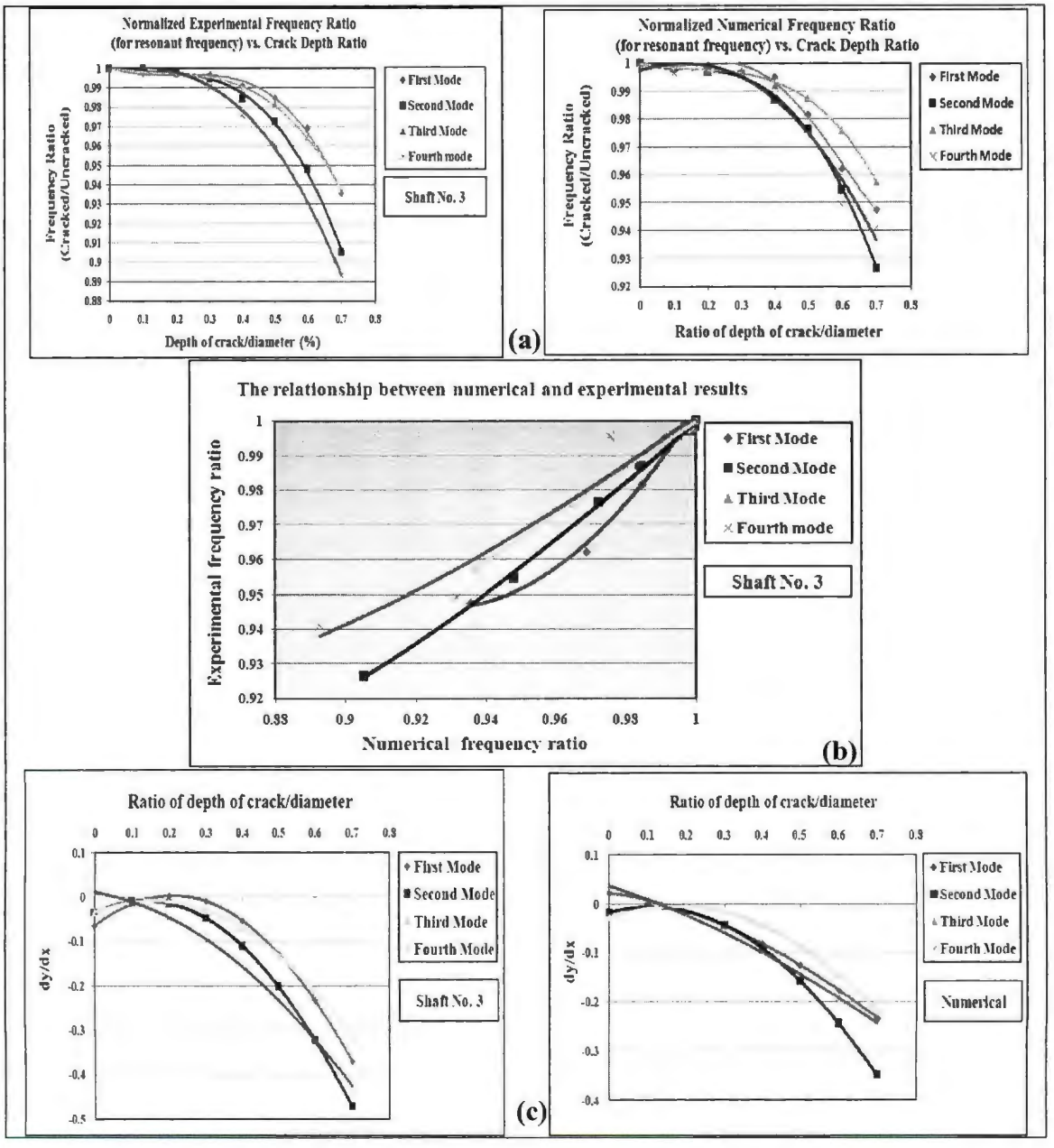

Figure J.1.2 Comparison of Experimental and Numerical Results of Shaft # 3 for (at Four Resonant Modes): a) Experimental and Numerical Frequency Ratio versus Crack Depth Ratio; b) Relationship between Numerical and Experimental Results of Frequency Ratio; and c) Experimental and Numerical Slope of the Frequency Ratio vs. Crack Depth Ratio Curves.

J.1.3: Comparison of Experimental and Numerical Results of Shaft # 1 for (at Two Anti-Resonant Frequency Ratios)

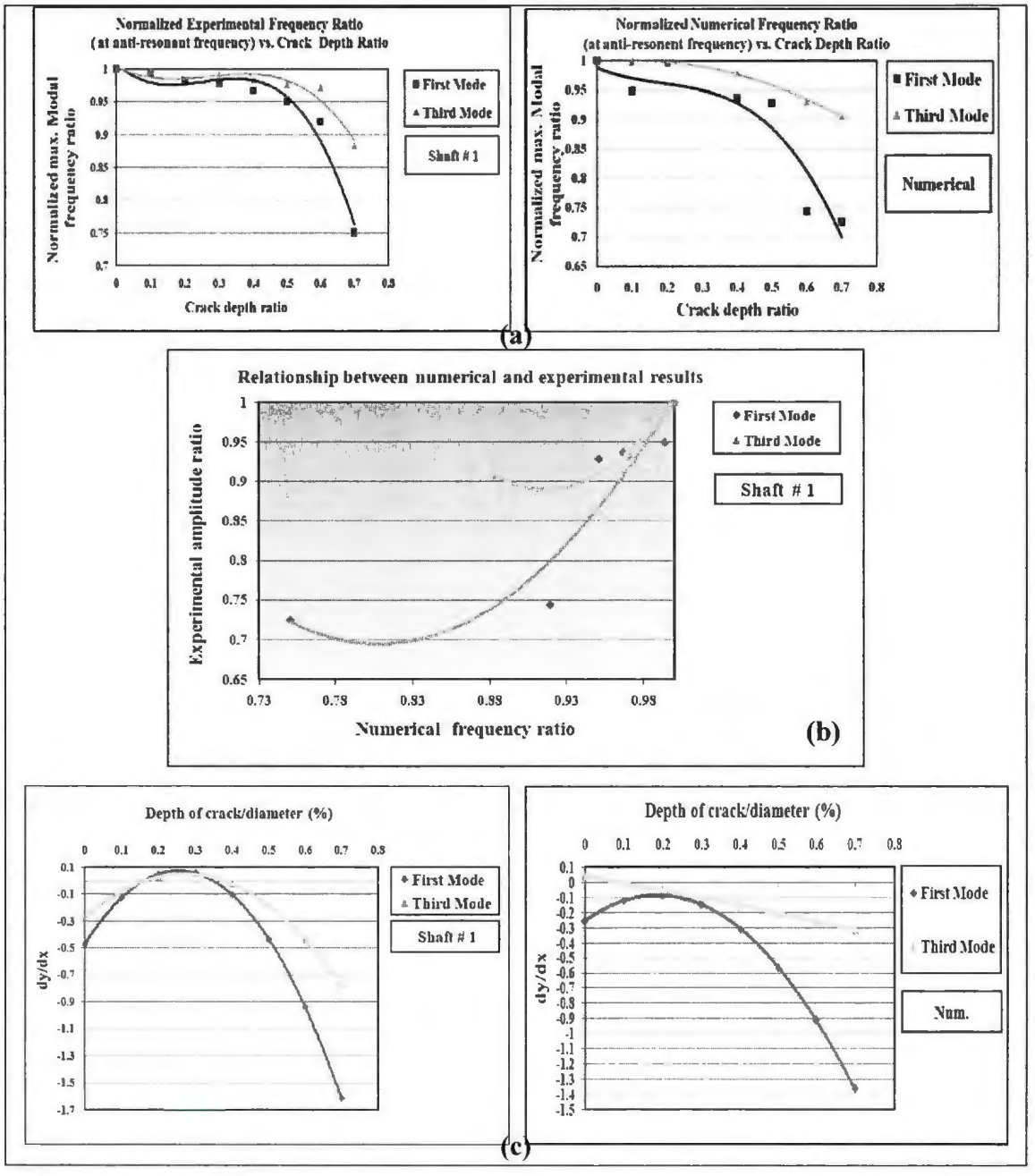

Figure J.1.3 Comparison of Experimental and Numerical Results for (First and Third Modal Frequencies): a) Experimental and Numerical Ant-Resonant Frequency Ratio versus Crack Depth Ratio; b) The Relationship between Numerical and Experimental Results of Anti-Resonant Frequency Ratio and c) Experimental and Numerical Slope of the Frequency Ratio vs. Crack Depth Ratio.

J.1.4 Comparison of Experimental and Numerical Results of Shaft # 3 for (at Two Anti-Resonant Frequency Ratios)

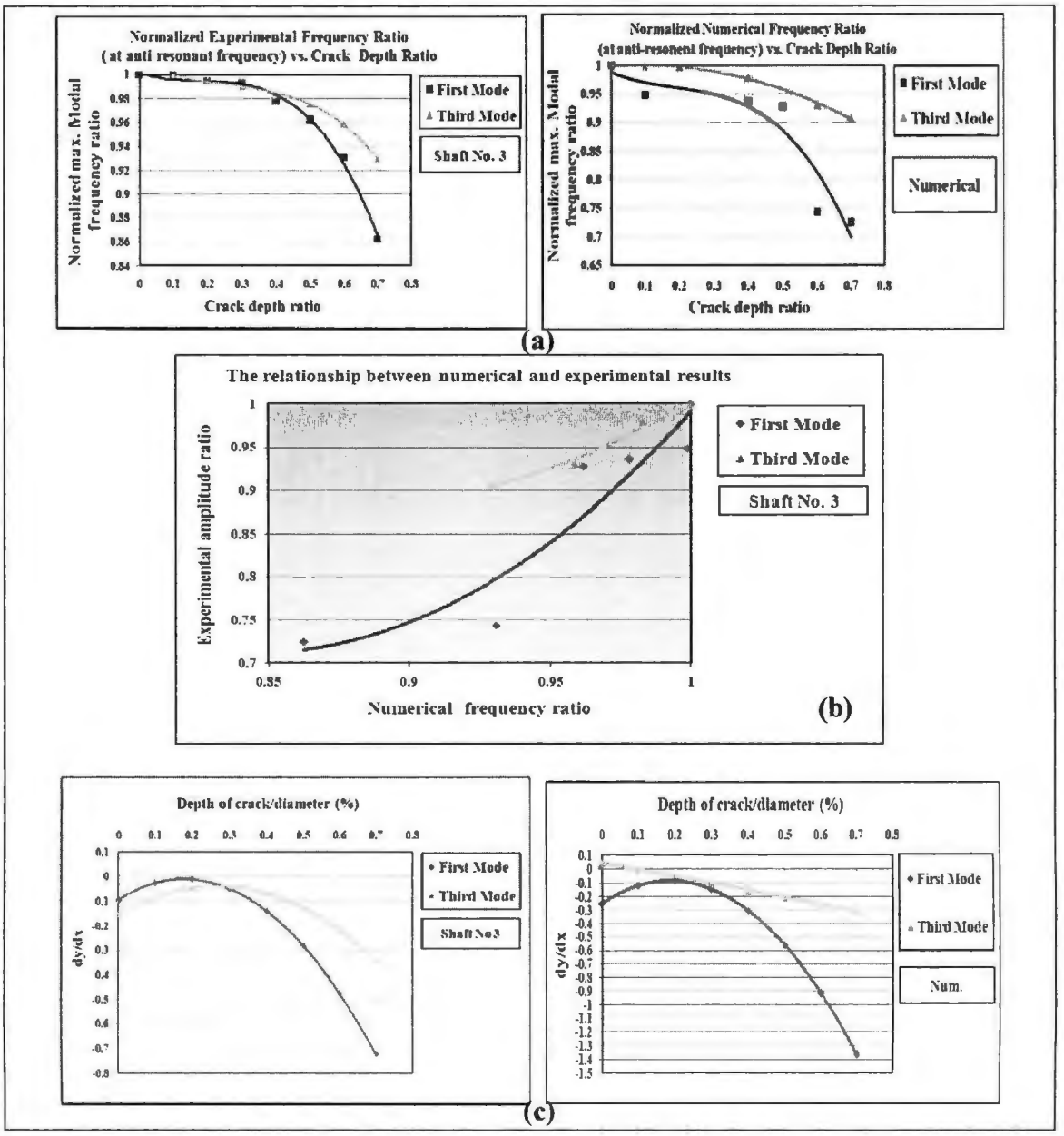

Figure J.1.4 Comparison of Experimental and Numerical Results for (First and Third Modal Frequencies): a) Experimental and Numerical Ant-Resonant Frequency Ratio versus Crack Depth Ratio; b) The Relationship between Numerical and Experimental Results of Anti-Resonant Frequency Ratio and c) Experimental and Numerical Slope of the Frequency Ratio vs. Crack Depth Ratio.

Appendix K – "Velocity Frequency Response of the Rotor Shaft system"

K.1.1: The Responses of the System under Test (Impact Excitation) for Experimental and Numerical Results. Shaft # 1

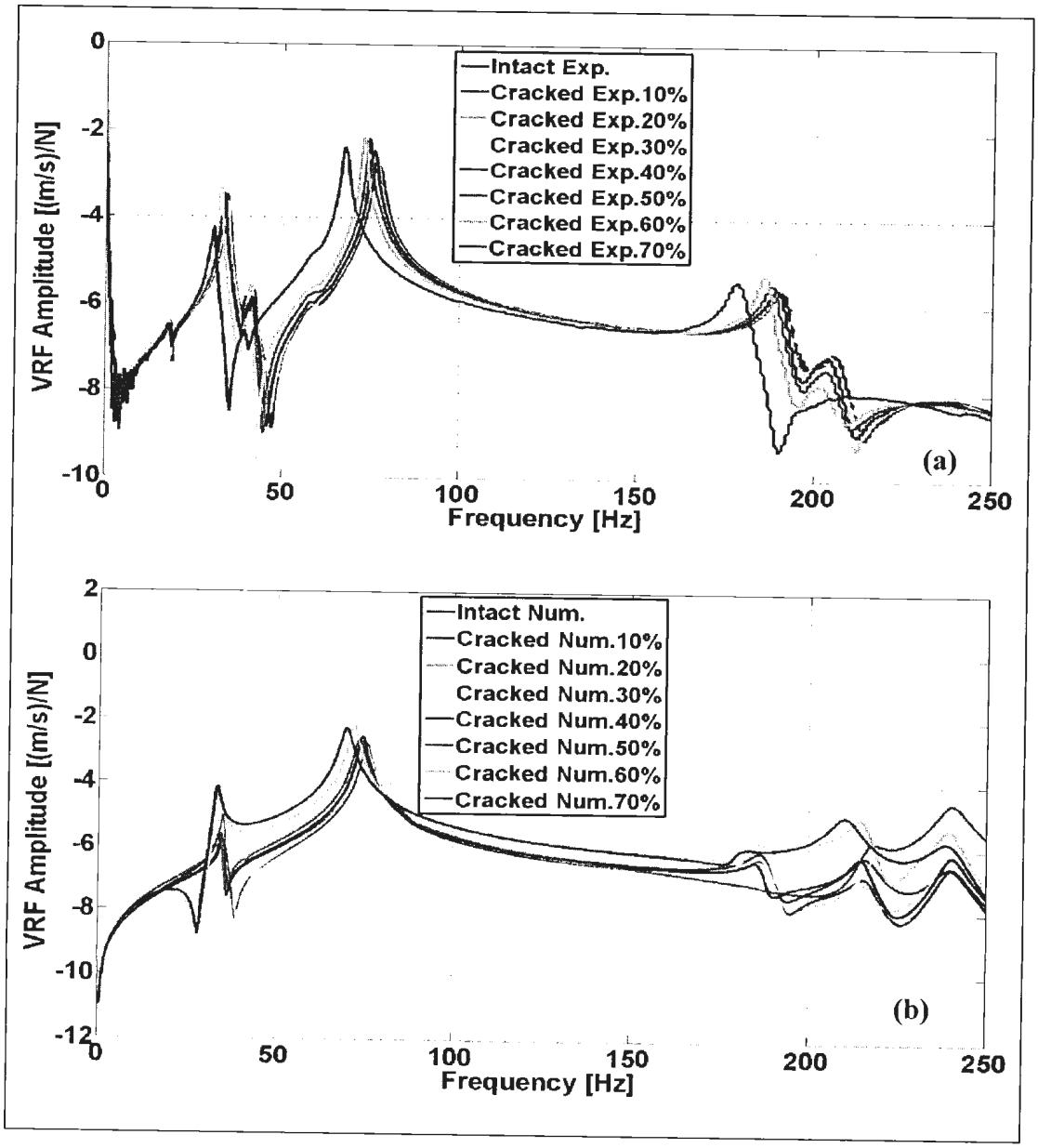

Figure K.1.1 Responses of the System for; a) Experimental; and b) Numerical Computations of Velocity Response Functions (VRFs) for Shaft # 1.

K.1.2: Comparisons for All Cases (Intact VRFs, Cracked 10% VRFs, Cracked 20% VRFs, Cracked 30% VRFs, Cracked 40% VRFs, Cracked 50% VRFs, Cracked 60% VRFs, and Cracked 70% VRFs.) For Response Functions of Experimental and Numerical Computations - Shaft # 1

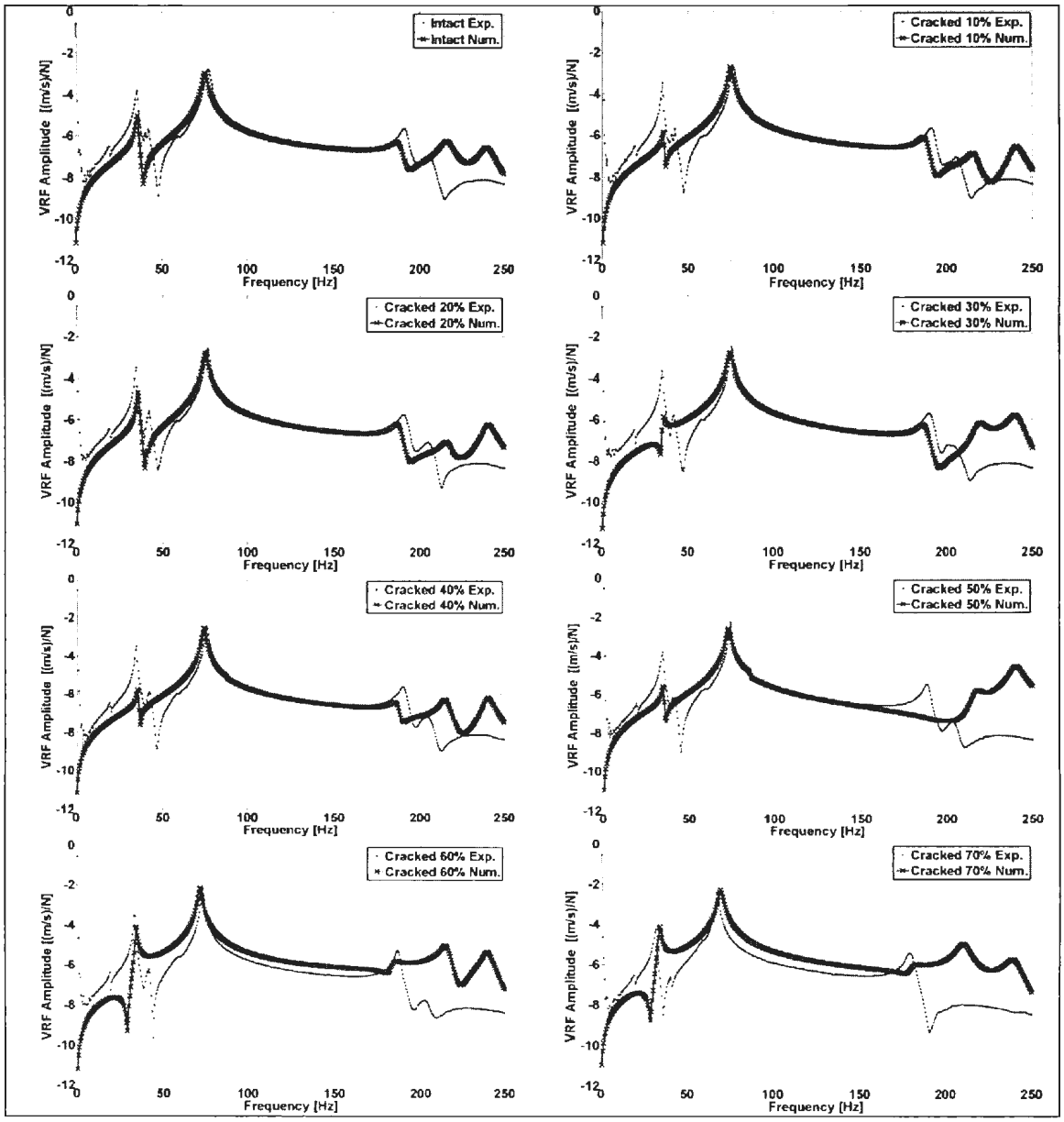

Figure K.1.2 Comparison of Velocity Responses Functions (VRF) in Experimental and Numerical Computations: Intact VRFs, Cracked 10% VRFs, Cracked 20% VRFs, Cracked 30% VRFs, Cracked 40% VRFs, Cracked 50% VRFs, Cracked 60% VRFs, and Cracked 70% VRFs; for Shaft # 1

K.1.3: The Velocity Responses of the System under Test (Impact Excitation) and the Corresponding Experimental and Numerical Results - Shaft # 3

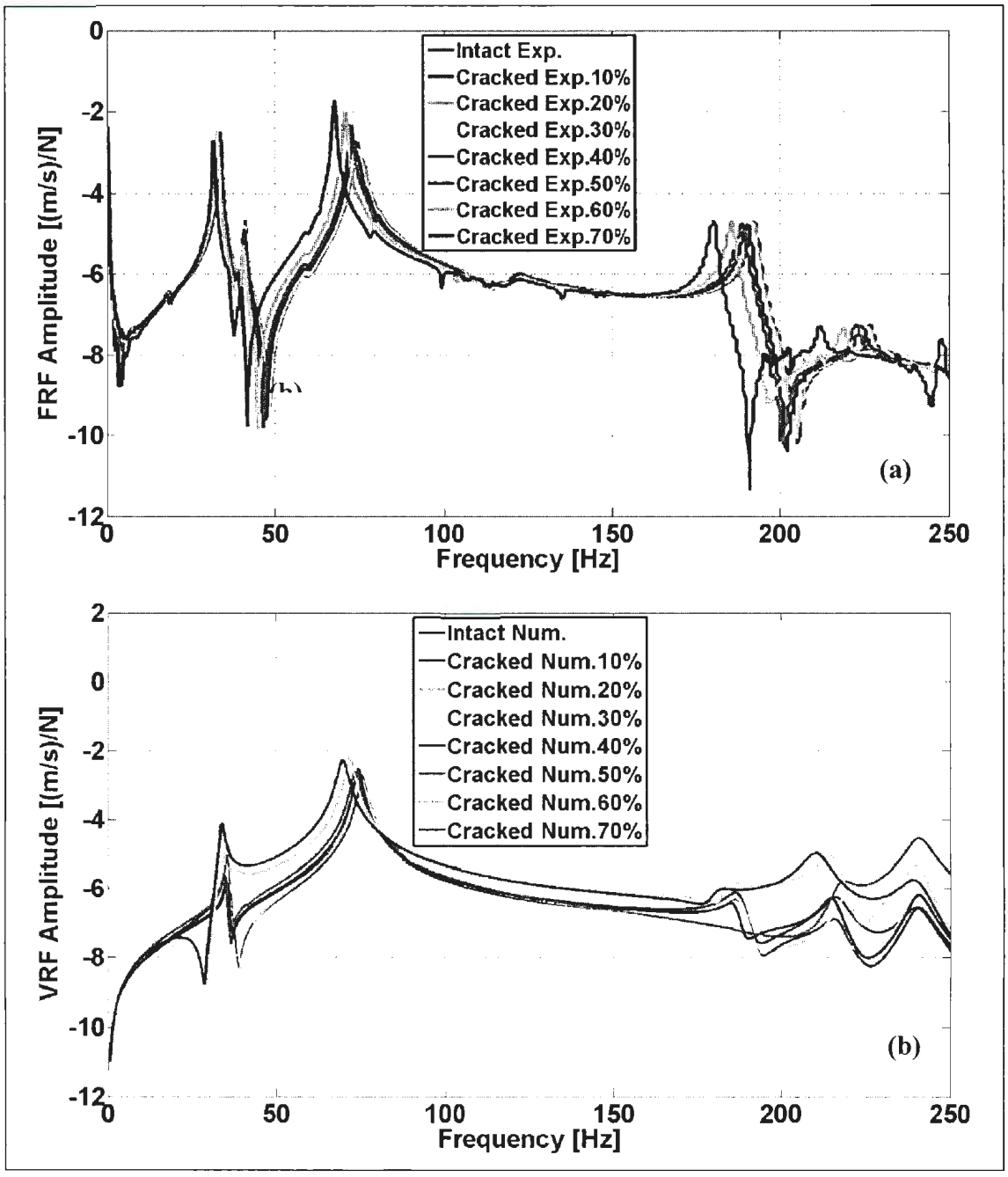

Figure K.1.3 Responses of the System for; a) Experimental; and b) Numerical Computations of Velocity Response Functions (VRFs) for Shaft # 3

K.1.4: Comparisons for all Cases (intact VRFs, cracked 10% VRFs, cracked 20% VRFs, cracked 30% VRFs, cracked 40% VRFs, cracked 50% VRFs, cracked 60% VRFs, and cracked 70% VRFs.) of Response Functions for Experimental and Numerical Computations - Shaft # 3

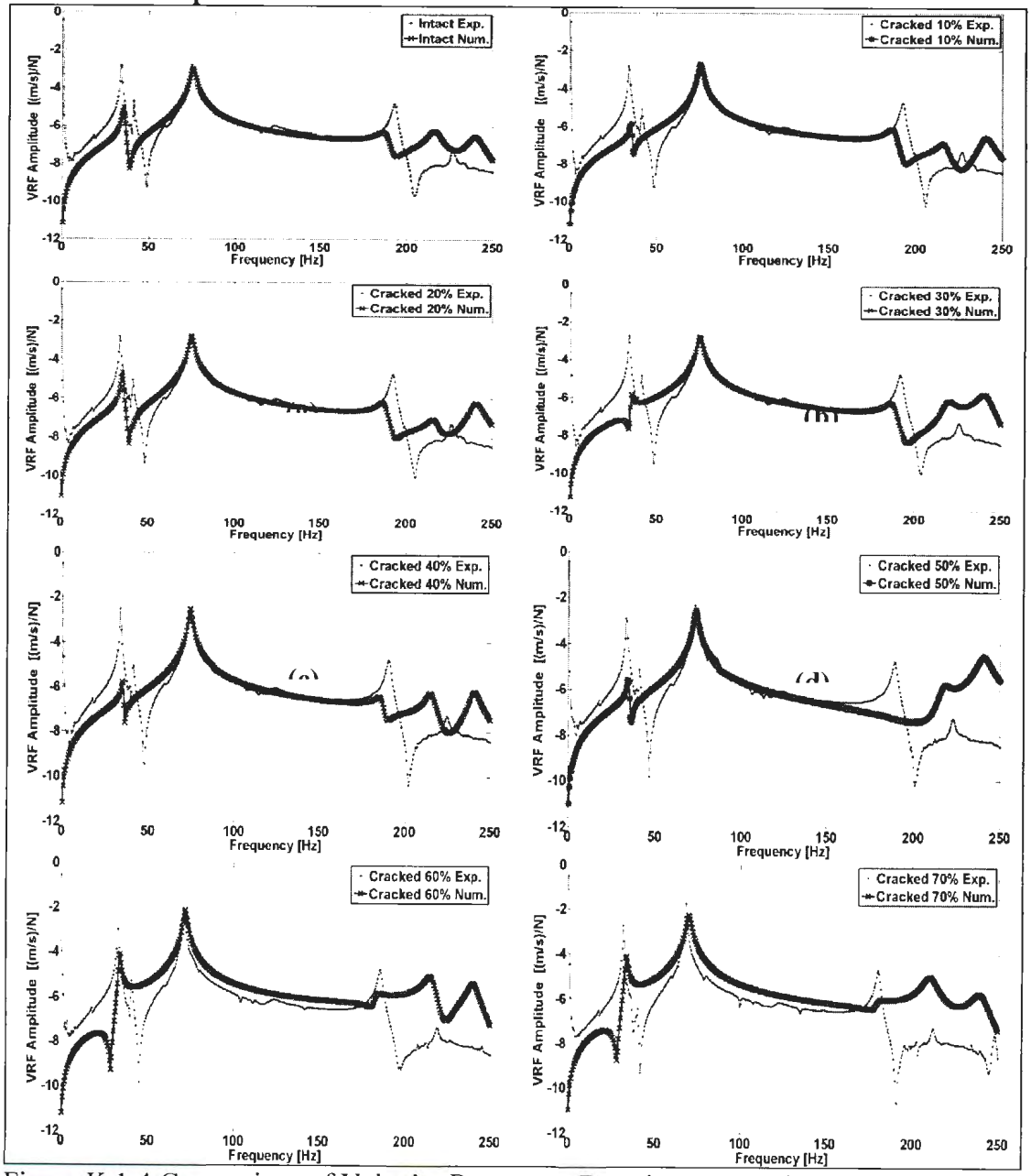

Figure K.1.4 Comparison of Velocity Responses Functions (VRF) in Experimental and Numerical Computations: Intact VRFs, Cracked 10% VRFs, Cracked 20% VRFs, Cracked 30% VRFs, Cracked 40% VRFs, Cracked 50% VRFs, Cracked 60% VRFs, and Cracked 70% VRFs; for Shaft # 3

Appendix L – "Mechanical Impedances of Rotor Shaft-propeller-bearing System Obtained for Vertical Vibrations"

L.1.1: The Computed Mechanical Impedances of the Rotor Shaft for the Various Crack Depth Ratios (0.0 To 0.7) – Shaft # 1

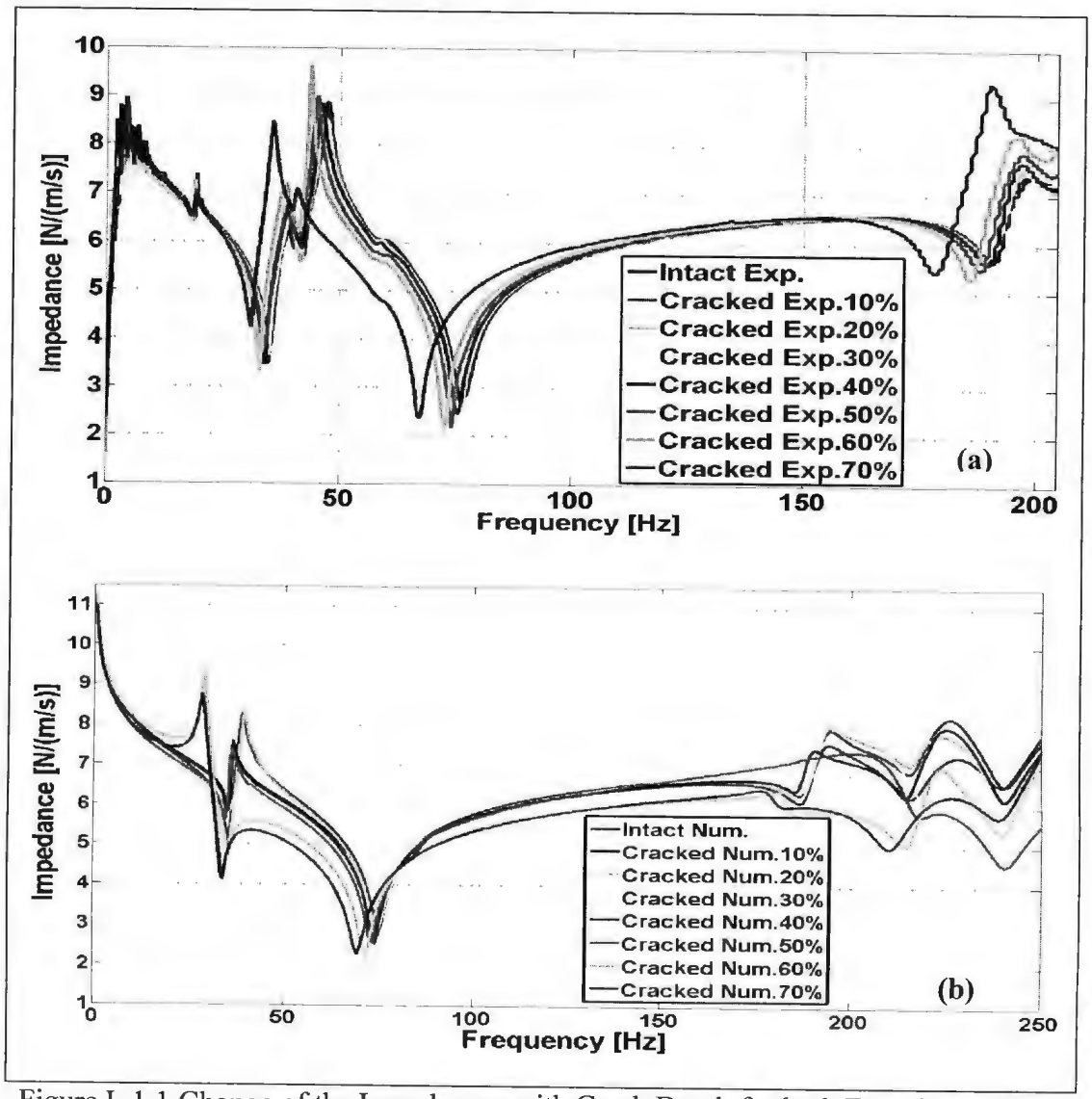

Figure L.1.1 Change of the Impedances with Crack Depth for both Experimental and Numerical Results for Shaft # 1

L.1.2.1: The Mechanical Impedances of Rotor Shaft-propeller-bearing System Obtained for Vertical Vibrations – Shaft # 1

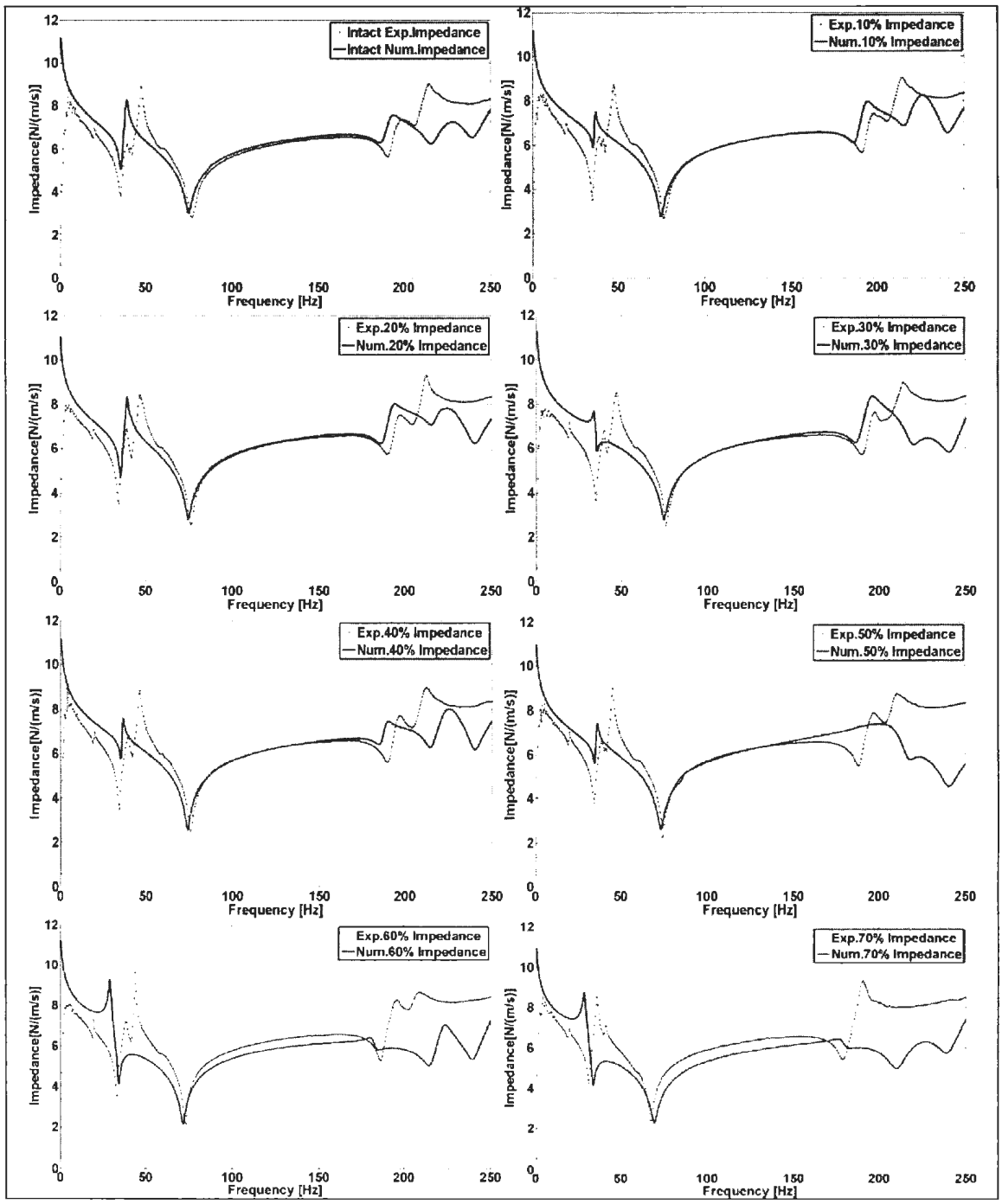

Figure L.1.2.1 Variation of Experimental and Numerical Impedance for Different Crack Depths for Shaft # 1

L.1.2.2: The Mechanical Impedances of Rotor Shaft-propeller-bearing System Obtained for Vertical Vibrations – Shaft # 3

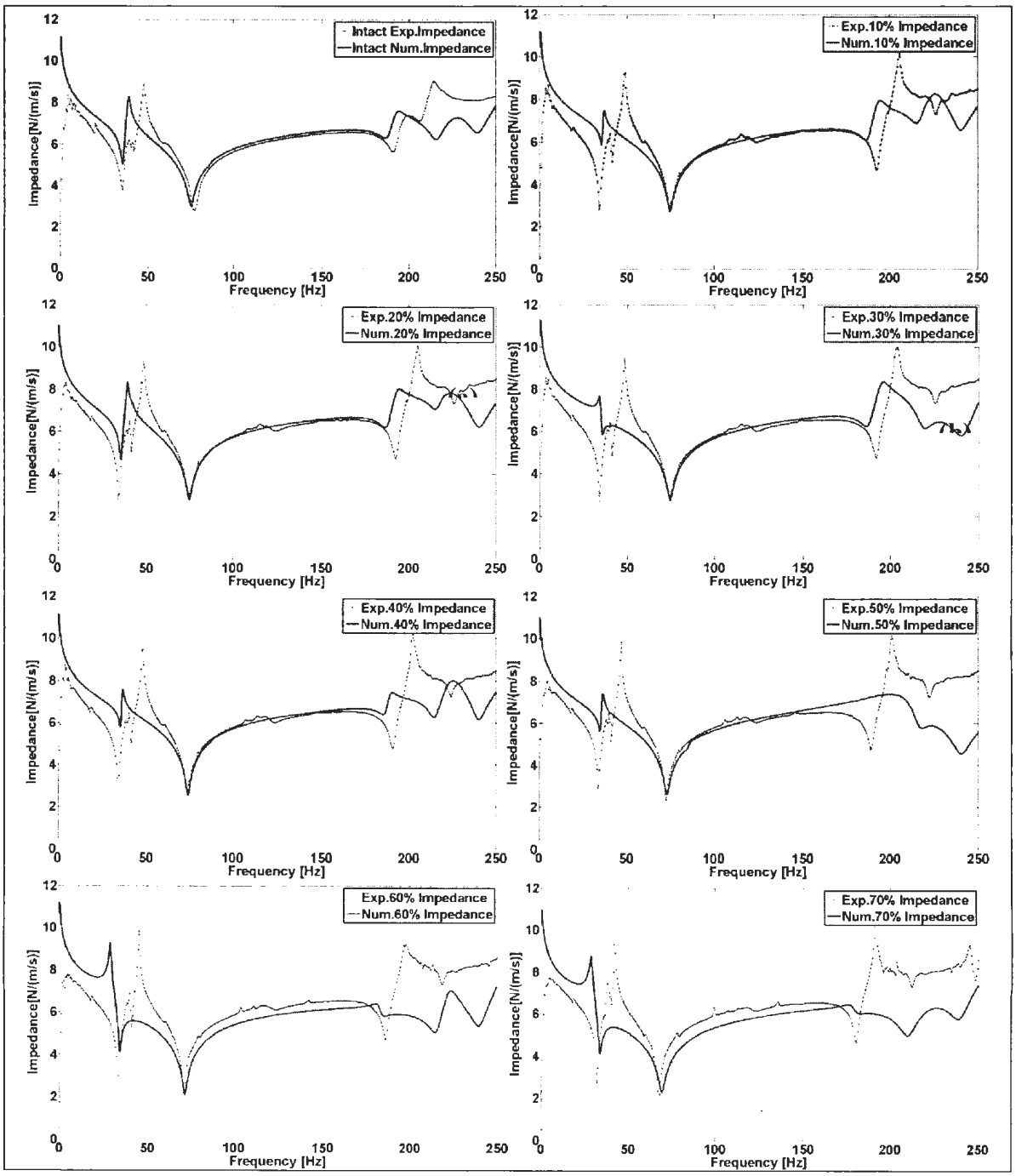

Figure L.1.2.2 Variation of Experimental and Numerical Impedance for Different Crack Depths for Shaft # 3

L.1.3: Experimental and Numerical Changes in Impedance and Mobility for Intact and 70% Crack Depths Ratios.

L.1.3.1: Experimental and Numerical Changes in Mobility for Intact and 70% Crack Depths Ratios.

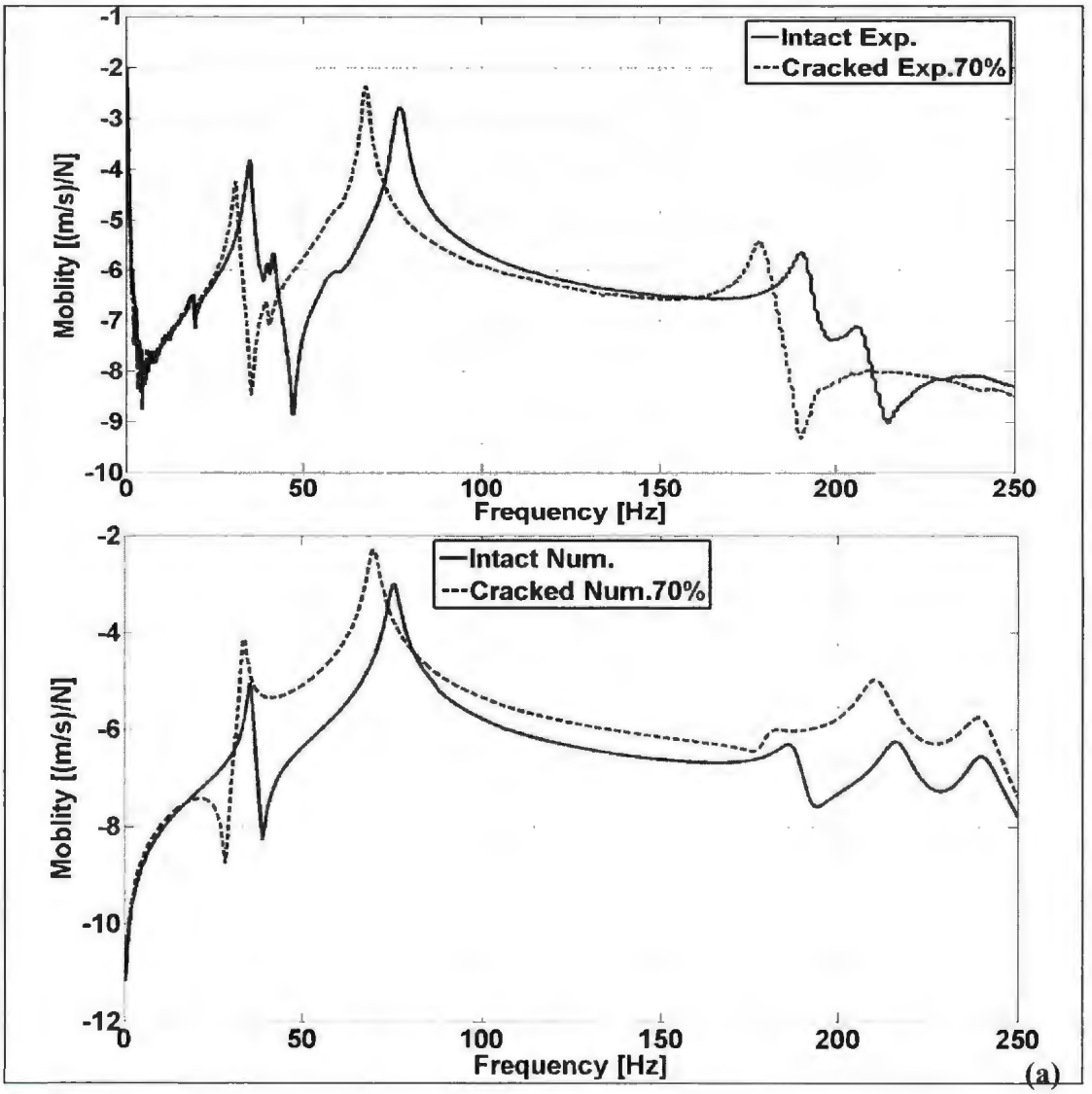

Figure L.1.3.1.1 Changes in the Mobility between Intact and 70% Crack Depth Ratio for Experimental and Numerical Results for Shaft # 1

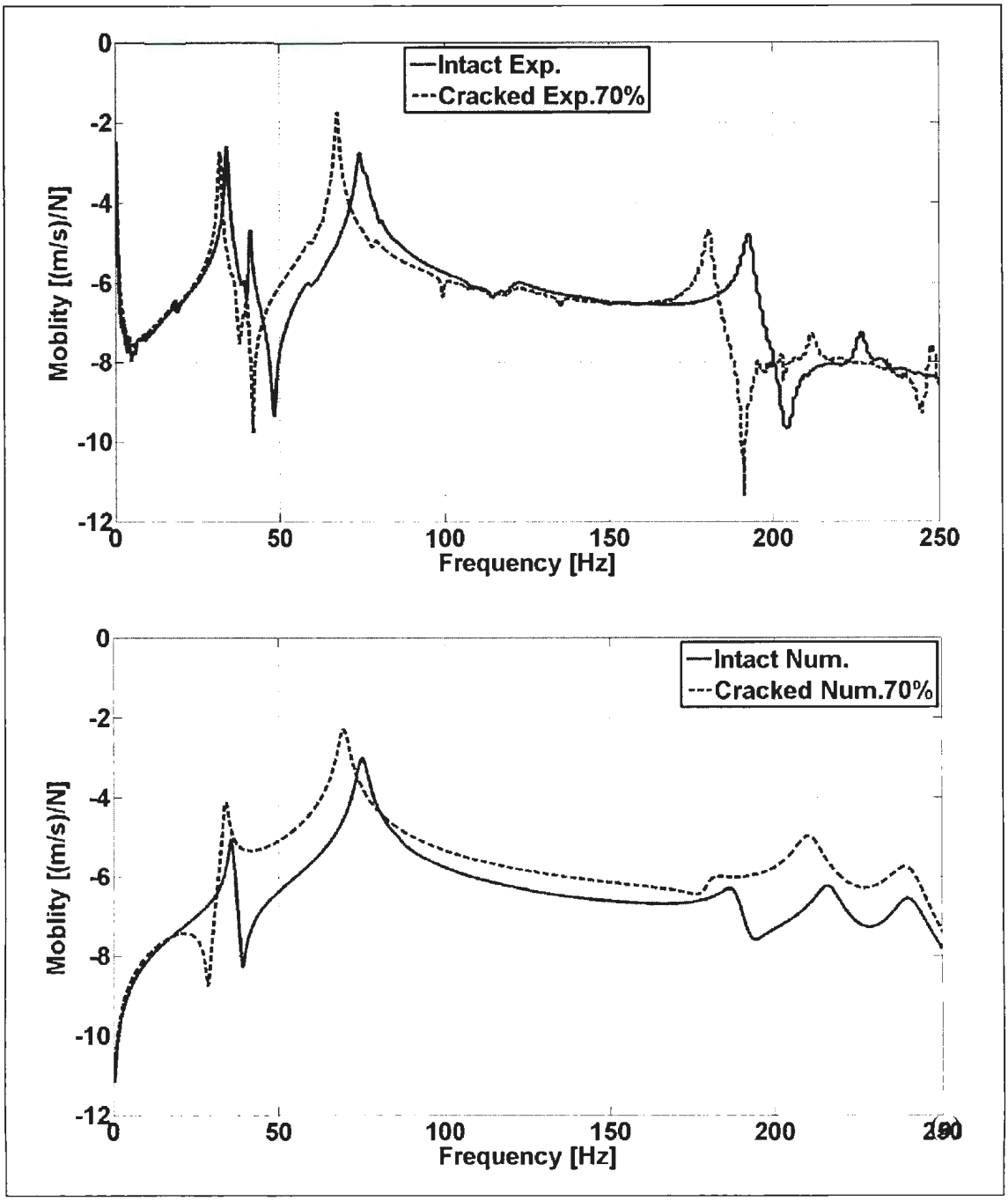

Figure L.1.3.1.2 Changes in the Mobility between Intact and 70% Crack Depth Ratio for Experimental and Numerical Results for Shaft # 3

L.1.3.2: Experimental and Numerical Changes in Impedance for Intact and 70% Crack Depths Ratios.

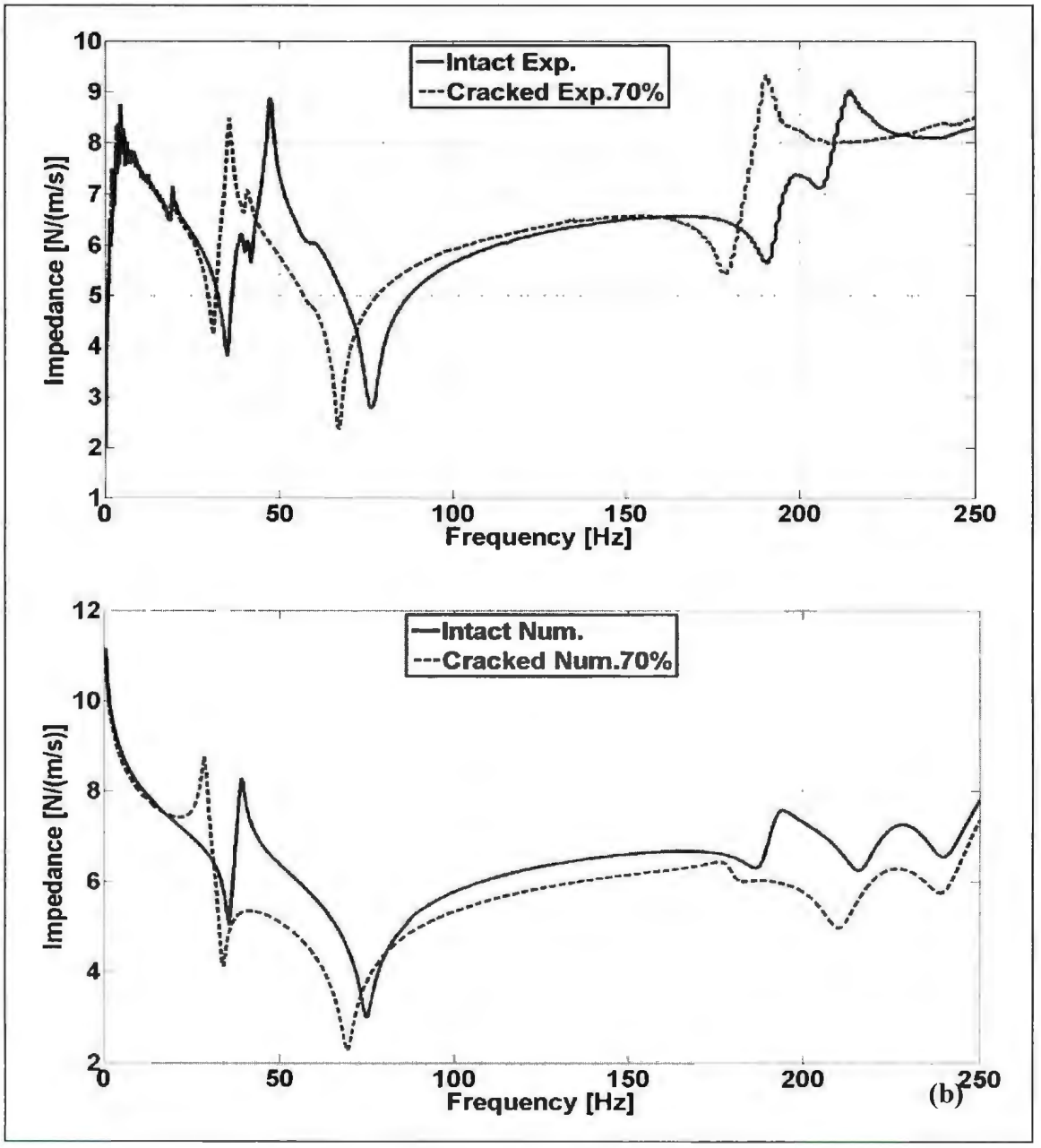

Figure L.1.3.2.1 Changes in the Impedance between Intact and 70% Crack Depth Ratio for Experimental and Numerical Results for Shaft # 1

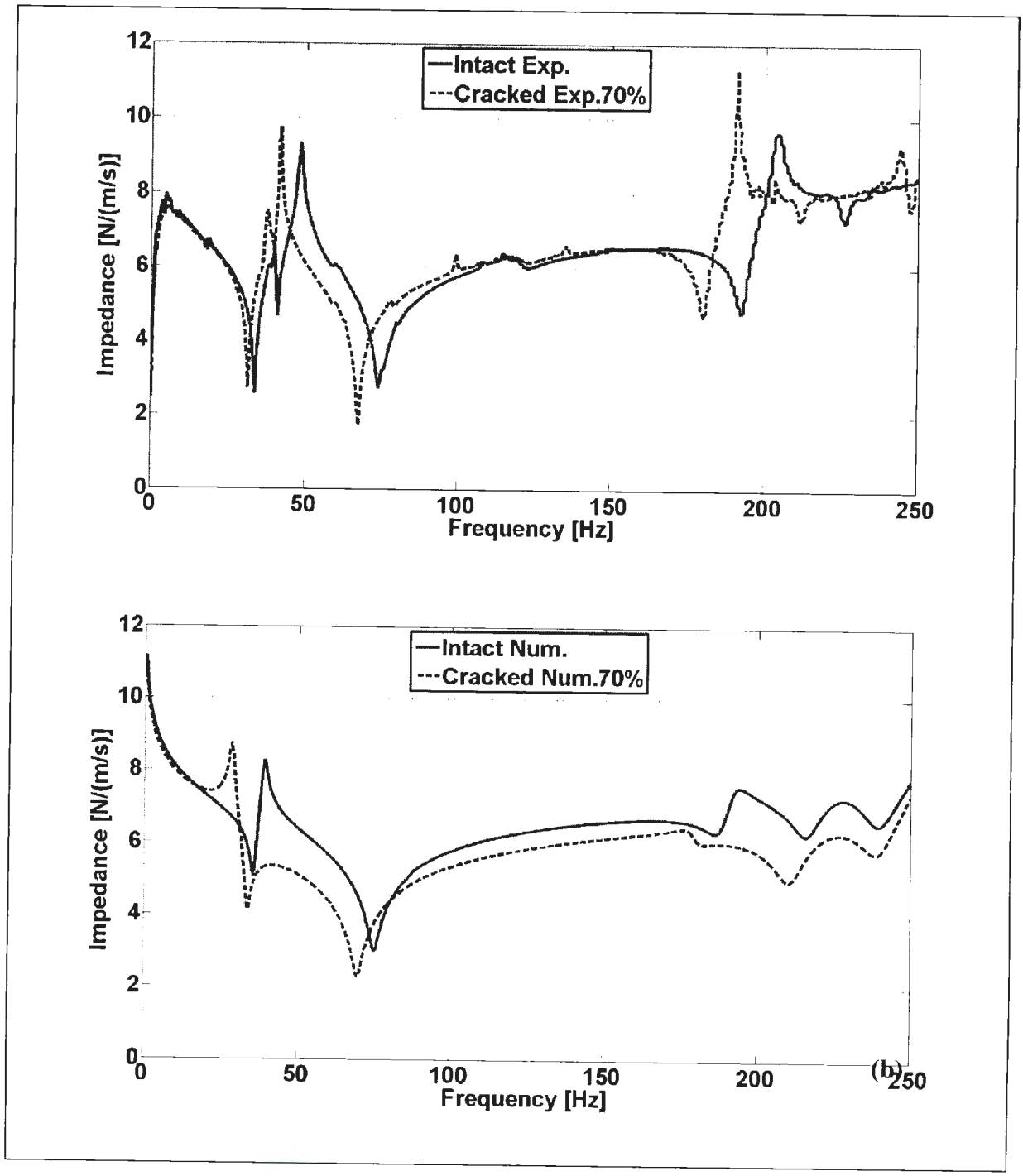

Figure L.1.3.2.2 Changes in the Impedance between Intact and 70% Crack Depth Ratio for Experimental and Numerical Results for Shaft # 3

L1.4 The Experimental Impedance Amplitude Ratio [(maximum impedance amplitude at zero crack)/ (maximum impedance amplitude at different crack depths)] Plots and Slope of Impedance as a Function of Crack Depth Ratio at Resonant Frequency

L.1.4.1 The Experimental Impedance Amplitude Ratio – shaft # 1

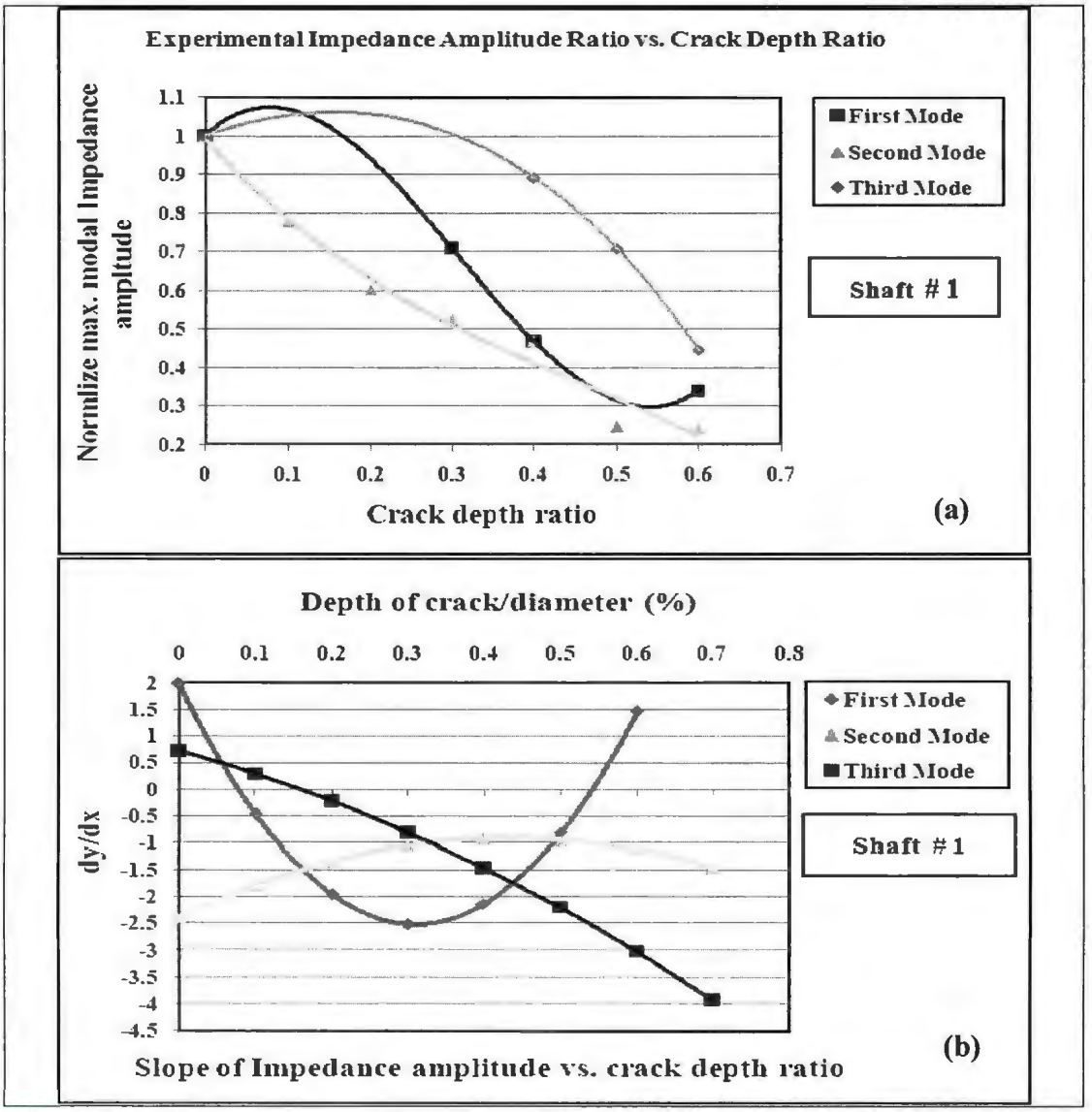

Figure L.1.4.1 Comparison of Experimental and Numerical Results for: a) Amplitude Ratio versus Crack Depth Ratio; and b) Slope of Impedance Amplitude versus Crack Depth Ratio – Shaft # 1

L.14.2 The Experimental Impedance Amplitude Ratio – shaft # 3

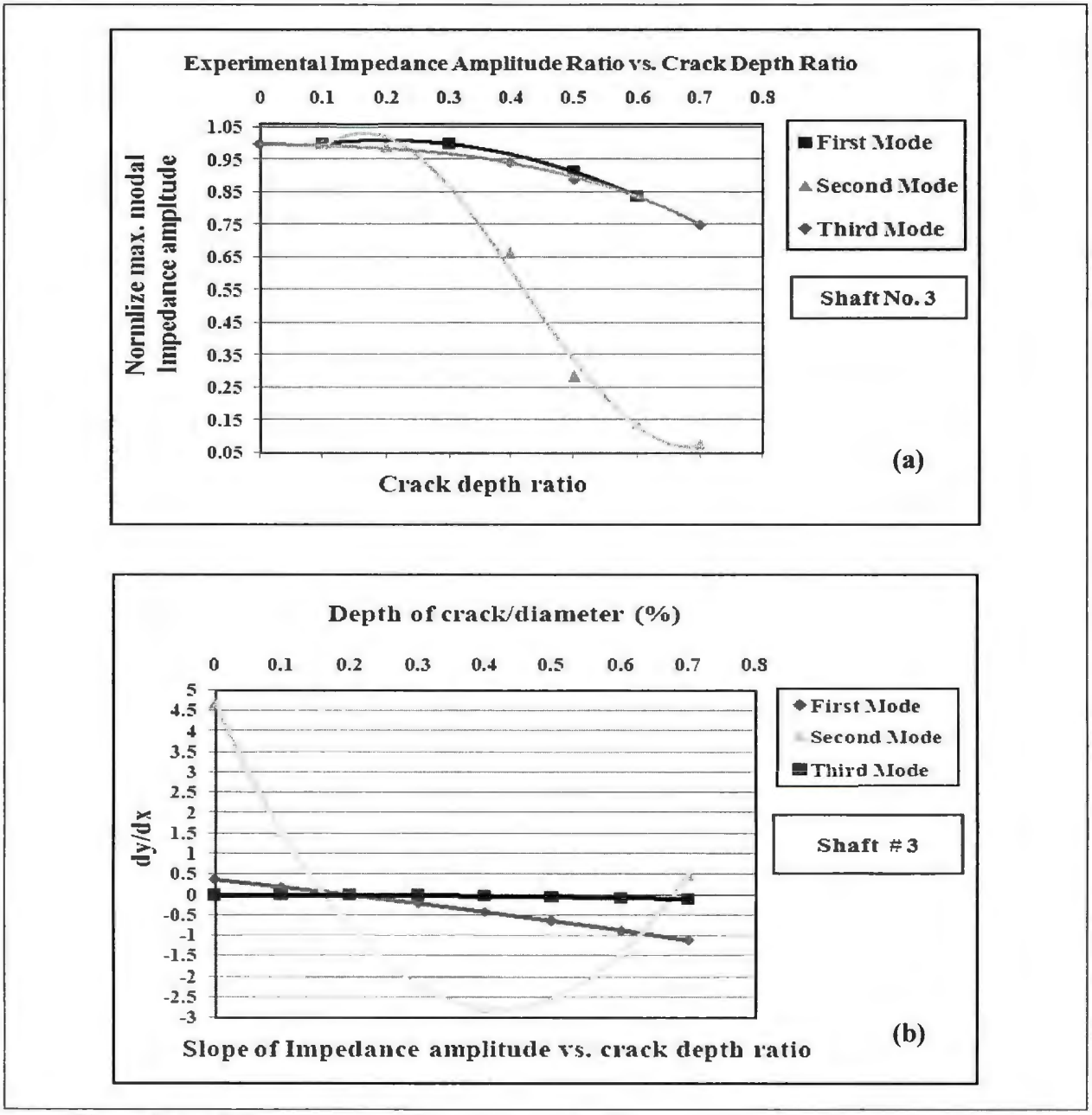

Figure L.1.4.2 Comparison of Experimental and Numerical Results for: a) Amplitude Ratio versus Crack Depth Ratio; and b) Slope of Impedance Amplitude versus Crack Depth Ratio – Shaft # 3

Thankfully much